Atrial Arrhythmia Diagnosis Using the 12-Lead ECG

Machine learning leveraging in silico and clinical signals

Zur Erlangung des akademischen Grades eines

DOKTORS DER INGENIEURWISSENSCHAFTEN (Dr.-Ing.)

von der KIT-Fakultät für

Elektrotechnik und Informationstechnik

des Karlsruher Instituts für Technologie (KIT)

genehmigte

DISSERTATION

von

Giorgio Luongo, M.Sc.

geb. in Turin, Italy

Abstract

The electrocardiogram (ECG) in general, and the 12-lead ECG in particular, is one of the most common and widely available digital device that can be found in clinical facilities to measure the electrical activity of the heart. Therefore, it is considered the gold standard tool for this purpose. It is an inexpensive and non-invasive monitoring device that allows for rapid diagnosis of cardiovascular diseases (CVD). Among the most common CVDs there are atrial fibrillation (AFib or AF) and atrial flutter (AFlut or AFl). These two arrhythmias play a central role in the world's healthcare systems, being among the main reasons for hospitalization, and responsible for very high costs in all countries. Moreover, even if they are not a direct cause of death, they can lead to multiple complications up to heart failure. For the reasons mentioned above, AFib, and AFlut are the focus of this thesis. The content of this thesis is divided into two projects. The overall goal is to develop methods with the help of biosignal processing, electrophysiological simulations, and machine learning to characterize the arrhythmia, support diagnosis, and predict complications or therapy outcomes.

In the first project, in silico 12-lead ECGs produced from simulations at multiscale level are used to develop two signal processing algorithms for several AFlut mechanisms characterization: individual component, and spatial reduced recurrence quantification analysis (icRQA, and srRQA, respectively). Moreover, an analysis of the influence that the atrial and torso models have on the cardiac simulation results, thus on the resulting ECGs, is described. The findings from these two previous analyses are incorporated into the final study of the project: hybrid (in silico plus clinical data) and feature-based machine learning discrimination of three main AFlut categories (cavotricuspid isthmus-dependent, peri-mitral, and other left atrium AFlut classes). The two RQA algorithms allowed us to extract relevant features for AFlut differentiation. Analysis of models' influence suggested that many atrial geometries should be used in the computational framework to avoid overfitting and thus leading to the incapacity of such in silico data in the clinical practice use. The final hybrid classifier demonstrated how an automatic and non-invasive discrimination of different AFlut mechanisms is possible using appropriate features, computational simulations, and taking into account the findings of the previous studies.

The second project aims at estimating the location of AFib drivers with the surface ECG. Rotors and focal sources are simulated and considered as AFib drivers. A machine learning approach only trained on in silico 12-lead ECGs is implemented to discriminate between AFib drivers located near the pulmonary veins (PVs) vs. extra-PVs atrial areas. Moreover, the success of acute AFib termination by ablation procedure is studied and linked to the

clinical relevance that such classifier may have in clinical practice. The last study of this second project aims at the prediction of one of the AFib complications (i.e., heart failure) using clinical single-lead ECG signals.

Machine learning enabled the identification of AFib drivers located near PVs, also suggesting that PV isolation (PVI) is the most suitable therapy to terminate the arrhythmia in such cases. On the contrary, when proceeding with PVI for AFib drivers located outside the PV areas, the arrhythmia did not terminate. In these cases, physicians should plan further ablation procedures. Moreover, the use of a classifier trained only on simulated data and demonstrating to be effective on clinical test data may open the door to the use of in silico data for machine learning. To conclude, the successful prediction of AFib-induced heart failure has proven the existence of a link between some AFib cases and this serious complication, thus providing physicians with a tool to recognize when urgent action is needed to reduce patient safety risks.

In all studies in which in silico ECGs are used to develop and tune the machine learning algorithms, tests on clinical data are performed to demonstrate the real applicability of these methods in healthcare. Advantages compared to existing approaches are discussed and all the studies have been published, or are under review, in peer-reviewed journals or in a conference proceeding. The results from the two projects demonstrate how simulated data can be used to develop, and improve adequate ECG signal processing methods, and how diagnosis, and therapy planning can be supported. Furthermore, the potential of the combination of simulations and machine learning for overcoming the problem of clinical data not available in large scale is demonstrated. The proposed methods can be used to support ablation procedure planning, arrhythmia diagnosis, complication prediction, and invasive procedure time reduction, and it is therefore likely to improve the outcome of the patients.

Zusammenfassung

Das Elektrokardiogramm (EKG) im Allgemeinen und das 12-Kanal-EKG im Besonderen gilt als gebräuchlichste Standardmethode zur Messung der elektrischen Aktivität des Herzens und ist in klinischen Einrichtungen weit verbreitet. Es ist ein kostengünstiges und nicht-invasives Überwachungsgerät, das eine schnelle Diagnose von Herz-Kreislauf-Erkrankungen (CVD) ermöglicht. Zu den häufigsten Herz-Kreislauf-Erkrankungen gehören das Vorhof-flimmern (AFib oder AF) und das Vorhofflattern (AFlut oder AFl). Diese beiden Herzrhyth-musstörungen spielen eine zentrale Rolle für die Gesundheitssysteme der Welt, da sie zu den Hauptgründen für Krankenhausaufenthalte gehören und daher in allen Ländern sehr hohe Kosten verursachen. Auch wenn sie keine direkte Todesursache sind, können sie zu zahlreichen Komplikationen bis hin zum Herzversagen führen. Aus diesem Grund stehen Vorhofflimmern und AFlut im Mittelpunkt dieser Arbeit. Das übergeordnete Ziel dieser Arbeit ist es, mit Hilfe von Biosignalverarbeitung, Computersimulationen und maschinellem Lernen Methoden zu entwickeln, um die Arrhythmie zu charakterisieren, die Diagnose zu unterstützen und Komplikationen oder Therapieergebnisse vorherzusagen.

Im ersten Projekt wurden mit Hilfe von simulierten in-silico 12-Kanal-EKGs zwei Sig-nalverarbeitungsalgorithmen für die Charakterisierung verschiedener AFlut-Mechanismen entwickelt: die individual component und die spatial reduced recurrence quantification anal-ysis (icRQA bzw. srRQA). Außerdem wurde eine Analyse des Einflusses der Vorhof- und Torsomodelle auf die Herzsimulation und damit auf die resultierenden EKGs beschrieben. Die Ergebnisse dieser beiden vorangegangenen Analysen flossen in die abschließende Studie ein: eine hybride (in-silico plus klinische Daten) und merkmalsbasierte Unterscheidung von drei Hauptkategorien von AFlut (Klassen mit Abhängigkeit vom cavotricuspidalen Isthmus, peri-mitrale und andere AFlut-Klassen des linken Vorhofs). Die beiden RQA-Algorithmen ermöglichten es, relevante Merkmale für die AFlut-Differenzierung zu extrahieren. Die Analyse des Einflusses der Modelle legte nahe, dass viele Vorhofgeometrien in die Simula-tionsstudien einbezogen werden sollten, um Overfitting zu vermeiden. Letzteres würde dazu führen, dass die Methode in der klinischen Praxis auf Grund fehlender Anpassungsfähigkeit nicht verwendet werden kann. Der abschließende hybride Klassifikator zeigte, wie eine automatische und nicht-invasive Unterscheidung verschiedener AFlut-Mechanismen unter Verwendung geeigneter Merkmale, elektrophysiologischer Simulationen und unter Berück-sichtigung der Erkenntnisse aus früheren Studien möglich ist. Das zweite Projekt zielte darauf ab, den Ort des Vorhofflimmerns anhand des Oberflächen-EKGs zu bestimmen. Es wurden Rotoren und fokale Quellen simuliert, die als Treiber von Vorhofflimmern in Frage

kommen. Ein maschineller Lernansatz, beiden nur mit in-silico 12-Kanal-EKGs trainiert wurde, wurde implementiert, um zwischen Vorhofflimmern in der Nähe der Pulmonalvenen (PVs) und außerhalb der PVs liegenden Vorhofbereichen zu unterscheiden. Darüber hinaus wurde der Erfolg der Terminierung des akuten Vorhofflimmerns durch Ablation untersucht sowie die klinische Relevanz eines solchen Klassifikators untersucht. Die letzte Studie dieses zweiten Projekts zielte auf die Vorhersage von Vorhofflimmer-Komplikationen bei Herzinsuffizienz unter Verwendung klinischer 1-Kanal-EKG-Signale ab. Mithilfe maschinellen Lernens konnten Vorhofflimmern-Treiber identifiziert werden, die sich in der Nähe von PVs befanden, was darauf hindeutete, dass die PV-Isolation (PVI) in solchen Fällen die geeignetste Therapiemethode zur Beendigung der Arrhythmie ist. Im Gegensatz dazu würde bei Vorhofflimmern außerhalb der PVs eine PVI nicht zur Terminierung der Arrhythmie führen, sodass die Ärzte weitere Ablationsverfahren planen sollten. Darüber hinaus könnte die Verwendung eines Klassifikators, der nur auf Simulationen trainiert wurde, aber auf klinischen Testdaten wirksam ist, die Tür zur Verwendung von in-silico Daten in der täglichen klinischen Praxis öffnen. Zusammenfassend lässt sich sagen, dass die erfolgreiche Vorhersage der durch Vorhofflimmern ausgelösten Herzinsuffizienz die Existenz eines Zusammenhangs zwischen einigen Fällen von Vorhofflimmern und dieser schwerwiegenden Komplikation bewiesen hat. Den Ärzten wurde somit ein Instrument an die Hand gegeben, das dringenden Handlungsbedarf erkennt, um die Risiken für die Patienten zu verringern.

In allen Studien, in denen in-silico EKGs zur Entwicklung und Optimierung der Algorithmen verwendet werden, wurden Tests mit klinischen Daten durchgeführt, um die tatsächliche Anwendbarkeit dieser Methoden in der klinischen Praxis zu demonstrieren. Die Vorteile gegenüber bestehenden Ansätzen wurden ausführlich erörtert, und alle Studien wurden in Fachzeitschriften mit Peer Review oder im Rahmen von Konferenzbeiträgen veröffentlicht bzw befinden sich derzeit unter Revision. Die Ergebnisse der beiden Projekte zeigen, wie simulierte Daten zur Entwicklung und Verbesserung geeigneter EKG-Signalverarbeitungsmethoden verwendet werden können und wie Diagnose und Operationsplanung unterstützt werden können. Darüber hinaus wird das Potenzial der Kombination von Simulationen und maschinellem Lernen zur Überwindung des Mangels an in großer Zahl verfügbaren klinischen Datensätze aufgezeigt. Die vorgeschlagenen Methoden können bei der Planung von Ablationsverfahren, der Arrhythmiediagnose, der Vorhersage von Komplikationen und der Verringerung der Prozedurzeit für invasive Eingriffe eingesetzt werden und sind daher geeignet, die Ergebnisse für die Patienten zu verbessern.

Acknowledgments

This thesis is the final product of my scientific work over the past few years at the Karlsruhe Institute of Technology (KIT) at the Institute of Biomedical Engineering (IBT). There are many people who have contributed to this success in different ways, and in the next few lines I would like to try to thank them all.

First of all, I would like to thank Prof. Olaf Dössel for giving me this incredible opportunity, providing a stimulating and friendly work environment. His always valuable recommendations have been one of the keys to staying on track. Moreover, I would like to thank Prof. Roberto Sassi and Dr. Massimo W Rivolta whom I consider as my Masters in the art of machine learning and computer science. Our collaboration and friendship that started in Milan, and continued throughout the PhD years, contributed significantly to the success of this project. Another thanks goes to Prof. Pablo Laguna and Prof. Juan Pablo Martínez Jiménez, who hosted me in Zaragoza and made me feel at home as only their research team can do, also managing to obtain excellent scientific results thanks to their deep knowledge of biosignals. Thanks also to Dr. Johan De Bie, Dr. Nicoletta Marzocchi, and Patrick Noffke for the opportunity they gave me to experience working in an R&D team of a worldwide company, thus I could test how my future could look like. A special thanks goes to Prof. Diogo C Soriano for teaching and guiding me in the use of the complex recurrence quantification analysis in collaboration with Dr. Tiago P Almeida (I come later for you). Finally, I would also like to thank Dr. Axel Loewe. Completing this PhD in such a short period of time and with so many accomplishments would have been impossible without your support. Your search for a balance between friendship and supervision, and between independency and monitoring have been perfect for the way I work, and I am convinced this have taught me a lot both from a scientific point of view and from the point of view of project management, relationships and thus life. Thanks again.

All my colleagues around Europe and more deserve a special thank you. These past few years would not have been the same without you. The laughs, the fun and the shared friendship have allowed us to live with happiness through the stress of the PhD. Our teamwork, support and technical/scientific advice were the secret of our success. Therefore, I would like to thank all my colleagues at IBT. I will never forget the life in our institute. In particular I thank: Claudia Nagel for her support and her always generous smiles; Dr. Ekaterina Kovacheva for our moments of comfort and our crazy laughs; Laura Unger for being a person I could always count on; Dr. Jorge Sánchez for our wonderful friendship and his deep scientific knowledge that has been supportive multiple times; and Dr. Ady Naber,

Andreas Wachter, Steffen Schuler, Dr. Yannick Lutz, and Dr. Nicolas Pilia for our scientific discussions and your support to integrate me into a new and different culture from my own. Thank you also to all the colleagues/friends that I could not mention (there are too many of you!!), both to the old ones that have guided me during these years and to the newcomers that make these last months together so enjoyable. I would also like to thank the whole My-Atria "world", starting with the coordinator of the consortium Prof. Luca Mainardi, and the always organized Prof. Valentina Corino, and ending with my 11 colleagues scattered in different parts of Europe. It has been an incredible journey together.

I would like to thank all my friends now. I have to start with my second family in Germany: Michele, Giulia, Deborah, and Luca! Without you all this experience would not have been the same. In every moment you have always been there ready and available for me, as only a true family can do. I couldn't not thank Tiago, besides being a colleague you also became a true friend always open to a quick chat (never shorter than an hour... ridiculous!!). And finally I would like to thank my friends who stayed in Rome, especially Emilia, Lorenzo, and Monia who always gave me all their love, even if at a distance, and made my returns to Italy special.

Finally I thank my family, all of them, for their deep and continuous love. Thank you Mamma, simply for EVERYTHING. Thank you Papà, for your unwavering support. Thank you Sergio and Antonella, the brother and sister-in-law that everyone should have and who have recently given life to Enea, uncle's love. Thank you Nonna, Zia and Veronica for being always willing to be there for me and us. Last but not least, thanks to the love of my life, Dario. A few months after we met I mentioned you in the acknowledgments of my master's thesis, and now after 4 years you are still here, mentioned in my doctoral thesis. You have been my rock in these last years, despite the distance and difficulties. I cannot wait to start the next chapter together. Thanks again to all of you, I am lucky to have you.

Contents

Abbreviations

Ca^{2+}	calcium-ion
Cl^-	chloride-ion
K^+	potassium-ion
Na^+	sodium-ion
AA	antiarrhythmic
AF	atrial fibrillation
AFib	atrial fibrillation
AFl	atrial flutter
AFlut	atrial flutter
ANN	artificial neural network
AP	action potential
AUC	area under the curve
AV	atrioventricular
BCL	basic cycle lengths
BEM	boundary element method
BSP	body surface potential
BSPM	body surface potential map
CFAE	complex fractionated atrial electrogram
CMP	cardiomyopathies
CNN	convolutional neural network
CTI	cavotricuspid-isthmus
CVD	cardiovascular disease
DFT	discrete Fourier transform
DP	distance plot
DT	decision tree
ECG	electrocardiogram
F-wave	flutter wave
f-wave	fibrillation wave
FaMaS	fast marching simulation
FFT	Fourier transform
G-mean	geometric mean
icRQA	individual component recurrence quantification analysis
KNN	k-nearest neighbour

LA	left atrium
LAA	left atrial appendage
LAD	left atrium dilatation
LAT	local activation time
LOAO	leave-one-atrium-out
LOOCV	leave-one-out cross-validation
LOTO	leave-one-torso-out
LSPV	left superior pulmonary vein
LVEDD	left ventricular end-diastolic diameter
LVEF	left ventricular ejection fraction
LVSD	left ventricular systolic dysfunction
MI	mitral isthmus
MRI	magnetic resonance imaging
PC	principal component
PCA	principal component analysis
PPV	positive predicted value
PV	pulmonary vein
PVI	pulmonary vein isolation
RA	right atrium
rbNN	radial basis neural network
RL	roofline
ROC	receiver operating characteristic
RP	recurrence plot
RQA	recurrence quantification analysis
RSPV	right superior pulmonary vein
SA	sinoatrial
SD	standard deviation
srRQA	spatial reduced recurrence quantification analysis
TGF-β1	transforming growth factor-β1
TIA	transient ischemic attack
TMV	transmembrane voltage

Introduction

1.1 Motivation

Cardiovascular diseases (CVDs) cause today more than 4.1 million deaths per year in Europe alone. About 43% of total deaths (47% in women, 39% in men) are caused by CVDs within European Society of Cardiology member countries, bringing them to be one of the major problems of the world health system [1]. In contrast, cancer accounts for only under 1.3 million deaths per year in Europe [2]. Moreover, CVD costs the European Union over 210 billion EUR per year due to healthcare costs, productivity loss, and informal care by caregivers. The exact cause of CVD can vary, but it is known that secondary prevention, i.e., treatment of other underlying diseases, just as early prevention in the life course, reduces the risk of CVD events [3, 4]. Among CVDs, atrial arrhythmias that can lead to several complications (i.e., atrial fibrillation - AFib) are increasing, especially among younger adults [4], and patients with atrial arrhythmias have a fourfold increased risk of mortality compared to the general population [5]. Focusing on two life-threatening arrhythmias, AFib and atrial flutter (AFlut), they mostly shared the same risk factors like diabetes, smoking, history of myocardial infarction, and history of heart failure [6–9]. Regarding these two atrial arrhythmias, but generally for all CVDs, an early diagnosis and therapy can help to improve the outcome of the patients [10, 11].

Drug therapy is one of the first procedures to terminate arrhythmias such as AFib and AFlut. However, in case the medicines are either not tolerated or not effective, catheter ablation is performed. Catheter ablation is an invasive but low-risk procedure that scars small areas of heart tissue with the aim of stopping the rapid and irregular heartbeats. Destroying this tissue helps restore the heart's regular rhythm (i.e., sinus rhythm) [12]. The most common, but few, risk factors of ablation procedures are related to the catheters that may damage blood vessels, cause bleeding, or infections. Furthermore, it is still unclear which ablation techniques are the most efficient and which are the best targets to be ablated (e.g., arrhythmic drivers, low voltage areas, etc.) [13–15].

The electrocardiogram (ECG) is the major monitoring tool of the electrical activity of the heart over time. The gold standard ECG acquisition and diagnosis modality is the

12-lead ECG due to its availability and usability in nearly every clinical setting, and due to its capability to capture activity from different positions and planes (see section 2.2). This allows for a quick, inexpensive and non-invasive measurement of the electrical heart activity. Indeed, there are multiple different configurations to acquire ECG signals, these range from single-lead ECG (2 electrodes) to methods with over 100-lead ECG also called body surface potential mapping (BSPM) [16, 17]. BSPM has been used in both experimental and clinical settings for the detection and diagnosis of various pathological conditions. Many studies have demonstrated higher diagnostic and prognostic value of BSPM as compared to the 12-lead ECG. Nonetheless, BSPM has not become a routinely used clinical method [18]. The clinical effectiveness of this procedure has not been established and the added value of BSPM over traditional 12-lead ECG has not justified the additional procedural complexity and expense [19].

The ECG is the first device applied to derive an initial diagnosis in CVD patients. Using information obtained from ECG data (i.e., rhythmic, and morphological features), physicians attempt to identify the optimal treatment for each patient. Unfortunately, the use of only visual information from ECGs is often no longer sufficient for today's diagnostic ambition. Moreover, outside the clinical setting, ECG measurement devices become more and more included into disposable and wearable devices [20, 21]. The automatic detection and evaluation of heart diseases using not only clearly interpretable clinical features but also more complex ones (e.g., non-linear features) has the potential to support physicians in planning and decision making before and during treatment. The algorithms created to perform this automated analysis must be very accurate since they directly affect the treatment of the patient and therefore the patient outcome. All types of data bias must be eliminated by trying to create algorithms with a strong ability to generalize to unseen data, so that they work on every patient despite the possibility of large inter-patient variability. This requires a large amount of data, which is usually not available due to accessibility, privacy, and technological limitations that are very common in healthcare facilities. in silico ECG might avoid or reduce these problems, being self-produced and with a reliable ground truth. Computational modeling of the heart offers the possibility to generate as much data as required to monitor all influences independently. Furthermore, arrhythmia and their basic mechanisms can be studied and characterized without the risk of secondary and unknown activities (e.g., ventricular far field, noise, unknown and secondary mechanisms). Despite these qualities, until now computational modeling alone has only proven to be useful to understand the physiology of the heart, and has mostly been used as a support towards clinical applications without succeeding in gaining an active role in clinical practice. Moreover, experimental and clinical data have always been needed to optimize the tuning of methods and certainly to test such approaches.

In this thesis, two important atrial arrhythmias were focused on: AFib, and AFlut. In both projects, simulations were utilized to develop methods applied to patient data, and support the detection, characterization, and treatment of the diseases. in silico data were used both as support for clinical data, but also as a unique tool for the training of machine learning algorithms that can, in turn, be employed for clinical applications. In addition,

non-invasive 12-lead ECGs were used instead of BSPM due to the potential applicability of the algorithms implemented in this work within every hospital worldwide, without the need for large investments by healthcare facilities to buy new, uncommon acquisition systems. Specifically, the P-wave component of the ECGs was mostly used in this thesis.

1.2   Objectives of the Thesis

The general aim of this thesis is to develop ECG- and machine learning-based tools to support physicians in the characterization, diagnoses, ablation procedure planning, and complication prediction for patients with AFib and AFlut. These can be used to reduce the invasive procedure time and, therefore, the related costs by supporting the physicians in finding diagnoses, personalizing treatment, and improving the patient outcomes. As already stated, two major topics will be incorporated into this thesis: The characterization and discrimination of different AFlut mechanisms, and the localization of AFib drivers with acute ablation success prediction, and AFib complications' risk analysis. The leading aims of the first project are:

○ Improve AFlut mechanism characterization implementing novel biosignal approaches to extract valuable features;

○ Evaluate the influence of atrial and torso geometries on ECG and therefore on feature extraction and classification;

○ Discriminate several AFlut mechanisms using both in silico and clinical ECG data with a machine learning-based approach and using findings from the first two studies.

The second topic described in this thesis covers the following aspects regarding AFib driver localization and complication prediction:

○ Implement an in silico-based machine learning algorithm to identify the AFib drivers located near the pulmonary veins (PVs), predict the success rate of PV isolation to terminate the arrhythmia, and test it on a clinical cohort of ECGs;

○ Identify likely connections between AFib and heart failure using beat-to-beat variation signals extracted from 1-lead ECG.

1.3   Structure of the Thesis

This is a cumulative thesis motivated by the large number of studies that have been published (or submitted)in high impact peer-reviewed journals, patent, and conferences and their high impact on the scientific community during the course of the PhD program. This cumulative thesis wants to show the actual contribution that has been reviewed and accepted by the scientific community both from the technical and clinical aspects of biomedical engineering.

Chapter 2 and 3 present selected fundamentals for understanding the methods, results, and discussion provided in this thesis:

○ **Chapter 2** contains the medical background being relevant for this work. Human heart anatomy, physiology, and basic knowledge regarding the ECG are explained as well as the AFlut, AFib, and ablation procedure that are the main clinical topics of this work;

○ **Chapter 3** presents an overview of the technical fundamentals. A basic introduction to computational modeling of the heart is given, focusing on the atria. Moreover, biosignal processing, statistics, and machine learning techniques pertinent to this project are presented.

Chapter 4 and 5 comprise the main body of the thesis. Here, introductions to the two major topics are given. The link between various manuscripts that are part of the same main topic is explained, followed by the related papers submitted, and published:

○ **Chapter 4** contains the projects related to AFlut. The main goals were to characterize AFlut signals with novel features (journal paper 1 [22]), estimate the ability of our simulations to generalize (conference paper [23]), and the implementation of a hybrid classifier to discriminate several AFlut mechanisms (journal paper 2 [24]);

○ **Chapter 5** outlines the studies related to AFib. The objectives were the implementation of an in silico trained classifier to discriminate clinical AFib drivers located near the PVs and to assess the acute PVI success in our AFib dataset (journal paper 3 [25]), and the realization of a machine learning algorithm able to predict the risk of AFib complication for heart failure (journal paper 4 [26]).

Chapter 6 summarizes the findings from all the studies from a general perspective. It gives insights into topics that would be interesting to work on as a follow-up to this thesis. Finally, it draws conclusions on this project in respect to the objectives set.

Appendix contains the supplementary material of each paper attached to this thesis, thus still having valid references in the manuscript texts.

During the three and a half years of research leading to this thesis, I published two journal papers and nine conference contributions as first author, and two additional journal publications are under review. As a co-author, four journal papers and three conference contributions were published, and one journal paper and one book contribution are under review. Moreover, I got invited to two international conferences as speaker, and I won an award for patient safety in biomedical engineering with one of the papers shown in this thesis [25]. To conclude, I supervised five student theses/projects that partly form the basis of the work presented here (cf. *List of Publications and Supervised Thesis* at the end of this thesis).

Chapter **2**

Medical fundamentals

In this chapter, the medical fundamentals essential to understand the studies presented in this thesis and to put them into context are described. Following a brief overview of the human heart anatomy and physiology focusing on the atrial anatomy, the electrocardiography is summarized. Then, atrial flutter, atrial fibrillation, and tachycardiomyopathy are introduced and the state of the art regarding ablation therapy is presented. The interested reader is referred to the cited references for a more in-depth introduction to the different topics.

2.1 Human heart anatomy and physiology

The human heart is a muscular hollow organ, which is centrally located in the thoracic cavity. The pericardium, a fibrous sac, encloses the heart in order to ensure several physiological functions, e.g., smooth movements during contraction or relaxation. The heart consists of four chambers: two atria and two ventricles. The septum separates the heart into a right and a left half, each comprising of an atrium and a ventricle. Both chambers are connected via atrioventricular valves (right: tricuspid valve, left: mitral valve), allowing a directed blood flow from the atrium to the ventricle (Figure 2.1) [27].

The heart supplies blood containing oxygen and nutrients to the organs and other body systems while carrying away carbon dioxide and metabolic waste from the organs in order to excrete them. Deoxygenated blood returns from the body to the right atrium via the superior and inferior vena cava. Due to the contraction of the right atrium, blood is injected into the right ventricle through the tricuspid valve. Subsequently, a ventricular contraction pushes the blood volume into the pulmonary system. After oxygenating the blood in the capillary lung bed, the blood enters the left atrium via three-to-five pulmonary veins (PVs), also described as left and right PVs. The blood then flows through the mitral valve into the left ventricle. Through a contraction of the left ventricle, the blood is pushed via the aortic valve in the systemic circulation [29].
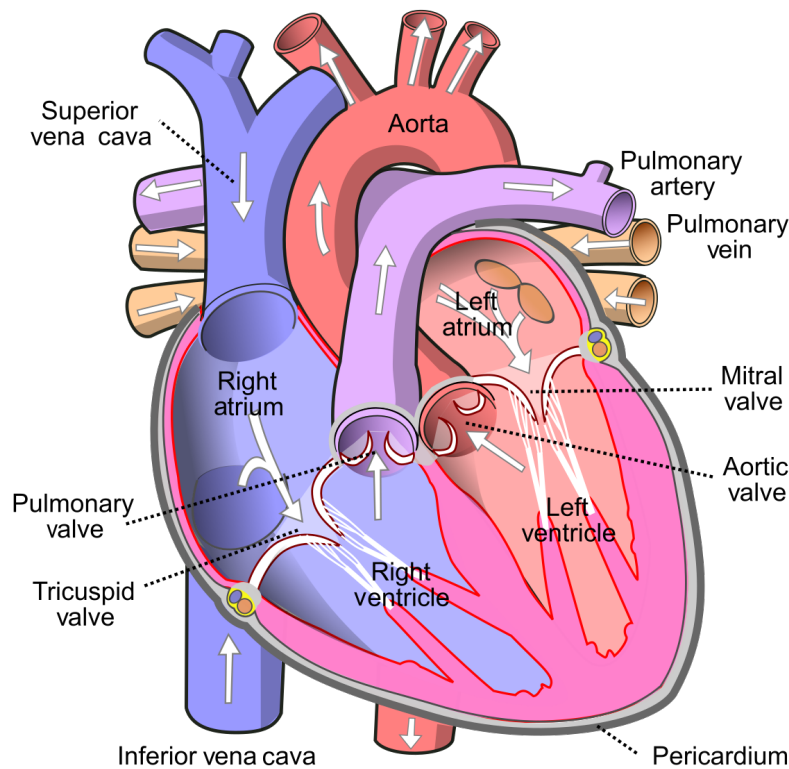
Figure 2.1: Anatomy of the human heart. Adapted from [28] and licensed under Creative Commons Attribution-Share Alike 3.0 Unported.

2.1.1 Atrial anatomy

The atria are divided into the right and the left chamber, and they are characterized by prominent muscular bundles and regions with distinct conduction properties (Figure 2.2). The right atrium (RA) can be divided into four regions: the smooth and rough parts of the posterior wall, the septum, and the right auricle or right atrial appendage (RAA). The ostia of superior and inferior venae cavae and the coronary sinus are located on the smooth posterior wall of the right atrium. Furthermore, it contains the fossa ovalis, the sinoatrial node (SA node) and the atrioventricular node (AV node). The smooth and rough regions are separated by a ridge called crista terminalis, which runs inferior and parallel to the openings of superior and inferior venae cavae [27]. The rough part of the RA posterior wall consists of 15 to 20 pectinate muscles [30]. Finally, the RA is connected to the ventricle through the atrioventricular opening (tricuspid valve annulus). The left atrium (LA) is located posteriorly in the thorax, with its posterior wall being adjacent to the oesophagus. As the endocardial surface of the LA is smooth [31], it exhibits a simpler structure than the RA. The ear-shaped left auricle or left atrial appendage (LAA) being located superior-anterior of the left superior pulmonary vein (LSPV) is an exception with its rough endocardial surface [32].
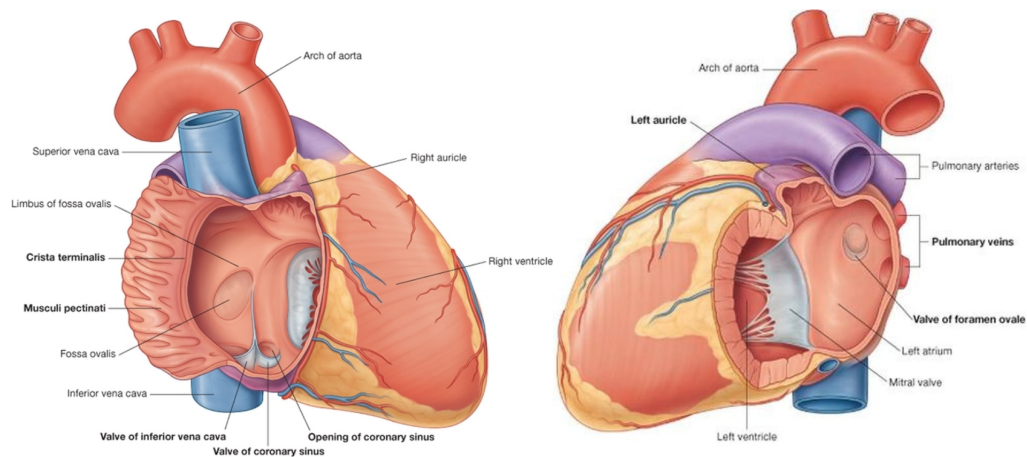
Figure 2.2: Anatomy of the atria. Left: Section of the right atrium (RA). Right: Section of the left atrium (LA). Adapted from [33, 34] and licensed under Creative Commons Attribution-Share Alike 3.0 Unported.

2.1.2 Conduction system of the heart

The stimulus to ensure the concurrent contraction of the heart is initiated by the sinus node. Specialized pacemaker cells of the atria are the source of regular electrical impulses. From the sinoatrial (SA) node (primary pacemaker of the heart), the electric impulse spreads via the walls of the atria to the second pacemaker, the atrioventricular (AV) node. In Figure 2.3, the excitation process is illustrated.

The AV node enables the contraction synchronization of the atria and the ventricles by delaying the stimulus conduction. Only after the blood from the atria is forwarded into the ventricles, the main chambers of the heart can contract. Moreover, the AV node prevents ventricular arrhythmias by blocking the signal transmission of irregular impulses. From the AV node, the signal is distributed through the so-called "Bundle of His" (third pacemaker) to three major channels. Two of these fascicles lead into the left ventricle and only one into the right. Branching off in the Purkinje fibers, the individual myocardium (heart muscle) fibers are eventually activated, causing the contraction. The cells forming all the pacemakers are self-depolarizing, i.e., after a certain time, they can provoke a new excitation of the heart.

Typically, in sinus rhythm, the heart of a healthy adult human contracts with a frequency between 60-80 beats per minute (bpm) in rest. The physiological rhythm of a healthy heart is created by the sinus node, while any other rhythm not regulated by the sinus node is considered an arrhythmia. If the SA node fails to trigger the excitation, the AV node can compensate for the primary dysfunction, delivering a heart rate of 40-50 bpm. Ultimately, the "Bundle of His" can initiate the heart electrical activity delivering a heart rate of 30-40 bpm [27].
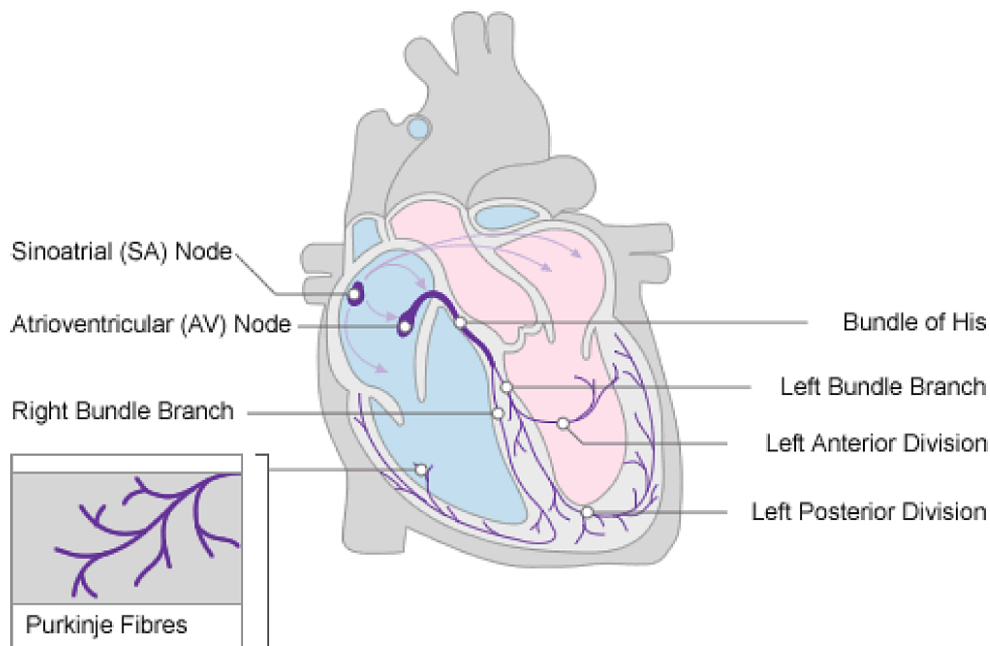
Figure 2.3: Anatomy and conduction system of the heart. Adapted from [35] and licensed under Creative Commons Attribution-Share Alike 3.0 Unported.

2.1.3 Electrophysiology

The excitation of a heart cell is determined by the change of the transmembrane voltage (TMV). Without external electrical stimulation, cardiomyocytes build a steady membrane resting potential of around -90 mV between the inner cellular potential and the outside of the cell. When a neighboring cell is depolarized, a small charge transfer is induced, which triggers the cell to change its TMV. This typical course is referred to as action potential (AP). An AP can be differentiated into four phases which can be observed in Figure 2.4. First, when a cell is getting excited, it induces a charge difference in the adjacent cells through the gap junction. This leads to a depolarization which culminates in a potential upstroke when it exceeds the threshold potential (-70 mV). The upstroke is caused by the opening of the sodium (Na^+) channels which close gradually after surpassing -40 mV, resulting in the overshoot of +20 mV (upstroke phase 0 and overshot phase 1 in Figure 2.4). Afterward, the cell partially repolarizes due to potassium (K^+) outward and chloride (Cl^-) inward currents. Next, the potential stagnates at about 0 mV leading to the long plateau phase during which calcium (Ca^{2+}) ions flow into the cell, balancing the repolarization currents (phase 2 in Figure 2.4). Dependent on the heart rate and the cell location, the Ca^{2+} inward currents last for 200-400 ms, also determining the length of the plateau. With the decay of these Ca^{2+} currents, the cell activation enters the repolarization phase (phase 3 in Figure 2.4). Mainly
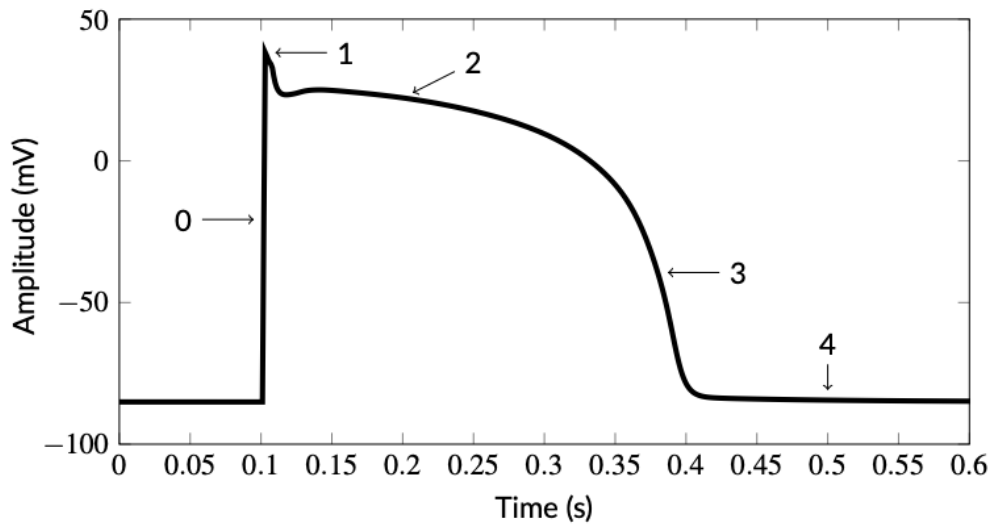
Figure 2.4: AP from a ventricular cardiomyocyte with the respective phases. Phase 0: Upstroke/De-polarization, fast Na^+ influx; Phase 1: Overshoot, Na^+ channels close; Phase 2: Plateau, Ca^{2+} influx; Phase 3: Repolarization, K^+ outflux; Phase 4: Resting membrane potential. Adapted from [37] and licensed under the Creative Commons Attribution-Share Alike 4.0 International License.

slow and rapid K^+ outward currents drive the TMV back to the resting potential of -90 mV. There, the rapid and slow K^+ outward channels close and certain inward K^+ channels open again that are enabled during the resting phase (phase 4 in Figure 2.4). Here, the cell can be activated again, whereas, during the plateau phase, the cell is in the absolute refractory period, i.e., a new activation is not possible. During the repolarization phase, the cell is in the relative refractory period allowing the cell to respond to an activation impulse but with an attenuated response due to partial repolarization [36].

2.2 Electrocardiography

Electrocardiography is one of the most common non-invasive diagnostic tools for heart diseases. As a basis for all electrophysiological investigations, it yields information about the individual excitation phases, gives insights into the activity and functional performance of the heart, and is capable of indicating both normal and abnormal heart electrical function. The main components of an ECG are illustrated in Figure 2.5.

The P-wave outlines the atrial depolarization or the atrial systole. In contrast, the QRS-complex refers to the ventricular systole, and the T-wave considers the ventricular diastole. The repolarization of the atria cannot be observed directly since this happens simultaneously as the ventricle contracts. Therefore, the lower amplitude of the atrial diastole is overlaid by the signal of the QRS-complex.

In Figure 2.6 the different stages of the blood exchange of the cardiac cycle and its correlations to the ECG are displayed. A different number of adhesive electrodes are required
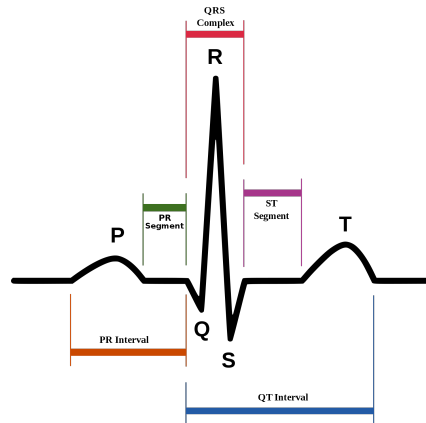
Figure 2.5: Illustration of normal sinus rhythm for a human heart as seen on ECG. Description of the ECG components (P-wave, QRS complex, and T-wave) is provided in Figure 2.6. The length of PR interval, PR segment, QRS complex, QT interval, and ST segment are common clinical metrics for cardiac activity characterization. Adapted from [38].
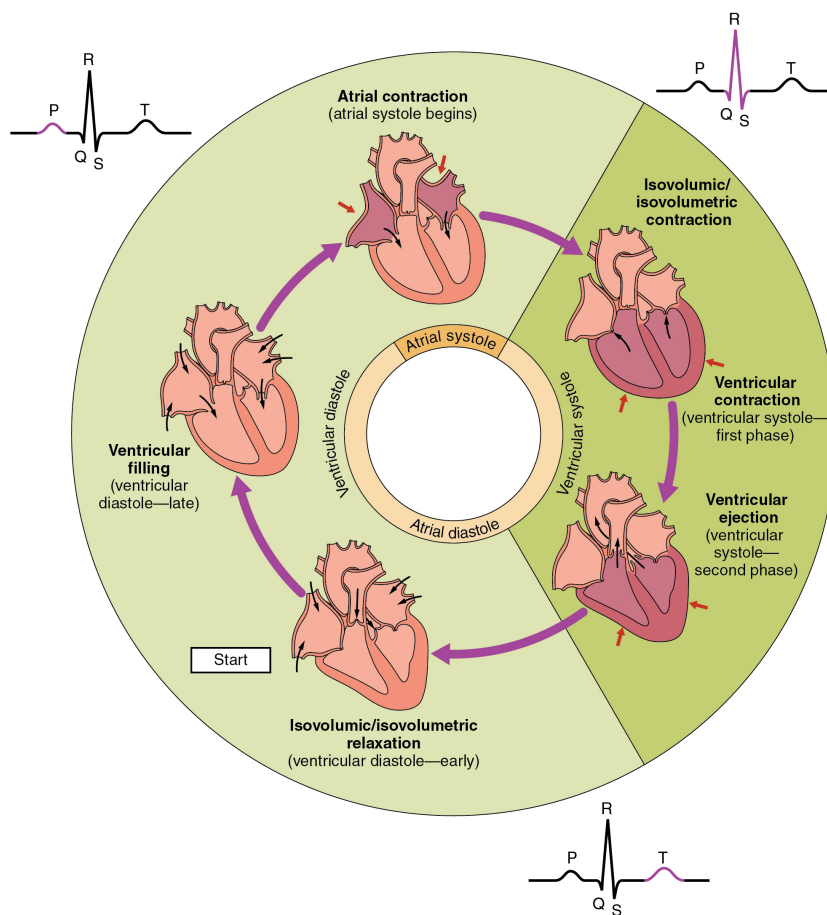

Figure 2.6: Cardiac cycle and its correlations with the ECG. Adapted from [39] and licensed under the Creative Commons Attribution License v4.0.

to record ECG signals, and the resulting potential difference between two electrodes is referred to as leads. With an increasing number of leads, the amount of information the ECG provides rises as well, even if this information might be redundant. The typical placement of the electrodes for a standard 12-lead ECG on the torso is shown in Figure 2.7, with six electrodes placed on the chest and four positioned on the limbs of the patient. The 12-lead ECG is calculated according to Einthoven (bipolar limb lead I, II, and III), Goldberger (augmented unipolar limb lead aVR, aVL, and aVF), and Wilson (precordial leads V1-V6) [39]. Although there are 12 voltages depicted, only nine electrodes suffice for an exact measurement. In total, the ECG provides information about the cardiac function from multiple views [40]:

- Inferior view: II, III and aVF;
- Anterior view: V1 to V4;
- Lateral view: I, aVL, V5, V6;
- Left ventricle cavity and right atrium: aVR and V1.

The three bipolar limb leads are obtained by measuring the voltage difference between the left arm, right arm, and left leg (electrodes 1-3 in Figure 2.7) in the following combinations:

$$I = V_{LA} - V_{RA}, \tag{2.1}$$

$$II = V_{LL} - V_{RA}, \tag{2.2}$$

$$III = V_{LL} - V_{LA}, \tag{2.3}$$

where V_{LA}, V_{RA}, and V_{LL} denote the voltage recorded on the left arm, right arm, and left leg, respectively. The augmented unipolar limb leads are defined as follows:

$$aVR = V_{RA} - \frac{V_{LA} + V_{LL}}{2}, \tag{2.4}$$

$$aVL = V_{LA} - \frac{V_{RA} + V_{LL}}{2}, \tag{2.5}$$

$$aVF = V_{LL} - \frac{V_{LA} + V_{RA}}{2}. \tag{2.6}$$

The precordial leads are positioned in succession on the front and left side of the chest (electrodes 4-9 in Figure 2.7). The six precordial leads are unipolar and related to a central terminal (V_{WCT}) which is defined by the average of the voltages measured on the right and left arms and the left leg,

$$V_{WCT} = \frac{V_{LA} + V_{RA} + V_{LL}}{3}. \tag{2.7}$$

The abbreviation WCT stands for Wilson central terminal to honor the physician who introduced the definition given in Eq. 2.7 [41].

The vectorcardiogram (VCG) is the spatial representation of electromotive forces generated during cardiac activity and is analyzed in three spatial planes (horizontal, frontal, and
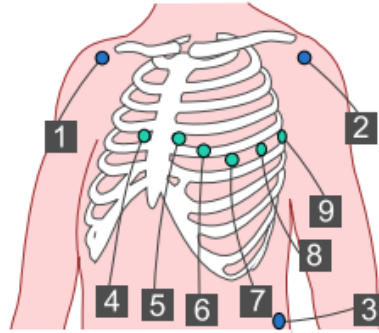
Figure 2.7: Standard 12-lead ECG electrodes placement. Electrodes 1-3 are used to measure the Einthoven and Goldberger leads, as well as to calculate Wilson central terminal. Electrodes 4-9 are used to measure the Wilson leads together with Wilson central terminal. Adapted from [44] and licensed under the Creative Commons Attribution-Share Alike 3.0 Unported license.

sagittal) [42]. The VCG can be estimated from a subset $\mathbf{S_{ECG}}$ of the 12-lead ECG (V1-V6, I, II) using the inverse Dower matrix $\mathbf{D}$ [43]:

$$\mathbf{S_{VCG}} = \mathbf{D}\,\mathbf{S_{ECG}}, \tag{2.8}$$

with

$$\mathbf{D} = \begin{pmatrix} -0.172 & -0.074 & 0.122 & 0.231 & 0.239 & 0.194 & 0.156 & -0.010 \\ 0.057 & -0.019 & -0.106 & -0.022 & 0.041 & 0.048 & -0.227 & 0.887 \\ -0.229 & -0.310 & -0.246 & -0.063 & 0.055 & 0.108 & 0.022 & 0.102 \end{pmatrix} \tag{2.9}$$

2.2.1 Body surface potential map

The body surface potential map (BSPM) extends the conventional ECG. The cardiac electrical fields, including the voltage distribution and current flow patterns arising from cardiac currents, exist within the entire body. Thus, the ECG can be measured from any surface site of the body.

More extensive sampling of ECG potentials is directly related to the selective spatial information obtained with additional leads. This automatically leads to the recording of BSPMs, which includes the definition of sites of activation in the ventricle, localization of accessory pathways in pre-excitation syndromes, localization of late potentials or pacing sites within the ventricular cavities as well as evidence of acute recognizable myocardial ischaemia not identifiable using standard criteria and the 12-lead ECG [45]. Colorized torso models as depicted in Figure 2.8 illustrate the computed torso potentials throughout the body surface (anterior and posterior view).
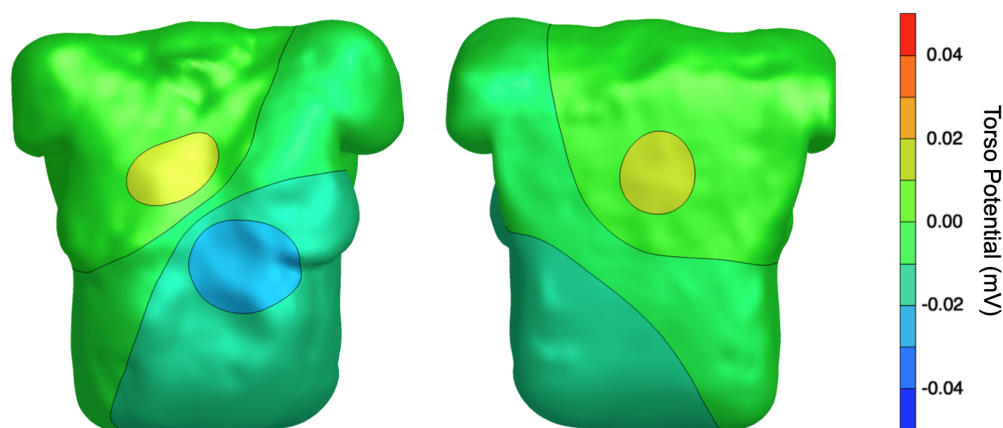
Figure 2.8: Example of an anterior and posterior view of the BSPM at a specific time instant under a condition of atrial flutter, respectively. The atrial activation was projected onto a torso model (see section 4).

2.3   Atrial flutter

Atrial Flutter (AFlut or AFl) is a common supraventricular arrhythmia with a consistent excitation pattern. It is defined as organized, macro-reentrant atrial tachycardia. It is perpetuated around a large central obstacle, which can be an anatomical structure, unexcitable scar tissue, or a functional line of block. As the ventricles cannot sustain this fast rhythm, 2:1 or 3:1 conduction block at the AV node is frequently observed.

AFlut is categorized into two major types: typical AFlut (also termed type I or cavotricuspid-isthmus (CTI) dependent form) and atypical AFlut (type II). Typical AFlut is characterized by mostly counterclockwise rotational activation around the tricuspid annulus. In $\approx 15\%$ of the cases, the excitation rotates in a clockwise direction [46]. On the contrary, atypical AFlut originates in several atrial regions, such as the mitral annulus, the superior vena cava, or the PVs. Atypical AFlut often develops after corrective atrial surgery (congenital and valvular heart disease) or atrial fibrillation (AFib) ablation [47–51] with the driving reentry circuit determined by the lesions. As a consequence of the widespread use of PV isolation (PVI) and other left atrial ablation procedures for the treatment of AFib, the prevalence of atypical left AFlut and of CTI-dependent flutter with atypical ECG patterns post ablation procedures increased in the recent years [52, 53]. However, atypical AFlut can also occur without previous surgery, driven by various reentry circuits.

Although AFlut is not directly a cause of death, it is associated with a significantly increased risk for stroke and other complications similar to those of AFib [54], described in more detail below. Antiarrhythmic drugs are used to treat AFlut. However, pharmacological therapy is often ineffective and more than half of the patients are treated with rate-control strategies due to the failure to maintain sinus rhythm [55]. Moreover, catheter ablation (see

section 2.5) is mainly recommended for patients with a first episode of typical AFlut and flutter appearing after antiarrhythmic treatment of AFib [46, 56].

2.4   Atrial fibrillation

Atrial fibrillation is the most common arrhythmia encountered in clinical practice affecting over 8 million people in the European Union [57]. AFib has a prevalence of 2% to 3% in the general western countries population [58] and is associated with significantly higher mortality accounting for 25% of all strokes [59]. AFib can cause several complications, e.g., severe and reversible left ventricle (LV) dysfunction in patients without structural heart disease (AF-induced cardiomyopathy and heart failure). Cardiomyopathy is a general term for heart muscle diseases, where the heart's ability to pump blood through the circulatory system is affected. Cardiomyopathy is one of many causes of heart failure. In patients with underlying structural heart disease and LV dysfunction, AFib is a harbinger of increased hemodynamic deterioration and increased mortality [60]. However, the mechanisms responsible for AFib-induced cardiomyopathy, and heart failure are not clearly understood yet.

AFib describes a chaotic and irregular excitation of the atrium, disturbing the sinus rhythm, and therefore, leading to heavy limitations in patients suffering from it [61]. Clinically, AFib is categorized as:

○ Paroxysmal, if episodes are self-terminating within a maximum of 7 days (typically within 48 hours);

○ Persistent, if the arrhythmia does not terminate within 7 days without pharmaceutical or electrical cardioversion;

○ Long-lasting persistent, if AFib lasts longer than one year;

○ Permanent, if no rhythm control strategy is pursued but only the rate is controlled [54].

Despite considerable research efforts, the mechanisms initiating and perpetuating AFib are far from being completely understood. The role of calcium handling, atrial fibrosis, and the drivers of AFib are under discussion [62, 63]. Regarding the AFib drivers, two separate mechanisms are suspected in current literature to be the main cause for AFib, namely focal sources and rotational re-entrant circuits called rotors [64]. Other mechanisms were also identified as likely AFib drivers, e.g., circus movement reentry, leading circle concept, and multiple wavelet hypothesis [56]. However, in this thesis, we only considered stable rotors and focal sources as AFib driver mechanisms. Rotors describe a spiral-shaped wave consisting of a wavefront and a wave tail that meet at a center point and continuously propagate in clockwise or counterclockwise direction. A focal source is a simple circular wave periodically propagating from a single cardiac tissue spot. While focal sources have a fixed point from where they start and propagate, rotors tend to meander around in a small area, typically following a star pattern. These mechanisms underlying AFib come with rapid basic cycle lengths (BCL) of around 120-200 ms. The rotor cycle is defined as one full circulation around the base point [65].

Diagnosis of AFib is made using either intracardiac catheters to map the atrial activity or non-invasive methods like the ECG. Even though intracardiac mapping is more precise and reliable, the usage of ECG is very attractive since it reveals valuable information without any invasive intervention for the patient. Nowadays, therapy of AFib can follow different approaches, which are chosen based on the age, the overall health of the patient, the type of fibrillation, the symptoms, and whether there is an underlying cause for the arrhythmia. The first option is to medicate the illness. This can be done either with drugs that just reduce the risk of stroke but do not reduce the fibrillation, or control the rate at which the heart beats and will therefore restore a normal heart frequency. However, medications come with side effects, for example, tiredness, nausea, constipation, and low blood pressure depending on the drug. Alternatively, cardioversion can be used to restore the normal rhythm of the heart. Cardioversion is an electrical shock given to the heart that instantly stops the arrhythmia by restoring the atrial electrical activity to sinus rhythm. Unfortunately, AFib might reoccur in some cases after cardioversion. Lastly, AFib can be treated by substrate modification using catheter ablation (see section 2.5).

2.5   Ablation therapy

In patients with recurrent AFib that are resistant to antiarrhythmic drugs, catheter ablation of atrial tissue is the recommended therapy [54]. This is the only therapy that shows effectiveness when all other methods fail in terminating AFib [12]. Ablation therapy destroys the diseased areas of the heart or introduces arbitrary lines of block with the aim to interrupt abnormal electrical circuits or pacing. To set an ablation line, the tissue is heated via radio-frequency currents (RF ablation) or cooled (cryo ablation). As a consequence, the tissue gets non-excitable with comparable success rates between the two methods [66]. The strategy for placing ablation lesions depends on the mechanism driving AFib and has to be selected individually for each patient. However, in the majority of patients, the AFib drivers are located close to the PVs, which is why pulmonary vein isolation (PVI) is the standard approach since the pioneering work of Haïssaguerre et al. [67]. PVI showed to be effective on persistent and long-standing persistent AFib patients, and in particular, on paroxysmal AFib patients (AFib recurrence rate up to 60%, and 45%, for persistent, and paroxysmal patients, respectively) [68, 69]. To improve the success of this therapy, several other strategies aiming at a modification of the atrial substrates have been proposed [13]: Roofline (RL) and mitral isthmus (MI) isolations; ablation of sites exhibiting complex fractionated atrial electrograms (CFAEs); ablation of sites exhibiting a high dominant frequency; and several others. However, a big randomized multi-center study demonstrated that the success rate of PVI in persistent AFib could not be increased by additional CFAE ablation as well as extra-linear lesions [70]. On the contrary, recent studies that remain to be reproduced reported remarkable success rates of focal sources and rotor ablation [14, 15]. Therefore, a controversial discussion regarding the optimal ablation strategy in different patient populations is still ongoing.

Technical fundamentals

In this chapter, the basic technical concepts of computational models of cardiac electro-physiology are introduced. Then, a brief description of the biosignal processing, statistical methods, and machine learning algorithms utilized in this thesis are summarized.

3.1 Cardiac electrophysiological modeling

Cardiac electrophysiological modeling, through either detailed biophysical or phenomeno-logical modeling, aims at mathematically describing the electrical behavior of the heart cells and tissue. In this section, selected approaches used in this thesis ranging from simulating the electrical activity of atrial cells to the electrical activity of the heart that can be detected on the surface of the torso will be presented.

3.1.1 Courtemanche model

The ionic membrane currents were firstly described by Hodgkin and Huxley as a mathemati-cal model in their work from 1952 [71]. The transmembrane voltage V_m is defined as the difference between the intracellular potential Φ_i and the extracellular potential Φ_e. The cell membrane is represented by an electric circuit with a capacitor and the different ion channels in parallel. The ion channels are expressed by variable resistors in line with the respective Nernst voltages represented by voltage sources. Thus, the membrane current is given as the sum of the ionic currents plus the capacitive current resulting in the following ordinary differential equation for V_m:

$$\frac{dV_m}{dt} = -\frac{I_{ion} + I_{stim}}{C_m},$$

(3.1)

where V_m is the transmembrane voltage (TMV), C_m is the capacity of the cell membrane, I_{stim} is the stimulation current and I_{ion} is the ion current through the membrane. Later on, a specific model of human atrial myocytes was proposed by Courtemanche et al. in 1998. This model has a different composition than the previously presented basic Hodgkin-Huxley
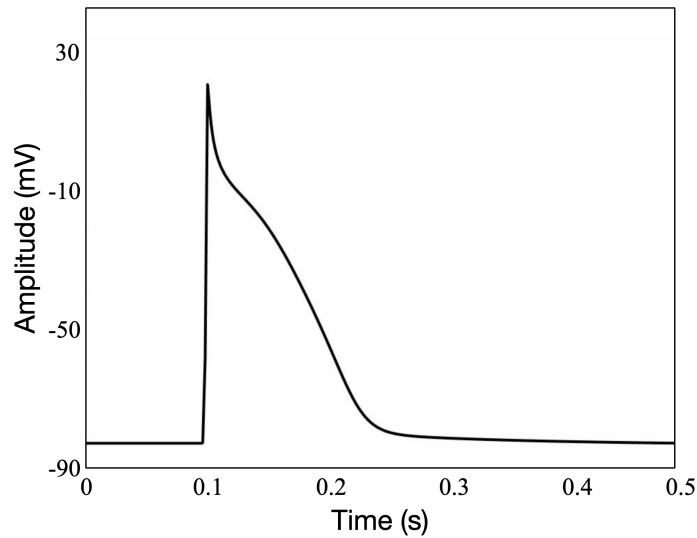
Figure 3.1: AP from an atrial myocyte under AFib remodeling conditions [56].

model. The model considers more different ionic currents corresponding to ion channels, exchangers, and pumps. Thus, the results of this model are better suited for the simulation of atrial activity [72]. Moreover, to leverage in silico methods to gain mechanistic insight into AFib patho-physiology and to evaluate therapeutic strategies, it is important to consider the remodeling processes that the atria undergoes when exposed to fibrillation for long time. Maximum conductivities of the ion currents were altered based on a rigorous literature research [56]. For this reason, a modification of the Courtemanche et al. model of human atrial myocytes was used in this thesis (Figure 3.1). The remodeled Courtemanche et al. model provides mechanistic descriptions of how remodeling increases susceptibility to reentry through shortened wavelength facilitating the initiation and maintenance of atrial arrhythmias.

3.1.2 Excitation propagation in the tissue

Moving from a microscopic single cell to macroscopic tissue simulations, a mathematical formulation of the coupling between cells is required. A detailed biophysical model is shown in section 3.1.2.1, in opposition to a more phenomenological approach shown in section 3.1.2.2.

3.1.2.1 Monodomain model

The monodomain model is introduced to incorporate the effect of coupled intracellular space with gap junctions by resistors or conductivity tensors. For each time step, the intracellular current source density is calculated and the status of the electrophysiological cell domain is

updated. The summarized intracellular current source density can be calculated based on a simplified version of the Poisson's equation:

$$\frac{1}{1+k}\nabla\cdot(\sigma_i\nabla V_m) = \beta(C_m\frac{dV_m}{dt}+I_{ion}+I_{stim}),$$ (3.2)

where $\sigma_{i/e}$ are the conductivity tensors for intracellular (i) and extracellular (e) space, k is the ratio of the tensor components ($\sigma_i = k\sigma_e$), V_m is the TMV, β is the cell surface to volume ratio, C_m is the membrane capacitance, I_{ion} is the ionic transmembrane current density (per surface), and I_{stim} is the optional external stimulus current density. The calculation of the monodomain solution is computationally less expensive than the standard excitation propagation model for cardiac tissue (e.g., bidomain models) [73].

3.1.2.2 Eikonal equation and Fast Marching algorithm

An established approach to phenomenologically describe the excitation spread over the heart tissue consists of solving the Eikonal equation [56, 74].

$$c\sqrt{\nabla t_a \mathbf{G} \nabla t_a} = 1,$$ (3.3)

with the speed $c(n)$ for each node n in the anatomical heart mesh, the node-wise activation time $t_a(n)$, and the tensor $\mathbf{G}$ introducing anisotropy in the conduction.

The fast marching simulation (FaMaS), introduced by James Sethian [75], is a numerical algorithm for solving the Eikonal equation. To solve Equation 3.3, i.e. calculating the activation times $t_a(n)$, the FaMaS is associated with lower computational costs compared to other methods (e.g., Newton's method) [76]. Moreover, FaMaS is also less computationally expensive than the monodomain method.

3.1.3 Forward problem of electrocardiography

For the extraction of ECGs in simulation environments, a Poisson's equation need to be solved to project epicardial potentials onto the torso. This is known as the forward problem of electrocardiology and can be formulated as:

$$\nabla\cdot\sigma\nabla\Phi = 0 \quad \text{in} \quad \Omega$$ (3.4)

$$\Phi = \Phi_0 \quad \text{on} \quad \sum \subseteq \Gamma_T \quad \text{and} \quad \sigma\nabla\Phi\cdot n = 0 \quad \text{on} \quad \Gamma_T,$$ (3.5)

where Φ is the quasi-electrostatic potential, σ is the conductivity tensor, Γ_T and Ω represent the surface and volume of the thorax. To evaluate the surface potentials, a surface-based approach using the boundary element method (BEM) algorithm can be used [77]. The BEM is a numerical computational method for solving linear partial differential equations, formulated as integral equations. Moreover, it is an edge-based discretization method that

only needs the grid values of the bounding area to compute the solution. Utilizing the Green second identity, the boundary integral equation is

$$\int_S (\mathbf{A}\nabla\mathbf{B} - \mathbf{B}\nabla\mathbf{A}) \cdot \bar{n}dS = \int_V (\mathbf{A}\nabla^2\mathbf{B} - \mathbf{B}\nabla^2\mathbf{A}) \cdot d\Omega, \qquad (3.6)$$

and taking the fundamental solution $u*$ which satisfies

$$\nabla^2 u* + \delta = 0, \qquad (3.7)$$

where δ denotes Dirac's delta function, it follows:

$$c(p)\Phi(p) - \int_S (u*\nabla\Phi - \Phi q*) \cdot dS = 0, \qquad (3.8)$$

where p is an arbitrary field point, $q*$ denotes $\nabla\frac{1}{r}$, while r is the distance between the source point and field point p, and $c(p)$ depends on the location of p: $c(p) = \pi$ when p is inside Ω; $c(p) = 0$ when p is outside Ω; $c(p) = 2\pi$ when p is on the smooth boundary [78]. This method is used to construct the transfer matrix $\mathbf{A}$ linking epicardial potentials x and body surface potentials (BSP) b as:

$$\mathbf{A}x = b. \qquad (3.9)$$

3.2   Biosignal processing

Biosignals contain useful information that can be exploited to understand the underlying physiological mechanisms of a specific biological event or system, and which may be useful for medical diagnosis. They can be space, time, or space–time records of a biological event. Biological signals can be classified according to various characteristics of the signal, including the waveform shape, statistical structure, and temporal properties. Digital signal processing techniques are applied to the biosignals to reduce noise and extract additional information that can improve the understanding of the physiological meaning of the original parameter [79]. In this section, the signal processing methods that have been used to analyze, and extract features from the biosignals (i.e., 12-lead ECGs) will be presented. The features extracted with these biosignal techniques in the context of this thesis, and their meaning are described in the chapters 4-5, and in the appendix A.1.

3.2.1 Fast Fourier transform

Fast Fourier transform (FFT) is an algorithm to compute the discrete Fourier transformation (DFT) of a time discrete signal. The DFT is defined by:

$$X_k = \sum_{n=0}^{N-1} x_n e^{-j\frac{2\pi}{N}kn}, \quad k = 0, 1, 2, ..., N-1, \qquad (3.10)$$

where N is the number of samples in the signal. The FFT algorithm speeds up the computation of the DFT from a runtime of $O(N^2)$ to $O(Nlog(N))$, and it is therefore commonly used in computational frequency analysis. This is achieved by using certain periodicity properties in the calculation of the DFT to obtain a more efficient implementation [80].

3.2.2 Wavelet decomposition

The wavelet transformation is the projection of the signal $x(t)$ on the scaled and temporal shifted analytical wavelet $\Psi_{a;b}(t)$:

$$W_X^\Psi(a,b) = \langle x(t), \Psi_{a,b}(t) \rangle = \frac{1}{\sqrt{|a|}} \int_{-\infty}^{\infty} x(t) \Psi(\frac{t-b}{a}) dt, \qquad (3.11)$$

with scale value a and time shift b. Ψ is the selected wavelet for the transformation. There are numerous possibilities for wavelets to use in the transformation, thus the wavelet function should be selected case sensitive [81].

3.2.3 Principal component analysis

Principal component analysis (PCA) is an orthogonal linear transformation that transforms the data to a new coordinate system so that the variance by a scalar projection of the data is maximized. The first principal component (PC) depicts the maximum variance of the input data, the second PC corresponds to the second coordinate, etc.. For M signals with each having N entries the row vectors $\mathbf{x}_M$ are assembled in the matrix $\mathbf{X}$.

$$\mathbf{X} = [\mathbf{x_1} \ \dots \ \mathbf{x_M}] = \begin{bmatrix} x_{11} & \dots & x_{1M} \\ \vdots & \ddots & \\ x_{N1} & \dots & x_{NM} \end{bmatrix} \qquad (3.12)$$

For each signal the mean over the whole dataset is being subtracted leading to a zero-mean signal matrix $\mathbf{Z}$. Now the covariance matrix $\mathbf{C}_{ZZ}$ can be calculated:

$$\mathbf{C}_{ZZ} = E[\mathbf{ZZ}^T] \approx \frac{1}{N} \mathbf{ZZ}^T. \qquad (3.13)$$

The eigenvalue matrix Λ_{ZZ} and the eigenvector matrix Φ are calculated, and through permutation the rows and columns are sorted according to the respective eigenvalues λ_n. With the help of the eigenvector matrix Φ, the covariance matrix $\mathbf{C}_{ZZ}$ is mapped to a diagonal matrix Λ_{ZZ} with eigenvalues λ_n.

$$\Lambda_{ZZ} = \Phi^T \mathbf{C}_{ZZ} \Phi \approx \Phi^T \frac{1}{N} \mathbf{ZZ}^T \Phi. \qquad (3.14)$$

Γ being the normalized eigenvector matrix resulting from the eigenvector matrix Φ and the eigenvalue matrix Λ_{ZZ} enable the calculation of:

$$\mathbf{Y} = \Gamma \cdot \mathbf{X}, \qquad (3.15)$$

where $\mathbf{Y}$ represents the resulting matrix of PCs. Therefore, the first element of $\mathbf{Y}$ holds the largest share of the total variance of the data $\mathbf{X}$, the second element the second largest share etc. [81].

3.2.4 Area under the power spectral density

Power spectral density for a signal sampled at discrete times $x_n = x(n\Delta t)$, and considering a window of $1 \leq n \leq N$ with N tending to infinity, is defined as:

$$S_{xx}(\omega) = \frac{(\Delta t)^2}{T} | \sum_{n=1}^{N} x_n e^{-i\omega n\Delta t} |^2, \qquad (3.16)$$

with T being the total duration of the signal, $\omega = 2\pi f$ representing the frequency, and Δt the sampling time interval. The area for a specific frequency interval can be calculated by summarizing the values corresponding to the desired frequency interval and dividing by the number of samples.

3.2.5 Shannon entropy and spectral entropy

The Shannon entropy of a variable is the average level of uncertainty, or information inherent in the variable's possible outcomes. Shannon entropy H is given by the formula:

$$H = - \sum_i s_i \, log_b \, s_i, \qquad (3.17)$$

where s_i is the probability of symbol number i appearing in the stream of symbols of the signal, and b is the base of the logarithm used. Common value of b is 2 when the corresponding unit of entropy are the bits [82, 83].

The spectral power entropy is a measure for spectral power distribution. It treats the signal's normalized power distribution in the frequency domain as a probability distribution and calculates the Shannon entropy of it [84, 85]. For a signal $x(n)$ the power spectrum is $S(m) = |X(m)|^2$ with $X(m)$ being the DFT of $x(n)$. The probability distribution is expressed as:

$$P(m) = \frac{S(m)}{\sum_i S(i)}. \qquad (3.18)$$

Therein, the Shannon entropy H is defined as expressed in equation 3.17 replacing s with P.

3.2.6 Recurrence Quantification Analysis

The recurrence quantification analysis (RQA) is a method of nonlinear data analysis that quantifies the number and duration of recurrences of a dynamical system presented by its state space trajectory. To quantify these factors, the RQA makes use of the recurrence plot

(RP). A RP is an advanced technique of nonlinear data analysis. It is a visualization (or a graph) of a square matrix, in which the matrix elements correspond to those times at which a state of a dynamic system recurs (columns and rows correspond then to a certain pair of times). Technically, the RP reveals all time stamps when the phase space trajectory of the dynamic system visits roughly the same area in the phase space [86, 87]. Measures based on RP's diagonal structures are able to find chaos-order transitions [88], measures based on RP's vertical (horizontal) structures are able to find chaos-chaos transitions (laminar phases) [89]. In chapter 4 a detailed description of the RQA method and its implementation is provided.

3.2.7 Hjort descriptors

In 1970, Bo Hjorth introduced indicators of statistical properties used in signal processing in the time domain called Hjorth descriptors after him [90]. The Hjorth descriptors are closely related to the spectral moments. The parameters are activity, mobility, and complexity (see A.1). They are commonly used in the analysis of biosignals (e.g., electroencephalogram) for feature extraction [41].

3.3   Statistics

The role of statistics in biomedical research starts at the planning stage of a clinical trial or laboratory experiment to establish the design and size of an experiment that will ensure a good prospect of detecting effects of clinical or scientific interest. Statistics is again used during the analysis of data to make conclusions valid in a wider population. Computation of simple quantities such as P-values, confidence intervals, standard deviations, standard errors or application of some standard parametric or non-parametric tests are needed to make relevant inferences from observed data [91]. The parametric and non-parametric tests are also called hypothesis tests in general. Hypothesis tests can be used for the statistical significance of differences between data [92]. In this section, the statistical analysis methods and parameters that have been implemented to infer and evaluate the results of this thesis will be presented.

3.3.1 Parametric tests

Parametric statistics is a branch of statistics that assumes a normal distribution of the sample data (fixed set of parameters to model the probability distribution of the data) [93]. A common parametric hypothesis test is the t-test. This test evaluates whether the expected values of Gaussian distributed observations are statistically equivalent by looking at the difference of the expected value of two distributions. We can identify two different cases for two sample data: paired data, in which there are one-to-one correspondences between the measurements in each sample, and unpaired data, in which there are no such correspondences.

The data are paired if we know which measurements correspond between the two samples (e.g., they were taken from the same patient) [92]. The test statistic of the t-test is known as the t-value. It is based on the standard error of the mean and is of the general form

$$t = \frac{\text{difference to be tested}}{\text{standard error of the mean}}.$$ (3.19)

Next, there is the definition of the test's hypothesis: Null hypothesis H_0 states that there is no difference between the two populations. Alternative hypothesis H_1 states that there is such difference. The selection of a degree of confidence is also needed. Usually, the degree of confidence is set to 95% or 99% depending on how robust the analysis should be. These degrees of confidence correspond to a significance level of $\alpha = 0.05$ or $\alpha = 0.01$, respectively. The lower the α, the more robust the analysis, but the more difficult it will be to obtain significance. The rejection of the null hypothesis is the aim of the test. It infers that the observations have statistically significant differences. In order to reject the null hypothesis, the t-value will have to turn out smaller than a critical value that can be obtained using statistical tables [92]. In the following chapters, the p-value will be used. The p-value represents the probability that the null hypothesis is true. If p-value $< \alpha$, then the null hypothesis is rejected.

Regarding statistical hypothesis tests where multiple (more than two) groups of data are given, the analysis of variance (ANOVA) is the most common parametric statistical test. The multiple groups of data must represent the same variable of interest (univariate analysis). ANOVA attempts to answer the specific question of whether all groups have the same mean or at least one pair of group means is significantly different [94]. Instead, if measures or records of different variables for each patient are given, then a multivariate analysis is needed. Multivariate analysis is important if we want to verify which are the links between the several variables extracted to analyze a phenomenon and which of the variables can best describe the phenomenon itself.

3.3.2 Non-parametric tests

Non-parametric statistics does not assume an explicit (finite-parametric) mathematical form of the distribution when modeling the data (non-normal distribution of the sample data). However, it may make some assumptions about that distribution, such as continuity or symmetry. Non-parametric tests tend to be less powerful than their parametric equivalents. Therefore, more data will typically be required to achieve statistical significance for the same degree of confidence. The procedure for the non-parametric hypothesis tests is similar to that shown in section 3.3.1 for the parametric tests. The difference between the two is that instead of using the mean of the data distributions, non-parametric tests use the median of the population. The Wilcoxon signed-rank test is the test used to analyze two paired distributions of data, while the Wilcoxon rank-sum test is used for unpaired distributions [95]. Regarding statistical hypothesis tests where multiple groups of data are given, the non-parametric Kruskal-Wallis test is the most common as opposed to the ANOVA for the parametric tests.
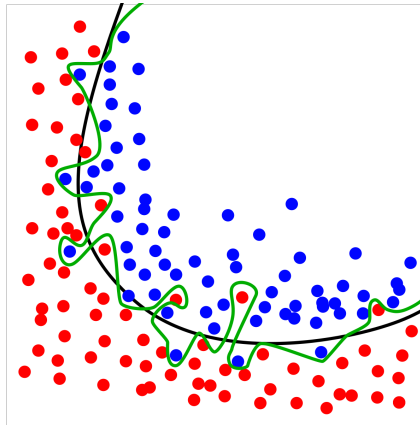
Figure 3.2: Example of an overfitted model (green line) and a regularized model (black line). The green line follows the training data best, however it is too dependent on that data loosing the capability of generalization, compared to the black line. Adapted from [98] and licensed under the Creative Commons Attribution-Share Alike 3.0 Unported license.

3.4 Machine learning

Machine learning is based on advanced algorithms operating on heterogeneous, large-scale datasets to reveal useful patterns that would be difficult or impossible for the human being to identify [96]. In this section, fundamental concepts in data science and selected machine learning approaches and algorithms used in this work will be described. They all belong to the class of supervised learning techniques, i.e., model fitting is based on given inputs (data, or features extracted from the data) and the corresponding known outputs which are often called labels. The pairs of known inputs and outputs is often referred to as training data.

3.4.1 Overfitting

A machine learning algorithm should be able to generalize (perform well on new and unseen inputs). The process of a learning method only memorizing the training data and loosing its generalization capability is called overfitting. Overfitting describes the phenomenon that a machine performs well on the given inputs but fails to work well on new inputs [97]. This can be caused by an over-complex model or an unbalanced training set. An example for overfitting is given in Figure 3.2. The dataset is divided in two classes, i.e., red and blue. The green line is a too complex model that follows the training data in a too exact way. On the contrary, the black line represents a simpler model that has reduced performance on the training set, but will most likely be more successful in generalizing to new data.
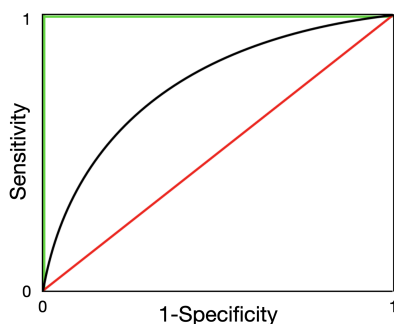
Figure 3.3: Example of ROC curve analysis. Three ROC curves are shown. The red curve represents a random classifier with AUC $=$ 0.5; The green curve represents an ideal classifier with AUC $=$ 1; And the black curve represents a common classifier with $0 <$ AUC < 1.

3.4.2 Greedy forward feature selection

The greedy forward selection technique is an iterative approach and problem-solving heuristic that attempts to identify the best combination of features by optimizing a given user-selected performance parameter. The algorithm starts with an empty feature set. In the first loop, the feature that leads to the best classifier performance is identified and added to the feature set. In subsequent loops, features that in combination with those already selected lead to the maximum performance increase are found and added to the feature set. The algorithm stops when performance based on the validation set can not be further increased. This type of algorithm produces a locally optimal solution but not the global optimum. When moving iteratively towards the optimum, the choice is always motivated by local observations, which can cause the algorithm to get stuck in a local optimum.

3.4.3 Receiver operating characteristic curve

The receiver operating characteristic (ROC) curve is an illustration of the classification performance of a binary classifier at various threshold settings. The ROC curve visualizes sensitivity against specificity-1, where sensitivity is on the y-axis and 1-specificity is on the x-axis. This graphical plot for binary classification is used for supervised learning. The algorithm operates as an optimization problem for sensitivity and specificity-1. From this optimization, the optimal threshold leading to the best sensitivity+specificity-1 value can be estimated. One of the most common classification model's evaluation parameter is the area under the curve (AUC). ROC is a probability curve and AUC represents the degree or measure of separability between classes. AUC ranges from 0 to 1, where 1 indicates the total ability to identify both classes without making any errors. In contrast, an AUC of 0.5 indicates no ability to find differences between classes, reducing the classifier to a random decision (Figure 3.3).

3.4.4 Decision tree

Decision tree is one of the most widely used tools for decision making due to its simplicity and explainability. It is a tree whose internal nodes can be considered as tests (on input data features) and whose leaf nodes can be considered as classes (of these data). These tests are filtered down through the tree to get the right output to the input pattern [99]. Therefore, a decision tree classifier is a supervised machine learning algorithm. It continuously splits the data according to some parameters (i.e., features). Classification trees have a categorical or discrete decision variable. This type of tree iteratively splits the data into binary partitions and then divides it further for each of the branches. Starting at the root, the decision tree classifier is built by splitting the data based on the feature that results in the largest information gain. A major risk of this method is overfitting by going too deep into the data splitting. For this reason, a depth-limit of the decision tree can be selected.

3.4.5 K-nearest-neighbor

Another very common classification method is the K-nearest-neighbor (KNN). Although the KNN classifier belongs to the simplest implementations, yet its performance is able to compete with most of the complex classifiers. This non-parametric classifier measures the similarity, or distance, between training, and test examples. It requires predefined K values and training data, to find the K-nearest-neighbor in reference to the distance metric. K is the number of training set neighbors that are used by the algorithm to classify each new test sample. The algorithm predicts the unknown class depending on the majority class of the included neighbors [100]. In the example in Figure 3.4, by setting $K = 3$, the test sample would have been classified as class 1 (red class). On the contrary, by setting $K = 5$, the test sample would have been classified as class 0 (blue class). Thus, the amount of neighbors to be considered and the distance metric are the most important hyper-parameters. In the context of this work, the Euclidean distance and several numbers of neighbors are used to discriminate the different test examples.

3.4.6 Artificial neural networks

Artificial neural networks (ANNs), also known as neural networks (NNs), are a subset of machine learning and form the core of deep learning algorithms. As the name may suggest, this method takes inspiration from the human brain, mimicking the way that biological neurons signal to one another. ANN is a more powerful method for classification than those previously described in this section, but also much more complicated and therefore less explainable. The smallest element of an ANN is the neuron. Each artificial neuron has an associated weight and threshold. If the output of a neuron is above the specific threshold, that node is activated. Threshold function (or activation function) can be chosen dependent on the network. If a node is activated, it sends data to the next neuron of the network. Neurons
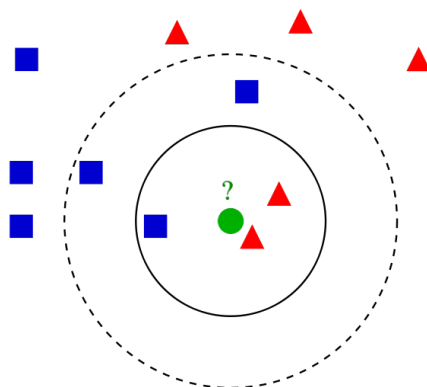
Figure 3.4: Example of a KNN binary classification approach with K = 3 neighbors (solid line circle) and K = 5 neighbors (dashed line circle). The blue squares represent the class 0 training samples, and the red triangles represent the class 1 training samples. The Euclidean distance is used to measure the similarity between the test sample (green circle) and the training samples. Adapted from [101], and licensed under the Creative Commons Attribution-Share Alike 3.0 Unported license.

are organized in layers. An ANN contains an input layer, one or more hidden layers, and an output layer. Each layer consists of a predefined number of neurons. The number of neurons in the output layer is fixed by the number of output variables (i.e., classes) [102]. In this thesis, radial basis neural networks (rbNN) were implemented. An rbNN uses Euclidean distances (between inputs and weights, which can be considered as centers) and (usually) Gaussian activation functions, which makes neurons more locally sensitive [103].

3.4.7 Deep learning

The machine learning approaches explained so far for classification purposes are all feature-based. Patient-acquired signals, i.e., ECGs, are not used directly as input to the algorithms. Instead, features describing a certain change that is expected to be visible are calculated in advance and these are used as inputs for the learning methods. The use of features requires very high background knowledge of the phenomenon under analysis. Moreover, the extracted features are many times fitted on the training data leading to overfitting issues. To avoid this, deep learning was designed. Deep learning describes neural networks with many layers (hence the name "deep") and directly accepts signals as input, performing an automatic feature extraction task. In this way, the machine can freely identify and extract any feature it considers relevant to pattern recognition, perhaps finding also something invisible to the human eye and therefore not exploitable for any feature-based approach. Unfortunately, this leads to a reduction in the explainability of these algorithms compared to the feature-based classifiers. In fact, it is not always possible (and never easy) to understand which are the characteristics in the input signals that led to the final classification.

Convolutional neural networks (CNNs) form a class of neural networks that are usually designed as deep neural networks. Commonly, a series of stages structure the architecture of a CNN. Thereby, the first few stages mainly consist of convolutional and pooling layers. The

main purpose of including convolutional layers lies in an automatic feature extraction. These convolutional layers apply different convolutional kernels on a given input yielding so-called feature maps. The input can be a two-dimensional signal, e.g., multi-lead ECG signals visualized as an image with its amplitude color- or greyvalue coded. Next, the pooling layers semantically merge similar features and downsample the size of the input. This cycle is repeated until the information is reduced to a set of images of a set size. The single values are then fed into a fully connected layer which calculates the output of the network. The weights of the final fully connected layer, as well as all the convolutional kernel coefficients, are considered the parameters to be optimized during training [104].

3.4.8 Performance metrics

Multiple metrics were used to evaluate the performance achieved by the machine learning algorithms in this thesis:

- ○ Accuracy: the fraction of predictions a model estimated right. It is defined as follows

$$\text{Accuracy} = \frac{\text{Number of correct predictions}}{\text{Total number of predictions}} = \frac{TP+TN}{TP+TN+FP+FN}, \quad (3.20)$$

  with TP = True Positives, TN = True Negatives, FP = False Positives, and FN = False Negatives. The right side of the expression is only meant for binary classification;

- ○ Sensitivity (or True Positive Rate): the proportion of cases that are positive and were predicted as positive out of all cases that are actually positive. Sensitivity is defined as follows

$$\text{Sensitivity} = \frac{TP}{TP+FN}; \quad (3.21)$$

- ○ Specificity (or True Negative Rate): the proportion of cases that are negative and were predicted as negative out of all cases that are actually negative. Specificity is defined as follows

$$\text{Specificity} = \frac{TN}{TN+FP}; \quad (3.22)$$

- ○ Positive Predictive Value (PPV): the proportion of cases that are positive and were predicted as positive out of all cases that were predicted as positive. PPV is defined as follows

$$\text{PPV} = \frac{TP}{TP+FP}; \quad (3.23)$$

- ○ Geometric-mean (G-mean), it is the central value in a set of numbers. G-mean is useful in machine learning applications because it can normalize numerical ranges of the dataset so that each item in the dataset can be directly compared. In this thesis, the G-mean was calculated between the sensitivity and the specificity. For binary classification the G-mean is defined as follows

$$\text{G-mean} = \sqrt{Sensitivity \cdot Specificity}. \quad (3.24)$$

Atrial flutter characterization and discrimination

Atrial flutter (AFlut) is an atrial arrhythmia that occurs when a reentrant circuit (short and circular electrical pathway) allows the electrical impulse to move rapidly through the atria in a self-sustaining way. AFlut may cause unpleasant symptoms such as shortness of breath, but also lead to stroke or heart failure [105, 106]. Usually, AFlut is diagnosed using the electrocardiogram (ECG), but the exact AFlut mechanism can only be identified during an invasive mapping procedure [107]. The invasive mapping can help to find the reentrant circuit using a narrow and flexible catheter that is manually guided through a vein into the chambers of the heart by a cardiologist. Once the mechanism supporting the flutter is identified, the clinician proceeds with an ablation procedure. The procedure aims to terminate the arrhythmia and restore sinus rhythm. For this reason, clinicians apply ablation lines or points at specific locations on the atria. The areas to ablate may differ for each type of AFlut and/or patient. During this procedure, the heart cells are destroyed by extreme heat or extreme cold. Manually locating the target areas for ablation using sequential catheter mapping can be very time consuming and does not allow real pre-operative planning by the doctor. This is why several manual rule-based methods for identifying the AFlut mechanism based on the 12-lead ECG have been proposed, with equivocal results. They usually rely on P-wave morphologies in the 12-lead ECG [108, 109]. A possible automatic solution is the utilization of the ECG signals in a machine learning framework. Indeed, machine learning-based algorithms are already extensively used for the detection of different cardiac arrhythmias [110, 111], but never until now to identify the exact mechanism that sustained the arrhythmia. The use of machine learning-based approaches could aid in the characterization of different AFlut mechanisms by identifying patterns among signals not visible by manual inspection. In addition, the algorithms would be less human operator dependent and thus more standardized leading to better performance outcome.

In the studies presented in this chapter, firstly, we sought to characterize 20 AFlut mechanisms developing two novel recurrence quantification analysis (RQA) approaches on a computational cohort of data and testing them on a clinical case: individual component

RQA and spatial reduced RQA [22]. The dynamic structures produced by the different mechanisms of AFlut led us to consider RQA as an interesting solution to characterize this arrhythmia. Moreover, RQA has already been widely used in cardiac signal analysis [112, 113]. We found that RQA-based features were sensitive and effective in characterizing the several AFlut mechanisms, proving to be potential features for subsequent machine learning approaches [22]. We computed in silico data to solve the common problem in clinical data analysis of shortage of properly labeled datasets. Our simulated AFlut cases provided an ideal and controlled environment, establishing a solid ground truth. Nevertheless, a major issue produced by the use of in silico data was the risk of overfitting on the atrial and torso models used to produce the dataset itself. Therefore, secondly, we wanted to focus on the influence that torso and atria models had on the 12-lead ECGs. To achieve this aim, we implemented basic machine learning classifiers to discriminate 20 different simulated AFlut mechanisms with a leave-one-atrium-out (LOAO) and a leave-one-torso-out (LOTO) algorithm, respectively. The paper showing the results thereof was published in a conference proceeding [23]. From the study, we observed that the atria models strongly influence the features selected for the classification, thus on the ECG signals. On the contrary, torso models do not affect the classification too much, not bringing any relevant change to the features and to the ECGs. These findings were also confirmed in a later work by Nagel et al. [114]. In conclusion, to solve the overfitting problem on the atrial models in use, we implemented a hybrid final classifier to discriminate 3 different types of AFlut mechanisms. The manuscript is at the moment under review [24]. The learning algorithm used both clinical and simulated data in the training dataset. In addition, in silico data were re-simulated on a larger amount of atrial models using a statistical atrial shape model [115], and the number of classes to be discriminated was reduced from 20 to three main AFlut categories. The algorithm tested on a full-clinical dataset showed ability to distinguish between the three selected AFlut classes, potentially leading to a non-invasive ablation target prediction [24].

Non-Invasive Characterization of Atrial Flutter Mechanisms Using Recurrence Quantification Analysis on the ECG: A Computational Study

Giorgio Luongo , *Member, IEEE*, Steffen Schuler, *Member, IEEE*, Armin Luik,
Tiago P. Almeida , *Member, IEEE*, Diogo C. Soriano , Olaf Dössel , *Senior Member, IEEE*,
and Axel Loewe , *Member, IEEE*

Abstract—*Objective:* Atrial flutter (AFl) is a common arrhythmia that can be categorized according to different self-sustained electrophysiological mechanisms. The non-invasive discrimination of such mechanisms would greatly benefit ablative methods for AFl therapy as the driving mechanisms would be described prior to the invasive procedure, helping to guide ablation. In the present work, we sought to implement recurrence quantification analysis (RQA) on 12-lead ECG signals from a computational framework to discriminate different electrophysiological mechanisms sustaining AFl. *Methods:* 20 different AFl mechanisms were generated in 8 atrial models and were propagated into 8 torso models via forward solution, resulting in 1,256 sets of 12-lead ECG signals. Principal component analysis was applied on the 12-lead ECGs, and six RQA-based features were extracted from the most significant principal component scores in two different approaches: individual component RQA and spatial reduced RQA. *Results:* In both approaches, RQA-based features were significantly sensitive to the dynamic structures underlying different AFl mechanisms. Hit rate as high as 67.7% was achieved when discriminating the 20 AFl mechanisms. RQA-based features estimated for a clinical sample suggested high agreement with the results found in the computational framework. *Conclusion:* RQA has been shown an effective method to distinguish different AFl electrophysiological mechanisms in a non-invasive computational framework. A clinical 12-lead ECG used as proof of concept showed the value of both the simulations and the methods. *Significance:* The non-invasive discrimination of AFl mechanisms helps to delineate the ablation strategy, reducing time and resources required to conduct invasive cardiac mapping and ablation procedures.

Index Terms—Atrial flutter, 12-lead ECG, non-invasive, biosignal processing, spatio-temporal, recurrence, RQA, nonlinear dynamic, PCA, cardiac modeling.

I. INTRODUCTION

ATRIAL flutter (AFl) is a common reentrant arrhythmia with 200,000 new annual cases estimated for the U.S. population [1]. This arrhythmia is characterized by self-sustained mechanisms and electrical signals that regularly propagate along various physiological pathways [2]–[4]. Although AFl is not a direct cause of death, it can cause significant symptoms and complications - e.g., palpitations, dyspnea, stroke and heart attacks.

Among the cardiac arrhythmias, the mechanisms perpetuating AFl have been extensively investigated and are relatively well known. This includes right atrial (RA) tachycardia [5]–[7] and left atrial (LA) AFl forms [8]–[10], occurrences after ablation for atrial fibrillation (AFib) [11]–[13] and macro reentrant mechanisms [14]. However, the characterization of the dynamical structures underlying electrophysiological (EP) phenomena from the perspective of non-linear and non-invasive time series analysis is still lacking. In fact, AFl mechanisms are usually discriminated from invasive intracardiac signals [3], [15], whereas non-invasive methods - using traditional 12-leads ECGs, for instance - are mostly used for the clinical detection of AFl with respect to AFib [16]. The non-invasive discrimination of AFl mechanisms would help to delineate the ablation strategy, reducing time and resources required to conduct invasive cardiac mapping and ablation procedures. Different AFl mechanisms

might culminate in different dynamic structures that could be captured by non-invasive data. The nature of this problem suggest that recurrence quantification analysis (RQA) might offer an interesting solution for the investigation of the underlying cardiac dynamic.

Interestingly, the development of RQA itself is intrinsically related to the analysis of cardiac signals. For instance, the work by Trulla *et al.* highlighted the promising applications of RQA on biomedical signals [17], describing the advantages of using RQA on investigating nonstationary and short-time cardiac datasets [18], [19]. Since then, RQA has been extensively used for characterizing the dynamics of heart rate variability [20], [21], cardiac restitution [22], or even combined with machine learning techniques for sudden cardiac death stratification [23] and ECG-based arrhythmia classification [24], [25], among other applications. RQA has been used to specifically characterize the dynamics of intracardiac signals during cardiac disorders [26], [27], [28], [29]. These investigations have shown that RQA-based features represent a promising set of tools to identify phase transitions and discriminate different EP characteristics related to the atrial tissue. Finally, Yang has proposed using recurrence plots (RPs) and RQA to analyze the spatial vectocardiogram for identifying cardiac disorders, being able to detect myocardial infarction with an average sensitivity of 96.5% and an average specificity of 75% [30].

In the present work, we sought to characterize different AFl mechanisms from the perspective of multivariate surface potentials and nonlinear time series. The present methodology stands out from previous investigations for considering an *in silico* ground truth followed by a clinical case application. The study was divided in two arms considering simulated 12-lead ECG signals: individual component RQA (icRQA) and (a novel) spatial reduced RQA (srRQA). The results suggest that RQA is effective in characterizing and discriminating the dynamic structures from distinct AFl mechanisms, and might help to define novel protocols for clinical planning and ablation strategy.

II. METHODS

A. Simulated AFl Scenarios

A database with computational AFl scenarios was organized based on: AFl mechanisms commonly described in the literature [31], [32]; documented clinical AFl cases [5]–[13]; and computational studies conducted in a previous work by Oesterlein *et al.* [33].

Cardiac excitation was modelled using the fast marching approach to solve the Eikonal equation [34], [35]. Propagation was simulated on the triangulated volumetric meshes of 8 biatrial anatomies, generated from segmented magnetic resonance imaging (MRI) data of healthy male and female subjects [36]. Interatrial connections were generated by a rule-based algorithm [37], [38]. Scars were added circumferentially around ipsilateral pulmonary veins (PVs), representing ablation scars from previous PV isolations.

In total, 20 mechanisms/scenarios of AFl were implemented, including right atrial (RA) flutter as well as left atrial (LA) forms like macroreentry around the valves (sc1-4), across the roof

TABLE I
DATABASE OF MANUALLY PARAMETERIZED AFL MECHANISMS

Mechanism	Atrium	Position	Direction	ID
Macroreentry	RA	Tricuspid Valve	ccw	sc1
Macroreentry	RA	Tricuspid Valve	cw	sc2
Macroreentry	LA	Mitral Valve	ccw	sc3
Macroreentry	LA	Mitral Valve	cw	sc4
Scar-related Reentry	LA	LPV	post	sc5
Scar-related Reentry	LA	LPV	ant	sc6
Scar-related Reentry	LA	RPV	post	sc7
Scar-related Reentry	LA	RPV	ant	sc8
Figure-8 Macroreentry	LA	Both PVs	ant	sc9
Figure-8 Macroreentry	LA	Both PVs	post	sc10
Figure-8 Macroreentry	LA	RPVs	ant	sc11
Focal Source	LA	RSPV anterior		sc12
Focal Source	LA	RSPV posterior		sc13
Focal Source	LA	LSPV anterior		sc14
Focal Source	LA	LSPV posterior		sc15
Microreentry	LA	ant MV annulus		sc16
Microreentry	LA	ant LAA		sc17
Microreentry	LA	ant RSPV		sc18
Figure-8 Microreentry	LA	ant		sc19
Microreentry	LA	post wall		sc20

Right atrium (RA), left atrium (LA), left pulmonary vein (LPV), right pulmonary vein (RPV), pulmonary veins (PVs), right superior pulmonary vein (RSPV), left superior pulmonary vein (LSPV), mitral valve (MV), left atrial appendage (LAA), clockwise (cw), counterclockwise (ccw), anterior (ant), posterior (post), scenario (sc).

(sc9-11), focal ectopy (sc12–15), and microreentries mediated by scars (sc5-8) or slow conduction areas (sc16-20). A complete list of scenarios is provided in Table I. For scar-related microreentry mechanisms, revitalized atrial tissue was introduced representing the critical isthmus. The 20 different AFl scenarios were constructed by changing the conduction velocity (CV) and refractory period, introducing heterogeneities in the atrial tissue. The simulations were initiated by manually placed triggers and refractory areas. They were continued for at least 5 s to confirm a stable excitation pattern.

The simulated excitation resulted in local activation times (LAT) for each anatomical node that was not isolated. The LATs were extracted in an interval of the simulation in which the specific AFl was formed. These LATs were projected on a new geometry (identical to the previous one), containing only the surface endo-\epicardial layers [37] in order to obtain a vector of LATs only from the surfaces. The transmembrane voltage (TMV) was calculated from the LATs using the Courtemanche *et al.* mathematical remodelled model of the human atrial action potential [39]. The TMV was used to estimate the body surface potential map (BSPM) onto 8 different triangulated surface models of torsos (9,951 nodes and 19,898 triangles on average). The torsos were generated by segmented MRI data of healthy male and female subjects [36], [40]. The boundary element method (BEM) was used to solve the forward problem of electrophysiology [41]. Finally, traditional bipolar ECGs were extracted from the BSPM, including the 12-lead ECGs [42].

Every 12-lead ECG signal has a length of 5 AFl loops and sampling frequency of 1 kHz. Since the ventricles were not included in the simulations, the resulting ECG signals contain only atrial activity represented by the P-waves (also called flutter waves or F-waves), without the QRS complex and T-wave (representing ventricular activity), since the ventricles are not included in the simulations (Fig. 1A-C).
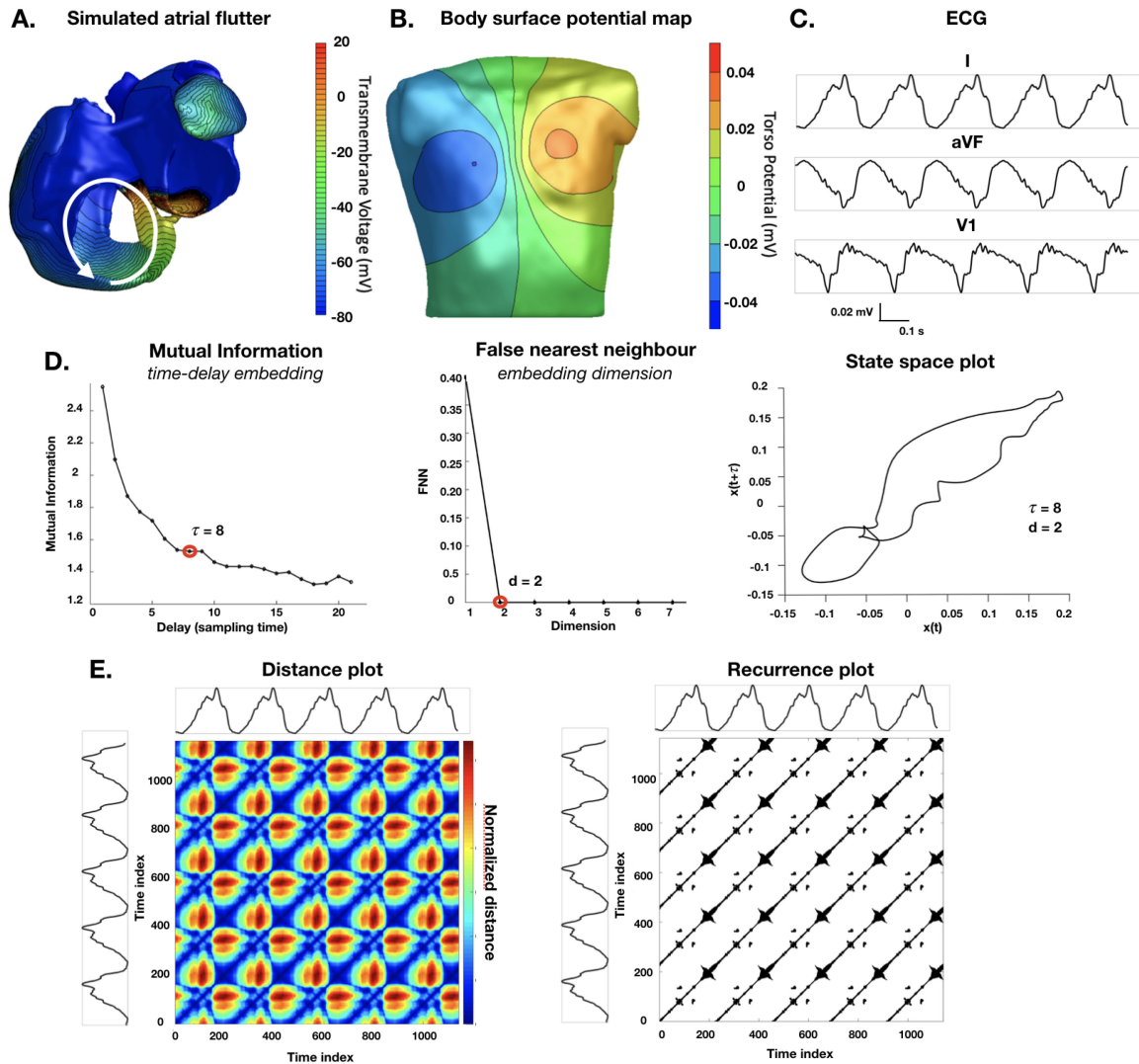
Fig. 1.   (A). Illustration of a simulated atrial flutter around the tricuspid valve with ccw direction on one of the atrial models generated from MRI. (B). Example of a BSPM on one of the torso models generated from MRI. The torso potential has been obtained solving the forward problem of electrophysiology from the simulated TMV on the atria. (C). Example of three of the 12-lead ECG signals extracted from the BSPM. Five complete loops of the AFl were taken into consideration. Principal component analysis (PCA) has been applied on the 12-lead ECGs. (D). Illustration of the state space reconstruction following Takens' theorem, with the corresponding time-delay embedding (τ) and embedding dimension (d). (E). The resulting distance plot based on the state space map and the subsequent recurrence plot (RP) after applying an adaptive threshold ε on the distance plot.

A total of 1,256 sets of 12-lead ECG were calculated from the 20 AFl simulated scenarios on 8 atria models and 8 torso models. Due to the proximity of the left inferior pulmonary vein to the mitral valve on one of the atrial models, the left pulmonary vein isolation blocked the signal propagation between these two anatomical points, hindering the implementation of scenarios sc12, sc13, and sc30 on this atria geometry.

B. Non-Redundant Spatial Information of ECGs

The 12-lead ECG signals were organized in a $N \times M$ matrix - where M is the number of leads and N is the number of samples on the leads - and principal component analysis (PCA) was applied. PCA is a linear transformation of a set of variables $\mathbf{X} = (X_1, X_2, .., X_n)^T$ [43]. This technique transforms the data with respect to an orthogonal basis Φ, such that the projections of $\mathbf{X}$ in this new coordinate system have maximum variance. The orthogonal vectors φ^i conforming Φ are ordered by decreasing variances. The variance of a variable is an important measure of its amount of information. Every component of the orthogonal basis Φ is called principal component (PC) and the projections of $\mathbf{X}$ with respect to that basis are called principal component scores - PCS, first PCS (PCS 1), second PCS (PCS 2), third PCS (PCS 3). PCA is primarily used for reduction of dimensionality of a

dataset while retaining the most relevant information contained in it [44], [45].

In the present work, PCA was used to reduce the size of each simulated 12-leads ECGs to the PCs that represent a cumulative variance greater than 95% of the total variance. This transformation aims to provide a new set of observations that considers the representative information of the electrical atrial dynamics collected from different sensors (i.e., non-redundant spatial diversity) [42]. PCA also allows to reduce the RQA computational cost, since we can proceed with a reduced space, as explained in II-D.

C. Embedding Parameters and RQA Features

A RP is a two-dimensional graphical technique introduced by Eckmann *et al.* [46], aiming to analyse the structure of multidimensional dynamical system's attractors [21]. It captures the reappearance of multidimensional states by means of a binary matrix $R_{i,j}$, associating the value 1 - represented by a black pixel - whenever states $\mathbf{x}_i$ and $\mathbf{x}_j$ are close to each other by ε, and 0 otherwise. The binary pattern exhibited in the RP is related to the underlying generative dynamics of the observation and can be used to assess different oscillatory properties characterized by diagonal lines - which capture the co-evolution of states in the phase space - and vertical lines - which capture the tendency of remaining in a given state [21]. The systematic quantification of the binary patterns in the RP defines the roots of RQA [18], and, currently, engenders a wide set of metrics that characterize the oscillatory behavior and also allow access to nonlinear invariants - e.g., correlation dimension, Kolmogorov entropy [21], [47] - and information theory [21].

When a single observation is available, the state space can be reconstructed using Takens' theorem [21], which aims to reveal a possible hidden low dimensional trajectory underlying the observation and, consequently, laminar RP structures - diagonals, verticals etc - as shown in Fig. 1D, [28]. In this case, auxiliary axes are defined as delayed samples of the uni-dimensional observation $\mathbf{x}(k)$, such as

$$\mathbf{x}(k) = \{x(k), x(k-\tau), \dots, x[k-(d_e-1)\tau]\}, \quad (1)$$

in which d_e is the embedding dimension - number of coordinates used for the $\mathbf{x}(k)$ representation - and τ represents the time-delay embedding among samples. These parameters are usually estimated by means of the false nearest neighbor test and the first local minimum of the self-mutual information [21], [48]. In this case, the recurrence matrix ($R_{i,j}$) can be defined in terms of the distance between the respective reconstructed states $\mathbf{x}^i$ and $\mathbf{x}_j$ and a chosen distance threshold ε, which can be expressed as:

$$R_{i,j}(\varepsilon) = \theta\{\varepsilon - \|\mathbf{x}_i - \mathbf{x}_j\|\}, \quad (2)$$

being θ the Heaviside function (Fig. 1E).

For a RP obtained from a time series of N samples, with frequency distribution $P(l)$ of diagonal line length, frequency distribution $P(v)$ of vertical line length, probability $p(l)$ of finding a diagonal of length l, and probability $p(v)$ of finding a

vertical line of length v, the RQA is associated with representative statistical measures of the matrix $R_{i,j}$ [21], used in the present work:

- The recurrence rate (RR), which represents the density of points in a RP:

$$RR = \frac{1}{N^2} \sum_{i,j=1}^{N} R_{i,j}. \quad (3)$$

- The ratio between recurrence points that form diagonal structures (with length $l \geq l_{min}$), referred to as determinism (DET):

$$DET = \frac{\sum_{l=l_{min}}^{N} lP(l)}{\sum_{l=1}^{N} lP(l)}. \quad (4)$$

- The Shannon entropy of diagonal lines in a RP (ENTR_diag), which can be considered as a measure of RPs complexity or organization in terms of the distribution of the diagonal lines:

$$ENTR\_diag = - \sum_{l=l_{min}}^{N} p(l) \ln p(l). \quad (5)$$

- The ratio between recurrence points that form vertical structures (with length $v \geq vmin$), referred to as laminarity (LAM):

$$LAM = \frac{\sum_{v=v_{min}}^{N} vP(v)}{\sum_{v=1}^{N} vP(v)}. \quad (6)$$

- The trapping time (TT), which represents the average length of the vertical lines:

$$TT = \frac{\sum_{v=v_{min}}^{N} vP(v)}{\sum_{v=v_{min}}^{N} P(v)}. \quad (7)$$

- The Shannon entropy of vertical lines in a RP (ENTR_vert), which can be considered as a measure of the RPs complexity or organization in terms of the distribution of the vertical lines:

$$ENTR\_vert = - \sum_{v=v_{min}}^{N} p(v) \ln p(v). \quad (8)$$

D. icRQA and srRQA

Two different RQA paradigms based on different premises were implemented to investigate the underlying dynamics and spatio-temporal structures of the AFl mechanisms. Therefore, the hyper-parameters for each paradigm (icRQA and srRQA) are expected to differ. Both paradigms were implemented considering the PCSs extracted from the simulated 12-lead ECGs.

1) icRQA: The first RQA paradigm (individual component RQA, icRQA) reconstructed the attractors following Takens' Theorem - same procedure as described in Section II-C - for each PCS considered relevant on the basis of their variance. In this case, each PCS had its own time delay and dimension embedding.

2) srRQA: The second - and novel - RQA paradigm (spatial reduced RQA, srRQA) defined the "embedding dimension" based on the number of selected PCSs and, therefore, did not consider Takens' Theorem for attractor reconstruction. Indeed, srRQA considers the first PCS1 as the first coordinate of the observed trajectory, PCS 2 as second coordinate, and so forth - i.e., it defines the AFl trajectory in the domain of PCSs. This leads to a space-time "embedding space" based on the uncorrelated PCSs to obtain minimal redundant spatial information. Consequently, no time embedding procedure was needed for the srRQA since the PCSs are already uncorrelated. The number of PCSs used to reconstruct the state space was chosen based on the best compromise between: the RR value; the maximum phase space diameter portion (maximum distance found in the distance plot); and the discrimination between the 20 AFl scenarios as explained in the following [48]. Once the state space was estimated, the procedure for calculating the RP was the same as described in Section II-C.

E. Defining Hyper-Parameters for RQA

After obtaining the respective state vectors for both paradigms, ε was determined. Previous works have suggested that ε should be chosen such that the resulting RR is approximately 1%, or ε should not exceed 10% of the maximum phase space diameter [21], [49]. Therefore, 12 and 10 different values for ε were tested for the icRQA and srRQA, varying from 0.5% to 11%, and from 1% to 10% of the maximum phase space diameter, respectively. Some preliminary results on the icRQA showed no need to test values lower and higher than the 10 selected for srRQA. For each ε, RR was calculated and the discrimination between the 20 different AFl scenarios was evaluated using the MATLAB function rankfeatures ("CriterionValue" set to "roc"). Hence, ε was defined looking for a suitable compromise among the resulting RR (not too high compared to the recommended 1%), the portion of the maximum phase space diameter (not exceeding 10%), and the discrimination between the 20 AFl scenarios.

Similarly, the minimum line lengths for the calculation of DET and LAM were defined considering the discrimination between the 20 different AFl scenarios. Using ε as defined above, both DET and LAM were calculated for 20 values of minimum line length, varying from 2 to 21 for both icRQA and srRQA. The minimum line lengths were also defined as a compromise between the resulting values for DET and LAM and the 20 AFl scenarios discrimination.

A more detailed description of the selection of optimal values for the hyper-parameters can be found in Almeida *et al.* [28].

F. Clinical Data Sample

A sample of clinical 12-lead ECG was used to evaluate the recurrence plots and RQA-based features obtained in the computational framework. The ECGs were collected during an episode of microreentrant AFl in the LA (1 kHz sampling frequency), representing sc17 (ant LAA, Table I). The AFl mechanism was identified and labelled by inspecting the LAT map recorded with a high density 3D electroanatomical mapping system (Rhythmia HDx, Boston Scientific). The signals were notch filtered at 50 Hz, band-pass filtered between 0.05 Hz - 100 Hz. The portion of signals between two QRS-T complexes was manually extracted from the 12-lead ECGs in order to extract the F-wave component related to the AFl activity. More precisely, all P-waves enclosed between the end of a T-wave until the following QRS complex were extracted.

Both icRQA and srRQA paradigms were tested on the clinical sample. The respective RQA-based features were extracted and compared with those obtained *in silico* to verify agreement between the clinical and synthetic scenarios.

All the experimental procedures were in accordance with the ethical standards of the responsible committee on human experimentation (institutional and national) and with the Helsinki Declaration of 1975, as revised in 2000. All patients provided written informed consent.

G. Statistical Analysis

All continuous normally distributed variables are expressed as mean $\pm$ SD. All continuous non-normally distributed variables are expressed as median $\pm$ interquartile range.

Non-parametric data were analyzed using the Kolmogorov-Smirnov test. The comparison between the 20 AFl scenarios was done using the Kruskal-Wallis non-parametric one-way analysis of variance [50], [51].

An iterative binary classification - AFl scenario vs. all other AFl scenarios - was computed to create receiver operating characteristic (ROC) curves. The ROC curves were computed using the MATLAB function perfcurve and the single RQA-based features as discriminators. The optimum sensitivity and specificity on the ROC curve was defined as the point on the curve with the shortest distance to the top left corner of the graph. Validation of the optimum point of operation for the classification was performed with leave-one-out cross-validation (LOOCV). p-values of less than 0.01 were considered statistically significant.

III. Results

A. PCA on the 12-Lead ECGs

Twelve PCs were estimated from the 12-lead ECGs using PCA, and only the main five were considered, explaining $99.97 \pm 0.03\%$ of the total variance. The icRQA paradigm was implemented on the first three PCSs since they explained $99.10 \pm 0.94\%$ of all variance. For the srRQA, however, different numbers of PCSs were tested to define the optimal number of dimensions. Up to five PCs were tested in descending order of total variance explanation, in which a PCS was added as a new dimension at each iteration, starting with the two main dimensions - PCS 1 and 2.

B. icRQA on Different AFl Mechanisms

1) Hyper-Parameters: The ε was tested for PCSs 1, 2, and 3. The area under the ROC curves (AUCROCs) for these PCSs suggest that 5% of the maximum phase diameter represents a suitable compromise among the resulting RR, the portion of the maximum phase space diameter, and the discrimination between
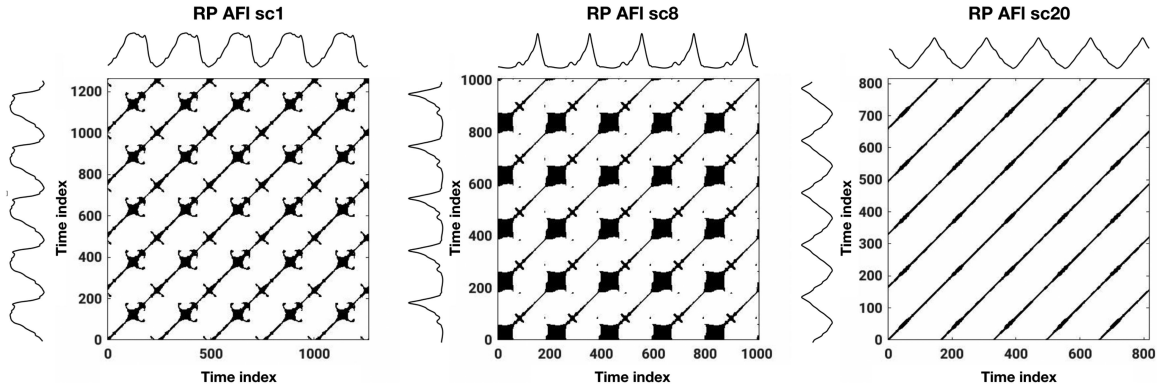
Fig. 2.   The effect of different AFl scenarios in the icRQA-based features. The RPs created for the PCS 1 calculated from the 12-lead ECGs extracted from the same atria and torso combination for three different AFl mechanisms. These examples show how different AFl mechanisms produced different icRQA RPs, highlighting the usefulness of the proposed method for discriminating these different mechanisms.
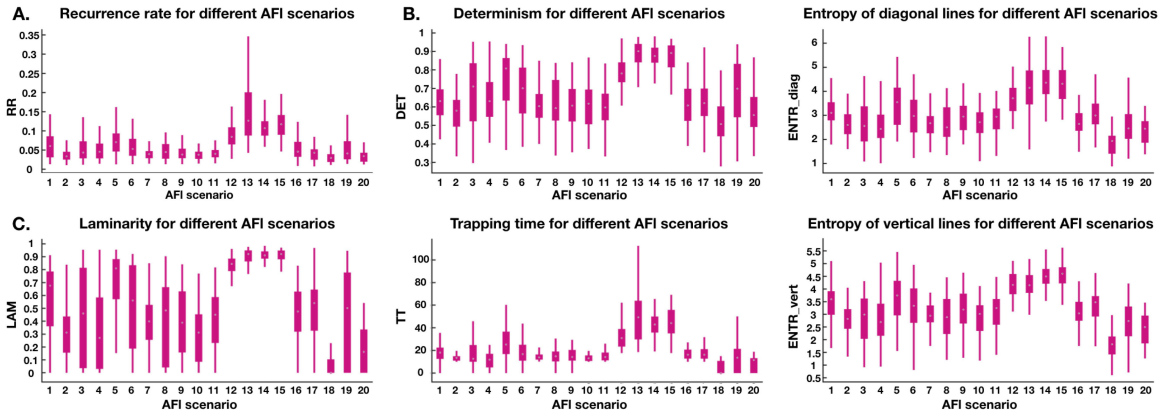

Fig. 3.   Effects of the 20 different AFl scenarios on the icRQA features calculated from PCS 3. (A). RR attribute. (B). Features related to diagonal lines. (C). Features related to vertical lines.

the 20 AFl scenarios. Similarly, the AUCROC values suggest that a minimal diagonal line length of 13, 16, 13 should be considered for the calculation of DET using the PCSs 1, 2, and 3, respectively, and a minimal vertical line length of 10, 11, 8 should be considered for the calculation of LAM. Other values of the maximum phase space diameter and minimal vertical or diagonal line length lead to higher AUCROC and maximal/minimal DET or LAM. However, this may be associated with an undesirable saturation behavior. Further details on these results are provided in the *Supplementary Materials*.

These hyper-parameters were used for the construction of the RPs and the evaluation of icRQA-based features for PCS 1, 2, and 3 in the subsequent parts of the study.

2) Discrimination of AFl Mechanisms: The RPs highlighted visual differences in dynamic structures peculiar to each AFl mechanism (Fig. 2). The icRQA-based features extracted from the PCS 3 between the 20 AFl scenarios are shown in Fig. 3.

All the icRQA features extracted from the individual PCSs (1, 2 and 3) showed significant differences ($p < 0.001$) between the AFl mechanisms. The RPs from all AFl scenarios and the

comparisons of the icRQA features within individual PCSs 1 and 2 are shown in the *Supplementary Materials*.

Sc18 resulted in the lowest values for all 6 icRQA features extracted from the three PCSs, whereas sc12, 13, 14, and 15 showed highest median values. Sc12, 13, 14, and 15 were always significantly different from all other cases for all icRQA features across the 3 PCSs. As exceptions, it can be noticed that: 1) PCS 1 DET and RR have shown no significant differences between sc12 vs. all other AFl scenarios; 2) PCS 2 ENTR_diag and PCS 1 TT for sc13 did not differ from all other AFl scenarios; 3) Sc5 has shown no significant differences from sc12, 13, 14, and 15 for any icRQA-based features for PCS 1.

Finally, the icRQA features were effective in discriminating the 20 AFl scenarios, with LOOCV hit rate as high as 67.7% (Table II).

C. srRQA on Different AFl Mechanisms

1) Hyper-Parameters: A similar protocol was followed for defining ε to the srRQA paradigm, the number of dimensions,

TABLE II
ROC CURVES FOR THE DISCRIMINATION OF 20 AFL SCENARIOS USING THE ICRQA-BASED FEATURES (MEAN±SD)

| PCS 1	RR	DET	LAM	TT	ENTR_diag	ENTR_vert
AUCROC	0.618±0.002	0.636±0.002	0.681±0.002	0.645±0.002	0.640±0.002	0.674±0.002
Sensitivity	0.323±0.002	0.341±0.002	0.294±0.002	0.378±0.003	0.363±0.003	0.346±0.002
Specificity	0.569±0.002	0.602±0.003	0656±0.003	0.687±0.003	0.636±0.001	0.701±0.002
LOOCV hit rate	0.616±0.045	0.627±0.058	**0.677±0.069**	0.642±0.069	0.632±0.058	0.674±0.082
PCS 2	RR	DET	LAM	TT	ENTR_diag	ENTR_vert
AUCROC	0.625±0.002	0.629±0.0002	0.669±0.0002	0.652±0.0002	0.630±0.0002	0.663±0.0002
Sensitivity	0.419±0.003	0.385±0.003	0.325±0.002	0.387±0.002	0.358±0.002	0.297±0.003
Specificity	0.670±0.001	0.643±0.001	0.668±0.002	0.691±0.002	0.626±0.002	0.625±0.002
LOOCV hit rate	0.621±0.059	0.627±0.076	0.627±0.088	0.644±0.096	0.629±0.072	0.659±0.087
PCS 3	RR	DET	LAM	TT	ENTR_diag	ENTR_vert
AUCROC	0.655±0.002	0.654±0.0002	0.673±0.0002	0.668±0.0002	0.655±0.0002	0.667±0.0002
Sensitivity	0.263±0.002	0.224±0.002	0.222±0.001	0.246±0.003	0.254±0.0002	0.281±0.002
Specificity	0.573±0.002	0.538±0.001	0.609±0.003	0.604±0.001	0.566±0.001	0.617±0.002
LOOCV hit rate	0.653±0.091	0.649±0.083	0.649±0.095	0.665±0.100	0.651±0.081	0.665±0.102
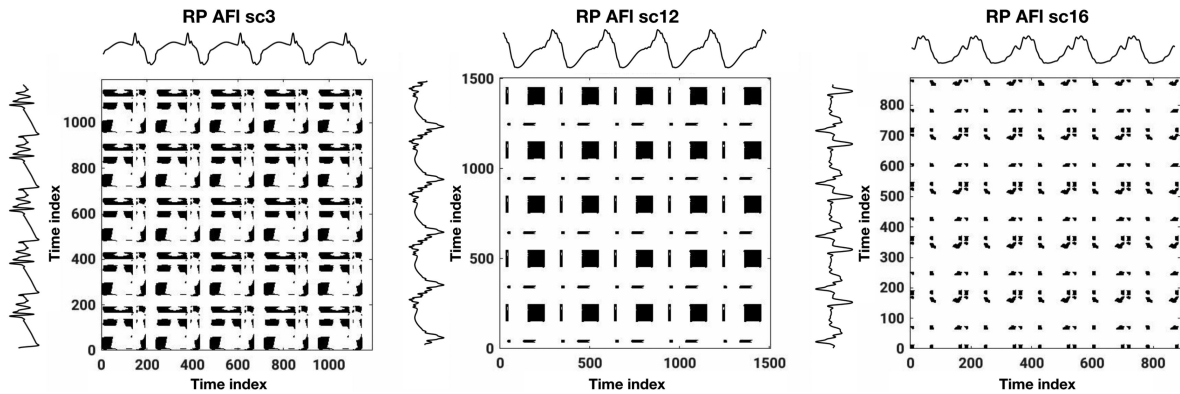
Fig. 4. The effect of different AFI scenarios in the srRQA. The RPs created using two different PCS as dimensions for three different AFI mechanisms. These examples showed how different AFI mechanisms produced different srRQA RPs, making the method promising in characterizing these several mechanisms.

and the minimal vertical/diagonal line length. The AUCROC values suggest that 5% of the maximum phase diameter and 3 as the number of dimensions with a good compromise among the resulting RR, the portion of the maximum phase space diameter, the discrimination between the 20 AFl scenarios and the computational complexity. Similarly, the AUCROC values suggest that a minimum diagonal line length of 6 should be considered for the calculation of DET, and a minimum vertical line length of 7 for the calculation of LAM to obtain a high class discrimination and also minimal and maximal bounds to the attributed estimates. Note that other values of the maximum phase space diameter and minimal vertical or diagonal length lead to higher AUCROC and maximal DET or LAM. These, however, may be associated to an undesirable saturation behavior. Further details on these results are provided in the *Supplementary Materials*.

The obtained srRQA hyper-parameters were used for the construction of the RPs and the evaluation of the RQA-based features in the subsequent parts of this work.

2) Discrimination of AFIs: The RPs estimated following the srRQA paradigm also helped to highlight the differences in the dynamic structures peculiar to each AFI scenario (Fig. 4).

Comparisons of the srRQA-based features within the 20 AFl scenarios are shown in Fig. 5.

All the srRQA features exhibited significant differences (p < 0.001) between the AFl mechanisms. The RPs for all AFl scenarios are shown in the *Supplementary Materials*.

Sc12, 14, and 15 exhibited highest values for all the srRQA features, whereas sc18 showed lowest values for all the features except for RR, where sc20 had the lowest distribution values. Sc12, 14, and 15 were significantly different from all other cases and features. Sc5 and sc13 have shown no significant differences from sc12, 14, and 15 for any srRQA features.

Finally, the srRQA-based features were effective in discriminating the 20 AFl scenarios with LOOCV hit rate as high as 65.4% (Table III).

D. AFI Characterization Using RQA-Based Features

Diagonal lines - related to deterministic structures - were found in all RPs calculated with the icRQA, Fig. 2, whereas deteriorated diagonal lines were found with the srRQA - blocks of recurrence, Fig. 4. Opposite situation for vertical lines - related to laminar structures that were found principally with the srRQA,
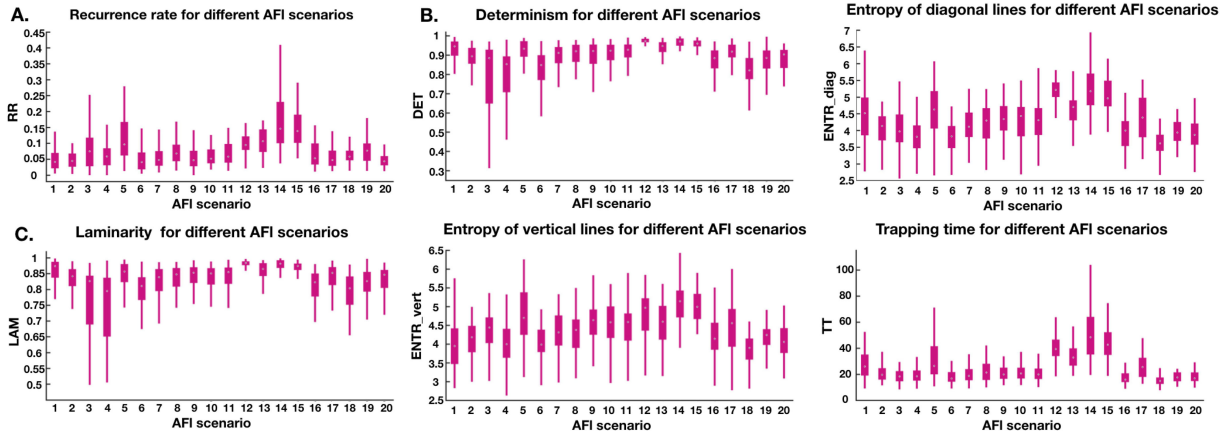
Fig. 5. Effects of the 20 different AFl scenarios on the srRQA features evaluated from the PCS 3. (A). RR attribute. (B). Features related to diagonal lines. (C). Features related to vertical lines.

TABLE III
ROC Curves for the Discrimination of 20 AFL Scenarios Using the srRQA-Based Features (mean±SD)

	RR	DET	LAM	TT	ENTR_diag	ENTR_vert
AUCROC	0.641±0.002	0.632±0.001	0.628±0.004	0.666±0.002	0.651±0.001	0.626±0.003
Sensitivity	0.325±0.001	0.303±0.001	0.350±0.002	0.215±0.003	0.232±0.001	0.340±0.002
Specificity	0.606±0.001	0.568±0.002	0613±0.001	0.540±0.002	0.542±0.001	0.591±0.001
LOOCV hit rate	0.635±0.078	0.635±0.073	0.625±0.063	**0.654±0.083**	0.650±0.085	0.621±0.058

due to the presence of blocks of recurrence in the calculated RPs Fig. 4.

The icRQA and srRQA-based features extracted from the clinical ECG fit perfectly into the interquartile range of the distribution curves of the parameters extracted from the synthetic data. The similarity between the results obtained from clinical and synthetic data could also be seen from the RPs, as shown in Fig. 6.

IV. DISCUSSION

The 12-lead ECGs are broadly used for cardiac diagnostic and to discriminate AFl from AFib [16]. However, they are rarely applied - if ever - to distinguish among macro-groups of AFl mechanisms - e.g., right-sided AFl vs. left-sided AFl [52].

In the present work, we implemented two RQA frameworks to characterize different AFl mechanisms from the perspective of multivariate surface potentials and nonlinear time series. An inside-out computational simulation generated 12-leads ECGs from 20 AFl mechanisms and different combinations of atrial and torso geometries. This provided an ideal and controlled environment, establishing a consistent ground truth for AFl perpetuation mechanisms without the influence of secondary - or unknown - interfering phenomena, e.g., other simultaneous AFls. Spatio-temporal analysis was achieved by combining PCA and RQA, allowing access to the dynamic structure of the heart activity from the non-invasive perspective.

A specific and representative clinical case of study - a microreentrant AFl in the LA, located at the ant LAA (sc17) - was also analyzed, highlighting the robustness and reliability of the
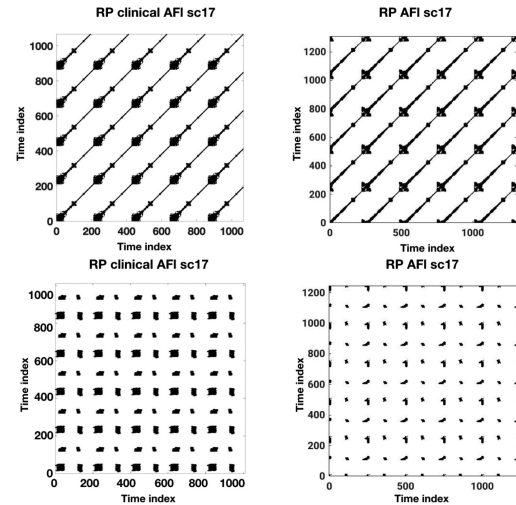
Fig. 6. RPs calculated from the clinical and the corresponding simulated case (left column, and right column, respectively), using icRQA on PCS 1 and srRQA (top line, and bottom line, respectively). The RPs showed how similar the results obtained from the clinical data are in comparison with the simulated ones, using the RQA methods optimized just with synthetic signals. This demonstrates the reliability of the simulated scenarios and the correct implementation of the methods for future clinical application.

proposal. Moreover, having obtained similar results from clinical and synthetic data also demonstrates how these simulated data could really be used in clinical practice. In fact, due to the

limited access to clinical data with a precise description of the ground truth for AFl perpetuation, these simulations could be used as clinical data substitutes to optimize and train RQA and classification algorithms in clinical practice.

Our results suggest that RQA is effective in characterizing and discriminating the dynamic structures from distinct AFl mechanisms, and might help to define novel protocols for clinical planning and ablation strategy.

A. RQA-Based Features Extracted From Simulated AFl 12-Lead ECGs

In the present study, rigorous steps for a proper reconstruction of the RPs and well-defined representative RPs structures (e.g., laminar diagonals, laminar verticals, well-defined blocks etc). Moreover, the introduction of PCA has been shown effective for building a minimal, non-redundant base for the representation of non-invasive multivariate AFl mechanisms. This is corroborated by the variance explained by the selected PCSs and the well-defined RPs structures observed after such coordinate transformation. The need for low dimensional (informative) state space is also justified by the underlying challenges concerning embedding definitions, in which redundant dimensions - as introduced by the spatial oversampling of cardiac activity by multi-lead recording - can contribute to a topological degenerated "attractor". In fact, the addition of non-informative embedding dimensions can introduce spurious RQA structures, as shown by [21], in which a higher dimensional space introduced spurious diagonal lines and inflated the determinism obtained from (uncorrelated) stochastic observations.

It also worth to mention that PCA allows to easily sort PCS according to their information content - explanation of the total variance. In the srRQA case, this allows to implement the state space starting from the two most relevant components - i.e., PCS 1 and PCS 2 -, and then adding new PCS/dimensions following the order of relevance - PCS 3, PCS 4, etc. This would not be possible by using the ECG directly, as there is no natural way to order the leads according to relevance. The 3 main PCSs were taken into account for the icRQA, whereas for the srRQA the embedding dimension used up to the first 5 PCSs. However, the best srRQA embedding dimension was the one using the first 3 PCS (see *Supplementary Materials*), confirming that the following PCS do not contain useful information for the analysis - the main 3 PCSs already explained $99 \pm 0.94\%$ of all variability of the phenomena.

A thorough investigation was then conducted to better define ε for each simulation. The determination of ε took into account the fact that 12-lead ECGs of AFl are usually quite regular - as shown in Fig. 1C - and exhibit high DET as an intrinsic behavior, which would contribute to a high RR and far from the suggested 1% recommendation [21]. The proposed approach aimed to choose an adaptive ε as a percentage of maximal phase space difference, leading to a relatively low RR and distinguishable between the 20 different AFl scenarios in the DET and LAM features.

The minimum diagonal/vertical line length for the calculation of both DET and LAM has also been assessed. The results suggest that DET and LAM are preserved even for different minimum line diagonal/vertical lengths. Undesirable saturation behavior was avoided and AFl discrimination was improved selecting the following minimum diagonal/vertical line lengths for DET and LAM determination: regarding the icRQA, a minimum diagonal length of 13, 16, and 13, and a minimum vertical length of 10, 11, and 18 were selected on PCS1, 2, and 3 respectively; regarding the srRQA, a minimum diagonal length of 6, and a minimum vertical length of 7 were selected.

B. Characterization of Simulated AFl Signals Using RQA

In this work we attempted to (i) assess changes in RQA-based features between different AFl mechanisms; (ii) implement a novel RQA paradigm that also considers spatial information and; (iii) evaluate 12-lead ECG classification using RQA-based features.

The RPs for both methods (icRQA and srRQA) highlighted the highly periodic behaviour of the AFl mechanisms Fig. 2, Fig. 4. These results are corroborated by the ground truth from the simulated AFl episodes, known to be periodic and stable phenomena.

Previous work have shown underlying deterministic structures present on activation sequences on AFib intra-cardiac electrograms [26], [53]. On the one hand, our results from the icRQA paradigm Fig. 2 - also highlights diagonal structures associated with deterministic behavior in the RPs. This may suggest the presence of stable periodic orbits that commonly drive AFl as a localized self-perpetuating loop. However, this deterministic behavior is clearly presented in the RPs obtained in the srRQA paradigm (Fig. 4), which is probably justified by the use of a completely different embedding space defined by the PCS. In this case, the introduction of spatial information seems to contribute to enhancing the laminar behavior - blocks in the RPs - instead of the diagonal lines associated with co-evolution of states. In fact, the AFl scenarios with evident blocks of recurrence are also the ones with the highest values of ENTR_vert, LAM, and TT - sc12, 13, 14, and 15 - for both methods Fig. 2, Fig. 4.

The only scenarios having an iso-line in their 12-lead ECGs are the four focal sources mechanism. These are the only mechanisms in which there is a clear phase of depolarization, repolarization, and rest of the atrial tissue. This might explain the so dominant laminar structure in comparison with all the other mechanisms.

Considering all the features calculated with both RQA methods, the focal source scenarios are the only ones presenting up-regulated RQA-features compared to the other mechanisms. Interestingly, despite representing a scar-related reentry mechanism, sc5 is the only scenario not statistically different from the focal sources episodes considering all srRQA and icRQA features extracted from PCS 1. More specifically, the focal sources on sc12 to sc15 are located nearby the PVs and, since sc5 represents a scar-related reentry within the LPV, the macroscopic behavior of these seemingly different EP are perceived as similar.

Finally, scenarios sc18 and sc20 have shown down-regulated RQA-features, suggesting that microreentries result in lower

deterministic and laminar phenomena in comparison with the other mechanisms.

C. RQA-Based Features Discrimination of Different AFl

Almeida *et al.* showed that RQA-based features are sensitive to EP characteristics of the atrial tissue [28]. Our results support this perspective, suggesting that the RQA-based features extracted from simulated 12-lead ECGs are sensitive to different AFl mechanisms.

Considering that a single feature classification of 20 classes, sometimes very similar between each other, is not trivial, an averaged LOOCV hit rate higher than 60% for all the features with both the methods confirm the hypothesis of using these features as discriminatory features.

Previous works have considered RQA features to classify AFib atrial substrate and use these features as complementary tools to help guide ablation [54]. RQA has also been used to distinguish atrial regions hosting spiral wave reentry from regions with multiple wavelet breakup [55]. Other works combined RQA with PCA on electrograms to discriminate persistent AFib from paroxysmal AFib [27] and non-linear features to discriminate AFib, AFl, VT, and VF [56], [16]. Finally, Yang combined RQA with spatial cardiac vectocardiogram signals to identify cardiovascular disorders [30]. To the best of our knowledge, ours represents the first study to use RQA in the discrimination of different AFl mechanisms from simulated 12-lead ECGs.

The icRQA-based variables Fig. 3 - related to the diagonal lines have shown a higher hit rate on the PCS 3, suggesting that small but important changes in the deterministic behavior of these different types of AFl are present. This can be explained considering that PCS 3 is a signal with a low explanation of the variability, and meaning that it contains only the details of the deterministic behavior of the AFls. By contrast, PCS 1, and 2 have a lower hit rate, likely because there are no major changes regarding the deterministic behavior between the 20 AFl scenarios. Substantially because being PCS 1, and 2 signals with most of the explanation of the variability, they capture the more general deterministic behavior of the mechanisms. The opposite was found for LAM and ENTR_vert, meaning that these AFl mechanisms have shown macro changes on the laminar behavior rather than micro changes.

The findings described here motivate further investigation regarding the use of RQA-based features as biological markers that can potentially be used as features for classification structures to inversely predict the mechanism driving AFl using RQA-features as a basis for a more complex multi-feature classifier with the perspective of guiding ablation procedures in the future.

V. LIMITATIONS

The current study is limited to simulated data and tested on only one clinical ECG.

Although 20 AFl mechanisms inspired by clinical situations have been implemented, they are just a general representation of the mechanisms that are most commonly found in the literature. More scenarios should be included in the dataset, considering

the heterogeneity found in the clinical practice - e.g., different locations of scar-related AFl or slow conduction areas.

Further investigations should be conducted on more clinical data to extend the value of the methods. Although the manual segmentation of the clinical ECG is not time consuming, in view of a future clinical application, automated segmentation of clinical ECG should be implemented to extract the F-wave.

The embedding for the estimation of RPs and, consequently, RQA parameters has been done considering the ability of the variables in discriminating the different types of AFl scenarios. The fact that 20 different classes have been used could have led to a biased parameters setting. Accordingly, while it could have increased the differences between some classes, it might have decreased the differences between others, leading to a non-optimal discrimination among them. Therefore, a reduction of the number of classes - e.g., by merging some cases in the same class - should be investigated. The merging could also lead to an increase in the hit rates, making the classification problem easier. The grouping could be done by gathering classes belonging to the same macro-areas - e.g. macroreentry, microreentry, scar-related reentry, figure-8, and focal sources - or in AFl classes that requires similar ablation procedures to be terminated.

The AFl mechanisms were simulated with atrial models without ventricles. Thus, the QRS-T complex was absent from our signals. This must be taken into account when applying the RQA methods to clinical data. In addition, the CV set in the simulations is constant and only 8 atria models were used. A change in the CV and the addition of other atria models could lead to a change in the results.

A single feature classification was performed to evaluate the potential of these variables to discriminate different AFl mechanisms. To implement a valid classifier able to inversely predict the AFl mechanism from the ECG signals and increase the hit rate with both the methods, a multi feature classification and different classification algorithms should be tested.

Despite of that, this work presents an important contribution for characterizing the dynamics of AFl mechanisms, which deserves a careful attention for setting the RQA general approach and parameters before class clustering and classification evaluation.

VI. CONCLUSION

In the present work, different AFl mechanisms were characterized from the perspective of multivariate surface potentials and nonlinear time series. Two methods for RQA were implemented to investigate different AFl scenarios. An inside-out computational simulation generated 12-leads ECGs from 20 AFl mechanisms and different combinations of atrial and torso geometries, in which the ground truth for AFl perpetuation were known. RQA was combined with PCA creating a spatial-temporal domain analysis, allowing access to the dynamic structure of the heart activity from the non-invasive perspective.

Our results suggest that RQA-based features are sensitive to the underlying EP phenomena, and are effective in characterizing the dynamic structures from distinct AFl mechanisms.

The focal source scenarios showed the highest RQA feature values using both paradigms, demonstrating how these cases have a significant deterministic and laminar behavior in the dynamic structure. In contrast, microreentries are less deterministic and laminar phenomena.

The use of the PCSs 1, 2, and 3 for the icRQA showed how there can be relevant small or major changes in the dynamic behaviors between these different AFl mechanisms, based on the ability to better or worse discriminate the AFl along the three PCSs.

RQA-based features could potentially be used to implement a multi-feature classifier able to inversely predict different mechanisms driving AFl from non-invasive signals in future works. This non-invasive RQA-based classifier could aid in planning and tailoring the ablation strategy, reducing time and resources required to conduct invasive cardiac mapping and ablation procedures.

To conclude, a clinical 12-lead ECG was used as a proof of concept to show the efficacy on using simulations in that cases in which to obtain reliable clinical data would be difficult, and to prove the validity of these two RQA methods to characterize and to classify these different AFl mechanisms.

ACKNOWLEDGMENT

REFERENCES

[1] J. Granada et al., "Incidence and predictors of atrial flutter in the general population," J. Amer. College Cardiol., vol. 36, no. 7, pp. 2242–2246, 2000.

[2] S. Bun et al., "Atrial flutter: More than just one of a kind," Eur. Heart. J., vol. 36, no. 35, pp. 2356–2363, 2015.

[3] F. G. Cosio et al., "Atrial flutter: An Update," Rev. Esp. Cardiol., vol. 59, no. 8, pp. 816–831, 2006.

[4] F. G. Cosio et al., "Atrial flutter mapping and ablation I: Studying atrial flutter mechanisms by mapping and entrainment," Pacing Clin. Electrophysiol, vol. 19, no. 5, pp. 841–853, 1996.

[5] R. J. Schilling et al., "Characterization of the anatomy and conduction velocities of the human right atrial flutter circuit determined by non-contact mapping," J. Am. Coll. Cardiol., vol. 38, no. 2, pp. 385–393, 2001.

[6] T. Itoh et al., "High correlation of estimated local conduction velocity with natural logarithm of bipolar electrogram amplitude in the reentry circuit of atrial flutter," J. Cardiovascular Electrophysiol., vol. 25, no. 4, pp. 387–394, 2014.

[7] G. Ndrepepa et al., "Activation patterns in the left atrium during counter-clockwise and clockwise atrial flutter," J. Cardiovascular Electrophysiol., vol. 12, no. 8, pp. 893–899, 2001.

[8] P. Jais et al., "Mapping and ablation of left atrial flutters," Circulation, vol. 101, no. 25, pp. 2928–2934, 2000.

[9] I. Deisenhofer et al., "Left atrial tachycardia after circumferential pulmonary vein ablation for atrial fibrillation: Incidence, electrophysiological characteristics, and results of radiofrequency ablation," Europace, vol. 8, no. 8, pp. 573–582, 2006.

[10] S. Ammar et al., "Ablation of perimitral flutter: Acute and long-term success of the modified anterior line," Europace, vol. 17, no. 3, pp. 447–452, 2015.

[11] A. M. Patel et al., "Atrial tachycardia after ablation of persistent atrial fibrillation: Identification of the critical isthmus with a combination of multielectrode activation mapping and targeted entrainment mapping," Circ. Arrhythmia Electrophysiol., vol. 1, no. 1, pp. 14–22, 2008.

[12] S. M. Markowitz et al., "Atrial tachycardias and atypical atrial flutters: mechanisms and approaches to ablation," Arrhythmia Electrophysiol. Rev., vol. 8, no. 2, pp. 131–137, 2019.

[13] R. De Ponti et al., "Treatment of macro-re-entrant atrial tachycardia based on electroanatomic mapping: Identification and ablation of the mid-diastolic isthmus," Europace, vol. 9, no. 7, pp. 449–457, 2007.

[14] P. Jais et al., "A deductive mapping strategy for atrial tachycardia following atrial fibrillation ablation: Importance of localized reentry," J. Cardiovascular Electrophysiol., vol. 20, no. 5, pp. 480–491, 2009.

[15] C. Pedrinazzi et al., "Atrial flutter: From ECG to electroanatomical 3D mapping," Heart Int., vol. 2, no. 3-4, pp. 161–170, 2006.

[16] U. R. Acharya et al., "Automated characterization of arrhythmias using nonlinear features from tachycardia ECG beats," in Proc. IEEE Int. Conf. Syst., Man, Cybern., Budapest, 2016, pp. 533–538.

[17] L. L. Trulla et al., "Recurrence quantification analysis of the logistic equation with transients," Phys. Lett. A, vol. 223, no. 4, pp. 255–260, 1996.

[18] C. L. Webber Jr. and J. P. Zbilut, "Dynamical assessment of physiological systems and states using recurrence plot strategies," J. Appl. Physiol., vol. 76, no. 2, pp. 965–973, 1994.

[19] J. P. Zbilut et al., "Recurrence quantification analysis as a tool for nonlinear exploration of nonstationary cardiac signals," Med. Eng. Phys., vol. 24, no. 1, pp. 53–60, 2002.

[20] N. Marwan et al., "Recurrence-plot-based measures of complexity and their application to heart-rate-variability data," Phys. Rev. E., vol. 66, no. 2, 2002, Art. no. 026702.

[21] N. Marwan et al., "Recurrence plots for the analysis of complex systems," Phys. Rep., vol. 438, pp. 237–329, 2007.

[22] H. Arce et al., "Recurrence analysis of cardiac restitution in human ventricle," in Recurrence Plots and Their Quantifications: Expanding Horizons, Springer Proceedings in Physics, vol. 180. Berlin, Germany: Springer, 2016, pp. 169–183.

[23] U. R. Acharya et al., "Automated prediction of sudden cardiac death risk using Kolmogorov complexity and recurrence quantification analysis features extracted from HRV signals," in Proc. IEEE Int. Conf. Syst., Man, Cybern., 2015, pp. 1110–1115.

[24] M. Tang et al., "An improved method for discriminating ECG signals using typical nonlinear dynamic parameters and recurrence quantification analysis in cardiac disease therapy," in Proc. IEEE Eng. Med. Biol., 2005, pp. 2459–2462.

[25] U. Desai et al., "Diagnosis of multiclass tachycardia beats using recurrence quantification analysis and ensemble classifiers," J. Mech. Med. Biol., vol. 16, no. 1, 2016, Art. no. 1640005.

[26] F. Censi et al., "Recurrent patterns of atrial depolarization during atrial fibrillation assessed by recurrence plot quantification," Ann. Biomed. Eng., vol. 28, pp. 61–70, 2000.

[27] S. Zeemering et al., "Recurrence quantification analysis applied to spatiotemporal pattern analysis in high-density mapping of human atrial fibrillation," in Proc. IEEE Eng. Med. Biol., 2015, pp. 7704–7707.

[28] T. Almeida et al., "Characterization of human persistent atrial fibrillation electrograms using recurrence quantification analysis," Chaos, vol. 28, no. 8, 2018, Art. no. 085710.

[29] T. Almeida et al., "The temporal stability of recurrence quantification analysis attributes from chronic atrial fibrillation electrograms," Res. Biomed. Eng., vol. 34, no. 4, pp. 337–349, 2018.

[30] H. Yang, "Mulstiscale recurrence quantification analysis of spatial cardiac vectorcardiogram signals," IEEE Trans. Biomed. Eng., vol. 58, no. 2, pp. 339–347, Feb. 2011.

[31] P. Jais et al., "A deductive mapping strategy for atrial tachycardia following atrial fibrillation ablation: Importance of localized reentry," J. Cardiovascular Electrophysiol., vol. 20, no. 5, pp. 480–491, 2009.

[32] J. E. Ban et al., "Relationship between complex fractionated atrial electrograms during atrial fibrillation and the critical site of atrial tachycardia that develops after catheter ablation for atrial fibrillation," J. Cardiovasc. Electrophysiol., vol. 25, no. 2, pp. 146–153, 2014.

[33] T. G. Oesterlein et al., "Automatic identification of reentry mechanisms and critical sites during atrial tachycardia by analyzing areas of activity," IEEE Trans. Biomed. Eng., vol. 65, no. 10, pp. 2334–2344, Oct. 2018.

[34] V. Jacquemet, "An eikonal approach for the initiation of reentrant cardiac propagation in reaction-diffusion models," IEEE Trans. Biomed. Eng., vol. 57, no. 9, pp. 2090–2098, Sep. 2010.

[35] J. Trächtler *et al.*, "Virtualizing clinical cases of atrial flutter in a fast marching simulation including conduction velocity and ablation scars," *Current Directions Biomed. Eng.*, vol. 1, no. 1, pp. 405–408, 2015.

[36] M. W. Krueger *et al.*, "Personalization of atrial anatomy and electrophysiology as a basis for clinical modeling of radio-frequency ablation of atrial fibrillation," *IEEE Trans. Med. Imag.*, vol. 32, no. 1, pp. 73–84, Jan. 2013.

[37] A. Wachter *et al.*, "Mesh structure-independent modeling of patient-specific atrial fiber orientation," *Current Directions Biomed. Eng.*, vol. 1, no. 1, pp. 409–412, 2015.

[38] A. Loewe *et al.*, "Influence of the earliest right atrial activation site and its proximity to interatrial connections on P-wave morphology," *Europace*, vol. 18, no. suppl 4, pp. iv35–iv43, 2016.

[39] A. Loewe, "Chronic AF induced remodeling," in *Modeling Human Atrial Patho-Electrophysiology From Ion Channels to ECG : Substrates, Pharmacology, Vulnerability, and P-Waves*, Karlsruhe, Germany: KIT Scientific Publishing, 2016, ch. 5.2, pp. 113–119.

[40] R.L. Lux *et al.*, "Body surface potential mapping techniques," in *Comprehensive Electrocardiology*. London, U.K.: Springer, 2010, pp. 1361–1374.

[41] M. Stenroos, "The transfer matrix for epicardial potential in a piece-wise homogeneous thorax model: The boundary element formulation," *Phys. Med. Biol.*, vol. 54, no. 18, pp. 5443–55, 2009.

[42] R. Schmidt *et al.*, "Herzerregung: Elektrokardiogramm (EKG)," in *Physiologie Des Menschen: Mit Pathophysiologie*, Berlin, Germany: Springer-Verlag, 2011, ch. 25.3, pp. 578–588.

[43] A. Izenman, "Linear dimensionality reduction," in *Modern Multivariate Statistical Techniques: Regression, Classification, and Manifold Learning*, New York, NY, USA: Springer, 2008, ch. 7.2, pp. 196–215.

[44] A. Khawaja, "Automatic ECG analysis using principal component analysis and wavelet transformation," Ph.D. dissertation, Dept. Elect. Info. Eng., Karlsruhe Inst. Technol., Karlsruhe, Germany, 2007.

[45] J. Shlens, "A tutorial on principal component analysis," 2014, *arXiv:1404.1100*.

[46] J.-P. ECKmann *et al.*, "Recurrence plots of dynamical systems," *Europhys. Lett.*, vol. 4, no. 9, pp. 973–977, 1987.

[47] P. Faure and H. Korn, "A new method to estimate the Kolmogorov entropy from recurrence plots: its application to neural signals," *Physica D: Nonlinear Phenom.*, vol. 122, pp. 265–279, 1998.

[48] N. Marwan, "How to avoid potential pitfalls in recurrence plot based data analysis," *Int. J. Bifurcation Chaos*, vol. 21, pp. 1003–1017, 2011.

[49] J. P. Zbilut and C. L. Webber Jr., "Embeddings and delays as derived from quantification of recurrence plots," *Phys. Lett.*, vol. 171, no. 3-4, pp. 199–203, 1992.

[50] M. Hollander *et al.*, *Nonparametric Statistical Methods*, 3rd ed., Hoboken, NJ, USA: Wiley, 2013, ch. 5-6.

[51] J. D. Gibbons and S. Chakraborti, "Tests of the equality of k indipendent samples," in *Nonparametric Statistical Inference*, 5th ed. Boca Raton, FL, USA: CRC Press, 2011, ch. 10, pp. 343–377.

[52] C. Medi and J. M. Kalman, "Prediction of the atrial flutter circuit location from the surface electrocardiogram," *Europace*, vol. 10, pp. 786–796, 2008.

[53] D. Gordon *et al.*, "Searching for "order" in atrial fibrillation using electrogram morphology recurrence plots," *Comput. Biol. Med.*, vol. 65, pp. 220–228, 2015.

[54] N. Navoret *et al.*, "Detection of complex fractionated atrial electrograms using recurrence quantification analysis," *IEEE Trans. Biomed. Eng.*, vol. 60, pp. 1975–1982, 2013.

[55] J. P. Hummel *et al.*, "A method for quantifying recurrent patterns of local wavefront direction during atrial fibrillation," *Comput. Biol. Med.*, vol. 89, pp. 497–504, 2017.

[56] D. DeMazumder *et al.*, "Dynamic analysis of cardiac rhythms for discriminating atrial fibrillation from lethal ventricular arrhythmias," *Circ. Arrhythmia Electrophysiol.*, vol. 6, no. 3, pp. 555–561, 2013.

Automatic ECG-based Discrimination of 20 Atrial Flutter Mechanisms: Influence of Atrial and Torso Geometries

Giorgio Luongo[1], Steffen Schuler[1], Massimo W Rivolta[2], Olaf Dössel[1], Roberto Sassi[2], Axel Loewe[1]

[1]Institute of Biomedical Engineering, Karlsruhe Institute of Technology (KIT), Karlsruhe, Germany
[2]Dipartimento di Informatica, Università degli Studi di Milano, Milan, Italy

Abstract

Atrial flutter (AFl) is a common heart rhythm disorder driven by different self-sustaining electrophysiological atrial mechanisms. In the present work, we sought to discriminate which mechanism is sustaining the arrhythmia in an individual patient using non-invasive 12-lead electrocardiogram (ECG) signals. Specifically, we analyse the influence of atrial and torso geometries for the success of such discrimination. 2,512 ECG were simulated and 151 features were extracted from the signals. Three classification scenarios were investigated: random set classification; leave-one-atrium-out (LOAO); and leave-one-torso-out (LOTO). A radial basis neural network classifier achieved test accuracies of 89.84%, 88.98%, and 59.82% for the random set classification, LOTO, and LOAO, respectively. The most discriminative single feature was the F-wave duration (74% test accuracy). Our results show that a machine learning approach can potentially identify a high number of different AFl mechanisms using the 12-lead ECG. More than the 8 atrial models used in this work should be included during training due to the significant influence that the atrial geometry has on the ECG signals and thus on the resulting classification. This non-invasive classification can help to identify the optimal ablation strategy, reducing time and resources required to conduct invasive cardiac mapping and ablation procedures.

1. Introduction

Atrial flutter (AFl) is an atrial tachycardia characterized by electrical signals that repeatedly propagate along various physiological pathways different from sinus rhythm [1]. This arrhythmia is driven by different self-sustaining reentrant mechanisms. Although AFl is not a direct cause of death, it can cause significant symptoms and complications - e.g., stroke and heart attacks. The most commonly used treatment to restore sinus rhythm from AFl conditions is ablation therapy. The problem of ablation therapy consists in identifying the type of AFl, as each mechanism requires a different ablation procedure. Therefore, the doctor needs to know clearly the type of AFl in progress before performing the ablation. To identify the AFl mechanism, an invasive mapping of the electrical activity of the atria is carried out using intracardiac catheters.

Using the 12-lead ECG to discriminate the type of AFl with which the patient is affected would give doctors the opportunity to plan the intervention in advance. Thus, reducing the procedure time for invasive mapping and ablation therapy. Multiple algorithms have been proposed to discriminate AFl from other types of cardiac arrhythmias, such as atrial fibrillation [2, 3]. Nevertheless, automatic discrimination of different AFl mechanisms has not yet been carried out.

In this preliminary study, we sought to discriminate 20 different simulated AFl mechanisms by using 12-lead ECG signals. Moreover, we focused on the role of the geometries of the atria and torso for the success of this automatic discrimination.

2. Methods

2.1. Simulated AFl scenarios

Based on the AFl mechanisms commonly differentiated in literature [4, 5], precisely resembling documented clinical AFl cases [6–8], and the simulations implemented in a previous work by Oesterlein *et al.* [9], a database of computational AFl scenarios was set up.

Cardiac excitation was modelled using the fast marching approach to solve the Eikonal equation [10, 11].

The atrial electrophysiological activity was simulated on the tetrahedral volume meshes of 8 bi-atrial anatomies, generated from segmented magnetic resonance imaging (MRI) data of healthy male and female subjects [12].

In total, 20 mechanisms/scenarios of AFl were implemented, including right atrial (RA) flutter as well as left atrial (LA) forms like macroreentry around the valves (sc1-4), across the roof (sc9-11), focal ectopy (sc12-15), and microreentries mediated by scars (sc5-8), and slow conduction areas (sc16-20). A complete list of scenarios is

Table 1. Database of clinically informed manually parameterized AFl mechanisms

Mechanism	Atrium	Position	Direction	ID
Macroreentry	RA	Tricuspid Valve	ccw	sc1
Macroreentry	RA	Tricuspid Valve	cw	sc2
Macroreentry	LA	Mitral Valve	ccw	sc3
Macroreentry	LA	Mitral Valve	cw	sc4
Scar-related Reentry	LA	LPV	post	sc5
Scar-related Reentry	LA	LPV	ant	sc6
Scar-related Reentry	LA	RPV	post	sc7
Scar-related Reentry	LA	RPV	ant	sc8
Figure-8 Macroreentry	LA	Both PVs	ant	sc9
Figure-8 Macroreentry	LA	Both PVs	post	sc10
Figure-8 Macroreentry	LA	RPVs	ant	sc11
Focal Source	LA	RSPV anterior		sc12
Focal Source	LA	RSPV posterior		sc13
Focal Source	LA	LSPV anterior		sc14
Focal Source	LA	LSPV posterior		sc15
Microreentry	LA	ant MV annulus		sc16
Microreentry	LA	ant LAA		sc17
Microreentry	LA	ant RSPV		sc18
Figure-8 Microreentry	LA	ant		sc19
Microreentry	LA	post wall		sc20

Right atrium (RA), left atrium (LA), left pulmonary vein (LPV), right pulmonary vein (RPV), pulmonary veins (PVs), right superior pulmonary vein (RSPV), left superior pulmonary vein (LSPV), mitral valve (MV), left atrial appendage (LAA), clockwise (cw), counterclockwise (ccw), anterior (ant), posterior (post), scenario (sc).

provided in Table 1.

Transmembrane voltages (TMV) were obtained by aligning a template of their time course with activation times. This TMV was calculated using the Courtemanche *et al.*'s mathematical model of the human atrial action potential including chronic atrial fibrillation remodeling [13]. From the TMV, the body surface potential map (BSPM) was calculated on 8 different triangulated torso surface models generated from segmented MRI data of healthy male and female subjects [12, 14]. The boundary element method was used to solve the forward problem of electrophysiology [15]. From the BSPM, the 12-lead ECG was extracted, including the 12-lead ECGs. A detailed description of the simulation procedure can be found in [16].

Each 12-lead ECG signal has a length of a single AFl loop and a sample frequency of 1 kHz. The 12-lead ECG signals are formed only by F-waves (flutter waves, P-waves during AFl) without the QRS complex and T-wave (representing ventricular activity) since the ventricles were not included in the simulations (Fig. 1A-C).

A total of 2,512 12-lead ECGs were calculated from 20 simulated AFl scenarios on 8 atrial models with two orientational variants each and 8 torso models. One of the atrial models was not able to sustain sc12, sc13, and sc30 for geometric reasons. Therefore, these AFl scenarios were not computed with this geometry.

2.2.   Correlation analysis

The influence of atrial and torso geometry was assessed by circular cross-correlation analysis. Correlation analysis was performed between ECG signals with different atrial models, keeping AFl mechanisms and torso models fixed. The same procedure was applied between ECG signals with different torso models while keeping AFl mechanisms and atrial models fixed. The correlation coefficients obtained were merged by averaging along the 12 leads.

2.3.   Feature extraction

151 features were extracted from the 12-lead ECGs using several biosignal processing methods from different domains, i.e., time, frequency, wavelet, entropy, and nonlinear recurrence analysis.

Among these features, and looking at the results, the F-wave duration feature proved to be particularly relevant. The F-wave duration was the duration time of a complete cycle of atrial electrical activation of each specific AFl mechanism, i.e., the length of the F-wave in the ECG signal. This feature was manually derived.

2.4.   Feature selection

Greedy forward selection algorithm was implemented to select a feature set. This algorithm started with an empty feature set and added the feature leading to the highest accuracy increase to the set at each iteration. The algorithm was stopped when performance based on the validation set could not be further increased. In order to handle possible correlations among features, the candidate feature to be added to the set was only added if the correlation coefficient with any of the already included features was <0.6.

2.5.   Classification

Three classifiers were implemented for a 20 classes discrimination: decision tree (DT), k-nearest neighbours (KNN), and radial basis neural network (rbNN).

First, we wanted to simulate the scenario of having similar geometries in each data subset. Therefore, the data were randomly divided in training set, validation set, and test set with ratios of 70%, 15%, and 15%, respectively. Second, classifications were performed with leave-one-atrium-out (LOAO) and leave-one-torso-out torso (LOTO) algorithms. In the LOAO algorithm, 7 atrial geometries were used in the training set and the remaining atrial geometry was used both in the validation and test set (50% of the ECGs from this geometry in each set). This procedure was cyclically repeated 8 times always changing the validation/test atrial geometry. The average accuracy of
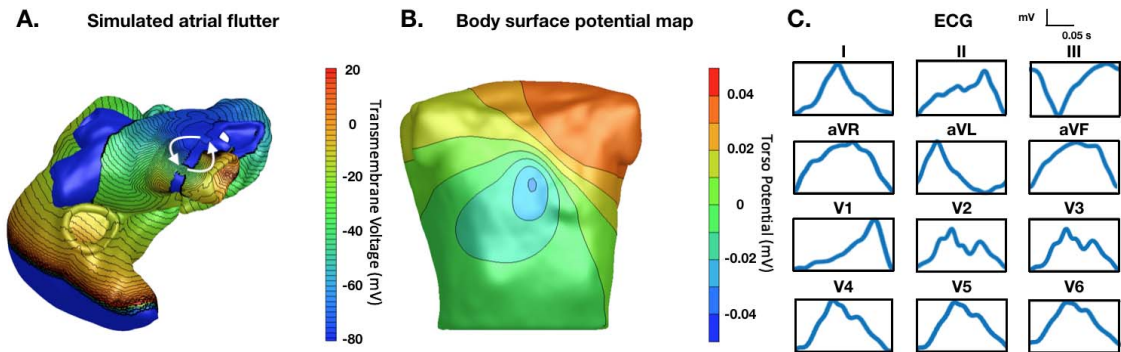
Figure 1. A. Simulated scar-related reentry AFl located on the LPV with anterior direction of rotation (sc6 - white arrows) on an atrial model generated from MRI. B. BSPM on torso model generated from MRI. The torso potential was obtained by solving the forward problem of electrophysiology from the simulated TMV on the atria. C. Example of the F-wave single loop of the 12-lead ECG signals extracted from the BSPM.

the 8 loops was used as performance parameter. The same procedure was applied for the LOTO.

3. Results

3.1. Torsos and atrial models influence on the ECG

The correlation distribution obtained from the correlation analysis between ECG signals of the same AFl types computed in the same torsos but on different atria showed a median of 0.44 and an interquartile range (IQR) of 0.13. On the contrary, a median of 0.78 and IQR of 0.11 was found from the correlation analysis between ECG signals of the same AFl types with the same atria but different torsos. Fig. 2 shows an example of the effect that different torso geometries and atrial geometries have on the 12-lead ECGs (Fig. 2A. and B. respectively).

3.2. Random set classification

The rbNN achieved the highest performance with 89.84% accuracy on the test set using 10 features. The KNN and DT classifiers achieved 83.25% and 81.02% accuracy on the test set using 12 and 5 features, respectively.

F-wave duration was the most discriminative feature for all classification algorithms. This single feature classified the AFl mechanisms with a test accuracy of 74%, while the entire feature set without F-wave duration reduced the test set accuracy to 33% (rbNN).
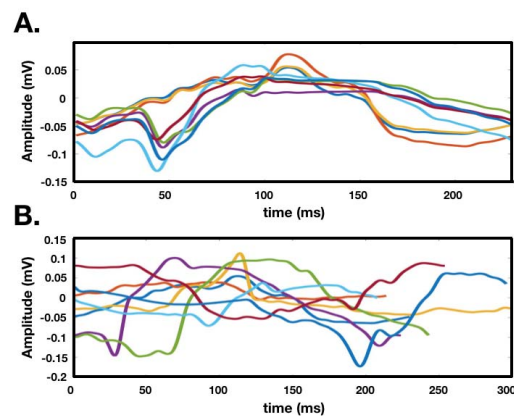
Figure 2. Example of simulated ECG (lead I) of the AFl scenario *sc1* with different torso and atrial models. A. Lead I simulated on the same atria model with 8 different torso geometries. B. Lead I simulated on 8 different atria models with the same torso geometry.

3.3. LOTO & LOAO

The LOTO and LOAO classifications with rbNN yielded a test accuracy of 88.98% and 59.82% using 7 and 6 features, respectively. In both cases, the F-wave duration was selected as the first feature in the feature set.

4. Discussion and Conclusions

Simulations provide ideal and controlled scenarios where the ground truth for AFl perpetuation is known in all cases, allowing the analysis of each mechanism with-

Page 3

out the influence of secondary - or unknown - mechanisms, e.g., other simultaneous AFls.

The results obtained with the random set classification show that an automatic classifier can potentially identify a high number of different AFl mechanisms using the 12-lead ECG, or more precisely a single F-wave loop, when similar geometries are present in each data subset. This non-invasive method can help physicians to plan the most appropriate treatment for the patients without the need of prior invasive mapping.

The F-wave duration is a key feature for this classification. The LOTO accuracy shows that the classifier is generalizing well to unseen torso geometries. The LOAO accuracy shows a lack of ability to generalize with new atrial geometries. These last three considerations can be linked since atrial geometries have an influence on the F-wave duration and on the ECG signals (Fig. 2B.). On the contrary, an additional torso to the set of 7 used for training does not yield much benefit, because different torso geometries do not bring relevant changes on the F-wave duration and on the ECG signals in general (Fig. 2A.), as also confirmed by the correlation analysis. Therefore, more than the currently used 8 atrial models should be included during training to cover the relevant anatomical variability.

Further tests on clinical data are necessary to effectively assess the proposed approach. Changes in conduction velocity would also change the F-wave duration irrespective of the geometry and should therefore also be varied.

Acknowledgments

References

[1] Cosio FG, Pastora A, Núñeza A, Magalhaesa AP, Awamleh P. Atrial flutter: an update. Rev Esp Cardiol 2006; 59(8):816–831.

[2] Acharya UR, Fujita H, Adam M, Lih OS, Hong TJ, Sudarsha VK, Koh JE. Automated characterization of arrhythmias using nonlinear features from tachycardia ecg beats. IEEE SMC Conference 2016;533–538.

[3] Taha B, Reddy S, Xue Q, Swiryn S. Automated discrimination between atrial fibrillation and atrial flutter in the resting 12-lead electrocardiogram. J Electrocardio 2000;33:123–125.

[4] Jais J, Matsuo S, Knecht S, Weerasooriya R, Hocini M, Sacher F, Wright M, Nault I, Lellouche N, Klein G, Clémenty J, Haïssaguerre M. A deductive mapping strategy for atrial tachycardia following atrial fibrillation ablation: importance of localized reentry. J Cardiovasc Electrophysiol 2009;20(5):480–491.

[5] Ban JE, Chen YL, Park HC, Lee HS, Lee DI, Choi JI, Lim HE, Park SW, Kim YH. Relationship between complex fractionated atrial electrograms during atrial fibrillation and the critical site of atrial tachycardia that develops after catheter ablation for atrial fibrillation. J Cardiovasc Electrophysiol 2014;25(2):146–153.

[6] Schilling RJ, Peters NS, Goldberger J, Kadish AH, Davies DW. Characterization of the anatomy and conduction velocities of the human right atrial flutter circuit determined by noncontact mapping. J Am Coll Cardiol 2001;38(2):385–393.

[7] Ndrepepa G, Zrenner B, Weyerbrock S, Schneider MA, Schmitt C. Activation patterns in the left atrium during counterclockwise and clockwise atrial flutter. J Cardiovasc Electrophysiol 2001;12(8):893–899.

[8] Markowitz SM, Thomas G, Liu CF, Cheung JW, Ip JE, Lerman BB. Atrial tachycardias and atypical atrial flutters: mechanisms and approaches to ablation. Circ Arrhythm Electrophysiol 2019;8(2):131–137.

[9] Oesterlein TG, Loewe A, Lenis G, Luik A, Schmitt C, Dössel O. Automatic identification of reentry mechanisms and critical sites during atrial tachycardia by analyzing areas of activity. IEEE Trans Biomed Eng 2018;65(10):2334–2344.

[10] Jacquemet V. An eikonal approach for the initiation of reentrant cardiac propagation in reaction-diffusion models. IEEE Trans Biomed Eng 2010;57(9):2090–2098.

[11] Trächtler J, Oesterlein T, Loewe A, Poremba E, Luik A, Schmitt C, Dössel O. Virtualizing clinical cases of atrial flutter in a fast marching simulation including conduction velocity and ablation scars. CDBME 2015;1(1):405–408.

[12] Krueger MW, Seemann G, Rhode K, Keller DU, Schilling C, Arujuna A, Gill J, O'Neill MD, Razavi R, Dössel O. Personalization of atrial anatomy and electrophysiology as a basis for clinical modeling of radio-frequency ablation of atrial fibrillation. IEEE Trans Med Imaging 2013;32(1):73–84.

[13] Wilhelms ALM, Dössel O, Seemann G. Influence of chronic atrial fibrillation induced remodeling in a computational electrophysiological model. Biomedizinische Technik 2014;59(S1):S929–S932.

[14] Lux RL. Body surface potential mapping techniques. Comprehensive Electrocardiology 2010;1361–1374.

[15] Stenroos M. The transfer matrix for epicardial potential in a piece-wise homogeneous thorax model: The boundary element formulation. Phys Med Biol 2009;54(18):5443–5455.

[16] Luongo G, Schuler S, Luik A, Almeida TP, Soriano DC, Dössel O, Loewe A. Non-invasive characterization of atrial flutter mechanisms using recurrence quantification analysis on the ecg: a computational study. IEEE Trans Biomed Eng 2020;accepted.

Address for correspondence:

Giorgio Luongo, Karlsruhe Institute of Technology (KIT)
Fritz-Haber-Weg 1, 76131 Karlsruhe, Germany
publications@ibt.kit.edu

Hybrid Machine Learning to Localize Atrial Flutter Substrates Using the Surface 12-lead ECG

Giorgio Luongo[1]*, Gaetano Vacanti[2]*, Vincent Nitzke[1], Deborah Nairn[1], Claudia Nagel[1], Diba Kabiri[2], Tiago P Almeida[3], Diogo C Soriano[4], Massimo W Rivolta[5], G André Ng[3], Olaf Dössel[1], Armin Luik[2], Roberto Sassi[5], Claus Schmitt[2], Axel Loewe[1]

[1]Institute of Biomedical Engineering (IBT), Karlsruhe Institute of Technology (KIT), Karlsruhe, Germany

[2]Medizinische Klinik IV, Städtisches Klinikum Karlsruhe, Karlsruhe, Germany

[3]Department of Cardiovascular Sciences, University of Leicester, NIHR Leicester Biomedical Research Centre, Leicester, UK

[4]Engineering, Modelling and Applied Social Sciences Centre, ABC Federal University, São Bernardo do Campo, Brazil

[5]Dipartimento di Informatica, Università degli Studi di Milano, Milan, Italy

Postal addresses:

[1]Kaiserstr. 12, 76131, Karlsruhe, Germany; [2]Haus D, Moltkestraße 90, 76133, Karlsruhe, Germany; [3]University Road, Leicester, LE1 7RH, UK; [4]Alameda da Universidade, Bairro Anchieta, São Bernardo do Campo, Brazil; [5]Via Festa del Perdono 7, 20122, Milan, Italy.

Corresponding authors (these authors contributed equally) *:

Giorgio Luongo, MSc, Fritz-Haber-Weg 1, 76131 Karlsruhe, Germany, Tel.: +49721608-42650, Fax: +49721608-42789, publications@ibt.kit.edu

Gaetano Vacanti, MD, Moltkestrasse, 90, 76182, Karlsruhe, Germany, Tel.: +497219742960, gaetano.vacanti@klinikum-karlsruhe.de

Abstract

Aims: Atrial flutter (AFlut) is a common reentrant atrial tachycardia driven by self-sustainable mechanisms that cause excitations to propagate along pathways different from sinus rhythm. Intracardiac electrophysiological mapping and catheter ablation are often performed without detailed prior knowledge of the mechanism perpetuating AFlut, likely prolonging the procedure time of these invasive interventions. We sought to discriminate the AFlut location (cavotricuspid isthmus-dependent, peri-mitral, and other left atrium AFlut classes) with a machine learning-based algorithm using only the non-invasive signals from the 12-lead electrocardiogram (ECG).

Methods: A hybrid 12-lead ECG dataset of 1,703 signals was used (1,424 in-silico ECGs, and 279 clinical ECGs from 93 patients – 3 different ECG segments over time were extracted from each patient). For each ECG, 77 features were extracted. A decision tree classifier with a hold-out classification approach was trained, validated, and tested on the dataset randomly split after selecting the most informative features. The clinical test set comprised 15 patients (45 clinical ECGs).

Results: The classifier yielded 82.2% accuracy on the clinical test set with a sensitivity of 90.9%, 66.7%, and 50.0% and a positive predictive value of 85.7%, 66.7%, and 75.0% for each class, respectively. Considering majority vote of the three segments taken from each patient, the cavotricuspid isthmus-dependent class was always classified correctly.

Conclusion: Our results show that a machine learning classifier relying only on non-invasive signals can potentially identify the location of AFlut mechanisms. This method could aid in planning and tailoring patient specific AFlut treatments.

Keywords

What's New?

- Non-invasive diagnostic algorithm for atrial flutter location discrimination;

- Identification of atrial flutter mechanisms using short F-wave segments (atrial activity in the 12-lead ECG);

- Hybrid machine learning classifier (training dataset: in-silico + clinical ECGs) for atrial flutter location discrimination;

- Machine learning algorithm based on selected features;

- Patient-specific ablation therapy.

1 Introduction

Atrial Flutter (AFlut) represents one of the most common supraventricular arrhythmias [1], [2]. They are defined as organized, macro-reentrant atrial tachycardias. The reentry could either revolve around the tricuspid annulus (so called typical forms or cavotricuspid-isthmus (CTI) dependent forms), or originating in other atrial regions, such as the mitral annulus, the superior vena cava, or the pulmonary veins (PV), mostly facilitated by previous atrial ablations [3], [4]. The widespread use of PV isolation and other left atrial ablation procedures for the treatment of atrial fibrillation may alter the normal activation patterns in the left atrium as well [5], [6]. As a consequence, the prevalence of atypical left AFlut and of CTI-dependent flutter with atypical ECG-patterns post ablation procedures increased in the recent years. These complex arrhythmias pose new diagnostic and classification challenges [7]–[9].

Clinical diagnosis of AFlut currently relies on the interpretation of a non-invasive 12-lead surface electrocardiogram (ECG). Although distinctive features for identifying typical CTI-dependent flutter have long been identified and often enable an easy diagnosis, atypical non-CTI-dependent flutter forms are more difficult to recognize [9]. Catheter ablation represents a curative therapy for all forms of AFlut. CTI-dependent flutter requires relatively straightforward, right-sided procedures with an anatomically well-characterized target: the CTI. Conversely, non-CTI-dependent flutter requires longer and technically more challenging procedures. In those procedures, transseptal puncture and electroanatomical mapping require additional preparation and additional diagnostic examinations such as transesophageal echocardiography, adding further possible complications for the patient [10]. Pre-procedural identification of the AFlut location to identify the most likely target prior to time-consuming and potentially riskier electroanatomic mapping is appealing for optimal planning of procedures and utilization of hospital resources.

Several clinical algorithms based on visual, non-computational, inspection of P-wave morphology of the surface 12-lead ECGs have been proposed, with equivocal results [11], [12]. Machine learning-based algorithms are an emerging tool in classifying many diseases and have shown promising results in the field of cardiac arrhythmia detection [13], [14]. Compared to clinical algorithms, machine learning classifiers have a larger flexibility to fit the data, and are less operator-dependent resulting in better performance and more standardized approaches. Moreover, a feature selected-based machine learning algorithm can lead to a clear interpretation of the results as clinical algorithms do. As opposed to a deep learning approach that is referred to as a black box model (data goes in, decisions come out, but the processes between input and output are not evident).

In a previous work, we developed a machine learning classifier that provides an accurate and reliable classification for AFlut location for in-silico signals [15]. After further training with in-silico and clinical ECGs (hybrid approach) to discriminate CTI-dependent AFlut vs. peri-mitral AFlut vs. other non-CTI-dependent flutter classes, we tested the performance of the classifier on clinical ECGs. In the present work, we offer a proof of concept for a clinical tool able to non-invasively predict the target location for therapeutic catheter ablation, fostering the enablement of a more personalized therapy and better allocation of medical resources.

2   Methods

2.1   Study population

Clinical data was retrospectively collected, including standard 12-lead surface ECGs and electrophysiological data of 93 consecutive patients who presented with AFlut on baseline ECGs between 2018 and 2020 and underwent an electrophysiological study and catheter ablation in Städtisches Klinikum Karlsruhe. Inclusion criteria were atrial arrhythmia ECG characteristics and subsequent invasively confirmed diagnosis of AFlut. Exclusion criteria were

the absence of complete and clinically evaluable 12-lead ECG documentation of atrial arrhythmia.

Exact arrhythmic mechanisms were confirmed invasively during the electrophysiological examination by termination of the arrhythmias after successful catheter ablation of the target site or non-inducibility of the arrhythmia by pacing or pharmaceutical challenge after catheter ablation. Seventy-two patients were diagnosed with CTI-dependent AFlut, 10 peri-mitral flutter, and 11 other non-CTI-dependent flutter with a critical isthmus in the left atrium ("other LA AFlut"). Patients with right atrial flutter with non-CTI-dependent mechanism (such as reentry in the superior vena cava) were not present in the study population. The clinical characteristics of the patient cohort are shown in Table 1.

From each patient, three different single AFlut segments were extracted from the standard 12-lead ECG (10 s length) to run the analysis, resulting in a total of 279 clinical signals (216 CTI-dependent AFlut, 30 peri-mitral AFlut, and 33 other LA AFlut). An AFlut segment is a single flutter cycle in-between two consecutive QRS-T complexes (red segments in Figure 1). The AFlut segments were manually derived from the ECGs, and then the three clearest and least compromised by QRS-T complexes AFlut segments were selected for the analysis. The 12-lead ECGs (1 kHz sampling frequency) were notch filtered at 50 Hz and band-pass Butterworth filtered between 0.05 Hz and 100 Hz (Figure 1).

2.2 In-silico population

A database with computational AFlut scenarios was setup based on computational studies conducted in previous work [16]. Cardiac excitation was modelled using the fast marching approach to solve the Eikonal equation on 100 bi-atrial anatomies generated from a statistical shape model [17]. Scars were added circumferentially around ipsilateral PVs representing previous PV isolation.

In total, 15 mechanisms of AFlut were implemented and merged into the three classes under analysis in this study: CTI-dependent, peri-mitral, and other LA AFlut mechanisms (a complete list of the in-silico mechanisms and their classification is shown in Table 2). The simulated cardiac excitation was used to compute the body surface potential map (BSPM) on the mean geometry derived from a statistical shape model of the torso [17]. Finally, conventional 12-lead ECGs were extracted from the BSPM (1 kHz sampling frequency). From the in-silico ECGs, the AFlut single cycle segments were extracted. A total of 1,424 sets of signals were obtained (198 CTI-dependent, 186 peri-mitral, and 1040 other LA AFlut mechanisms). Due to anatomical reasons, the implementation and/or sustainment of some scenarios was not possible on some atrial geometries.

2.3   Feature extraction & selection

Seventy-seven features were extracted from the signals using several biosignal processing methods from different domains, i.e., time, frequency, wavelet, entropy, and non-linear recurrence analysis. A table summarizing the features and more information regarding the feature extraction methods are provided in the *Supplementary Material.*

Among these features some proved to be particularly relevant in pilot analysis: The F-wave (flutter wave, P-wave during AFlut) duration, the duration of a complete cycle of atrial electrical activation of each specific AFlut mechanism, i.e., the length of the F-wave in the ECGs (the feature was manually derived), wavelet features which are able to extract spectral and temporal information simultaneously from the signals, recurrence quantification analysis features to analyse the regularity and stability of time domain signals [16], morphological features such as the fragmented conduction index, the optimal model order (number of gaussian functions needed to model the signals) [18], and symbolic dynamic features.

The optimal set of features was selected with a greedy forward selection technique. This algorithm starts with an empty feature set and adds the feature which leads to the highest

increase of classification accuracy in each iteration. The algorithm was stopped when the performance, based on the validation set, could not be further increased. In order to handle possible correlations among features, the candidate feature was only added to the set if the correlation coefficient with any of the already included features was <0.6.

Shapley calculation was implemented to analyse a posteriori the importance of the features selected for classification once the model was trained. Shapley calculation was run 1000 times with random samples (Bootstrap approach) to calculate the standard deviation (SD).

2.4   Machine learning classification

A decision tree was implemented for 3-class classification: CTI-dependent AFlut, peri-mitral AFlut, and other LA AFlut. The classifier was trained and applied using the MATLAB (The MathWorks, Inc) functions *fitctree* and *predict*, respectively. The dataset used to train, validate, and test the classifier was a hybrid of the in-silico and clinical datasets with a total of 1,703 signals. First, a multi-feature classification was performed with the feature set selected as described in the previous section. Hold-out classification was performed randomly, dividing the dataset into a training set, validation set, and test set with a ratio of 70%, 15%, and 15%, respectively. Signal segments from the same patient were always used solely in one the sets to avoid overfitting. The training set was used to tune the classifier parameters, while the validation set was used for the greedy feature selection optimization. During training, class imbalance was addressed by assigning a weight to each sample in a given class (by setting the *weights* parameter and the *Prior* model parameter to *uniform* in the MATLAB *fitctree* function). The weight was inversely proportional to the number of samples in the class and extra weights was added for clinical cases to give them more importance during the training phase. Lastly, the trained classifier was tested on the clinical test set (45 segments data from 15 patients – 33, 6, and 6 ECG segments for each class, respectively).

2.5   Statistical analysis

Classifier performance was evaluated using the accuracy (ACC), sensitivity, and positive predictive value (PPV). Sensitivity and PPV were calculated for each class, considering the specific class as positive and the remaining classes as negative. The clinical characteristics of our patient cohort and the extracted features were evaluated with the ANOVA test between the classes (p-values <0.05 considered significant; Table 1, Univariate column). Next, multivariate regression analysis was performed on variables that differed between groups with a p-value <0.1 (from the previous ANOVA test) and the machine learning classifier (Table 1, Multivariate column). Age and sex were included in the multivariate model for their clinical relevance.

3   Results

Patient characteristics with associated univariate and multivariate analysis are provided in Table 1. The multivariate regression analysis between the variables age, sex, body mass, left ventricular ejection fraction (LVEF), left ventricular end-diastolic diameter (LVEDD), previous catheter ablation, and our classifier showed that the classifier was the only significant variable (p = 0.02). As such, it adds value beyond the routine clinical parameters.

The decision tree for 3-class classification (CTI-dependent AFlut, peri-mitral AFlut, and other LA AFlut) achieved an accuracy of 82.2% on the clinical test set with a sensitivity of 90.9%, 66.7%, and 50.0% and a PPV of 85.7%, 66.7%, and 75.0% for each class, respectively. Table 3 shows the confusion matrix obtained from the decision tree classifier on the clinical test set. The 3 AFlut segments misclassified for the CTI-dependent AFlut classes belong to 3 different patients, this means that two out of three segments in the same 10 s ECG of these 3 given patients were correctly classified. Whereas the 2 segments misclassified for the peri-mitral AFlut class and the 3 segments misclassified for the other LA AFlut class belong to the same patient.

The greedy forward selection technique reached the maximum accuracy with 18 features. The 18 selected features were: F-wave duration, 8 features from the dynamic symbolic analysis (the number of high valued segments, low valued segments, bottom valued segments, isolines, sequence of top-top, low-zero, low-low, and bottom-low segments in the signals), the minimum and mean optimal model orders to model each ECG lead with Gaussian functions, the 7th, 8th, and 9th coefficients from the discrete cosine transformation, the mean prominence of the 5th and 6th order wavelets, the minimum fragmented conduction index, and the vertical entropy calculated with the individual component recurrence quantification analysis on the 3rd principal component ($icRQA_{PC3}$).

The Shapley calculation to analyse a posteriori the importance of the 18 selected features showed that the most relevant features for the implemented classification were the F-wave duration, the mean prominence on the 5th order wavelet, the $icRQA_{PC3}$ vertical entropy, and the mean optimal model order.

The definition of all extracted features, the feature set, and the detailed feature importance analysis can be found in the *Supplementary Material*.

4   Discussion

Our results suggest that a non-invasive machine learning approach based on surface ECG analysis can aid in the discrimination of the location of the substrate which is sustaining AFlut. This could improve protocols for clinical therapeutic decision-making and ablation procedure planning.

The 12-lead ECG is broadly used for cardiac diagnostics, including diagnosis and classification of AFlut from other cardiac rhythms [11], [12], [13], [14]. Many ECG-based clinical algorithms have been proposed, with mixed results. Due to novel and widespread left atrial ablation procedures in the last decades, rare clinical entities with diagnostic challenges

(i.e. left AFlut or right AFlut with atypical ECG-features) are increasing in prevalence and entering the routine of electrophysiology labs [7]–[9].

To the best of our knowledge, ours represent the first work to implement a decision tree classifier to discriminate the location of AFlut mechanisms by using in-silico and clinical non-invasive ECG signals. The computational 12-lead ECG simulations provided an ideal and controlled environment to generate a consistent ground truth dataset of AFlut mechanisms. This in-silico dataset served as a reinforcement to the clinical dataset to solve the problematic availability of clinical data where ground truth was ascertained by invasive electrophysiological analysis. The clinical data used during training helped to bridge the domain gap between simulated and measured ECGs. In addition, the machine learning algorithm implemented in this project uses carefully selected features. As a result, clinical knowledge is used to optimize the algorithm, rendering also the interpretation of the results easier than a deep learning approach.

This study builds on our previous work [15] and presents a first application of the resulting classifier on clinical data. Of note, no other clinical characteristics were statistically relevant in correctly classifying the AFlut (Table 1).

4.1   Feature analysis

The Shapley calculation showed that, of the 18 features in the feature set needed for classification, 4 were most relevant: The F-wave duration, the mean prominence on the 5th order wavelet, the icRQA$_{PC3}$ vertical entropy, and the mean optimal model order. The F-wave duration already proved to be a fundamental feature in the AFlut characterization in our previous works [15], [19] together with the vertical entropy icRQA$_{PC3}$. In fact, several previous results have reported how RQA approaches can be useful in the characterization and discrimination of different cardiac arrhythmias [16], [20]. These two features showed to be significantly higher in values in the "other LA AFlut" class in comparison with the other

classes. In contrast, there was no significant difference between the CTI-dependent and the peri-mitral AFlut classes, probably due to the similarity in the size and shape of the two valves. On the other hand, regarding the mean prominence on the 5th order wavelet and the mean optimal model order, there was no significant difference between the 3 classes. Therefore, the importance identified by the Shapley evaluation for these two last features, but not observed by the significance analysis among the classes, must be solely due to their use in the algorithm to better define the classification. The feature importance analysis, and the distribution of the values of the 4 most important features is shown in the *Supplementary Material*.

4.2 Classification

Many studies have sought to find consistent and reliable non-invasive predictors of location for AFlut. The most investigated and promising features have been the morphology of the atrial waves in 12-lead ECGs [11], [12]. Many algorithms based on such features have been proposed with mixed results and there is currently no consensus on how to classify AFlut based on the surface ECG. Nevertheless, as different AFlut types require different ablation procedures with more challenging preparations for left atrial types, a pre-procedural diagnosis and characterization of the location of ablation targets would increase the efficacy of the procedure by permitting direct targeting of the region of interest. Moreover, it would also allow tailoring the procedure in a time- and resource-saving fashion, avoiding potential unnecessary complications or delays.

Our decision tree classifier based on the surface 12-lead ECGs achieved an accuracy of 82.2% on the clinical test set, demonstrating the ability to correctly classify most of the AFlut segments extracted from the 12-lead ECGs. In particular, the high sensitivity and PPV for the CTI-dependent AFlut (90.9%, and 85.7%, respectively) show that most of the segments belonging and classified into this group were correct, making our classifier robust in the identification of these patients. Regarding the peri-mitral and other LA AFlut classes, the results

indicate a good classification ability, negatively influenced by the lower number of cases for these two classes in our dataset.

As Table 3 shows, 3 segments got misclassified for the CTI-dependent AFlut class. These segments belong to different patients, thus indicating that the classifier correctly identified 100% of the patients in this group when considering the majority prediction from the three segments of each patient.

As the therapy spectrum for atrial ablation broadens, the prevalence of AFlut with atypical characteristics increases leading to new diagnostic challenges. For example, CTI-dependent flutters, which occurs after left atrial procedures tends to present atrial waves with unusual morphologies. Such cases can easily be misinterpreted as left AFlut and lead to unnecessary, lengthier and potentially more dangerous workup and procedures. Our classifier was able to correctly identify the nature of the AFlut also for such challenging cases.

In Figure 2, we present the case of a patient who developed, after a pulmonary vein isolation ablation and a further ablation of a peri-mitral AFlut, a CTI-dependent AFlut. Despite the unusual characteristics in the surface ECGs (positive atrial waves in leads II, III, aVF and V1 through V6), our classifier correctly identified its location.

Limitations

The current study is limited to a small clinical test set. As a next step, the algorithm should be tested on a more extensive patient cohort. In particular, more patients for the peri-mitral and other LA AFlut classes should be collected and added to the training set to improve the classifier performance. Even though the manual segmentation of the clinical ECG is not time-consuming, in view of future clinical applications, automated segmentation of clinical ECG should be implemented to extract the F-wave.

Although 15 AFlut mechanisms related to clinical situations have been implemented, they are just a general representation of the mechanisms that are most commonly found in the

literature. More mechanisms could be included in the dataset, considering the heterogeneity seen in the clinical practice, e.g., slow conduction areas.

Conclusions

The results presented in this study show that a machine learning feature-based classifier can distinguish between CTI-dependent AFlut vs. peri-mitral AFlut vs. other LA AFlut using single AFlut loop segments. Additionally, a hybrid approach (in-silico data + clinical data) to train the classifier can be successful when it is difficult to get enough clinical data for purely clinical machine learning. As such, a machine learning-based classifier leveraging the routinely available non-invasive ECG signal can be valuable for clinical decision-making and increase the personalization of therapy. Our machine learning classifier can correctly non-invasively predict ablation targets avoiding the need for transseptal catheterization and LA mapping and consequently even pre-procedural transesophageal echocardiography in some cases.

Acknowledgements

Funding

participating states and from the European Union's Horizon 2020 research and innovation programme under grant MedalCare 18HLT07. The funders were not involved in the design and execution of this study.

Ethics statement

The authors designed the study, gathered and analysed the data according to the Helsinki Declaration guidelines on human research. The research protocol used in this study was reviewed and approved by the institutional review board.

Patient consent & authorship

All patients provided written informed consent. All authors attest they meet the current Committee on Publication Ethics (COPE) and ICMJE criteria for authorship.

Data availability

Patient-derived data, and the trained classifier related to this article will be shared with interested parties for non-commercial reuse on reasonable request to the corresponding authors and approval from the Institutional Review Board.

References

[1]   J. Granada *et al.*, "Incidence and predictors of atrial flutter in the general population," *J. Am. Coll. Cardiol.*, vol. 36, no. 7, pp. 2242–2246, 2000, doi: 10.1016/S0735-1097(00)00982-7.

[2]   R. L. Page *et al.*, "2015 ACC/AHA/HRS guideline for the management of adult patients with supraventricular tachycardia: A report of the American College of Cardiology/American Heart Association Task Force on Clinical Practice Guidelines and the Heart Rhythm Society," *Circulation*, vol. 133, no. 14. Lippincott Williams and Wilkins, pp. e506–e574, Apr. 2016, doi: 10.1161/CIR.0000000000000311.

[3]   C. FG, "Atrial Flutter, Typical and Atypical: A Review," *Arrhythmia Electrophysiol. Rev.*, vol. 6, no. 2, pp. 55–62, Jun. 2017, doi: 10.15420/AER.2017.5.2.

[4]   S. N *et al.*, "A classification of atrial flutter and regular atrial tachycardia according to electrophysiological mechanisms and anatomical bases; a Statement from a Joint Expert Group from The Working Group of Arrhythmias of the European Society of Cardiology and the ," *Eur. Heart J.*, vol. 22, no. 14, pp. 1162–1182, 2001, doi: 10.1053/EUHJ.2001.2658.

[5]   C. Pappone *et al.*, "Atrial electroanatomic remodeling after circumferential radiofrequency pulmonary vein ablation," *Circulation*, vol. 104, pp. 2539–2544, 2001.

[6]   A. Loewe *et al.*, "Patient-Specific Identification of Atrial Flutter Vulnerability–A Computational Approach to Reveal Latent Reentry Pathways," *Front. Physiol.*, vol. 9, p. 1910, 2019, doi: 10.3389/fphys.2018.01910.

[7]   C. E. Mesas *et al.*, "Left atrial tachycardia after circumferential pulmonary vein ablation for atrial fibrillation: Electroanatomic characterization and treatment," *J. Am. Coll. Cardiol.*, vol. 44, no. 5, pp. 1071–1079, Sep. 2004, doi: 10.1016/J.JACC.2004.05.072.

[8]   A. Chugh *et al.*, "Catheter Ablation of Atypical Atrial Flutter and Atrial Tachycardia Within the Coronary Sinus After Left Atrial Ablation for Atrial Fibrillation," *J. Am. Coll. Cardiol.*, vol. 46, no. 1, pp. 83–91, Jul. 2005, doi: 10.1016/J.JACC.2005.03.053.

[9]   K. S. Hoffmayer *et al.*, "Predictors of Unusual ECG Characteristics in Cavotricuspid Isthmus-Dependent Atrial Flutter Ablation," *Pacing Clin. Electrophysiol.*, vol. 34, no. 10, p. 1251, 2011, doi: 10.1111/J.1540-8159.2011.03137.X.

[10]   L. Tabbernor, "The radiofrequency ablation of atrial flutter," *Br. J. Card. Nurs.*, vol. 1, no. 4, pp. 191–197, Apr. 2006, doi: 10.12968/bjca.2006.1.4.20979.

[11]   E. P. Gerstenfeld *et al.*, "Surface electrocardiogram characteristics of atrial tachycardias occurring after pulmonary vein isolation," *Heart Rhythm*, vol. 4, no. 9, pp. 1136–1143, Sep. 2007, doi: 10.1016/J.HRTHM.2007.05.008.

[12]   P. Pascale *et al.*, "Useful Electrocardiographic Features to Help Identify the Mechanism

of Atrial Tachycardia Occurring After Persistent Atrial Fibrillation Ablation," *JACC Clin. Electrophysiol.*, vol. 4, no. 1, pp. 33–45, Jan. 2018, doi: 10.1016/J.JACEP.2017.07.018.

[13]   M. E. Hemam, A. S. Dave, M. Rodríguez-Mañero, and M. Valderrábano, "Epiphenomenal Re-Entry and Spurious Focal Activation Detection by Atrial Fibrillation Mapping Algorithms," *JACC Clin. Electrophysiol.*, vol. 7, no. 7, pp. 923–932, Jul. 2021, doi: 10.1016/j.jacep.2020.12.005.

[14]   G. Luongo *et al.*, "Machine learning enables noninvasive prediction of atrial fibrillation driver location and acute pulmonary vein ablation success using the 12-lead ECG," *Cardiovasc. Digit. Heal. J.*, vol. 2, no. 2, pp. 126–136, Apr. 2021, doi: 10.1016/J.CVDHJ.2021.03.002.

[15]   G. Luongo, S. Schuler, M. W. Rivolta, O. Doessel, R. Sassi, and A. Loewe, "236Automatic classification of 20 different types of atrial tachycardia using 12-lead ECG signals," *EP Eur.*, vol. 22, no. Supplement_1, 2020.

[16]   G. Luongo *et al.*, "Non-Invasive Characterization of Atrial Flutter Mechanisms Using Recurrence Quantification Analysis on the ECG: A Computational Study," *IEEE Trans. Biomed. Eng.*, vol. 68, no. 3, pp. 914–925, 2021, doi: 10.1109/TBME.2020.2990655.

[17]   C. Nagel, S. Schuler, O. Dössel, and A. Loewe, "A bi-atrial statistical shape model for large-scale in silico studies of human atria: model development and application to ECG simulations," *Med. Image Anal.*, no. 1361–8415, 2021, doi: 10.1016/j.media.2021.102210.

[18]   F. Censi *et al.*, "P-Wave Morphology Assessment by a Gaussian Functions-Based Model in Atrial Fibrillation Patients," *IEEE Trans. Biomed. Eng.*, vol. 54, no. 4, pp. 663–672, 2007, doi: 10.1109/TBME.2006.890134.

[19]   G. Luongo, S. Schuler, M. W. Rivolta, O. Dössel, R. Sassi, and A. Loewe, "Automatic

ECG-based Discrimination of 20 Atrial Flutter Mechanisms: Influence of Atrial and Torso Geometries," in *2020 Computing in Cardiology*, 2020, pp. 1–4, doi: 10.22489/CinC.2020.066.

[20] U. Desai, R. J. Martis, U. R. Acharya, C. G. Nayak, G. Seshikala, and R. Shetty K, "Diagnosis of multiclass tachycardia beats using recurrence quantification analysis and ensemble classifiers," *J. Mech. Med. Biol.*, vol. 16, no. 1, p. 1640005, 2016, doi: 10.1142/S0219519416400054.

Tables

Table 1: Patient characteristics mean values with univariate ANOVA test between groups (p-values <0.05). Multivariate regression analysis performed between the variables with a univariate p-value <0.1 and our classifier.

	All patients n=93	CTI-dependent AFlut n=72	Peri-mitral AFlut n=10	Other LA AFlut n=11	Univariate (p-value)	Multivariate (p-value)
Age (years)	69 (11.5)	60 (10.0)	57 (12.6)	68 (4.3)	0.54	0.32
Female	16 (17.2)	10 (13.9)	3 (30)	4 (36.4)	0.48	0.43
Body mass index (kg/m^2)	28 (4.0)	28 (4.0)	27 (4.4)	28 (3.8)	0.06	0.07
Coronary artery disease	27 (29.0)	22 (30.6)	2 (20)	2 (18.2)	0.56	-
LVEF (%)	53 (9)	52 (7)	60 (8)	56 (9)	0.10	0.09
LVEDD (mm)	48 (5.1)	49 (6.2)	47 (4.8)	44 (7.2)	0.06	0.06
LAD (mm)	43 (5)	43 (5)	43 (5)	46 (6)	0.37	-
Previous catheter ablation	20 (21.5)	6 (8.3)	7 (70)	7 (63.6)	<0.01	0.07
Machine learning classifier	-	-	-	-	-	0.02

Left ventricular ejection fraction (LVEF), left ventricular end-diastolic diameter (LVEDD), left atrial diameter (LAD). Values are given as mean (± standard deviation) or number (%).

Table 2: In-silico AFlut mechanisms and attribution to the 3 classes under analysis.

Mechanism	Atrium	Position	Direction	Class
Macro-reentry	RA	Tricuspid Valve	ccw	CTI-dependent
Macro-reentry	RA	Tricuspid Valve	cw	CTI-dependent
Macro-reentry	LA	Mitral Valve	ccw	Peri-mitral
Macro-reentry	LA	Mitral Valve	cw	Peri-mitral
Scar-related reentry	LA	LPV	post	Other LA
Scar-related reentry	LA	LPV	ant	Other LA
Scar-related reentry	LA	RPV	post	Other LA
Scar-related reentry	LA	RPV	ant	Other LA
Figure-8 macro-reentry	LA	Both PVs	ant	Other LA
Figure-8 macro-reentry	LA	Both PVs	post	Other LA
Figure-8 macro-reentry	LA	RPVs	ant	Other LA
Focal source	LA	RSPV anterior		Other LA
Focal source	LA	RSPV posterior		Other LA
Focal source	LA	LSPV anterior		Other LA
Focal source	LA	LSPV posterior		Other LA

Right atrium (RA), left atrium (LA), left pulmonary vein (LPV), right pulmonary vein (RPV), pulmonary veins (PVs), right superior pulmonary vein (RSPV), left superior pulmonary vein (LSPV), clockwise (cw), counterclockwise (ccw), anterior (ant), posterior (post).

Table 3: Clinical test set confusion matrix for 3-class classification per ECG-segment.

		True class		
		CTI-dependent	Peri-mitral	Others
	CTI-dependent	30	2	3
Predicted class	Peri-mitral	2	4	0
	Others	1	0	3

Figures
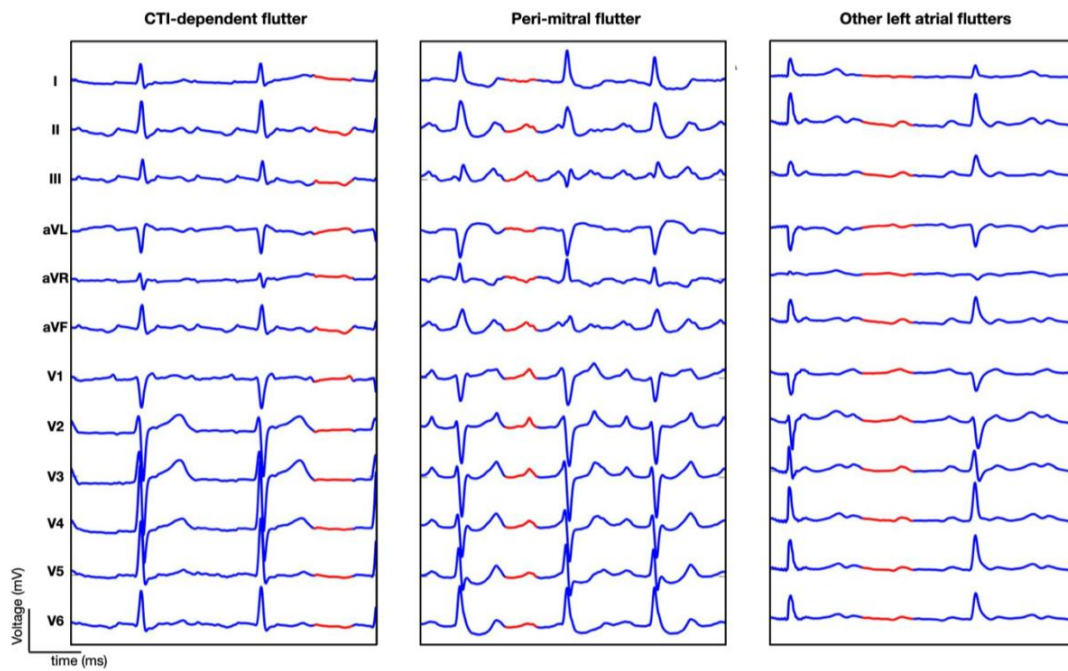
Figure 1: Example of clinical CTI-dependent, peri-mitral, and other LA AFlut 12-lead ECGs, respectively. The red segments represent one of the three AFlut single cycles extracted and used in this work for this specific patient.
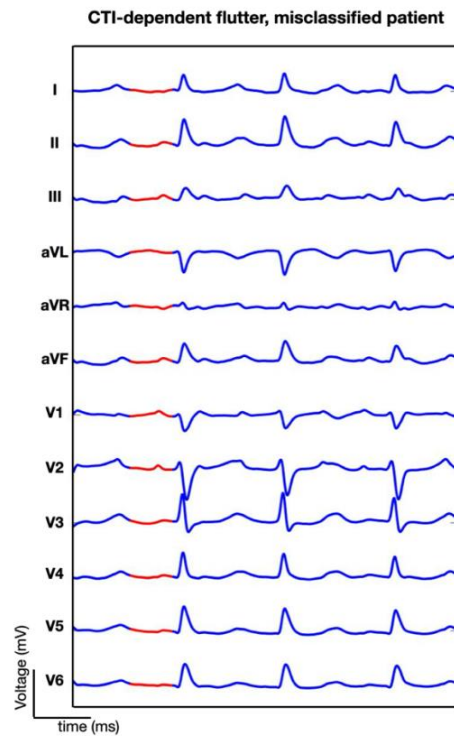
Figure 2: Clinical CTI-dependent case with atypical ECG-features (positive atrial waves in lead II, III, aVF and V1 to V6) correctly classified by the classifier. The red segments represent one of the three AFlut single cycles extracted and used in this work for this specific patient.

Atrial fibrillation driver localization and complication prediction

Atrial fibrillation (also called AFib or AF) is a quivering or irregular arrhythmia that can lead to blood clots, stroke, heart failure and other heart-related complications. It is estimated that 12.1 million people in the United States will have AFib in 2030 [116, 117]. AFib happens when abnormal electrical impulses suddenly start firing in the atria. These impulses overrule the heart's natural pacemaker, which can no longer control the rhythm of the heart. This causes a highly irregular pulse rate. In AFib, the heart's upper chambers (atria) contract randomly and sometimes so fast that the heart muscle cannot relax properly between contractions. This reduces the heart's efficiency and performance. The cause of AFib is not fully understood, but it tends to affect certain groups of people, such as older people and people living with long-term (chronic) conditions such as heart disease, high blood pressure or obesity [118]. Moreover, the link between AFib and other cardiac diseases, such as cardiomyopathy, and heart failure, are not well understood yet. Indeed, sometimes AFib can occur concomitantly with heart failure, and sinus rhythm restoration leads to drastic improvements or normalization of left ventricular systolic dysfunction (LVSD) within days to weeks [119–121]. However, it is currently not fully understood why certain patients develop severe heart failure symptoms and LVSD in AFib (AF-induced heart failure and cardiomyopathy). As for atrial flutter, the most common non-pharmacological therapy for AFib is catheter ablation with the aim to terminate the arrhythmia and to restore the sinus rhythm [122]. One of the major problems with catheter ablation for treating AFib is deciding what to ablate. Indeed, there is no common rule about which targets are most suitable to terminate the arrhythmia and avoid future recurrences. Typically, AFib drivers that trigger and support the arrhythmia perpetuation are targeted during ablation [123]. Diagnosis of AFib is made by using either intracardiac catheters or with non-invasive methods like the electrocardiogram (ECG). A major limitation of AFib catheters mapping and ablation is that the mechanisms that sustain AFib are not easy to be identified [124].

This leads to a significantly long invasive procedure duration with no possibility of pre-operative planning. For this reason the usage of ECG is very attractive since it gives valuable prior information without any invasive intervention on the patient. The application of the ECG signals in a machine learning framework might be an automated solution to get prior information regarding the position of the drivers sustaining AFib in the atria and the possible complications that AFib might ensue (i.e., heart failure). The application of machine learning algorithms based on ECG signals to diagnose AFib in comparison to other heart rhythms has been widely investigated [110, 125]. In contrast, the use of such systems to identify targets for ablation and for the prediction of possible complications or recurrence is a novel and innovative approach. The combination of noninvasive signals and machine learning techniques could lead to a prediction of ablation procedure success, pre-operative planning, reduction of invasive procedure duration, and rendering the clinical follow-up more cost-effective. In the studies presented in this chapter, firstly, we sought to discriminate the location of the AFib drivers (pulmonary veins (PVs) vs. extra-PV regions) using the 12-lead ECG, and to predict the acute success of pulmonary vein isolation (PVI) [25]. The implemented classifier showed to be able to localize the AFib driver positions also suggesting whether the PVI procedure alone would have been enough to terminate the arrhythmia. In addition, the clinical applications of the in silico data were demonstrated by having trained the algorithm on simulated data only and then having successfully tested it on clinical data. Using in silico data where the ground truth is precisely known could really lead to solving the problem of the small amount of correctly labeled clinical data in biomedical engineering. To conclude, we investigated possible connections between AFib and heart failure using beat-to-beat variation signals (i.e., RR-intervals) extracted from 24h Holter 1-lead ECG signals. This manuscript is at the moment under review [26]. The identification of patterns and characteristics between AFib and heart failure could assist the physicians in deciding on the cases of AFib in which arrhythmia termination could lead to a reduced risk of heart failure and complications. The implemented algorithm was able to recognize AFib cases that were linked to heart failure, also suggesting which time of the day is the best to perform such an analysis [26]. The algorithm is currently under patenting process.

Machine learning enables noninvasive prediction of atrial fibrillation driver location and acute pulmonary vein ablation success using the 12-lead ECG

Giorgio Luongo, MSc,* Luca Azzolin, MSc,* Steffen Schuler, MSc,*
Massimo W. Rivolta, PhD,[†] Tiago P. Almeida, PhD,[‡] Juan P. Martínez, PhD,[§]
Diogo C. Soriano, PhD,[||] Armin Luik, MD,[¶] Björn Müller-Edenborn, MD,[#]
Amir Jadidi, MD,[#] Olaf Dössel, PhD,* Roberto Sassi, PhD,[†] Pablo Laguna, PhD,[§]
Axel Loewe, PhD*

*From the *Institute of Biomedical Engineering, Karlsruhe Institute of Technology, Karlsruhe, Germany,*
[†]*Dipartimento di Informatica, Università degli Studi di Milano, Milan, Italy,* [‡]*Department of
Cardiovascular Sciences, University of Leicester, Leicester, United Kingdom,* [§]*I3A, Universidad de
Zaragoza, and CIBER-BNN, Zaragoza, Spain,* [||]*Engineering, Modelling and Applied Social Sciences
Centre, ABC Federal University, São Bernardo do Campo, Brazil,* [¶]*Medizinische Klinik IV, Städtisches
Klinikum Karlsruhe, Karlsruhe, Germany, and* [#]*Department of Electrophysiology,
University-Heart-Center Freiburg-Bad Krozingen, Bad Krozingen Campus, Bad Krozingen, Germany.*

BACKGROUND Atrial fibrillation (AF) is the most common supraventricular arrhythmia, characterized by disorganized atrial electrical activity, maintained by localized arrhythmogenic atrial drivers. Pulmonary vein isolation (PVI) allows to exclude PV-related drivers. However, PVI is less effective in patients with additional extra-PV arrhythmogenic drivers.

OBJECTIVES To discriminate whether AF drivers are located near the PVs vs extra-PV regions using the noninvasive 12-lead electrocardiogram (ECG) in a computational and clinical framework, and to computationally predict the acute success of PVI in these cohorts of data.

METHODS AF drivers were induced in 2 computerized atrial models and combined with 8 torso models, resulting in 1128 12-lead ECGs (80 ECGs with AF drivers located in the PVs and 1048 in extra-PV areas). A total of 103 features were extracted from the signals. Binary decision tree classifier was trained on the simulated data and evaluated using hold-out cross-validation. The PVs were subsequently isolated in the models to assess PVI success. Finally, the classifier was tested on a clinical dataset (46 patients: 23 PV-dependent AF and 23 with additional extra-PV sources).

RESULTS The classifier yielded 82.6% specificity and 73.9% sensitivity for detecting PV drivers on the clinical data. Consistency analysis on the 46 patients resulted in 93.5% results match. Applying PVI on the simulated AF cases terminated AF in 100% of the cases in the PV class.

CONCLUSION Machine learning–based classification of 12-lead-ECG allows discrimination between patients with PV drivers vs those with extra-PV drivers of AF. The novel algorithm may aid to identify patients with high acute success rates to PVI.

KEYWORDS Atrial fibrillation; Atrial ablation; Machine learning; Noninvasive; 12-lead electrocardiogram; Pulmonary vein isolation; Cardiac simulations

Introduction

Atrial fibrillation (AF) is the most common sustained arrhythmia in clinical practice and a leading cause of hospitalization and death.[1,2] Recent evidence from experimental and clinical studies suggests that AF may be maintained by localized AF drivers,[3–5] which are organized reentrant circuits (rotors)[6,7] or focal sources[8] that disorganize into AF.

Catheter ablation is a common nonpharmacological therapy that aims to terminate AF, restoring sinus rhythm.[9,10,1] Typically, "triggers" that start AF and the "substrate" that supports perpetuation are targeted during ablation. Moreover, Narayan and colleagues[11] showed the importance of localizing and ablating rotors, focal source drivers, or organized fibrillation sources to terminate the arrhythmia.[11] However, one of the major limitations of AF ablation is that the mechanisms that sustain AF are not easy to identify,[1,12,13] in contrast to many other arrhythmias in which the perpetuating mechanism is the primary target for ablation. The seminal

Address reprint requests and correspondence: Mr Giorgio Luongo, Fritz-Haber-Weg 1, 76131 Karlsruhe, Germany. E-mail address: publications@ibt.kit.edu.

observations by Haissaguerre and colleagues[10] revealed that AF triggers and sustaining mechanisms are often localized around the pulmonary veins (PVs).[10] Thus, pulmonary vein isolation (PVI) is established as the cornerstone of AF ablation,[1] being highly effective in patients with triggers confined to the PVs.[10,9] Nevertheless, PVI results remain suboptimal in the presence of extra-PV sources maintaining AF.[1,14] Pre-procedural information regarding the confinement of the driving mechanism to the PVs would be valuable for decision-making pro/contra ablation and procedure planning. To date, the best available proxy to plan the ablation procedure is the classification of the arrhythmia into paroxysmal/ persistent AF.[15] This classification, however, is based on observed AF episodes, and it might correlate poorly with the actual AF burden—and, consequently, with the extension of substrate remodeling—in many patients.[16] Moreover, in the case of extra-PV drivers, a subsequent classification whether the left atrium (LA) or right atrium (RA) is responsible could lead to prior planning regarding the need for transseptal access or not.

Traditionally, invasive mapping approaches have been applied to identify the location of AF drivers as targets for catheter ablation.[17,18] In contrast, noninvasive methods (ie, the 12-lead electrocardiogram [ECG]) are mostly used for the clinical and automatic detection of AF vs sinus rhythm[19] or other arrhythmia.[20] The use of a noninvasive technique, such as the ECG, could help to guide ablation procedures by identifying the location of the AF drivers pre-procedure, and hence target more specific affected atrial regions for ablation.

In the present work, we sought to discriminate AF drivers located near the PVs compared to extra-PV atrial sites based solely on the 12-lead ECG. Towards this end, we trained an automatic machine learning classifier on data from computer simulations and evaluated its performance on clinical ECGs. Moreover, we assessed the acute success of PVI in the in silico cases to predict whether PVI in cases of AF drivers located near the PVs would be sufficient to terminate AF (ie, restoration of sinus rhythm, or AF conversion into atrial flutter). In this case, AF drivers identified in the PVs could be directly targeted for ablation without prior time-consuming electroanatomic mapping.

Methods
Simulation setup
A database of simulated AF scenarios driven by localized rotors and focal sources was computed on 2 volumetric biatrial anatomies generated from segmented magnetic resonance imaging data of healthy subjects (#3 and #5 from ref 21). The atrial geometries were modeled with ≈ 11 million tetrahedral elements with fiber direction computed by a semiautomatic rule-based algorithm.[22] Cellular atrial electrophysiology was represented by the Courtemanche-Ramirez-Nattel model, including AF-induced remodeling[23] in 5 regions with different conduction velocities[21] to take into account heterogeneity and anisotropy in the atria. The

atrial geometries were considered with and without fibrotic tissue. Transmural fibrotic tissue was modeled as 2 circular patches with a radius of 14 mm in which 50% of the elements were almost nonconductive (conductivity of 10^{-7} S/m) to model the presence of scar tissue, and the other 50% included ionic changes to represent the effect of cytokines (TGF-β1) as described by Roney and colleagues.[24]

AF rotor episodes were induced using the phase singularity distribution method,[25] which consists of placing phase singularities in the atria, estimating an activation time map by solving the Eikonal equation, and using this as an initial state for a monodomain simulation with openCARP.[26,27] In addition, localized focal source episodes were induced by $30 \frac{\mu A}{cm^2}$ current applied for 2 ms to a cubic region with edge length of 3 mm centered around the stimulation point in monodomain simulations. The focal source pacing cycle lengths were chosen in the 130–200 ms range following the same distribution observed from the rotor cycle lengths. The phase singularities and the focal stimulation points were placed in 300 uniformly distributed points in the atria, and 3 seconds of activation was computed (Figure 1A.1 and 1B.1). The following cases were excluded for further analysis: (1) the single rotors were not maintained for the whole simulation time; and (2) the focal source episodes induced reentry that led to the termination of the focal activity. This led to a dataset of 141 biatrial simulations (10 simulations with the AF drivers located in the PVs; 131 simulations located in extra-PV areas, of which 106 were in the RA and 25 in the LA). PV areas were defined as determined by the semiautomatic algorithm used to compute the fiber directions and anatomical labels[22] (Figure 2A).

The monodomain simulations resulted in spatiotemporal transmembrane voltage distributions. The transmembrane voltage distributions were subsequently interpolated on a coarser surface mesh with sufficient resolution for the calculation of body surface potentials[28] (≈ 75,000 triangular elements). Body surface potential maps (BSPMs) were calculated for each AF episode using the boundary element method.[29] For each AF episode BSPMs were computed using 8 different torso models (19,898 triangles on average) generated from segmented magnetic resonance imaging data of healthy male and female subjects (Figure 1A.2 and B.2).[21] From the BSPM, the 12-lead ECG was extracted with 3-second duration (Figure 1A.3 and 1B.3). The simulated 12-lead ECG signals contain only f-waves and no QRS-T complexes, since the ventricles were not included in the simulations. A total of 1128 12-lead ECGs composed the final dataset (80 ECGs with the AF drivers located in the PVs; 1048 ECGs located in extra-PV areas, of which 848 were in the RA and 200 in the LA).

Simulated ablation procedures
To assess the effect of PVI procedure on the mechanisms driving AF, nonconducting scars were added circumferentially around ipsilateral PVs in the simulations (Figure 3A). PVI was applied after the initial 3 seconds of simulation.
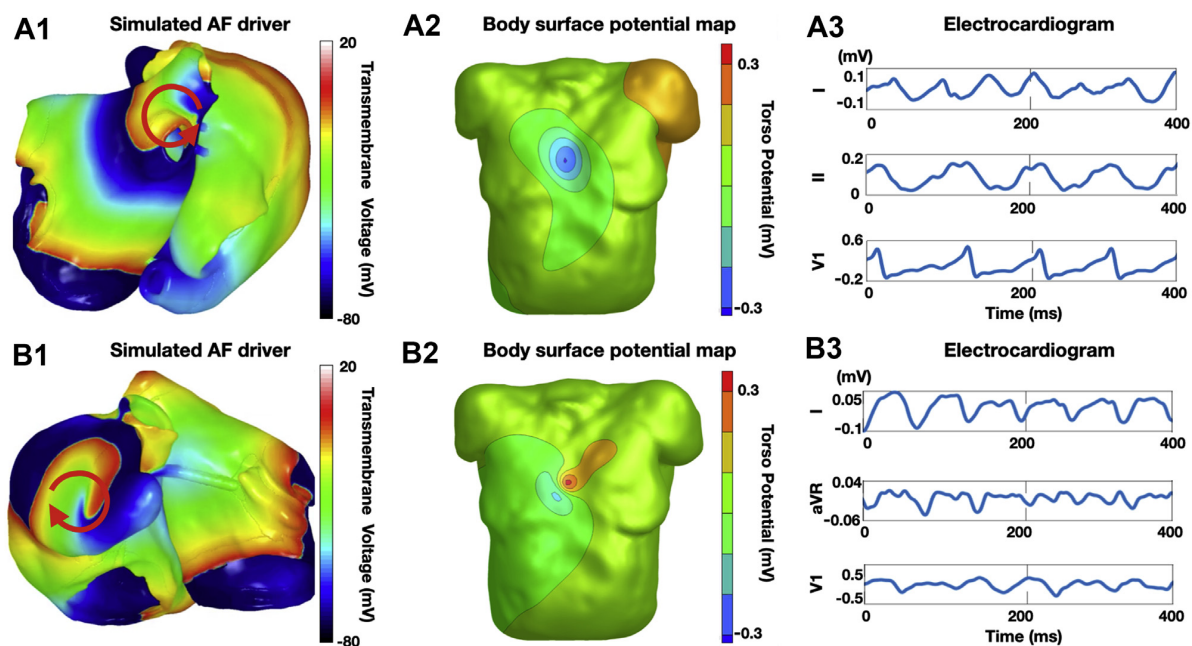
Figure 1   **A.1:** Example of simulated atrial fibrillation (AF) driver located near the pulmonary veins (PVs). **B.1:** Example of simulated AF driver located in an extra-PV region (right atrial appendage in this case). The red arrows show the AF driver position and propagation direction. **A.2, B.2:** Body surface potential maps (BSPMs) on 1 magnetic resonance imaging–derived torso model. The torso potentials were obtained by solving the forward problem of electrocardiography from the simulated transmembrane voltages on the atria. **A.3, B.3:** f-waves for leads I, II, and V_1 from the 12-lead electrocardiogram signals extracted from the BSPMs.

After PVI, simulations were continued for another 1 second to check for arrhythmia termination or a change on the driving mechanisms (eg, conversion to atrial flutter). In the cases where PVI did not terminate AF, a roofline (RL) was applied (Figure 3B). If the RL did not terminate the AF either, an additional ablation scar was applied between the mitral valve and the left PVI line (mitral isthmus [MI], Figure 3C). Prior to applying subsequent ablation lines, the simulations were always computed for 1 second to capture any change of the arrhythmia dynamics.

Feature extraction

One hundred and three features were extracted from the signals using several biosignal processing methods, such as Hjorth descriptors to analyze the spectral moments from the time-domain signals[30,31]; recurrence quantification analysis (RQA) on the vectorcardiogram,[32] spatial reduced RQA, and individual component RQA[33] to analyze the topological structure of multidimensional dynamical systems; principal component analysis (PCA) eigenvalues to observe the variability shown by the principal components (PCs)
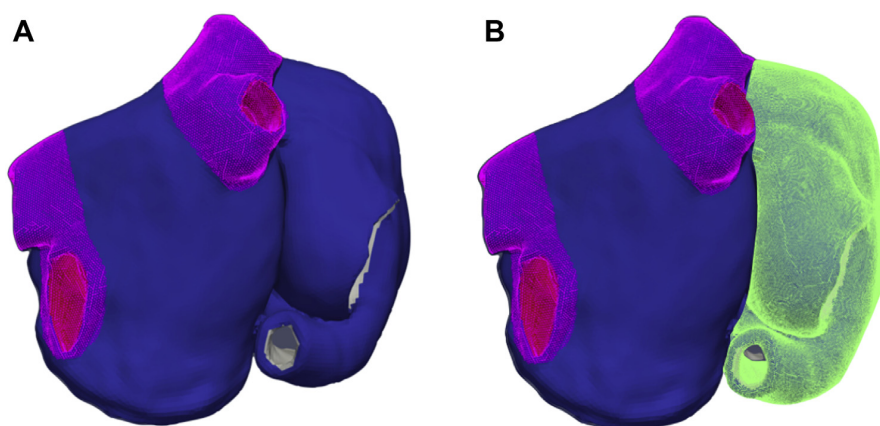

Figure 2   Example of the atrial regions used to define the classes in which the atrial fibrillation drivers are located. **A:** Pulmonary veins (PVs) (*pink*) and extra-PV areas (*blue*) for binary classification. **B:** PVs (*pink*), extra-PV left atrium areas (*blue*), and right atrium (*green*) for 3-class classification.
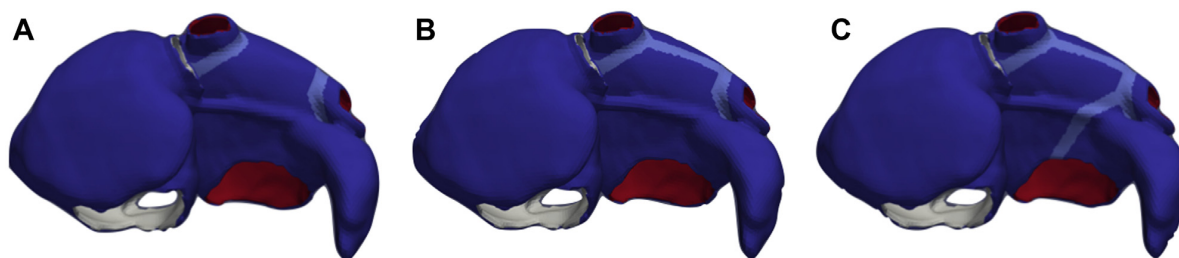
Figure 3   Scar lines were applied on the atrial models to simulate several ablation procedures. In the atrial model, the right endocardium is shown in white, the left endocardium in red, both epicardia in blue, and the scar lines in cyan. **A:** Pulmonary vein isolation (PVI): Scars added circumferentially around ipsilateral PVs. **B:** PVI+RL: Roofline scar added between the left PVI and the right PVI. **C:** PVI+RL+MI: Scar added between the left PVI and the mitral valve (mitral isthmus ablation).

over time and between them; ratio of the PCA eigenvalues to increase and highlight the differences between the PCA eigenvalues; and organization index and spectral entropy to study the variability and stability of these mechanisms in time and frequency domains.[30,34,35] No features were derived for any single ECG leads to avoid an undesirable influence of atria orientation on the resulting calculated ECGs.[36] Hence, all features were averaged over the 12 leads or calculated over the PCs. A summary of the features and more information regarding the feature extraction methods are provided in the Supplemental Material.

Feature selection

Features were selected with a greedy forward selection technique to implement a feature set. This algorithm started with an empty feature set and added, in each iteration, the feature that led to the highest classification performance increase assessed using the geometric mean (G-mean) between sensitivity and specificity of a decision tree classifier (more details about the implemented classifier are discussed in the following section). The algorithm stopped when performance based on the validation set could not be further increased. Candidate features with a correlation coefficient >0.6 with any of the features already included in the set were not considered. This correlation threshold was chosen as a compromise between avoiding redundant information and allowing physiological explanation.

Machine learning classification

In this study, a decision tree classifier was implemented for binary classification (AF drivers located at the PVs vs extra-PV drivers) owing to its simplicity and explainability (similar results obtained with other machine learning algorithms for the binary classification are provided in the Supplemental Material). The decision tree was trained and applied using the MATLAB functions fitctree and predict, respectively.

First, a multifeature classification was performed with the feature set selected as described in the paragraph on feature selection. Hold-out cross-validation was performed randomly, dividing the simulated dataset into a training set, validation set, and test set with a ratio of 70%, 15%, and 15%, respectively. The training set was used to tune classifier

parameters, while the validation set was used for the greedy feature selection optimization. To reduce the random division's influence, the process was repeated 100 times (training and validation sets were recalculated at each loop, while the test set was saved and kept the same for all experiments). The classes have been balanced by setting the Prior model parameter in the MATLAB fitctree function to uniform. Sensitivity, specificity, and positive predictive value (PPV) were calculated considering the PV class as positive and the extra-PV class as negative. Lastly, the classifier trained again with all the simulated data and the resulting feature set from the previous analysis was tested on the clinical dataset, which was not used during algorithm development.

Second, binary classification using the same feature set extracted from the first approach was performed with different cross-validation strategies: leave-one-atrium-out (LOAO) and leave-one-torso-out (LOTO). These strategies were applied to verify that the atrial geometries did not have a significant influence on the features extracted from the simulated signals.[36] For LOAO, 1 atrial geometry was used in the training set and the other atrial geometry was used in both the validation and the test set (50% of the ECGs from this geometry in each set). This procedure was repeated twice to cover all permutations of validation and test atrial geometry. The average G-mean of the 2 iterations was used as performance parameter. The same process was applied for LOTO with 8 repetitions, since 8 torso geometries were used in this study.

Finally, thanks to the ground truth given by the simulations, and to estimate how feasibly a machine learning approach can discriminate the position of AF drivers, a classifier was implemented for a 3-class classification. The 3 classes were defined as AF drivers located in the PVs, extra-PV LA areas, and RA areas. A new feature set was selected with the greedy technique similar to the first approach described in this section, and hold-out cross-validation was used on the simulated dataset. The classes have been balanced in a similar manner to the binary classification.

Statistical analysis

Classifier performance was evaluated using the G-mean between sensitivity and specificity metric:

Table 1 Patient characteristics with univariate *t* test analysis between groups

	All patients n=46	Acute AF termination by PVI n=23	No acute AF termination by PVI n=23	P
Age (years)	64 (10.5)	64 (10.5)	64 (10.8)	.966
Female sex	29 (63.0)	14 (60.9)	15 (65.2)	.680
Body mass index (kg/m^2)	28.1 (3.8)	28.1 (4.2)	28.3 (3.5)	.907
Arterial hypertension	25 (54.3)	11 (47.8)	14 (60.9)	.475
Prior stroke or TIA	7 (15.2)	5 (21.7)	2 (8.7)	.203
Structural CMP	10 (21.7)	5 (21.7)	5 (21.7)	.938
Coronary artery disease	9 (19.6)	3 (13.0)	6 (26.0)	.307
Persistent atrial fibrillation	33 (71.7)	15 (65.2)	18 (78.3)	.456
CHADS$_2$-VASc score	2.0 (1.6)	2.3 (1.7)	1.7 (1.4)	.217
Prior AA therapy	19 (41.3)	11 (47.83)	8 (34.8)	.312
AA therapy on admission	23 (50.0)	11 (47.8)	12 (52.2)	.887
Amiodarone	19 (41.3)	9 (39.1)	10 (43.5)	.843
Flecainide	2 (4.3)	1 (4.3)	1 (4.3)	.952
Sotalol	0 (0.0)	0 (0.0)	0 (0.0)	-
Dronedarione	1 (2.2)	0 (0.0)	1 (4.3)	.334
Propafenone	1 (2.2)	0 (0.0)	1 (4.3)	.334
LVEF (%)	57 (9)	59 (6)	54 (10)	.062
LVEDD (mm)	50.1 (4.7)	49.2 (4.4)	52.7 (5.1)	.127
LAD (mm)	44 (6)	52 (5)	46 (6)	.052
Renal dysfunction	20 (43.5)	13 (59.1)	7 (30.4)	.062

Values are given as mean ($\pm$ standard deviation) or number (%).
Multivariate analysis is detailed in Supplemental Material.
AA = antiarrhythmic; CMP = cardiomyopathies; LAD = left atrium dilatation; LVEDD = left ventricular end-diastolic diameter; LVEF = left ventricular ejection fraction; TIA = transient ischemic attack.

$$G - Mean = \sqrt{Sensitivity \cdot Specificity} \qquad (1)$$

The G-mean metric strikes a balance for binary classification performance on both the majority and minority classes.[37] A low G-mean indicates a poor performance in the classification of the positive cases even if the negative cases are correctly classified as such. As such, it can avoid overfitting the negative class and underfitting the positive class and vice versa.

For the third classification approach, the G-mean metric was modified to make it suitable for 3-class classification:

$$G - Mean = \frac{2}{K \cdot (K-1)} \sum_{i \neq j}^{K} \sqrt{Sensitivity_{ij} \cdot Specificity_{ij}} \qquad (2)$$

with K being the number of classes, and i and j the classes considered as positive and negative, respectively.[38]

Patient characteristics were evaluated with the *t* test between case and control groups (*P* values < .01 considered significant; Table 1). Multivariate regression analysis was performed on variables that differed between groups with a *P* value < .1 (Table 1) and our classifier. Age and sex were included in the multivariate model for their clinical relevance.

Clinical data

We retrospectively included a total of 46 consecutive patients (72% persistent AF, 70% male; Table 1) who presented between 2019 and 2020 with spontaneous AF (as baseline rhythm) on admission day and during electrophysiology study and who met the following criteria: first ablation for AF without any prior LA ablations (eg, Wolff-Parkinson-White patients, etc were excluded) and AF termination (sinus rhythm restoration or conversion to atrial flutter) during or within 1 minute after completion of PVI (case group/PV class, n = 23). Patients meeting the above-mentioned criteria but without termination of AF during/immediately following PVI were included as controls (control group/extra-PV class, n = 23).

A dataset of 46 clinical AF 12-lead ECGs was used to validate the classifier, which was trained solely on synthetic data generated using the computational framework described above. Three-second clinical ECGs were collected intraprocedurally prior to PVI during ongoing AF. The signals were notch filtered at 50 Hz and bandpass-filtered between 0.05 Hz and 100 Hz (examples of the 12-lead ECGs can be found in the Supplemental Material). The QRS-T complexes were automatically removed and replaced by a sigmoid function to connect the remaining f-wave segments using an interpolation method explained in Pilia and colleagues.[39] All the features extracted and selected from the simulated signals by the feature selection algorithm were extracted from the clinical signals too. A second set of 3-second clinical 12-lead ECGs was collected from the same 46 patients during the same procedure prior to PVI during ongoing AF. This ECG set was also provided to the classifier to check the consistency of the classification.

Patient information was de-identified and the study was exempt from Institutional Review Board approval.

Results
Patient characteristics

Patient characteristics with associated *P* values between case and control groups are provided in Table 1.

The multivariate regression analysis performed between the variables left ventricular ejection fraction, LA dilatation, renal dysfunction, sex, age, and our classifier showed that the classifier is the only significant variable ($P = .049$, hazard ratio = 11.8), indicating that the classifier has added value beyond the routine clinical parameters for detecting patients who require more than a "PVI-only" approach (the whole multivariate regression analysis table is provided in the Supplemental Material).

Acute ablation outcome

The following results are summarized in Table 2. Virtual PVI was applied in all 141 atrial simulated scenarios (Figure 3A). In 13 cases, PVI had a consequence on the ongoing arrhythmia; in 6 cases, the arrhythmia was terminated and sinus rhythm restored, whereas the remaining 7 cases converted to different types of atrial flutter. These 13 cases consisted of 10 simulations belonging to the PV class (100% of all scenarios in the PV class, including all 6 simulations where PVI restored sinus rhythm) and 3 simulations belonging to the extra-PV class LA (12.5% of the total extra-PV LA simulations).

RL ablation was applied to the 135 simulations where PVI did not lead to sinus rhythm restoration (Figure 3B). The additional RL terminated the arrhythmia in 2 cases that had converted to atrial flutter after PVI (1 case in PV class and 1 case in extra-PV LA). MI ablation was then applied to the 133 simulations where PVI+RL did not restore sinus rhythm (Figure 3C). PVI+RL+MI terminated the arrhythmia in another 3 cases, all of which had become atrial flutter after PVI (1 case in PV class, 2 cases in extra-PV LA).

Binary classification on synthetic data

The decision tree for binary classification (AF drivers located in the PVs vs extra-PV drivers) was repeated 100 times to reduce the random division's influence on the classifier performance. Eleven is the number of features to which the greedy forward selection technique has reached the maximum G-mean, and therefore, it was used as the number of features in the feature set. The 11 most frequently selected features in the 100 iterations were as follows: the recurrence rate extracted with individual component RQA from the second and third PC of the 12-lead ECGs; the variance of the mobility; λ_7, λ_5, λ_{12}, $\sigma_{\lambda 5}$, and $\sigma_{\lambda 6}$; R_{PC}; the recurrence rate extracted from the vectorcardiogram, and the organization index averaged over the 12-lead ECG. The selected features

Table 2   Simulated atrial fibrillation episodes converted to sinus rhythm or atrial flutter after stepwise ablation

Sinus rhythm/atrial flutter	PVs	Extra-PV LA	RA
PVI	6/4	-/3	-
PVI success (%)	100%	12.5%	0%
RL	1/-	1/-	-
MI	1/-	2/-	-

LA = left atrium; MI = mitral isthmus; PV = pulmonary vein; PVI = pulmonary vein isolation; RA = right atrium; RL = roofline.

can be seen in Figure 4A. All the selected features showed a significant difference between the 2 classes. Extra information regarding the extracted features and a feature importance analysis are provided in the Supplemental Material.

The binary classifier achieved a G-mean of 85.3% ± 9.4% on the in silico test set with a sensitivity of 95.5% ± 1.4% and a specificity of 76.3% ± 13.1% on the simulated dataset (PV considered as the positive class). Classifiers trained using the LOAO and LOTO strategies yielded test G-means of 84.3% ± 2.9% and 85.3% ± 3.7%, respectively.

Three class localization: PV vs extra-PV LA vs RA

The 3-class decision tree achieved 75.1% ± 9.9% test G-mean with a feature set comprising, on average, 13 features. The most often selected features are shown in Figure 4B.

Performance on clinical ECGs

The 11 features shown in Figure 4A were used to train the binary classifier solely on the simulated data. The resulting classifier was subsequently evaluated on the 46 clinical ECGs acquired from 46 patients. On this unseen clinical dataset, the classifier achieved 78.1% G-mean with a sensitivity of 73.9%, a specificity of 82.6%, and PPV of 80.9%. On the clinical dataset extracted for the consistency analysis, the classifier achieved 71.7% G-mean with a sensitivity of 69.6%, a specificity of 73.9%, and PPV of 72.7%. Only 3 cases were classified differently compared to the test performed with the first set, reaching a matching rate of 93.5%. Table 3 shows the confusion matrix obtained from the decision tree classifier on the clinical ECGs (the confusion matrix obtained on the "consistency" ECG dataset is provided in the Supplemental Material).

Discussion

Our results suggest that a noninvasive machine learning approach can discriminate the source area of the mechanisms sustaining AF, which could improve protocols for clinical therapeutic decision-making and ablation procedure planning.

The 12-lead ECG is broadly used for cardiac diagnostics and to discriminate AF from other cardiac rhythms.[20] However, to the best of our knowledge, they have never been used so far to infer AF driver positions, as opposed to invasive intracardiac mapping, which is the most commonly used approach.[17,18]

In the present work, we implemented a decision tree classifier to discriminate the location of AF drivers by using only the noninvasive ECG signals (similar results obtained with other machine learning algorithms are provided in the Supplemental Material). An inside-out computational simulation generated 12-lead ECGs from spatially distributed rotors and focal sources sustaining AF with different combinations of atrial and torso geometries. This provided an ideal and controlled environment to generate a consistent ground truth dataset of AF perpetuation mechanisms without
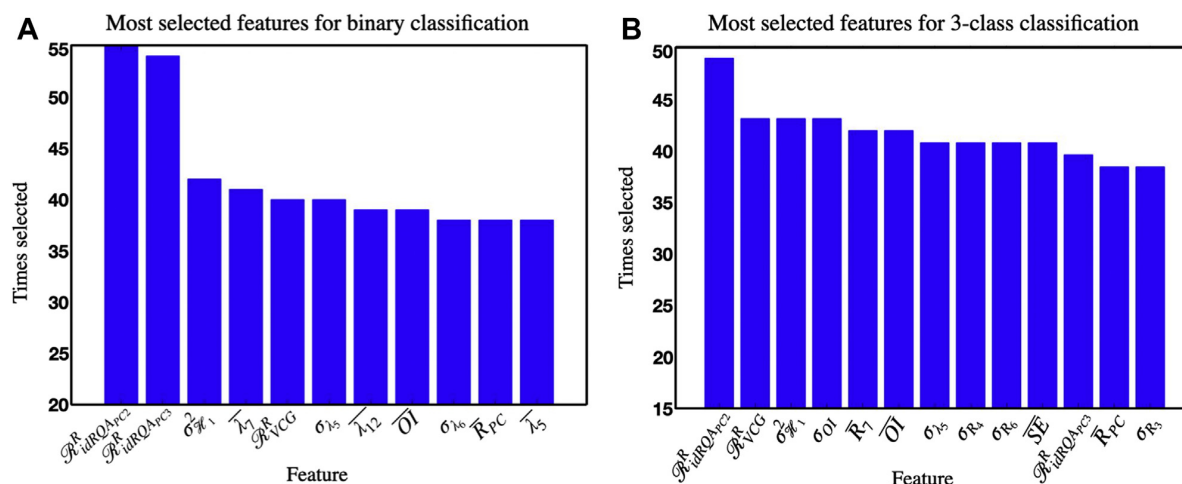
Figure 4   **A:** Histogram of the 11 most selected features in the 100 iterations of the binary hold-out cross-validation classification for atrial fibrillation (AF) driver localization (pulmonary vein [PV] vs extra-PV). These 11 features were used as a feature set for the clinical test. **B:** Histogram of the 13 most selected features in the 100 iterations of the 3-class hold-out cross-validation classification: PV vs extra-PV left atrial vs right atrial AF drivers.

the influence of secondary, or unknown, interfering phenomena.

This study builds on our previous work[30,40] and expands to different atrial geometries and different AF driving mechanisms adding focal sources, and presents a first application of the resulting classifier on clinical data. Moreover, an acute ablation procedure outcome analysis was implemented in the in silico cases.

Acute PVI success prediction
PVI is the most common AF ablation therapy[1] owing to the often localized AF drivers in the PVs.[10] Hence, we aimed to identify the PV driving mechanisms using the 12-lead ECG. We also wanted to verify whether AF would be terminated following PVI, or at least converted into more organized rhythms that are often easier to treat, such as atrial flutter.

The results of applying PVI in silico (Table 2) help to illustrate the efficacy of this ablation procedure in cases where AF is driven by mechanisms located in the PVs. Accordingly, 100% of the cases labeled as PV showed AF organization: 6 terminated and 4 converted to atrial flutter. Interestingly, the extra-PV cases were not affected by the PVI, as expected: only 3 arrhythmias driven by extra-PV LA areas converted into atrial flutter, probably owing to the

Table 3   Clinical test set confusion matrix for pulmonary vein vs extra-pulmonary vein atrial fibrillation driver location classification

	True class	
	PV	Extra-PV
Predicted class		
PV	17	4
Extra-PV	6	19

PV = pulmonary vein.

proximity of the AF driving mechanisms to the PVs even if not labeled as belonging to the PV class. Therefore, the proposed classifier could assist on clinical decision-making for the delineation of the optimum mapping and ablation strategy according to patient-specific characteristics. For instance, if a new case is identified as belonging to the PV class by our classifier, the suggested procedure to treat the fibrillation would be PVI. It could also be considered to use cryoablation, skipping the use of the time-consuming and costly electroanatomical mapping step prior to PVI in these cases, as identified by our novel ECG-based machine learning classifier. On the contrary, for the cases identified as extra-PV class, PVI showed to be not effective to acute sinus rhythm restoration or to atrial flutter conversion. Nevertheless, there are many studies that have certified the benevolent effects of performing PVI,[41,42] even if it does not lead to an acute AF termination. However, based on the indications of our classifier, electrophysiologists would know a priori the need for subsequent ablation procedures in addition to PVI (thus a patient-specific preparation of surgical instrumentation) to achieve acute AF termination.

Finally, the clinical dataset was labeled using the acute PVI success as decision parameter (ie, PVI-terminated AF leads to PV class). The results regarding the PVI procedure on our simulations support the perspective that the labeling on the clinical dataset was properly performed, owing to the obvious link between PV mechanisms and the success of PVI.

Acute RL and MI outcome prediction
In addition to PVI, 2 common post-PVI ablation lines were investigated: RL and MI (Figure 3B and 3C and Table 2). RL and MI led to the termination of atrial flutter resulting from PVI. However, the additional ablation created during RL and MI had no influence on acute AF mechanism termination by PVI considered in this study, as suggested in

previous work.[43] Nevertheless, it is recognized that these linear ablations can be effective to prevent some postablation atrial flutter (eg, perimitral atrial flutter) segmenting the atria into isolated regions.[44]

Feature sets

Compelling results were reported previously for RQA approaches and PCA eigenvalue ratios regarding the characterization and discrimination of different arrhythmias.[32,45,33,40,46] Indeed, RQA and the ratio of PCA eigenvalues were also key features for the binary classification implemented in this study. Nine of the 11 most selected features were obtained with RQA or ratios of PCA eigenvalues (Figure 4A), probably owing to their sensitivity in detecting changes in the dynamic behavior over time.[47] We observed that AF drivers located in the PVs produced a more regular activity than the extra-PV cases (Figure 1A–1B.3). In fact, in the simulated episodes, the irregular activity driven by PV cases was limited to a small portion of tissue owing to the presence of anatomical obstacles (eg, the PV sleeves) that prevented the driving mechanisms from meandering to the remaining parts of the atria. Therefore, in the remaining atrial areas, the signal was propagated as an organized single wavefront. Contrarily, AF driving mechanisms located in extra-PV areas were free to meander throughout the tissue owing to the fewer anatomical constraints, which yielded more irregular ECGs. The selected features succeeded in detecting these irregularities and differences between classes. This information was also quantified by the selected RQA and PCA eigenvalue ratio parameters, resulting in significantly higher values for the PV and extra-PV classes, respectively.

Regarding the 3-class classification, 7 out of the 13 most selected features (Figure 4B) were the same features selected for the binary classification (Figure 4A). This supports the considerations about the higher regularity of the signals produced by the PV cases compared to the extra-PV cases. The PV cases have been shown more regular than the extra-PV LA, and even more regular than the RA cases owing to fewer anatomical constraints starting from the PV cases and ending with the RA cases. These observations corroborate our previous studies.[30,40] Some of the features are different between the 2 sets, and more features are required to solve the 3-class classification, since this represents a consecutive approach more complex than the binary one. Therefore, different information may be required to perform this discrimination task. Accordingly, more features were needed to characterize the increasingly irregular activity generated by the 3 classes, starting from the PVs class up to the RA class. This was the case with σ_{OI} and $\overline{SE}$, which showed significantly lower and higher values from class PVs to class RA, respectively. However, some features differing between the 2 classification approaches did indeed measure similar characteristics of the signal (and were very correlated), so they could be interchangeable, ie, the average eigenvalue $\overline{\lambda_7}$ and the average ratio $\overline{R_7}$ from the 3-class and binary classification, respectively. Both these parameters analyze the variability of PC 7 over time, but $\overline{R_7}$ emphasizes this variability more than $\overline{\lambda_7}$.

AF driver localization

Previous works have considered ECGs to classify AF from sinus rhythm,[19,48] or to automatically diagnose multiple types of abnormal heart beats.[20,49] To the best of our knowledge, ours represents the first study to use the 12-lead ECG directly for automatic and noninvasive discrimination of the location of AF drivers to guide clinical decision-making and procedure planning (electroanatomical mapping required? LA access required?).

The high performance on the simulated dataset achieved for PV vs extra-PV AF driver classification with old-out cross-validation indicates the potential of using the features extracted in this work to identify the location of the sustaining AF mechanism using only the noninvasive 12-lead ECG signals. The classifier trained in the computational framework was subsequently tested on a clinical dataset, each consisting of 12-lead ECGs acquired from 46 patients (23 labeled as PV class, and 23 as extra-PV class). The G-mean of 78.1% reached on the clinical test set suggests that such a noninvasive classification might provide valuable complementary information in clinical practice. The specificity of 82.6% and PPV of 80.9% indicate the algorithm's robustness in identifying the extra-PV cases, suggesting that a PVI-only approach (eg, using a cryoballoon) might not be sufficient in these patients to treat AF. Instead, physicians may choose an ablation technology that is able to detect non-PV trigger (eg, electroanatomic mapping and additional extra-PVI radiofrequency ablation). Also, the sensitivity of the classifier is comparably high (73.9%), indicating robustness of the classifier in identifying the cases where PVI is sufficient to terminate or convert the arrhythmia (PV class). In these cases, direct cryoablation without prior mapping might suffice to treat the patient. In addition, the consistency test performed on the ECG set of clinical data extracted from the same patients confirmed the nonrandomness of the classification implemented in this project, matching 93.5% of the results between the 2 sets (only 3 more cases were misclassified in the second analysis than in the first one, 2 belonging to the PV class and 1 to the extra-PV class).

The 3-class classifier demonstrated the potential of this machine learning approach to identify the atrial position of the mechanisms sustaining AF even more deeply. The G-mean metric was only slightly lower than the binary classification G-mean (75.1% vs 85.3%). The 3-class approach could provide important information regarding the need to perform a transseptal access to the LA during the electrophysiologic study or whether catheter access to the RA should suffice.

Influence of torso and atrial geometries

From the literature, it is known that the atrial models used to generate ECG signals can have a strong influence on the

signals themselves, likely introducing a bias in machine learning approaches based on simulated training data.[36] Such anatomical bias can lead to a misclassification of the signals generated from unseen atrial geometries. Therefore, in the present study, we focused on features that are not prone to be affected by the specific torso and atria models used to simulate the AF mechanisms. We used a multi-lead feature-extraction approach to avoid focusing on a single lead, ie, a specific projection of cardiac activity, which could be strongly influenced by atrial geometry and orientation. As such, it is easier for the multi-lead approach to generalize well. The LOAO and LOTO analyses confirmed the good generalization properties of our classifier regarding unseen atrial and torso models.

Limitations

The simulated AF drivers used to train the machine learning classifiers in this study are limited to stable long-standing rotors and focal sources. Thus, the classifier was not specifically trained to localize other drivers such as multi-wavelet reentry,[50,51] meandering rotors,[52] or intramural reentry.[53] Moreover, in silico analysis of acute PVI success in this study may not lead to the same results in clinical practice because of the presence of remodeled tissue. Nevertheless, the performance on the clinical data containing in vivo AF drivers was not markedly lower as on the synthetic dataset.

The AF episodes were simulated with atria-only models without the ventricles. Thus, the QRS-T complex was absent from our simulated signals. Nevertheless, the removal of QRS-T complex and its replacement with a sigmoid function, as done here, or other forms of QRS-T cancellation[54] has proven to robustly extract the f-wave component from the clinical 12-lead ECG, so that the signals can be analyzed by our classifier without relevant disturbance from ventricle activity. Further refinements of the synthetic dataset could focus on including heterogeneous atrial wall thickness[55,56] or extending the dataset to cover even more anatomical torso, atrial,[57] and conduction velocity variability.

Three-second-long signals were simulated and used to train the classifier implemented in this study for computational limitations. As an outlook, a test of the classifier with clinical signals of a longer length could be performed to verify the robustness of the classifier.

A decision tree was chosen as a machine learning classifier for its simplicity. However, other classification algorithms could be optimized and tested to investigate more robust methods (eg, support vector machines or artificial neural networks; Supplemental Material).

To strengthen the statistical power, the classifier could be prospectively applied on further clinical data. Clinical signal labeling (PV and extra-PV classes) was done retrospectively at acute PVI success (termination of AF or conversion to atrial flutter). Nevertheless, there is no exact information about the AF driver mechanisms and their positions. Therefore, the ground truth of the clinical dataset between the extra-PV LA and RA classes could not be labeled. In a follow-up study, the predictive power of the classifier should be tested regarding recurrence of AF after PVI (long-term PVI outcome).

Conclusion

The results presented in this study show that (1) a machine learning classifier to distinguish between AF drivers located in the PVs vs in other atrial regions is feasible (82.6% specificity, 73.9% sensitivity on a clinical dataset using 12-lead ECG; 93.5% of results matching on a set of different ECG segments extracted from the same 46 patients for a consistency analysis); (2) classifiers trained on simulated data for which the ground truth is known can generalize well to unseen clinical data; (3) AF drivers identified in the PVs could be considered to be treated with cryoballoon PVI without prior time-consuming and costly electroanatomic mapping; (4) AF drivers identified in extra-PV areas using the ECG are unlikely to terminate or convert upon PVI. Prospective studies are needed to confirm points 3 and 4.

As such, a machine learning–based classifier leveraging the routinely available noninvasive ECG signal could prove to be valuable for clinical decision-making and increase personalization of therapy.

Disclosures

The authors have no conflicts to disclose.

Ethics Statement

The authors designed the study and gathered and analyzed the data according to the Helsinki Declaration guidelines on human research. The research protocol used in this study was reviewed and approved by the institutional review board.

Patient Consent

All patients provided written informed consent.

Authorship
All authors attest they meet the current ICMJE criteria for authorship.

Acknowledgement
Patient-derived data, synthetic data, and code related to this article will be shared with interested parties for noncommercial reuse on reasonable request to the corresponding author and approval from the Institutional Review Boards.

Appendix
Supplementary data
Supplementary data associated with this article can be found in the online version at https://doi.org/10.1016/j.cvdhj.2021.03.002.

References

1. Calkins H, Kuck KH, Cappato R, et al. 2012 HRS/EHRA/ECAS expert consensus statement on catheter and surgical ablation of atrial fibrillation: recommendations for patient selection, procedural techniques, patient management and follow-up, definitions, endpoints, and research trial design. Heart Rhythm 2012; 9:632–696.
2. Chugh SS, Havmoeller R, Narayanan K, et al. Worldwide epidemiology of atrial fibrillation. Circulation 2014;129:837–847.
3. Narayan SM, Krummen DE, Shivkumar K, Clopton P, W-J Rappel W-J, Miller JM. Treatment of atrial fibrillation by the ablation of localized sources. J Am Coll Cardiol 2012;60:628–636.
4. Haissaguerre M, Hocini M, Denisothers A, et al. Driver domains in persistent atrial fibrillation. Circulation 2014;130:530–538.
5. Miller JM, Kalra V, Das MK, et al. Clinical benefit of ablating localized sources for human atrial fibrillation. J Am Coll Cardiol 2017;69:1247–1256.
6. Vaquero M, Calvo D, Jalife J. Cardiac fibrillation: From ion channels to rotors in the human heart. Heart Rhythm 2008;5:872–879.
7. Skanes AC, Mandapati R, Berenfeld O, Davidenko JM, Jalife J. Spatiotemporal periodicity during atrial fibrillation in the isolated sheep heart. Circulation 1998; 98:1236–1248.
8. Sahadevan J, Ryu K, Peltzothers L, et al. Epicardial mapping of chronic atrial fibrillation in patients. Circulation 2004;110:3293–3299.
9. Hindricks G, Potpara T, Dagres N, et al. 2020 ESC Guidelines for the diagnosis and management of atrial fibrillation developed in collaboration with the European Association for Cardio-Thoracic Surgery (EACTS): The Task Force for the diagnosis and management of atrial fibrillation of the European Society of Cardiology (ESC) Developed with the special contribution of the European Heart Rhythm Association (EHRA) of the ESC. Eur Heart J. https://doi.org/10.1093/eurheartj/ehaa612.
10. Haissaguerre M, Jaïs P, Shah DC, et al. Spontaneous initiation of atrial fibrillation by ectopic beats originating in the pulmonary veins. N Engl J Med 1998; 339:659–666.
11. Narayan SM, BaykanerT, Cloptonothers P, et al. Ablation of rotor and focal sources reduces late recurrence of atrial fibrillation compared to trigger ablation alone. J Am Coll Cardiol 2014;63:1761–1768.
12. Allessie MA, de Groot NMS, Houbenothers RPM, et al. Electropathological substrate of long-standing persistent atrial fibrillation in patients with structural heart disease. Circ Arrhythm Electrophysiol 2010;3:606–615.
13. SNattel S. New ideas about atrial fibrillation 50 years on. Nature 2002; 415:1476–4687.
14. Lin WS, Tai CT, Hsiehothers MH, et al. Catheter ablation of paroxysmal atrial fibrillation initiated by non-pulmonary vein ectopy. Circulation 2003; 107:3176–3183.
15. Margulescu AD, Mont L. Persistent atrial fibrillation vs paroxysmal atrial fibrillation: differences in management. Expert Rev Cardiovasc Ther 2017; 15:601–618.
16. Charitos EI, Pürerfellner H, Glotzer TV, Ziegler PD. Clinical classifications of atrial fibrillation poorly reflect its temporal persistence: insights from 1,195 patients continuously monitored with implantable devices. J Am Coll Cardiol 2014;63:2840–2848.

17. Zaman JAB, Schricker A, Lalani GG, Trikha R, Krummen DE, Narayan SM. Focal impulse and rotor mapping (firm): Conceptualizing and treating atrial fibrillation. J Atr Fibrillation 2014;7:1103.
18. Narayan SM, Krummen DE, Rappel WJ. Clinical mapping approach to diagnose electrical rotors and focal impulse sources for human atrial fibrillation. J Cardiovasc Electrophysiol 2012;23:447–454.
19. Padmavathi K, Ramakrishna KS. Classification of ECG signal during atrial fibrillation using autoregressive modeling. Procedia Computer Science 2015;46:53–59.
20. Acharya UR, Fujita H, Adam M, et al. Automated characterization of arrhythmias using nonlinear features from tachycardia ECG beats, 2016 IEEE International Conference on Systems, Man, and Cybernetics (SMC); 2016;. p. 533–538.
21. Loewe A, Krueger MW, Holmqvist F, Dössel O, Seemann G, Platonov PG. Influence of the earliest right atrial activation site and its proximity to interatrial connections on p-wave morphology. Europace 2016;18(suppl 4):iv35–iv43.
22. Wachter A, Loewe A, Krueger MW, Dössel O, Seemann G. Mesh structure-independent modeling of patient-specific atrial fiber orientation. CDBME 2015; 1:409–412.
23. Loewe A. Chronic AF induced remodeling, Modeling Human Atrial Patho-Electrophysiology From Ion Channels to ECG: Substrates, Pharmacology, Vulnerability, and P-Waves. KIT Scientific Publishing; 2016. p. 113–119. Ch. 5.2.
24. Roney CH, Bayer JD, Zahidothers S, et al. Modelling methodology of atrial fibrosis affects rotor dynamics and electrograms. Europace 2016;18:iv146–iv155.
25. Jacquement V. An eikonal approach for the initiation of reentrant cardiac propagation in reaction-diffusion models. IEEE Trans Biomed Eng 2010; 57:2090–2098.
26. Vigmond EJ, Hughes M, Plank G, Leon LJ. Computational tools for modeling electrical activity in cardiac tissue. J Electrocardiol 2003;36:69–74.
27. Sánchez J, Nothstein M, Neic A, et al. openCARP: An open sustainable framework for in-silico cardiac electrophysiology research. In: Computing in Cardiology Conference (CinC) 2020;47.
28. Schuler S, Tate JD, Oostendorp TF, MacLeod RS, Dössel O. Spatial downsampling of surface sources in the forward problem of electrocardiography, of Lecture Notes in Computer Science. In: Functional Imaging and Modeling of the Heart 2019;11504;. p. 29–36.
29. Stenroos M. The transfer matrix for epicardial potential in a piece-wise homogeneous thorax model: The boundary element formulation. Phys Med Biol 2009; 54:5443–5455.
30. Luongo G, Azzolin L, Rivolta MW, et al. Non-invasive identification of atrial fibrillation driver location using the 12-lead ECG: Pulmonary vein rotors vs. other locations, IEEE 2020 EMB Conference; 2020;. p. 410–413.
31. Sörnmo L, Laguna P. Chapter 3 - EEG signal processing. In: Sörnmo L, Laguna P, eds. Bioelectrical Signal Processing in Cardiac and Neurological Applications. Burlington: Academic Press; 2005. p. 55–179.
32. Yang H. Multiscale recurrence quantification analysis of spatial cardiac vectorcardiogram signals. IEEE Trans Biomed Eng 2011;58:339–347.
33. Luongo G, Schuler S, Luik A, et al. Non-invasive characterization of atrial flutter mechanisms using recurrence quantification analysis on the ECG: a computational study. IEEE Trans Biomed Eng 2021;68:914–925.
34. Uldry L, Van Zaen J, Prudat Y, Kappenberger L, Vesin JM. Measures of spatiotemporal organization differentiate persistent from long-standing persistent atrial fibrillation. Europace 2012;14:1125–1131.
35. Vakkuri A, Yli-Hankala A, Talja P, et al. Time-frequency balanced spectral entropy as a measure of anesthetic drug effect in central nervous system during sevoflurane, propofol, and thiopental anesthesia. Acta Anaesthesiol Scand 2004;48:145–153.
36. Luongo G, Schuler S, Rivolta MW, Dössel O, Sassi R, Loewe A. Automatic ECG-based discrimination of 20 atrial flutter mechanisms: Influence of atrial and torso geometries. Comput Cardiol 2020;2020.
37. Akosa J. Predictive accuracy: A misleading performance measure for highly imbalanced data, In: Proceedings of the SAS Global Forum 2017 Conference, Cary, NC: SAS Institute Inc;; 2017. 942-2017.
38. Espíndola RP, Ebecken NFF. On extending f-measure and g-mean metrics to multi-class problems. WIT Transactions on Information and Communication Technologies 2005;35:25–34.
39. Pilia N, Nagel C, Lenis G, Becker S, Dössel O, Loewe A. ECGdeli - an open source ecg delineation toolbox for MATLAB. SoftwareX 2021;13:100639. https://doi.org/10.1016/j.softx.2020.100639.
40. Luongo G, Azzolin L, Rivolta MW, et al. Machine learning to find areas of rotors sustaining atrial fibrillation from the ECG Comput Cardiol 2020, 2020.
41. Salinet J, Schlindwein FS, Stafford P, et al. Propagation of meandering rotors surrounded by areas of high dominant frequency in persistent atrial fibrillation. Heart Rhythm 2017;14:1269–1278.
42. Almeida TP, Chu GS, Li X, et al. Atrial electrogram fractionation distribution before and after pulmonary vein isolation in human persistent atrial fibrillation—a retrospective multivariate statistical analysis. Front Physiol 2017; 8:589.

43. Arbelo E, Guiu E, Ramos P, et al. Benefit of left atrial roof linear ablation in paroxysmal atrial fibrillation: A prospective, randomized study. J Am Heart Assoc 2014;3:e000877.

44. Báez-Escudero JL, Morales PF, Dave AS, et al. Ethanol infusion in the vein of marshall facilitates mitral isthmus ablation. Heart Rhythm 2012;9:1207–1215.

45. Hummel JP, Baher A, Buck B, Fanarjian M M, Webber CL Jr, Akar JG. A method for quantifying recurrent patterns of local wavefront direction during atrial fibrillation. Comput Biol Med 2017;89:497–504.

46. Almeida TP, Schlindwein FS, Salinet J, et al. Characterization of human persistent atrial fibrillation electrograms using recurrence quantification analysis. Chaos 2018;28:085710.

47. Almeida TP, Schlindwein F, Salinet J, et al. The temporal stability of recurrence quantification analysis attributes from chronic atrial fibrillation electrograms. Research on Biomedical Engineering 2018;34:337–349.

48. Attia ZI, Noseworthy PA, Lopez-Jimenez F, et al. An artificial intelligence-enabled ECG algorithm for the identification of patients with atrial fibrillation during sinus rhythm: a retrospective analysis of outcome prediction. Lancet 2019; 394:861–867.

49. Kashou AH, Ko WY, Attia ZI, Cohen MS, Friedman PA, Noseworthy PA. A comprehensive artificial intelligence enabled electrocardiogram interpretation program. Cardiovasc Digital Health J 2020;1:62–70.

50. Moe GK. On the multiple wavelet hypothesis of atrial fibrillation. Arch Int Pharmacodyn Ther 1962;140:183.

51. Allessie MA. Experimental evaluation of Moe's multiple wavelet hypothesis of atrial fibrillation. Cardiac Electrophysiology and Arrhythmias 1985;265–275.

52. Zlochiver S, Yamazaki M, Kalifa J, Berenfeld O. Rotor meandering contributes to irregularity in electrograms during atrial fibrillation. Heart Rhythm 2008; 5:846–854.

53. Hansen BJ, Zhao J, Csepe TA, et al. Atrial fibrillation driven by micro-anatomic intramural re-entry revealed by simultaneous sub-epicardial and sub- endocardial optical mapping in explanted human hearts. Eur Heart J 2015;36:2390–2401.

54. Sörnmo L, Petrenas A, Laguna P, Marozas V. Extraction of f waves, Atrial Fibrillation from an Engineering Perspective. Springer; 2018. p. 137–220.

55. Azzolin L, Luongo G, Rocher S, Saiz J, Dössel O, Loewe A. Influence of gradient and smoothness of atrial wall thickness on initiation and maintenance of atrial fibrillation, Computing in Cardiology Conference. CinC); 2020.

56. Andlauer R, Seemann G, Baron L, et al. Influence of left atrial size on p-wave morphology: differential effects of dilation and hypertrophy. Europace 2018; 20:iii36–iii44.

57. Nagel C, Schuler S, Dössel O, Loewe A. A bi-atrial statistical shape model for large-scale in silico studies of human atria: model development and application to ECG simulations. 2021. arXiv:2102.10838, https://arxiv.org/abs/2102.1083.

Machine Learning Using a Single-lead ECG to Identify Patients with Atrial Fibrillation-Induced Heart Failure

Giorgio Luongo[1]*, Felix Rees[2]*, Deborah Nairn[1], Massimo W Rivolta[3], Olaf Dössel[1], Roberto Sassi[3], Christoph Ahlgrim[2], Louisa Mayer[2], Franz-Josef Neumann[2], Thomas Arentz[2], Amir Jadidi[2], Axel Loewe[1], Björn Müller-Edenborn[2]

[1]Institute of Biomedical Engineering (IBT), Karlsruhe Institute of Technology (KIT), Karlsruhe, Germany

[2]Division of Cardiology and Angiology II, University Heart Center Freiburg-Bad Krozingen, Bad Krozingen, Germany

[3]Dipartimento di Informatica, Università degli Studi di Milano, Milan, Italy

* these authors contributed equally

Postal addresses:

[1]Kaiserstr. 12, 76131, Karlsruhe, Germany; [2]Südring 15, 79189 Bad Krozingen, Germany; [3]Via Festa del Perdono 7, 20122, Milan, Italy.

Corresponding author:

Giorgio Luongo, MSc, Fritz-Haber-Weg 1, 76131 Karlsruhe, Germany, Tel.: +49721608-42650, Fax: +49721608-42789, publications@ibt.kit.edu.

26 **Abstract**

27   <u>Aims:</u> Atrial fibrillation (AF) and heart failure often co-exist. Early identification of AF

28 patients at risk for AF-induced heart failure (AF-HF) is desirable to reduce both morbidity and

29 mortality as well as health care costs. We aimed to leverage the characteristics of beat-to-beat-

30 patterns in AF to prospectively discriminate AF patients with and without AF-HF.

31   <u>Methods:</u> A dataset of 10,234 5-minute length RR-interval time series derived from 26 AF-

32 HF patients and 26 control patients was extracted from single-lead Holter-ECGs. A total of 14

33 features were extracted, and the most informative features were selected. Then, a decision tree

34 classifier with 5-fold cross-validation was trained, validated, and tested on the dataset randomly

35 split. The derived algorithm was then tested on 2,261 5-min segments from six AF-HF and six

36 control patients and validated for various time segments.

37   <u>Results:</u> The algorithm based on the spectral entropy of the RR-intervals, the mean value

38 of the relative RR-interval, and the root mean square of successive differences of the relative

39 RR-interval yielded an accuracy of 73.5%, specificity of 91.4%, sensitivity of 64.7%, and PPV

40 of 87.0% to correctly stratify segments to AF-HF. Considering the majority vote of the

41 segments of each patient, 10/12 patients (83.33%) were correctly classified.

42   <u>Conclusion:</u> Beat-to-beat-analysis using a machine learning classifier identifies patients

43 with AF-induced heart failure with clinically relevant diagnostic properties. Application of this

44 algorithm in routine care may improve early identification of patients at risk for AF-induced

45 cardiomyopathy and heart failure.

46

49   **What's New?**

50   -   Novel diagnostic algorithm for atrial fibrillation-induced cardiomyopathy and AF-

51   mediated heart failure with reduced ejection fraction (HFrEF);

52   -   Feature identification to predict atrial fibrillation complication;

53   -   Machine learning algorithm using non-invasive and short single-lead ECG signals

54   -   Determination of daytime as best circadian time for signal acquisition and diagnosis of

55   atrial fibrillation-induced heart failure

56   -   Personalized patient care treatment for early diagnosis and management of heart failure

57   in patients with atrial fibrillation with potential reduction of cardiovascular mortality

58   -   Potential application to a variety of wearables and pocket ECG monitors

59 **1 Introduction**

60   Atrial fibrillation (AF), and heart failure share many common risk factors, predispose to

61 each other, and often coexist (1). AF can occur concomitantly with heart failure without

62 causative relation, and restoration of sinus rhythm in these patients results in only modest

63 improvements of left ventricular systolic dysfunction (LVSD). In a potentially large subset of

64 patients with AF, and heart failure however, sinus rhythm restoration leads to drastic

65 improvements or normalization of LVSD (2–5) within days to weeks.

66   It is currently not fully understood why certain patients develop severe heart failure

67 symptoms, and LVSD during AF (AF-induced heart failure; AF-HF). Current guidelines

68 emphasize the importance of AF in this context, and recommend routine clinical follow-up in

69 AF patients to recognize cardiac deterioration early (6). Given the ever-increasing prevalence

70 of AF in the European population, easily applicable screening tools to identify patients at risk

71 are desirable to tailor patient care, and reduce costs for health care systems.

72   We hypothesize that specific patterns of ventricular beat-to-beat variations, and arrhythmia

73 characteristics in AF are associated with the clinical phenotype of AF-HF, potentially enabling

74 early identification of susceptible patients.

75

76 **2 Methods**

77   This prospective observational study was approved by the local institutional review board,

78 and patients gave informed consent. Inclusion criteria were persistent or longstanding persistent

79 AF with left ventricular ejection fraction in AF ≤40% determined using biplane Simpson

80 method averaged over three consecutive beats, absence of left- or right-sided significant

81 valvulopathies (moderate or severe), and absence of relevant coronary artery disease as

82 evidenced using coronary angiography or non-invasive imaging within 12 months of screening.

83   Patients younger than 18 years, and those with a history of ischemic heart disease requiring

84   revascularization with or without myocardial infarction were excluded.

85

86   *2.1   Study protocol*

87   All study participants underwent standard 12-lead ECG, 24h Holter single-lead ECG, and

88   transthoracic echocardiography within 24h from study inclusion. Patients with LVEF ≤40%

89   were scheduled for electro-cardioversion on the next working day, and underwent additional

90   follow-up including echocardiography at day 40. Those patients who experienced an absolute

91   improvement of LVEF of 15% or more within 40 days in sinus rhythm were considered to have

92   AF-HF, and remained in the study for further analysis. Patients who either experienced AF-

93   recurrence within 40 days from cardioversion or who experienced an improvement in LVEF of

94   <15% despite sinus rhythm were excluded from this study. Patients with LVEF >50% in AF

95   were considered as control group (CTR). A total of 52 patients were included in the final

96   analysis: 26 patients with AF-HF, and 26 CTR. The primary endpoint was the determination,

97   and validation of an algorithm to identify AF-HF patients from 5-minute Holter ECG segments

98   recorded during daytime (8 AM to 10 PM). Secondary endpoints were the performance of the

99   feature set for nighttime (10 PM to 8 AM), and full-day times (8 AM to 8 AM).

100

101   *2.2   ECG data extraction*

102   Consecutive RR-intervals (RR) were extracted from the single-lead 24h Holter ECG raw

103   data set using the Cardioday software (Getemed Medizintechnik, Teltow, Germany). Relative

104   RR-intervals (relRR) were calculated as a percentage of the current RR-interval N with respect

105   to the previous RR-interval N-1. Based on the conventional short-term recording standards (7),

106   intervals were grouped in segments of 5 minutes each, resulting in a total of 10,234 segments.

107   2,104 AF-HF and 2,301 CTR daytime segments (recorded between 8 AM to 10 PM) were

108   analyzed. Moreover, a full-day set, and a night set (from 10 PM to 8 AM) were analyzed to

109   check the circadian differences in performance. The full-day set comprised 5,266 segments in

110   the AF-HF group, and 4,968 segments in the CTR group, whereas the night set comprised 3,162

111   AF-HF, and 2,667 CTR segments.

112

113   *2.3   Feature extraction*

114   Fourteen features were extracted from the signals (8 from RR, and 6 from relRR series)

115   using several clinical heart rate variability (HRV), and advanced biosignal processing

116   parameters to derive information regarding the regularity, and complexity of the time series:

117   the mean RR, and mean relRR intervals ($\overline{RR}$, and $\overline{relRR}$), time between all adjacent heartbeats;

118   the standard deviation of the RR, and relRR intervals ($SDRR$, and $SDRR_{rel}$) to measure how

119   these intervals vary over time; the root mean square of successive differences between

120   heartbeats ($RMSSD_{RR}$, and $RMSSD_{relRR}$) reflecting the beat-to-beat variance in heart rate (HR)

121   (8); the deceleration capacity (DC) providing a measure of cardiac vagal modulation; the

122   deceleration reserve (DR) to measure the balance between deceleration, and acceleration

123   capacity emphasizing asymmetric growing, and decaying HR trends, and non-stationarity (9);

124   the Shannon entropy of the RR, and relRR series ($ShanEn_{RR}$, and $ShanEn_{relRR}$) to assess the

125   complexity of the signals based on information theory; the sample entropy ($SampEn_{RR}$, and

126    $SampEn_{relRR}$) measuring the complexity of the time series (8); and spectral entropy

127   ($SpecEn_{RR}$, and $SpecEn_{relRR}$) indicating the spectral complexity of these time series (10).

128   More information regarding the feature extraction methods are provided in the *Supplementary*

129   *Material*.

130

131   *2.4   Feature selection & evaluation*

132   A greedy forward selection technique was implemented to select the optimal feature set

133   out of the 14. This algorithm started with an empty feature set and added, in each iteration, the

134   feature which led to the highest classification performance increase assessed using the accuracy

135   of a decision tree classifier (see section 2.4 for details about the classifier). The algorithm

136   stopped when performance based on the validation set (subset of data utilized to tune the

137   algorithm's parameters) could not be further increased. Candidate features to be added to the

138   set were only added if the correlation coefficient with any of the already included features was

139   < 0.6. The correlation threshold was optimized looking for the best compromise between

140   redundant information, and physiological explanation.

141   Shapley calculation was implemented to analyze a posteriori the importance of the

142   features selected for classification once the model was trained (11). The Shapley calculation

143   was run 1000 times with random samples to calculate the standard deviation (SD).

144

145   *2.5   Machine-learning classification*

146   A decision tree classifier was implemented for binary classification (AF-HF vs. CTR) for

147   the daytime set. The decision tree algorithm was selected due to its simplicity and

148   explainability. The decision tree was trained, and applied using the MATLAB functions

149   *fitctree*, and *predict*, respectively.

150   The multi-feature classification was performed with the feature set selected as described

151   in section 2.4. 5-fold cross-validation was performed by randomly dividing the dataset into a

152   training set, validation set, and test set with 32, 8, and 12 patients in each set, respectively

153   (Figure 1). Training, and validation sets were recalculated at each iteration while the test set

154   was excluded, and used only once on the final classifier. The final classifier was obtained by

155   re-training it with all the data (training + validation sets). This approach allowed us not to

156   include RR series from the same patient in different sets, and not to use the test set during

157   algorithm development, thus avoiding overfitting on the data. The classes were always balanced

158   between the two groups, however for shrewdness the *Prior* model parameter in the MATLAB

159   *fitctree* function was set to *uniform*. Sensitivity, specificity, and positive predictive value (PPV)

160   were calculated considering the AF-HF group as positive, and the CTR group as negative.

161   Moreover, a decision tree single-feature classification was implemented with each

162   individual feature of the set to compare their individual classification power against that of the

163   multi-feature classifier.

164   Regarding the full-day set, and the nighttime set, we first computed classifiers using the

165   feature set extracted for the daytime set. Then, we implemented two new classifiers where the

166   feature sets were optimized for the full-day, and nighttime set by greedy selection (see Section

167   2.4), respectively.

168

169   *2.6   Statistical analysis*

170   Statistical analysis was performed using SPSS version 25.0 for macOS (IBM Corporation,

171   Armonk, New York), or GraphPad Prism version 8 for macOS (GraphPad Software, La Jolla,

172   California). Normally distributed data are expressed as mean±SD, skewed data are expressed

173   as median (interquartile range). Intergroup comparisons were performed using student's t-test,

174   or Mann-Whitney-test depending on normality.

175   Classifier performance was evaluated using accuracy (ACC), sensitivity, specificity, and

176   PPV. Accuracy was also calculated for each individual patient in the test set (ACC$_i$, with *i* as

177   test set patient ID, Table 2) by counting how many segments belonging to the same patient were

178   correctly classified with respect to their total number.

179   The comparison between the feature distributions, and AF-HF, and CTR groups was done

180   using the Wilcoxon rank sum test (one-tailed, p-values <0.05 considered significant).

181

182   **3   Results**

183   *3.1   Patient characteristics*

184   A total of 52 patients (26 with AF-HF and 26 CTR) were included in the study.

185   Descriptive data of study participants are given in Table 1. Patients with AF-HF had higher

186   NYHA stages, higher average heart rates, and were more often on ACE inhibitors and

187   aldosterone antagonists, as well as on antiarrhythmics.

188

189   *3.2   Feature selection and algorithm performance to detect atrial fibrillation-induced heart*

190   *failure*

191   Splitting the longitudinal Holter ECG data into intervals of five minutes each, and

192   selecting only segments recorded during daytime (8AM to 10 PM) resulted in a total of 4,405

193   segments (2,104 segments for AF-HF and 2,301 segments for CTR). Greedy forward selection

194   on these data led to a feature set composed of three out of the 14 features extracted in total:

195    $SpecEn_{RR}$, $\overline{relRR}$, and $RMSSD_{relRR}$. Evaluation of the relative contribution of each feature to

196   the overall classification demonstrated the highest contribution for $SpecEn_{RR}$, followed by

197    $\overline{relRR}$ and $RMSSD_{relRR}$ (Figure 2).

198   Application of the decision tree classifier with this feature set on the patients in the test

199   set (475 AF-HF, and 525 CTR 5-minute segments from six AF-HF, and six CTR patients,

200   respectively) yielded an overall accuracy to correctly assign a given 5-minute segment to AF-

201   HF or CTR of 73.5%, with a specificity of 91.4%, sensitivity of 64.7%, and PPV of 87.0%

202   (Figure 3). When applying a 50% threshold on the fraction of segments correctly classified for

203   a given patient, 10 out 12 patients (83.3%) were correctly assigned to AF-HF or CTR (6/6

204   patients in the CTR group and 4/6 in the AF-HF group; Figure 3). The accuracy achieved for

205   each individual patient in the daytime test set is given in Table 2.

206

207 *3.3 Circadian performance differences on the classification*

208   The decision tree classifiers derived from Holter recordings during daytime as described

209 above ($\overline{relRR}$, $RMSSD_{relRR}$, and $SpecEn_{RR}$) yielded an accuracy of only 56.5% when applied

210 on all available 5-minute-segments (recorded between 8 AM, and 8 AM the next day, n=2,261),

211 and 49.3% for segments recorded during nighttime (10 PM to 8 AM, n=1,261).

212   An optimized feature set for all segments (recorded between 8 AM, and 8 AM the next

213 day) based on the greedy forward selection was composed of 10 features out of the 14 extracted

214 ($ShanEn_{RR}$, $RMSSD_{relRR}$, $ShanEn_{relRR}$, $\overline{RR}$, DR, $SampEn_{RR}$, $SpecEn_{RR}$, DC, $SpecEn_{relRR}$,

215 and $SDRR$). The classifier retrained on this optimized feature set yielded an improved accuracy

216 on all segments of the test set of 60.5%, specificity, and sensitivity of 64.2%, and 57.3%,

217 respectively, and a PPV of 62.2%. With respect to the total number of segments for each patient,

218 10/12 patients (83.3%) were classified correctly (5/6 CTR patients, and 5/6 AF-HF patients,

219 table in the *Supplementary Material*).

220   Optimization for segments recorded during nighttime (10 PM to 8 AM) led to a feature

221 set that comprised four features out of the 14 extracted features (DC, $SDRR$, $SpecEn_{relRR}$, and

222 $RMSSD_{relRR}$). The classifier retrained on this optimized feature set yielded a nighttime test set

223 accuracy of 50.4%, specificity of 47.6%, sensitivity of 53.2%, and PPV of 50.7%, and 7/12

224 patients (58.3%) were classified correctly (3/6 CTR patients, and 4/6 AF-HF patients). The

225 difference in accuracy between the three different classifiers is visually shown in the

226 *Supplementary Material*, whereas an overview of the performance that the decision tree

227 classifier achieved in the different datasets using the respective feature sets is shown in Figure

228 4.

229

230   **4   Discussion**

231   The current study reports three main findings: First, patients with AF-HF differ from

232   CTR patients without heart failure with regard to heart beat entropy ($SpecEn_{RR}$) and beat-to-

233   beat variation ($\overline{relRR}$, and $RMSSD_{relRR}$) during AF. Second, incorporation of these individual

234   features in a machine learning algorithm correctly stratifies a majority of test patients to AF-

235   HF or CTR. Third, circadian analysis of algorithm performance demonstrates superior

236   discriminative properties during daytime.

237

238   *4.1   Heart rate in AF and development of LVSD – the fast and the furious?*

239   Epidemiological studies demonstrate that heart failure and atrial fibrillation predispose to

240   each other, and often co-exist (12). AF may worsen heart failure symptoms in patients with

241   various underlying cardiomyopathies such as ischemic or valvular heart disease ("AF-

242   associated" cardiomyopathy), or serve as the only causative reason for LVSD (AF-HF). The

243   pathophysiology of AF-HF is not entirely understood, and proposed mechanisms include

244   immunological alterations (13) as well as abnormalities in energy metabolism or calcium

245   handling (14).

246   Rapid ventricular heart rates during AF are often being associated with AF-HF. As such,

247   rapid atrial pacing is a common model to induce LVSD in animals, and heart rate control was

248   shown to be non-inferior to rhythm control in older heart failure trials (15). However, average

249   heart rates below 100 bpm in AF may equally lead to severe forms of AF-HF (2), demonstrating

250   that heart rate alone is likely not a suitable discriminator for AF-HF in clinical practice.

251   In the current study, we investigated various features that describe entropy, variability

252   but also beat-to-beat heart rate in patients with AF-HF. The most important features for

253   discrimination of patients with AF-HF from CTR patients were all related to entropy and

254   variability ($SpecEn_{RR}$, $RMSSD_{relRR}$, and $\overline{relRR}$), while the mean heart rate ($\overline{RR}$) did not differ

255 between groups. This finding is in line with the clinical observation that arrhythmia-induced

256 heart failure occurs not only in the context of chronic tachycardia but also with frequent

257 premature atrial or ventricular contractions (14).

258

259 *4.2   Machine-learning for patient stratification*

260 For the current study, fourteen features commonly used for the analysis of heart rate

261 variability and regularity were extracted from 5-minute RR-series segments. The 5-minute

262 intervals were chosen following the recommendation given by the European Society of

263 Cardiology and the North American Society of Pacing and Electrophysiology regarding the

264 standardization of physiological and clinical studies (7). The decision tree classifiers for binary

265 classification of AF-HF vs. CTR achieved a clinically useful specificity and positive predictive

266 value of 91.4% and 87.0%, respectively, using only three features ($SpecEn_{RR}$, $\overline{relRR}$, and

267 $RMSSD_{relRR}$). The most important contribution to the algorithm's performance was given by

268 $SpecEn_{RR}$ (Figure 2), with lower $SpecEn_{RR}$ values corresponding to decreased spectral

269 complexity (the number of frequencies of which the signal is composed) in patients with AF-

270 HF.

271 Remarkably, the abovementioned features that were automatically selected for the

272 classifier are relatively novel, and the scientific literature reporting on their application in

273 patients with AF is scarce. In this context, spectral entropy was previously shown to predict

274 outcomes in AF patients, and to discriminate between persistent, and long-standing AF (16). In

275 patients with sinus rhythm, analysis of spectral entropy was successfully used to discriminate

276 healthy patients from patients with heart failure (17). In line with our findings, heart failure in

277 this study was associated with lower a spectral entropy.

278 $\overline{relRR}$ has been proposed as a robust, simple, and reliable measure of heart rate

279 variability, aiming to overcome the shortcomings of conventional measures of HRV, with

280    $RMSSD_{relRR}$ being a direct derivative (18). $\overline{relRR}$ was successfully applied in machine learning

281   algorithms to differentiate atrial fibrillation from sinus rhythm (19). To our knowledge, the

282   current study is the first clinical evaluation of the performance of these parameters for

283   stratification of AF-induced heart failure.

284   In contrast to the good performance of the algorithm when derived from, and applied to

285   RR-intervals recorded during the day, application of the algorithm to data recorded at nighttime

286   performed significantly worse even after optimization of the feature set. It is possible that

287   influences of for example physical activity, or autonomic nervous tone, and the concentration

288   of catecholamines in serum are pronounced during the day and blunted at night, although the

289   current study does not allow to draw causative relations in this context.

290

291   **5   Future Perspective**

292   Current clinical guidelines (6) emphasize the association of heart failure, and AF both

293   during the initial diagnostic workup for new-onset AF, as well as during follow-up: they request

294   a baseline echocardiogram in patients with new-onset AF, and they recommend regular clinical

295   follow-up for the development of heart failure in patients with known AF. The algorithm

296   reported in the current study may be particularly useful for the latter part, i.e., detection of

297   LVSD in patients with AF. Due to its high specificity, and positive predictive value, it can act

298   as an indicator, and trigger for prompt clinical follow-up to detect, and manage heart failure

299   early, and potentially reduce mortality (20). In this context, the general applicability of the

300   algorithm to all kinds of 5-minute samples of RR intervals without the need for more than one

301   lead (such as data derived from pulse wave analysis, oximetry derived heart rate or single-lead

302   smart watch recordings) might enable the translation to a variety of wearables, and pocket ECG

303   monitors.

304

305 **6   Limitations**

306   The current study was restricted to the analysis of beat-to-beat intervals that were extracted

307 from a single-lead ECG. This approach is however potentially also applicable to any device

308 offering beat-to-beat annotations of the cardiac cycle, which may include widely applicable

309 devices such as e.g. photo-plethysmography in smart phones although this will require

310 additional validation.

311

312 **7   Conclusion**

313   The current work demonstrates that machine learning with the simple input of beat-to-beat

314 intervals from a single-lead ECG allows discriminating AF patients with, and without AF-

315 induced heart failure with diagnostic properties that are immediately clinically applicable.

316 Given the ever-increasing prevalence of AF, the algorithm described in this study may allow in

317 the future to identify patients who require cardiological care earlier, and render the clinical

318 follow-up more cost-effective.

319

328

329 **Ethics statement**

330   The authors designed the study, gathered and analyzed the data according to the

331   Helsinki Declaration guidelines on human research. The research protocol used in this study

332   was reviewed and approved by the institutional review board.

333

334   **Patient consent & authorship**

335   All patients provided written informed consent. All authors attest they meet the current

336   Committee on Publication Ethics (COPE) and ICMJE criteria for authorship.

337

338   **Data availability**

339   Patient-derived data and the trained classifier related to this article will be shared with

340   interested parties for non-commercial reuse on reasonable request to the corresponding authors

341   and approval from the Institutional Review Board.

342

343   **References**

344   1.   Cha Y-M, Redfield MM, Shen W-K, Gersh BJ. Atrial Fibrillation and Ventricular

345   Dysfunction. Circulation. 2004;109(23):2839–43.

346   2.   Müller-Edenborn B, Minners J, Allgeier J, Burkhardt T, Lehrmann H, Ruile P, et al.

347   Rapid improvement in left ventricular function after sinus rhythm restoration in patients

348   with idiopathic cardiomyopathy and atrial fibrillation. EP Eur. 2019;21(6):871–8.

349   Available from: https://doi.org/10.1093/europace/euz013

350   3.   Prabhu S, Taylor AJ, Costello BT, Kaye DM, McLellan AJA, Voskoboinik A, et al.

351   Catheter Ablation Versus Medical Rate Control in Atrial Fibrillation and Systolic

352   Dysfunction: The CAMERA-MRI Study. J Am Coll Cardiol. 2017;70(16):1949–61.

353   Available   from:

354   https://www.sciencedirect.com/science/article/pii/S073510971739349X

355   4.   Anselmino M, Matta M, D'Ascenzo F, Bunch TJ, Schilling RJ, Hunter RJ, et al. Catheter

356   Ablation of Atrial Fibrillation in Patients With Left Ventricular Systolic Dysfunction.

357   Circ Arrhythmia Electrophysiol. 2014;7(6):1011–8.

358   5.   Hsu L-F, Jaïs P, Sanders P, Garrigue S, Hocini M, Sacher F, et al. Catheter Ablation for

359   Atrial Fibrillation in Congestive Heart Failure. N Engl J Med. 2004;351(23):2373–83.

360   Available from: https://doi.org/10.1056/NEJMoa041018

361   6.   Hindricks G, Potpara T, Dagres N, Arbelo E, Bax JJ, Blomström-Lundqvist C, et al.

362   2020 ESC Guidelines for the diagnosis and management of atrial fibrillation developed

363   in collaboration with the European Association for Cardio-Thoracic Surgery (EACTS):

364   The Task Force for the diagnosis and management of atrial fibrillation of the Europea.

365   Eur   Heart   J.   2020;42(5):373–498.   Available   from:

366   https://doi.org/10.1093/eurheartj/ehaa612

367   7.   of the European Society of Cardiology the North American Society of Pacing

368   Electrophysiology TF. Heart Rate Variability. Circulation. 1996;93(5):1043–65.

369   8.   Shaffer F, Ginsberg JP. An Overview of Heart Rate Variability Metrics and Norms. Front

370   Public   Heal.   2017;5:258.   Available   from:

371   https://www.frontiersin.org/article/10.3389/fpubh.2017.00258

372   9.   Rivolta MW, Stampalija T, Frasch MG, Sassi R. Theoretical Value of Deceleration

373   Capacity Points to Deceleration Reserve of Fetal Heart Rate. IEEE Trans Biomed Eng.

374   2020;67(4):1176–85.

375   10.   Staniczenko PPA, Lee CF, Jones NS. Rapidly detecting disorder in rhythmic biological

376   signals: A spectral entropy measure to identify cardiac arrhythmias. Phys Rev E. 2009

377   Jan;79(1):11915. Available from: https://link.aps.org/doi/10.1103/PhysRevE.79.011915

378   11.   Shapley LS. A value for n-person games. In: Roth AEE, editor. The Shapley Value:

379   Essays in Honor of Lloyd S Shapley. Cambridge University Press; 1988. p. 31–40.

380   12.   Santhanakrishnan R, Wang N, Larson MG, Magnani JW, McManus DD, Lubitz SA, et
381   al. Atrial Fibrillation Begets Heart Failure and Vice Versa. Circulation.
382   2016;133(5):484–92.

383   13.   Mueller KAL, Heinzmann D, Klingel K, Fallier-Becker P, Kandolf R, Kilias A, et al.
384   Histopathological and Immunological Characteristics of Tachycardia-Induced
385   Cardiomyopathy. J Am Coll Cardiol. 2017;69(17):2160–72. Available from:
386   https://www.sciencedirect.com/science/article/pii/S0735109717359740

387   14.   Martin CA, Lambiase PD. Pathophysiology, diagnosis and treatment of
388   tachycardiomyopathy. Heart. 2017;103(19):1543–52. Available from:
389   https://heart.bmj.com/content/103/19/1543

390   15.   Roy D, Talajic M, Nattel S, Wyse DG, Dorian P, Lee KL, et al. Rhythm Control versus
391   Rate Control for Atrial Fibrillation and Heart Failure. N Engl J Med.
392   2008;358(25):2667–77. Available from: https://doi.org/10.1056/NEJMoa0708789

393   16.   Uldry L, Van Zaen J, Prudat Y, Kappenberger L, Vesin J-M. Measures of spatiotemporal
394   organization differentiate persistent from long-standing atrial fibrillation. EP Eur.
395   2012;14(8):1125–31. Available from: https://doi.org/10.1093/europace/eur436

396   17.   Pandian P, Srinivasa MG. Application of Entropy Techniques in Analyzing Heart Rate
397   Variability using ECG Signals. Int J Recent Innov Trends Comput Commun. 2019;7:9–
398   16.

399   18.   Vollmer M. A robust, simple and reliable measure of heart rate variability using relative
400   RR intervals. In: 2015 Computing in Cardiology Conference (CinC). 2015. p. 609–12.

401   19.   Vollmer M. Arrhythmia classification in long-term data using relative RR intervals. In:
402   2017 Computing in Cardiology (CinC). 2017. p. 1–4.

403   20.   Greene SJ, Butler J, Albert NM, DeVore AD, Sharma PP, Duffy CI, et al. Medical
404   Therapy for Heart Failure With Reduced Ejection Fraction. J Am Coll Cardiol.

405   2018;72(4):351–66.

406

407   **Tables**

408   Table 1: Descriptive patient characteristics

	All n=52	**AF-HF** n=26	**CTR** n=26	p-value
Age (years)	68.3 (11.7)	70.48 (11.83)	66.3 (11.54)	0.204
Male sex	26 (50)	18 (69.2)	17 (65.5)	1.000
BMI (kg/m²)	29.1 (4.9)	29.59 (5.84)	28.74 (4.03)	0.416
Systolic blood pressure (mmHg)	135.7 (21.1)	132.4 (22.66)	139 (19.25)	0.264
Diastolic blood pressure (mmHg)	87.42 (13.1)	85.81 (13.77)	89.04 (12.49)	0.380
NYHA stages				<0.001
NYHA I	8 (15)	1 (3.8)	7 (26.9)	
NYHA II	10 (19)	2 (7.7)	8 (30.8)	
NYHA III	19 (36.5)	9 (34.6)	10 (38.5)	
NYHA IV	15 (28.8)	14 (53.8)	1 (3.8)	
Diabetes	7 (13.5)	0 (0)	7 (26.9)	0.01
Hypertension	35 (67)	17 (65.4)	18 (69.2)	1.000
Hyperlipidemia	26 (50)	12 (46.2)	14 (53.8)	0.782
Medications				
ß Blocker	37 (71)	19 (73.1)	18 (69.2)	1.000
ACE Inhibitors	22 (42.3)	16 (61.5)	6 (23.1)	0.011
ATRA	10 (19.2)	4 (84.6)	6 (76.9)	0.726
Aldosteron	14 (26.9)	12 (46.2)	2 (7.7)	0.004
Diuretics	21 (40.4)	13 (50)	8 (30.8)	0.160
Digoxin	2 (3.8)	0 (0)	2 (7.7)	0.490
Antiarrhythmics (class 1c and class 3 cumulative)	19 (36.5)	16 (61.5)	3 (11.5)	<0.001
Echocardiography				
LVEF	44.8 (15.9)	29.25 (6.78)	59.15 (2.64)	<0.001
LVESD (mm)	39 (9.9)	45.67 (8.78)	31.9 (4.75)	0.004
LVEDD (mm)	52 (7.0)	55.48 (7.80)	49.92 (5.03)	<0.001
LAD (mm)	45 (6.4)	48.54 (4.86)	42.38 (6.4)	<0.001
LAV (mm)	96.4 (27.4)	106.84 (18.13)	75.6 (31.17)	0.002
LAVI (ml/kg/BW)	49 (9.6)	51.94 (7.35)	42.38 (11.47)	0.017

409   Body mass index (BMI), New York Heart Association (NYHA), angiotensin converting enzyme (ACE),
410   all-trans retinoic acid (ATRA), left ventricular ejection fraction (LVEF), left ventricular end-systolic
411   diameter (LVESD), left ventricular end-diastolic diameter (LVEDD), left atrial diameter (LAD), left
412   atrial volume (LAV), left atrial volume index (LAVI). Values are given as mean (± standard deviation)
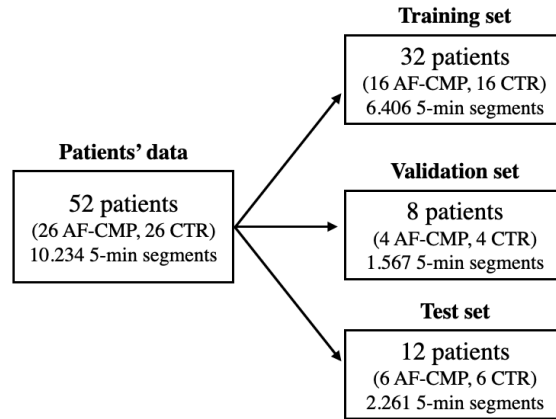413   or number (%).
414
415
416
417
418
419
420
421

422
423
424
425

Table 2: Number of segments and accuracy for each individual patient in the test set (%) for the daytime dataset. Patients who were correctly classified over all segments (ACC_P_i > 50%) are highlighted in green. Patients who got misclassified over all segments (ACC_P_i < 50%) are highlighted in red.

Test set patient ID	No. of segments	Class	ACC_P_i
1	72	AF-HF	76.19
2	77	AF-HF	56.10
3	85	AF-HF	57.14
4	64	AF-HF	81.43
5	78	AF-HF	43.80
6	99	AF-HF	17.81
7	85	CTR	85.39
8	88	CTR	92.13
9	112	CTR	96.34
10	78	CTR	97.06
11	96	CTR	93.59
12	66	CTR	85.19

426

427   **Figures**

428

Patients' data

52 patients
(26 AF-CMP, 26 CTR)
10.234 5-min segments

Training set

32 patients
(16 AF-CMP, 16 CTR)
6.406 5-min segments

Validation set

8 patients
(4 AF-CMP, 4 CTR)
1.567 5-min segments

Test set

12 patients
(6 AF-CMP, 6 CTR)
2.261 5-min segments

429

430   Figure 1: Flow chart showing the dataset division of the 52 patients' signals into training, validation,
431   and test sets, respectively. The number of all 5-min segments acquired from the patients is reported as
432   well.

Shapley values

$SpecEn_{RR}$

$\overline{relRR}$

$RMSSD_{relRR}$

Feature value contribution
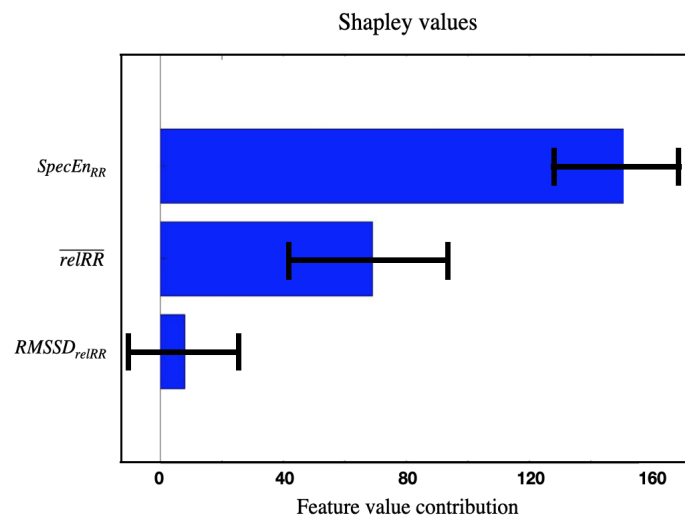
433

434   Figure 2: Shapley feature importance calculation on the three features selected for the daytime binary
435   classification AF- HF vs. CTR. The Shapley calculation was run 1000 times with random samples to
436   calculate the SD (error bars in the plot).

437

438

439
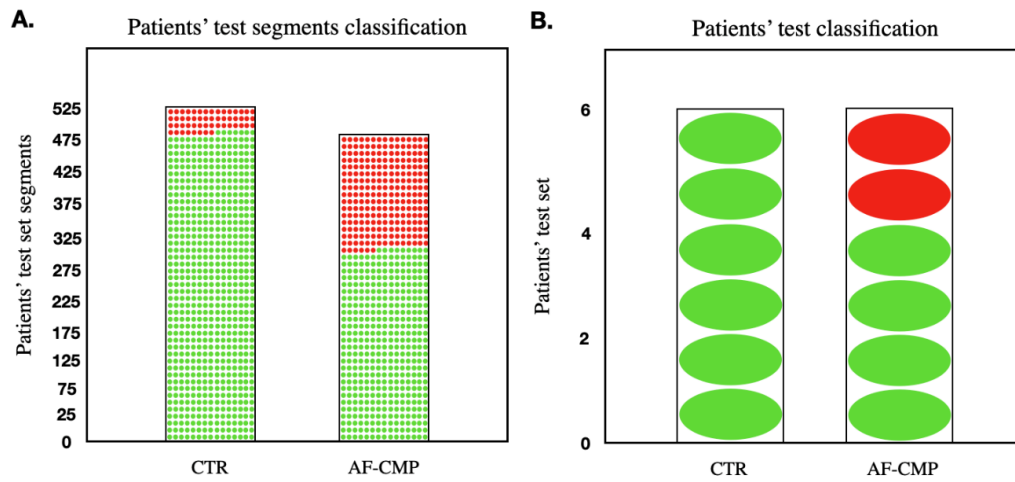
Figure 3: A. Visual representation of the number of segments in the test set that were correctly classified for both CTR and AF-HF groups (91.4%, and 64.7% of the segments correctly classified for each group, respectively). B. Visual representation of the number of individual patients in the test set that were correctly classified for both CTR and AF-HF groups (100%, and 83.3% of the patients correctly classified for each group, respectively). The red dots represent segments/patients misclassified; the green dots represent segments/patients correctly classified.

440

441
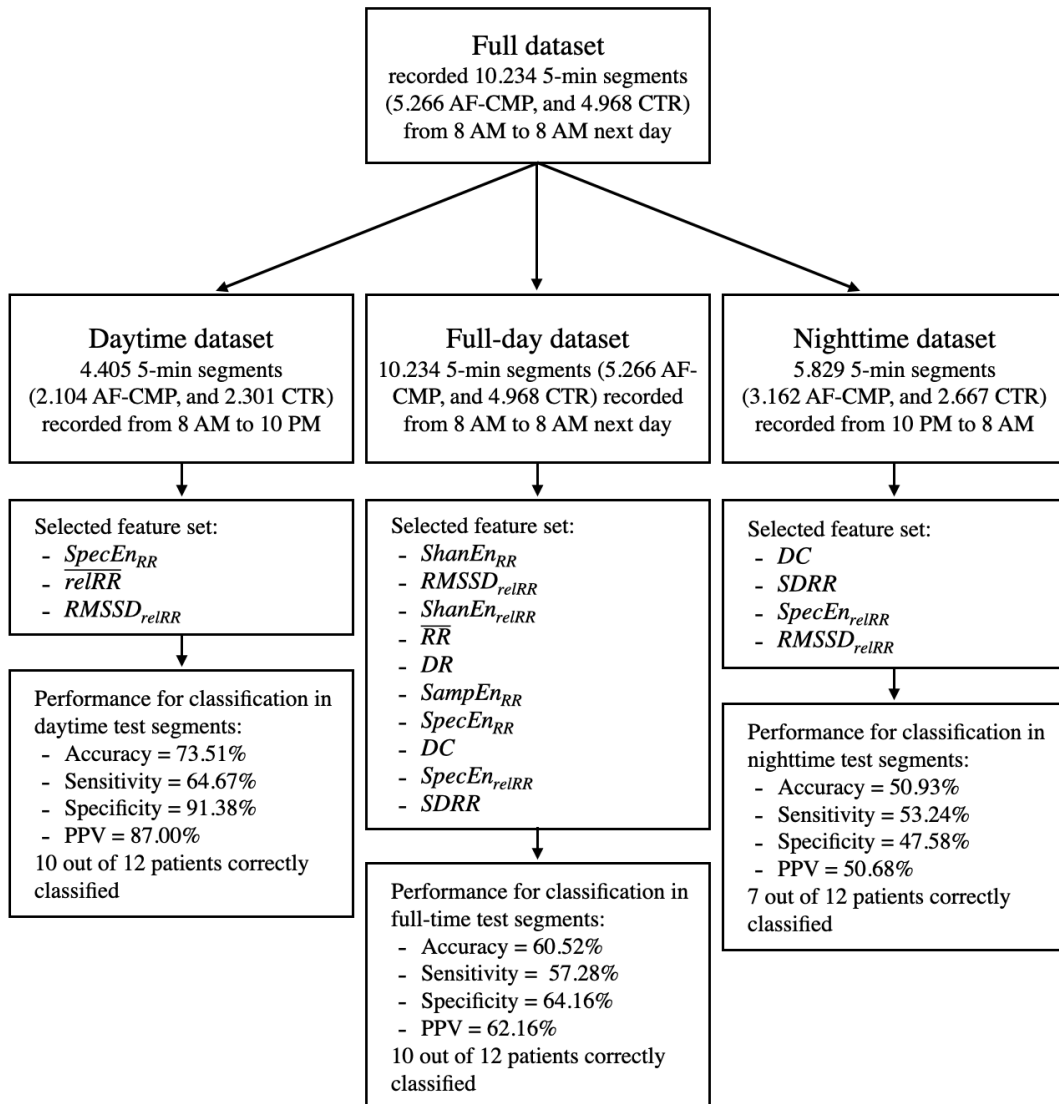
442   Figure 4: Overview of the decision tree classifier performance on the optimal feature sets selected
443   from the different datasets utilized in this work.

Summary, outlook, and conclusion

In this thesis, two major studies were presented. In both, simulated electrocardiogram (ECG) signals were computed to extend a clinical dataset, or substitute it, for the implementation of novel methods applicable in clinical practice. These methods enabled the extraction of information related to atrial flutter (AFlut) and atrial fibrillation (AFib) activities. The underlying algorithms, and the results obtained by using them, were discussed and compared to existing approaches in detail in Chapter 4 and 5. In the first presented project, two new recurrence quantification analysis (RQA) methods have been implemented to derive useful features for discriminating different AFlut mechanisms: individual component RQA, and spatial reduced RQA. These two methods were implemented and tuned on simulated data and tested on clinical data. The results obtained showed that some of the RQA features have the potential to discriminate between AFlut mechanisms. In particular, the focal source mechanisms showed to be significantly deterministic and laminar in contrast to microreentries. The first three principal components derived from the 12-lead ECG demonstrated the presence of relevant small or major changes in the dynamic structure of these AFlut phenomena. The proof of concept of the methods on simulated data also matched the clinical data results [22]. However, a thorough analysis of the influence of the atrial and torso geometries used for the simulations needed to be performed, thus to avoid the algorithm's failure on clinical data due to overfitting to simulated data. Poor performance in analyzing the influence of atrial models (classification accuracy of 59.8% with leave-one-atrium-out approach) demonstrated how fundamental it is to build in silico studies on a large number of atrial geometries in order to produce a faithful representation of atrial ECG variability as the one seen in clinical practice. In contrast, high performance achieved for the torso models' influence analysis (classification accuracy of 89.0% with leave-one-torso-out approach) showed that a large number of torso models is not necessarily required in the simulation framework. The torso models do not have a significant influence on the resulting ECG during AFlut in contrast to atrial models, indeed [23]. Considering the findings obtained from the previous two studies, the final AFlut study was then conducted. A machine learning algorithm capable of discriminating three

different macro categories of AFlut has been implemented (cavotricuspid isthmus-dependent, peri-mitral, and other left atrium AFlut mechanisms). New simulations were performed using a large number of atrial geometries (100). In addition, the classifier was trained using a hybrid approach (simulated plus clinical data). Thus, overfitting on the simulated data and on the atrial geometries used was drastically reduced. The final accuracy of 82.2% obtained on a small clinical database demonstrated how this approach is capable of identifying the location of AFlut mechanisms relying only on non-invasive signals (i.e., 12-lead ECG) [24]. The final results obtained from the latter two works also confirmed that F-wave duration is a key feature for AFlut discrimination.

In the second project, the identification of the AFib drivers located near the pulmonary veins (PVs) has been performed using the 12-lead ECGs. An automated learning algorithm trained only on in silico ECGs was successful in the underlying discrimination on a clinical dataset yielding a test set specificity of 82.6%, and sensitivity of 73.9%. Moreover, 93.5% of the predictions matched between two different sets of ECG segments extracted from the same patient for a consistency analysis. The successful use of computational simulations in support of clinical data, or in total replacement of them, proved the true potential of simulations in clinical practice. Moreover, analysis of the success of some common ablation procedures (i.e., PV isolation (PVI), roof line, and mitral isthmus ablation) to terminate AFib conferred more value to the implemented classification. 100% of PVI ablations on AFib drivers located near PVs resulted in acute termination of the arrhythmia. In contrast, the combination of all three ablation procedures almost never terminated the arrhythmia for AFib drivers located in other areas than the PVs (12.5% of the cases). Thus, the algorithm, besides localizing the location of the AFib drivers, can also predict the acute success of PVI in terminating the arrhythmia [25]. Another key, but still unresolved, issue with AFib is its link to some even more serious cardiovascular diseases such as heart failure, and cardiomyopathy, which led us to the last study in this thesis. A decision tree classifier using RR-interval series extracted from 1-lead ECG Holter signals showed that there are patterns allowing the discrimination of AFib cases inducing heart failure in respect to AFib cases without this induction (classification accuracy, and specificity of 73.5%, and 91.4%, respectively). In AFib-induced heart failure cases predicted by the algorithm, the physicians are advised to proceed with cardiological care as soon as possible (e.g., applying cardioversion) to reduce the risk of such complication [26]. The implemented algorithm is currently under patenting process.

Future projects could be developed from this thesis and its limitations. Recurring themes in almost all the works presented in this thesis are the synergy between machine learning and computer simulations. Both aspects hold great potential for future development. Simulated 12-lead ECG signals were used in 4 out of 5 studies described in this thesis [22–25]. These in silico ECGs were composed by only P-waves (F-wave and f-wave for AFlut and AFib, respectively). The QRS-T complexes were missing due to the absence of the ventricles in the implemented simulations. Each algorithm was tested on clinical data for providing a proof of their effectiveness and clinical applicability. However, the use of ventricles and therefore the

creation of an ECG covering one full heartcycle would make the pre-processing of clinical data easier, being able to directly use the raw signals for feature extraction. In addition, other relevant information could be extracted from QRS-T complexes.

The simulations produced in this thesis were generated from a limited number of atrial and torso geometries. Initially, for modeling reasons: Our institute was provided of a limited number of anatomical models due to the complexity and time these models require to be developed. Then, after the creation of an atrial statistical shape model [115], time constraints limited the implementation of a bigger cohort of data. In the future, new simulations are expected to be generated from an increasing number of atrial and thoracic geometries derived from their respective shape models, so that an increasingly large and variable dataset of AFlut/AFib scenarios can be created. The anisotropy ratios is another parameter that could be additionally modified to increase size of the datasets. Moreover, concerning both AFlut and AFib scenarios, different types of mechanisms could be included in the work. Regarding AFlut, other mechanisms besides the 20 that were implemented in the studies presented in this thesis could be added, following the clinical prevalence indications and statistics. As well, stable long-standing rotors and focal sources have been simulated for AFib, therefore other drivers such as multi-wavelet reentry [126, 127], meandering rotors [128], or intramural reentry [129] could be included in the analysis.

In general, the problem of lack of properly labeled clinical data, and thus without verified ground truth, is the biggest issue in signal processing and machine learning applied to biomedical engineering. For this reason, more detailed data acquisition protocols should be planned. Any signal acquisition in conjunction with an invasive cardiac activity mapping system should be succeeded by accurate labeling by the physicians.

Feature-based machine learning methods were used in this thesis. Convolutional neural networks (CNNs) are becoming more and more popular in ECG processing, e.g., for arrhythmia classification [130]. The obtained results often outperform classical approaches. The classification of several AFlut mechanisms using CNN on body surface potential (BSPM) map videos was tested during Linder's master thesis (see section 6) performed in the course of this project. Although the results were not superior to the performance obtained with the algorithms described in this thesis, new future tests with deep learning approaches and ECG or BSPM could be implemented.

Discrimination of AFlut, and AFib drivers could be implemented with finer localization. Regarding AFlut more classes to discriminate could be tested. Regarding AFib, other AF driver areas could be differentiated instead of a general extra-PV AFib driver class (e.g., left atrial appendage area). In addition, a discrimination of which AFib driver was localized (whether a rotor, or a focal source) could be implemented (preliminary analyses in this regard have been investigated in Bernhart's and Nitzke's bachelor's theses during this project - see section 6).

In a follow-up study of the AFib drivers localization, the predictive power of the classifier should be tested regarding long-term recurrence of AFib after PVI (PVI outcome).

The general aims of this thesis were to support and accelerate diagnosis and therapy planning to improve the patient outcome by using knowledge from real data and simulations. In this thesis, important aspects of human atrial patho-electrophysiology have been investigated using computational models and clinical data. This work investigated the ECG signals on the body surface. The studies presented in this thesis advanced the state of the art in machine learning using in silico and clinical data of atrial patho-electrophysiology in several aspects. Novel methods to extract features from the signals, to quantify the influence of the models on the ECGs, to discriminate the location of the arrhythmia driving mechanisms, to predict the risk of AFib complication, and to foresee the success of ablation/cardioversion therapy to terminate the arrhythmia were presented. Summing up, this thesis presents methods paving the way to tailor AFib and AFlut therapy. By translating the methods and insights into clinical practice, appropriate and more efficient therapy can be applied in a shorter time. In this way, the socio-economical costs of AFib/AFlut, the individual patient's burden, and the invasive procedure time to terminate the arrhythmia can be reduced eventually, whereas better planning of the therapies, and a personalized treatment might improve the patient's outcome.

Appendix

A.1 Supplementary Materials

Non-Invasive Characterization of Atrial Flutter Mechanisms Using Recurrence Quantification Analysis on the ECG: a Computational Study Supplementary Materials

Giorgio Luongo*, *Member, IEEE,* Steffen Schuler, *Member, IEEE,* Armin Luik, Tiago P. Almeida, *Member, IEEE,* Diogo C. Soriano, Olaf Dössel, *Senior Member, IEEE* and Axel Loewe, *Member, IEEE,*
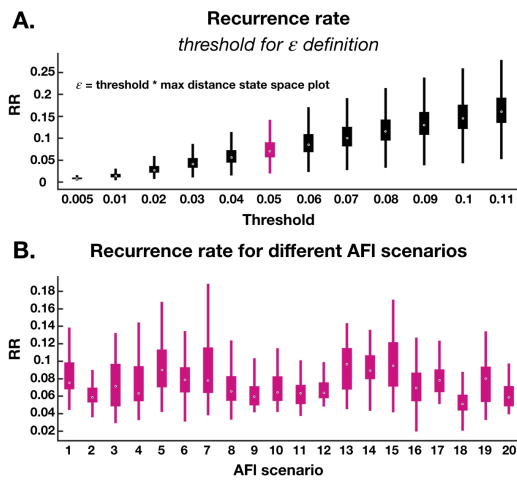
Fig. S1. Definition of ε for icRQA on PCS 1. A. RR for varying choices of ε. B. Different scenarios' RR with the selected threshold of 0.05 as highlighted in A. The threshold highlighted in A is the selected value. It is the value with the best compromise between: the resulting RR - not too high compared to the recommended 1%; the portion of maximum phase space diameter - not exceed 10%; and the discrimination between the 20 AFl scenarios shown in B and in Table S1.
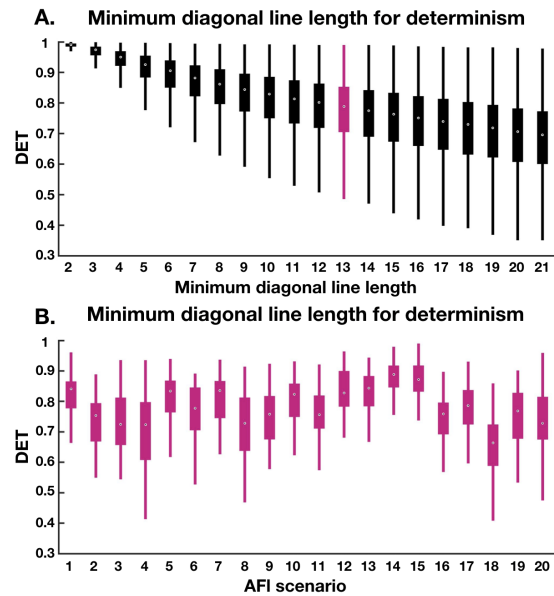
Fig. S2. Definition of the minimum diagonal line length for icRQA determinism on PCS 1. A. DET for varying choices of minimum diagonal line length. B. Different scenarios' DET with the selected minimum diagonal line length of 13, as highlighted in A. The minimum diagonal line length highlighted in A is the selected one. It is the value with the best compromise between: the resulting values - not too high to avoid undesirable saturation behavior; and the discrimination between the 20 AFl scenarios shown in B and in Table S2.

TABLE S1

AUCROC FOR THE DISCRIMINATION BETWEEN 20 AFL SCENARIOS CONSIDERING icRQA-RR AS DISCRIMINATOR (MEAN±SD)

% of max phase space distance	1%	2%	3%	4%	5%	6%	7%	8%	9%	10%
PCS1	0.609±0.068	0.606±0.071	0.607±0.071	0.608±0.069	**0.609±0.067**	0.609±0.066	0.610±0.065	0.609±0.064	0.608±0.063	0.605±0.062
PCS2	0.615±0.091	0.613±0.096	0.611±0.094	0.610±0.090	**0.668±0.102**	0.664±0.097	0.660±0.092	0.658±0.089	0.655±0.086	0.653±0.083
PCS3	0.660±0.123	0.659±0.119	0.659±0.117	0.658±0.116	**0.658±0.114**	0.656±0.112	0.655±0.111	0.653±0.110	0.652±0.109	0.650±0.108

TABLE S2

AUCROC FOR THE DISCRIMINATION BETWEEN 20 AFL SCENARIOS CONSIDERING icRQA-DET AND icRQA-LAM AS DISCRIMINATOR (MEAN±SD)

Min line length	7	8	9	10	PCS 1 11	12	13	14	15	16
DET	0.622±0.076	0.622±0.076	0.623±0.078	0.624±0.080	0.625±0.081	0.623±0.082	**0.624±0.083**	0.622±0.084	0.621±0.085	0.620±0.085
LAM	0.658±0.101	0.662±0.105	0.665±0.106	**0.667±0.106**	0.665±0.107	0.664±0.107	0.663±0.107	0.661±0.106	0.659±0.106	0.655±0.108
Min line length	7	8	9	10	PCS 2 11	12	13	14	15	16
DET	0.617±0.104	0.619±0.106	0.620±0.106	0.620±0.107	0.622±0.107	0.622±0.106	0.624±0.106	0.624±0.106	0.624±0.107	**0.625±0.107**
LAM	0.646±0.121	0.652±0.121	0.654±0.121	0.656±0.121	**0.657±0.123**	0.658±0.124	0.659±0.125	0.659±0.125	0.660±0.126	0.660±0.124
Min line length	7	8	9	10	PCS 3 11	12	13	14	15	16
DET	0.646±0.122	0.647±0.120	0.649±0.119	0.650±0.117	0.651±0.115	0.651±0.113	**0.652±0.112**	0.651±0.111	0.651±0.111	0.649±0.111
LAM	0.663±0.139	**0.666±0.140**	0.668±0.141	0.670±0.140	0.674±0.140	0.676±0.140	0.680±0.139	0.686±0.139	0.694±0.137	0.698±0.136

TABLE S3

AUCROC FOR THE DISCRIMINATION BETWEEN 20 AFL SCENARIOS CONSIDERING srRQA-RR AS DISCRIMINATOR (MEAN±SD)

% of max phase space distance	1%	2%	3%	4%	5%	6%	7%	8%	9%	10%
2 dim	0.599±0.080	0.599±0.080	0.599±0.081	0.600±0.083	0.601±0.080	0.601±0.080	0.602±0.082	0.603±0.083	0.604±0.080	0.605±0.081
3 dim	0.622±0.086	0.624±0.087	0.625±0.086	0.626±0.086	**0.627±0.086**	0.627±0085	0.627±0.086	0.627±0.087	0.627±0.086	0.627±0.086
4 dim	0.621±0.088	0.624±0.087	0.625±0.087	0.625±0.087	0.626±0.086	0.627±0.086	0.627±0.085	0.628±0.085	0.628±0.085	0.627±0.085
5 dim	0.620±0.088	0.622±0.087	0.624±0.087	0.625±0.086	0.626±0.086	0.627±0.085	0.628±0.085	0628.±0.085	0.627±0.084	0.627±0.084

TABLE S4

AUCROC FOR THE DISCRIMINATION BETWEEN 20 AFL SCENARIOS CONSIDERING srRQA-DET AND srRQA-LAM AS DISCRIMINATOR(MEAN±SD)

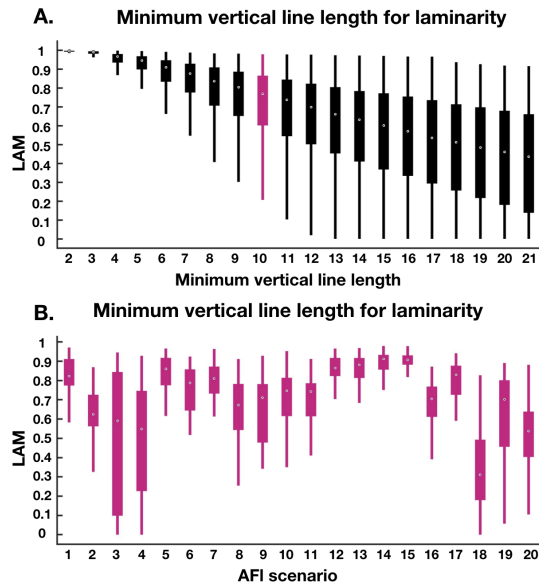| Min line length	2	3	4	5	6	7	8	9	10
DET	0.637±0.106	0.635±0.104	0.638±0.107	0.639±0.110	**0.640±0.109**	0.638±0.111	0.639±0.111	0.639±0.109	0.640±0.106
LAM	0.614±0.096	0.624±0.107	0.626±0.104	0.629±0.107	0.631±0.106	**0.631±0.107**	0.630±0.105	0.628±0.104	0.628±0.103

Fig. S3. Definition of the minimum vertical line length for icRQA laminarity on PCS 1. A. LAM for varying choices of minimum vertical line length. B. Different scenarios' LAM with the selected minimum vertical line length of 10, as highlighted in A. The minimum vertical line length highlighted in A is the selected one. It is the value with the best compromise between: the resulting values - not too high to avoid undesirable saturation behavior; and the discrimination between the 20 AFl scenarios shown in B and in Table S2.
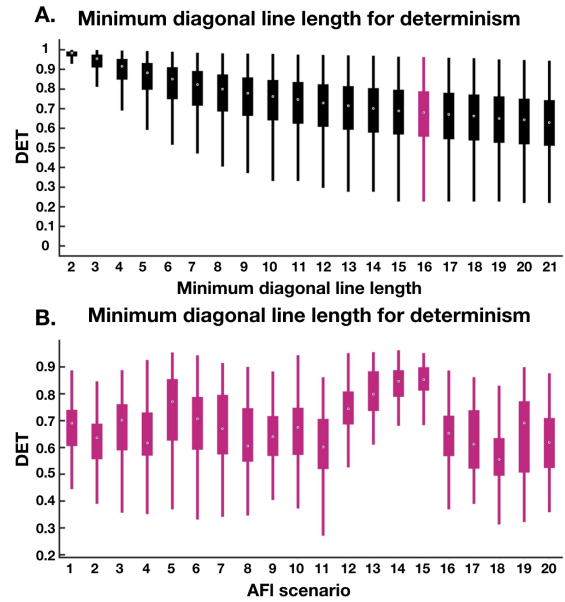
Fig. S5. Definition of the minimum diagonal line length for icRQA determinism on PCS 2. A. DET for varying choices of minimum diagonal line length. B. Different scenarios' DET with the selected minimum diagonal line length of 16 as highlighted on A. The minimum diagonal line length highlighted in A is the selected one. It is the value with the best compromise between: the resulting values - not too high to avoid undesirable saturation behavior; and the discrimination between the 20 AFl scenarios shown in B and in Table S2.
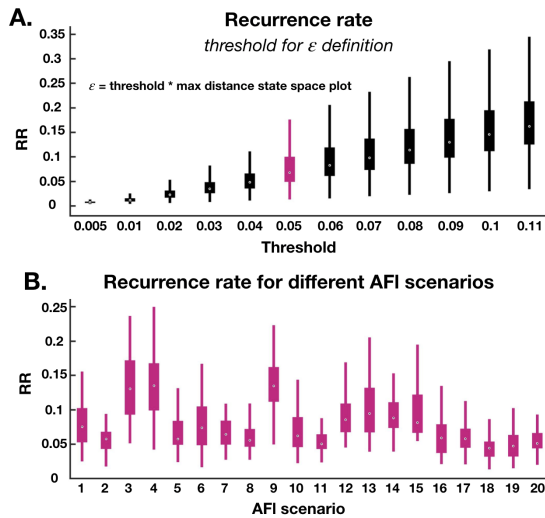
Fig. S4. Definition of ε for icRQA on PCS 2. A. RR for varying choices of ε. B. Different scenarios' RR with the selected threshold of 0.05 as highlighted on A. The threshold highlighted in A is the selected value. It is the value with the best compromise between: the resulting RR - not too high compared to the recommended 1%; the portion of maximum phase space diameter - not exceed 10%; and the discrimination between the 20 AFl scenarios shown in B and in Table S1.
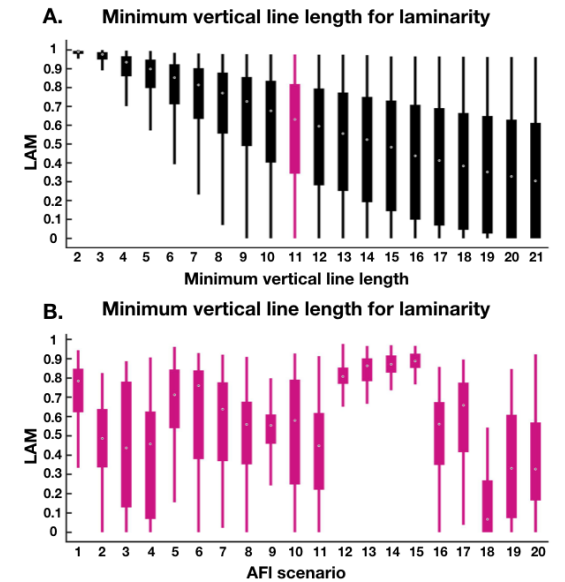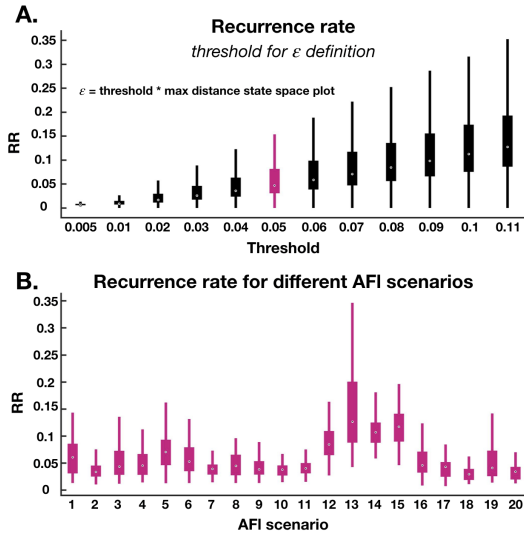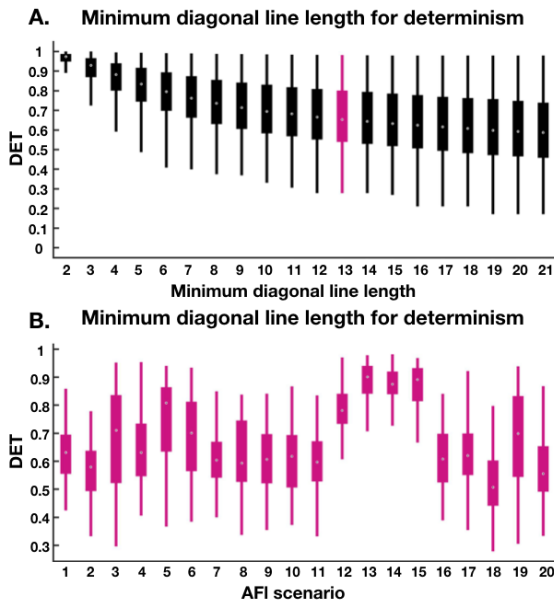

Fig. S6. Definition of the minimum vertical line length for icRQA laminarity on PCS 2. A. LAM for varying choices of minimum vertical line length. B. Different scenarios' LAM with the selected minimum vertical line length of 11 as highlighted on A. The minimum vertical line length highlighted in A is the selected one. It is the value with the best compromise between: the resulting values - not too high to avoid undesirable saturation behavior; and the discrimination between the 20 AFl scenarios shown in B and in Table S2.

A.

Recurrence rate

threshold for ε definition

ε = threshold * max distance state space plot

B.

Recurrence rate for different AFl scenarios

Fig. S7. Definition of ε for icRQA on PCS 3. A. RR for varying choices of ε. B. Different scenarios' RR with the selected threshold of 0.05 as highlighted on A. The threshold highlighted in A is the selected value. It is the value with the best compromise between: the resulting RR - not too high compared to the recommended 1%; the portion of maximum phase space diameter - not exceed 10%; and the discrimination between the 20 AFl scenarios shown in B and in Table S1.

A. **Minimum diagonal line length for determinism**

B. **Minimum diagonal line length for determinism**

Fig. S8. Definition of the minimum diagonal line length for icRQA determinism on PCS 3. A. DET for varying choices of minimum diagonal line length. B. Different scenarios' DET with the selected minimum diagonal line length of 13 as highlighted on A. The minimum diagonal line length highlighted in A is the selected one. It is the value with the best compromise between: the resulting values - not too high to avoid undesirable saturation behavior; and the discrimination between the 20 AFl scenarios shown in B and in Table S2.

A. **Minimum vertical line length for laminarity**

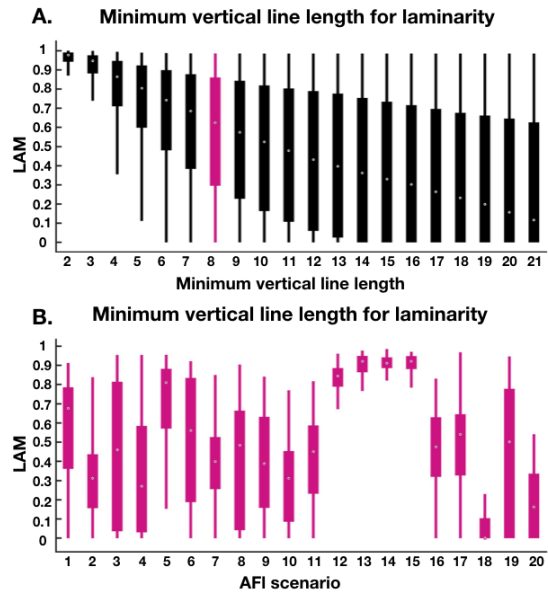**B.** **Minimum vertical line length for laminarity**

Fig. S9. Definition of the minimum vertical line length for icRQA laminarity on PCS 3. A. LAM for varying choices of minimum vertical line length. B. Different scenarios' LAM with the selected minimum vertical line length of 8 as highlighted on A. The minimum vertical line length highlighted in A is the selected one. It is the value with the best compromise between: the resulting values - not too high to avoid undesirable saturation behavior; and the discrimination between the 20 AFl scenarios shown in B and in Table S2.
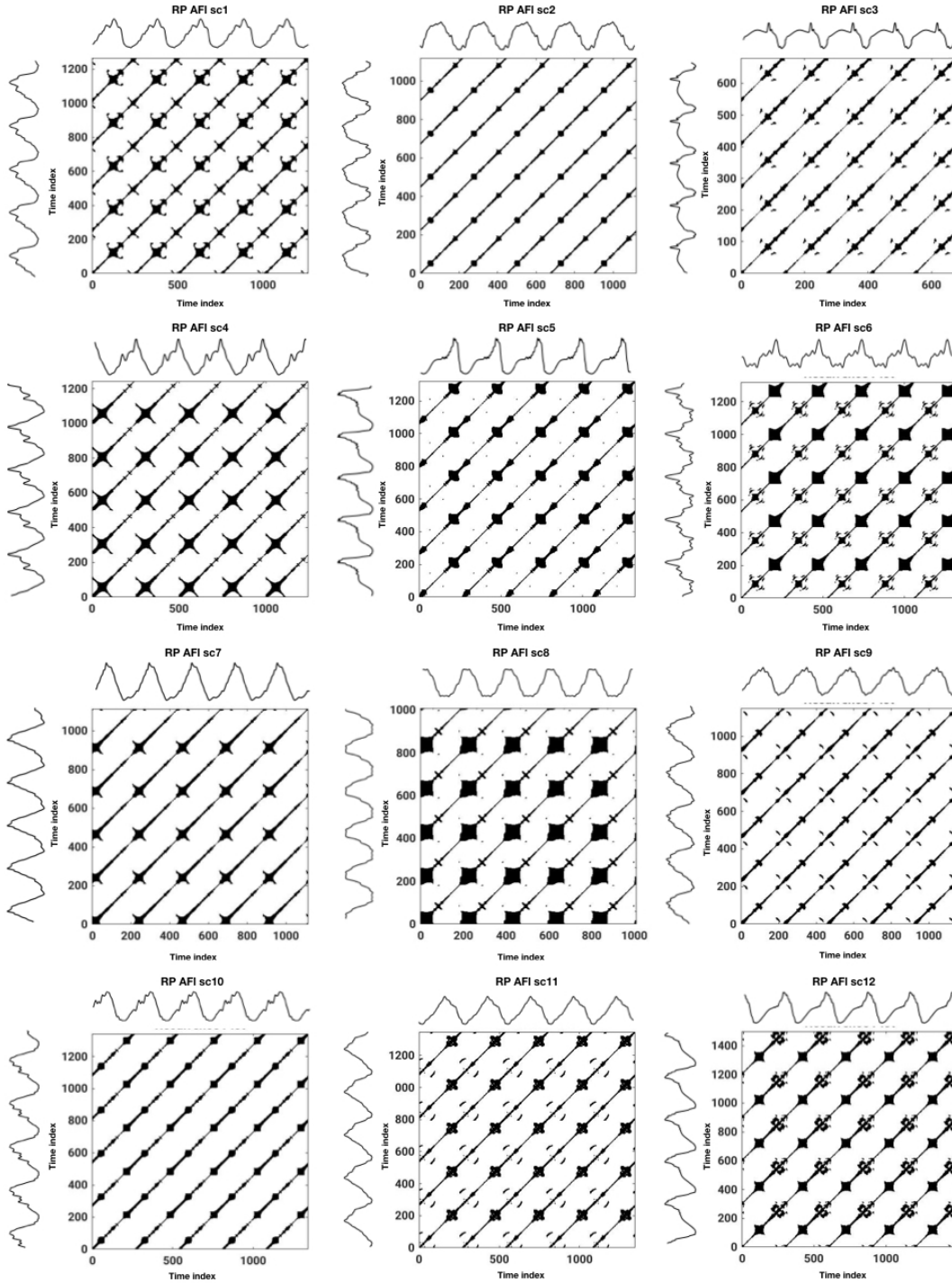
Fig. S10. The effect of different AFl scenarios in the icRQA. The RPs created for the PCS 1 calculated from the 12-lead ECGs extracted from the same atria and torso combination for the all AFl mechanisms - from sc1 to sc12.
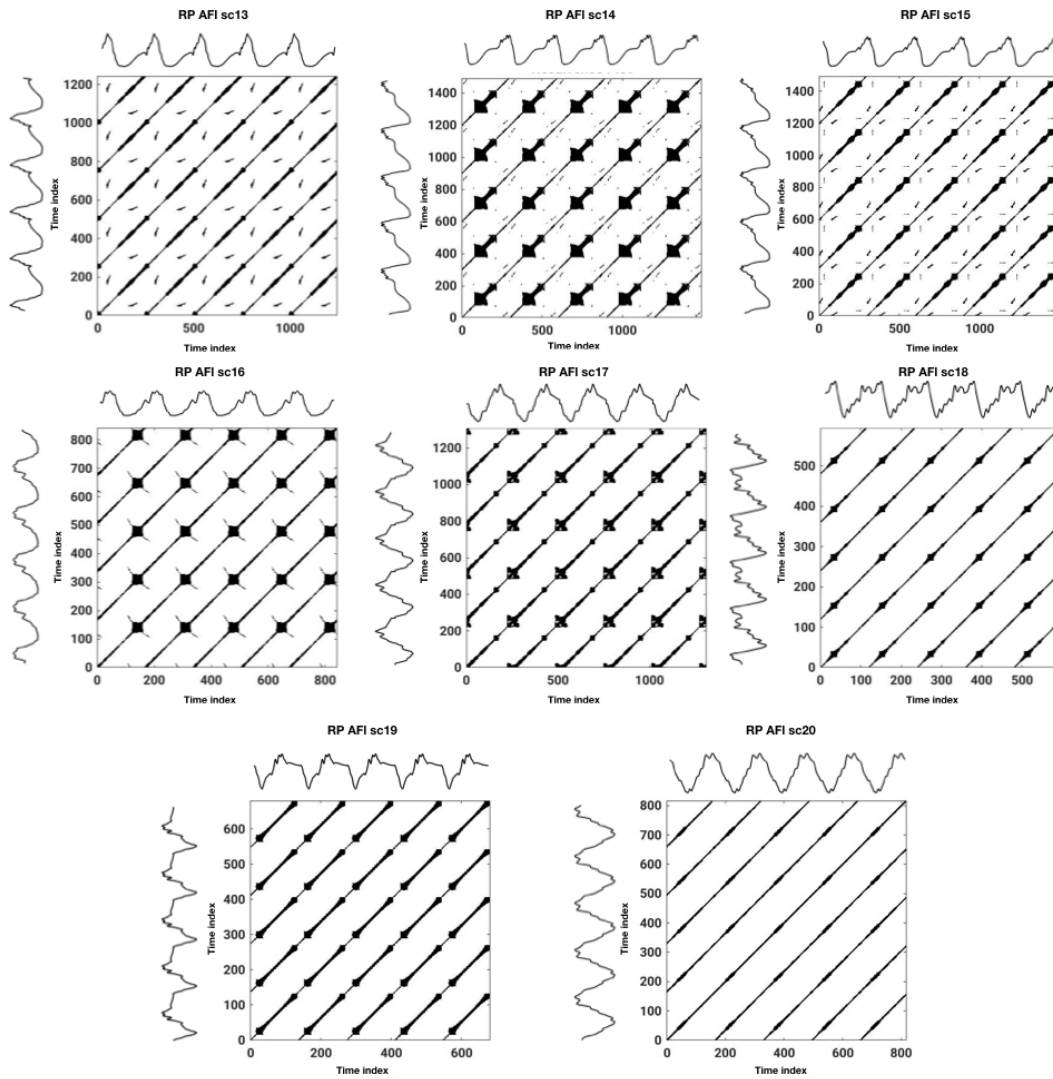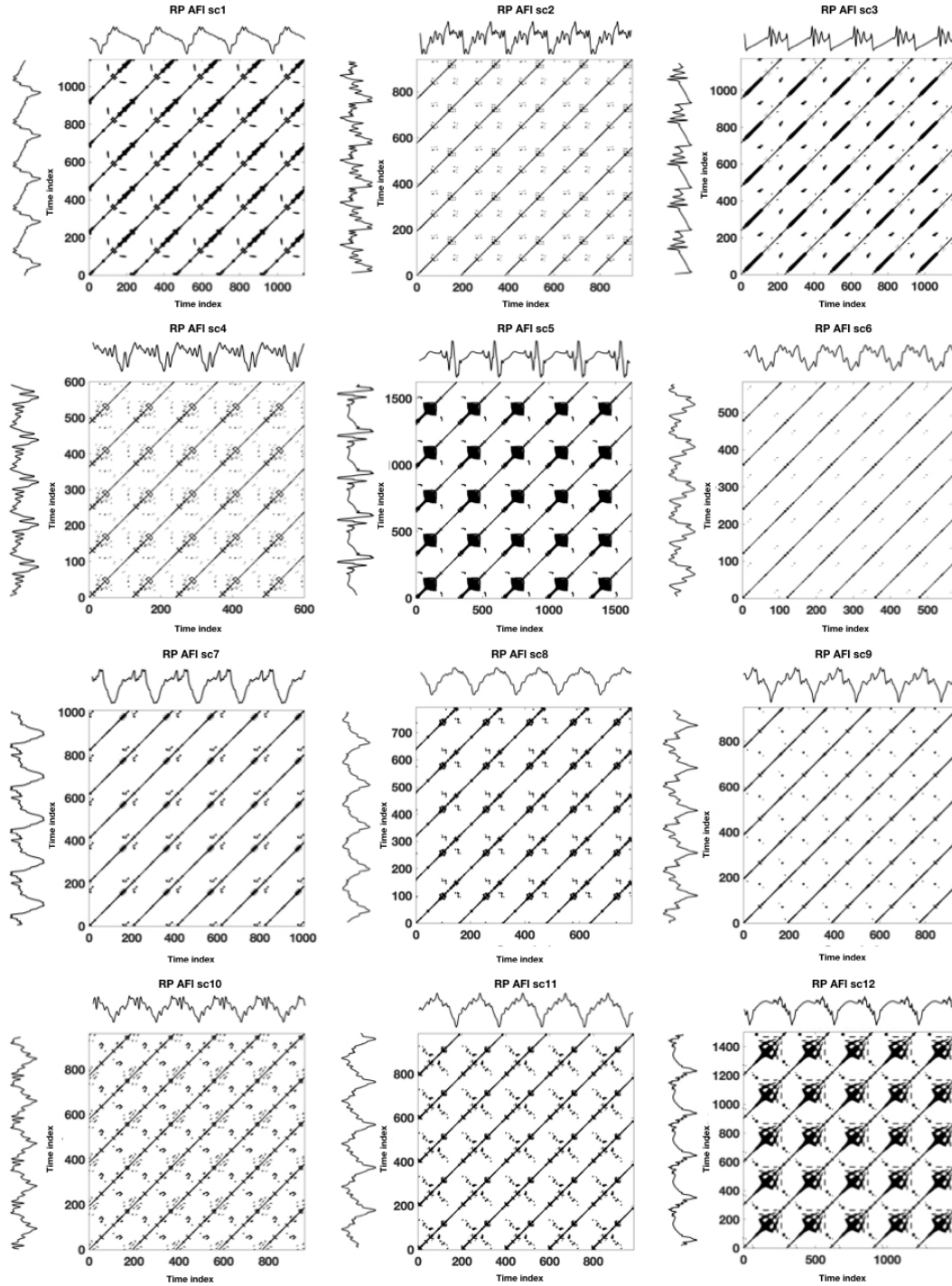
Fig. S11. The effect of different AFl scenarios in the icRQA. The RPs created for the PCS 1 calculated from the 12-lead ECGs extracted from the same atria and torso combination for the all AFl mechanisms - from sc13 to sc20.
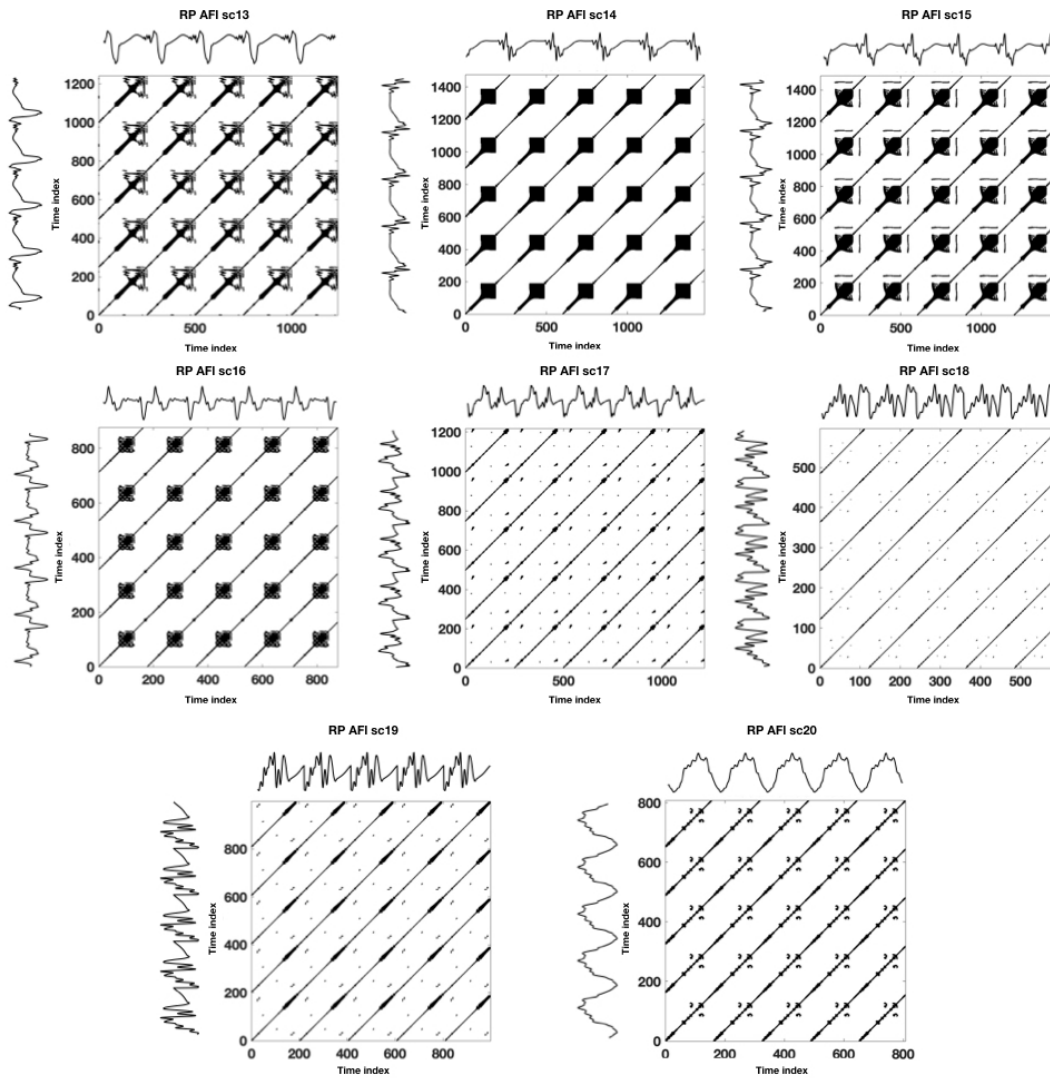
Fig. S12. The effect of different AFl scenarios in the icRQA. The RPs created for the PCS 2 calculated from the 12-lead ECGs extracted from the same atria and torso combination for the all AFl mechanisms - from sc1 to sc12.

Fig. S13. The effect of different AFl scenarios in the icRQA. The RPs created for the PCS 2 calculated from the 12-lead ECGs extracted from the same atria and torso combination for the all AFl mechanisms - from sc13 to sc20.
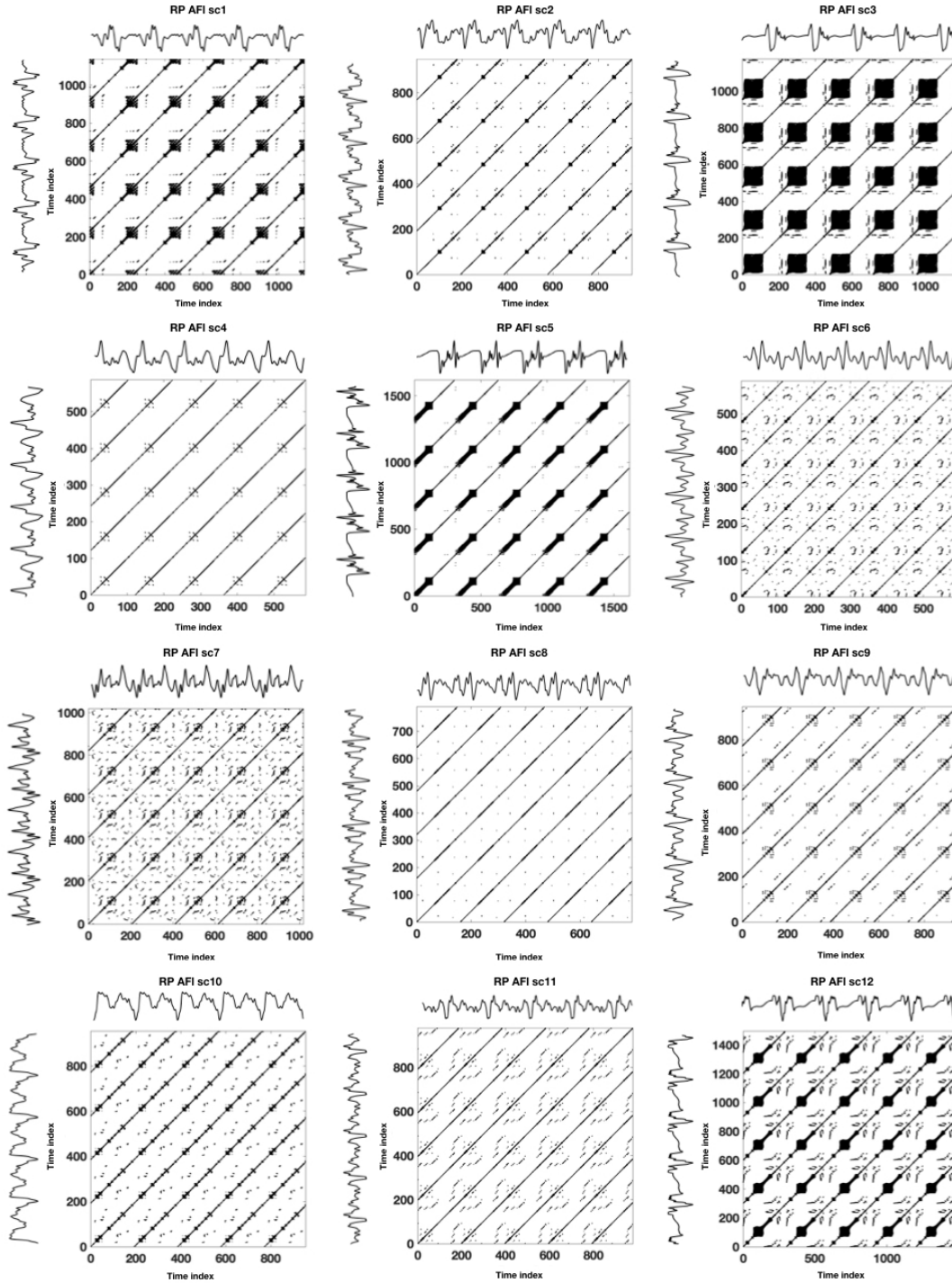
Fig. S14. The effect of different AFl scenarios in the icRQA. The RPs created for the PCS 3 calculated from the 12-lead ECGs extracted from the same atria and torso combination for the all AFl mechanisms - from sc1 to sc12.
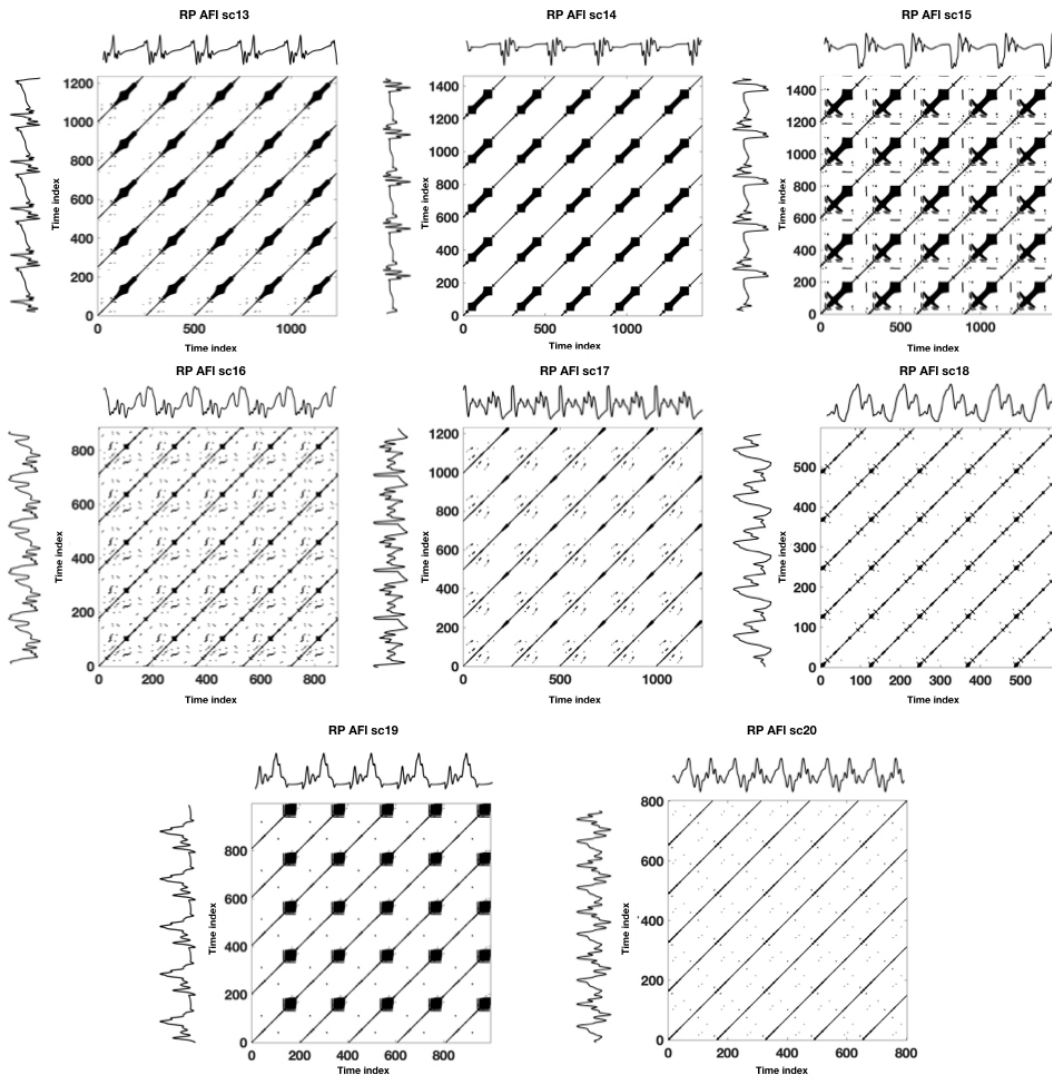
Fig. S15. The effect of different AFl scenarios in the icRQA. The RPs created for the PCS 3 calculated from the 12-lead ECGs extracted from the same atria and torso combination for the all AFl mechanisms - from sc13 to sc20.
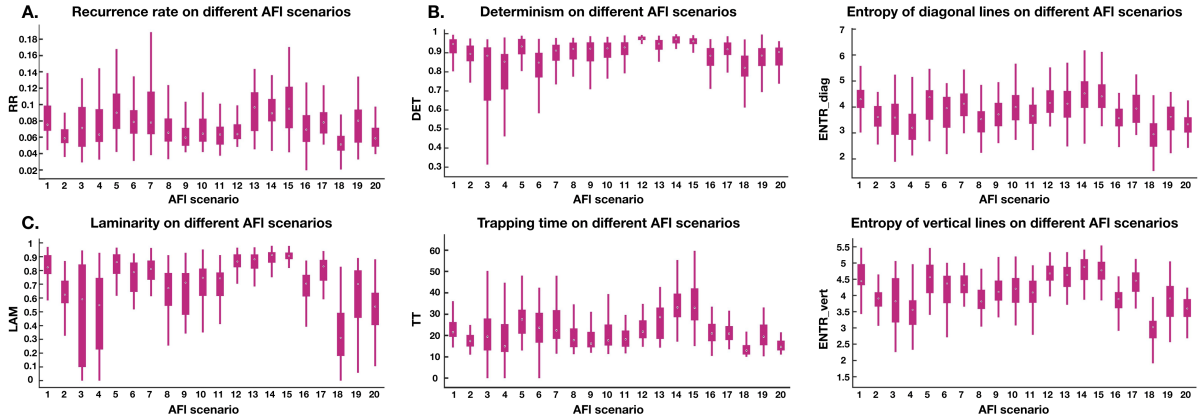
Fig. S16. icRQA variables calculated from the PCS 1 for the 20 different AFl scenarios. A. RR variable. B. Variables related to diagonal lines. C. Variables related to vertical lines.
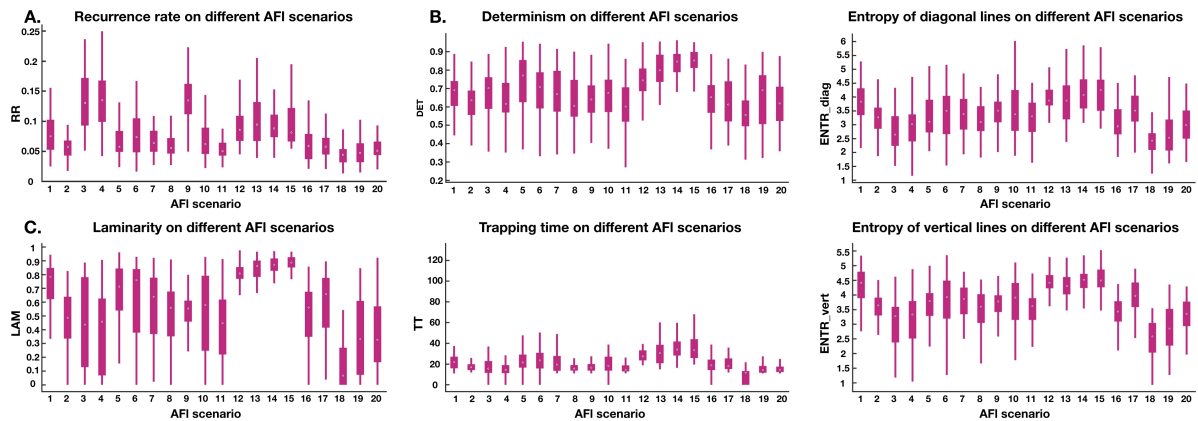

Fig. S17. icRQA variables calculated from the PCS 2 for the 20 different AFl scenarios. A. RR variable. B. Variables related to diagonal lines. C. Variables related to vertical lines.
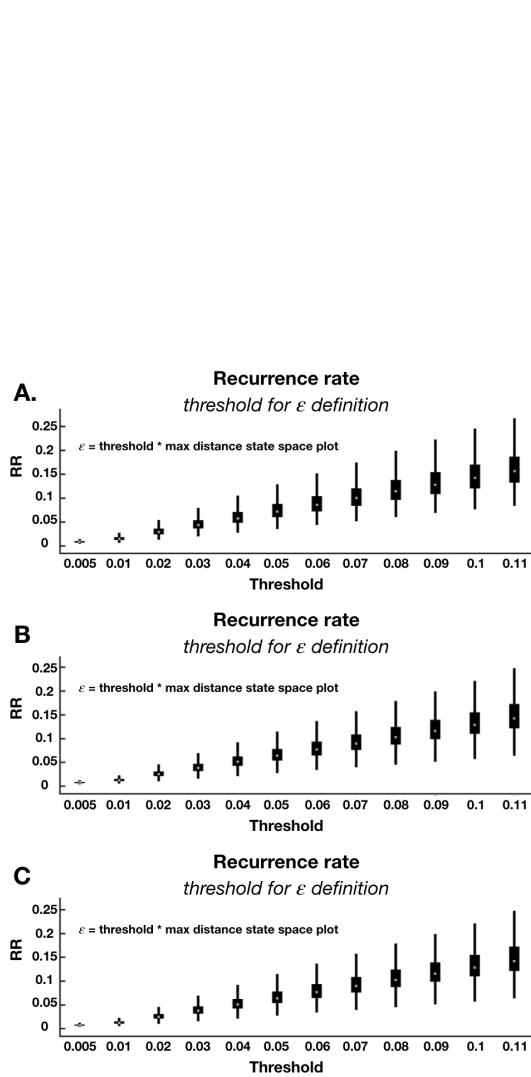
Fig. S18. Definition of ε for srRQA with several embedding dimension numbers. A. RR for varying choices of threshold for ε definition with an embedding dimension $d=2$. B. RR for varying choices of threshold for ε definition with an embedding dimension $d=4$. C. RR for varying choices of threshold for ε definition with an embedding dimension $d=5$.
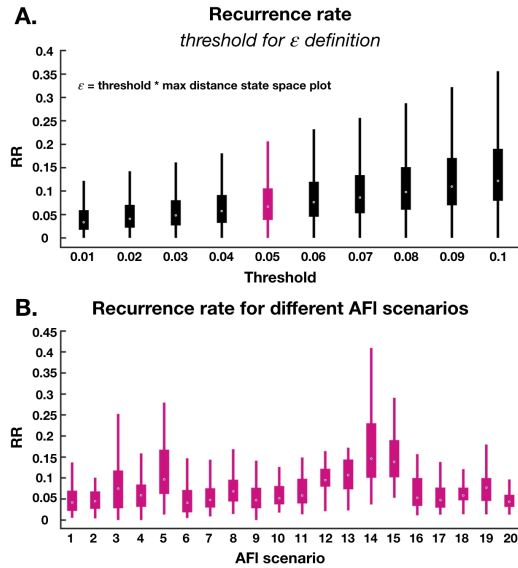

Fig. S19. Definition of ε for srRQA with an embedding dimension $d=3$. A. RR for varying choices of threshold for ε definition. B. Different scenarios' RR with the selected threshold of 0.05, as highlighted in A. The threshold highlighted in A is the selected value. It is the value with the best compromise between: the resulting RR - not too high compared to the recommended 1%; the portion of maximum phase space diameter - not exceed 10%; and the discrimination between the 20 AFl scenarios shown in B and in Table S3

Fig. S20. Definition of the minimum diagonal line length for srRQA determinism. A. DET for varying choices of minimum diagonal line length. B. Different scenarios' DET with the selected minimum diagonal line length of 6, as highlighted in A. The minimum diagonal line length highlighted in A is the selected one. It is the value with the best compromise between: the resulting values - not too high to avoid undesirable saturation behavior; and the discrimination between the 20 AFl scenarios shown in B and in Table S4.

A.   **Minimum vertical line length for laminarity**

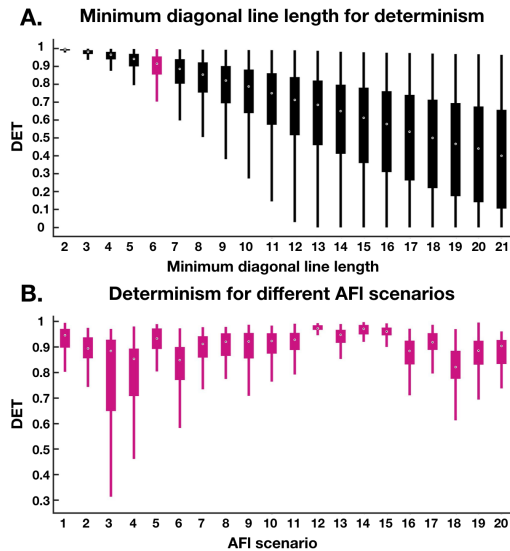**B.**   **Minimum vertical line length for laminarity**

Fig. S21. Definition of the minimum vertical line length for srRQA laminarity. A. LAM for varying choices of minimum vertical line length. B. Different scenarios' LAM with the selected minimum vertical line length of 7, as highlighted in A. The minimum vertical line length highlighted in A is the selected one. It is the value with the best compromise between: the resulting values - not too high to avoid undesirable saturation behavior; and the discrimination between the 20 AFl scenarios shown in B and in Table S4.
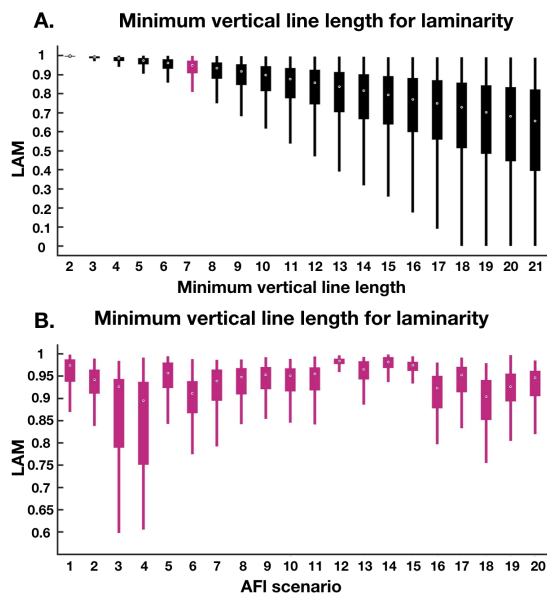
Fig. S22. The effect of different AFl scenarios in the srRQA. The RPs created using two different PCS (PCS 1 above, PCS 2 on the left) as dimensions for the all AFl mechanisms - from sc1 to sc12.
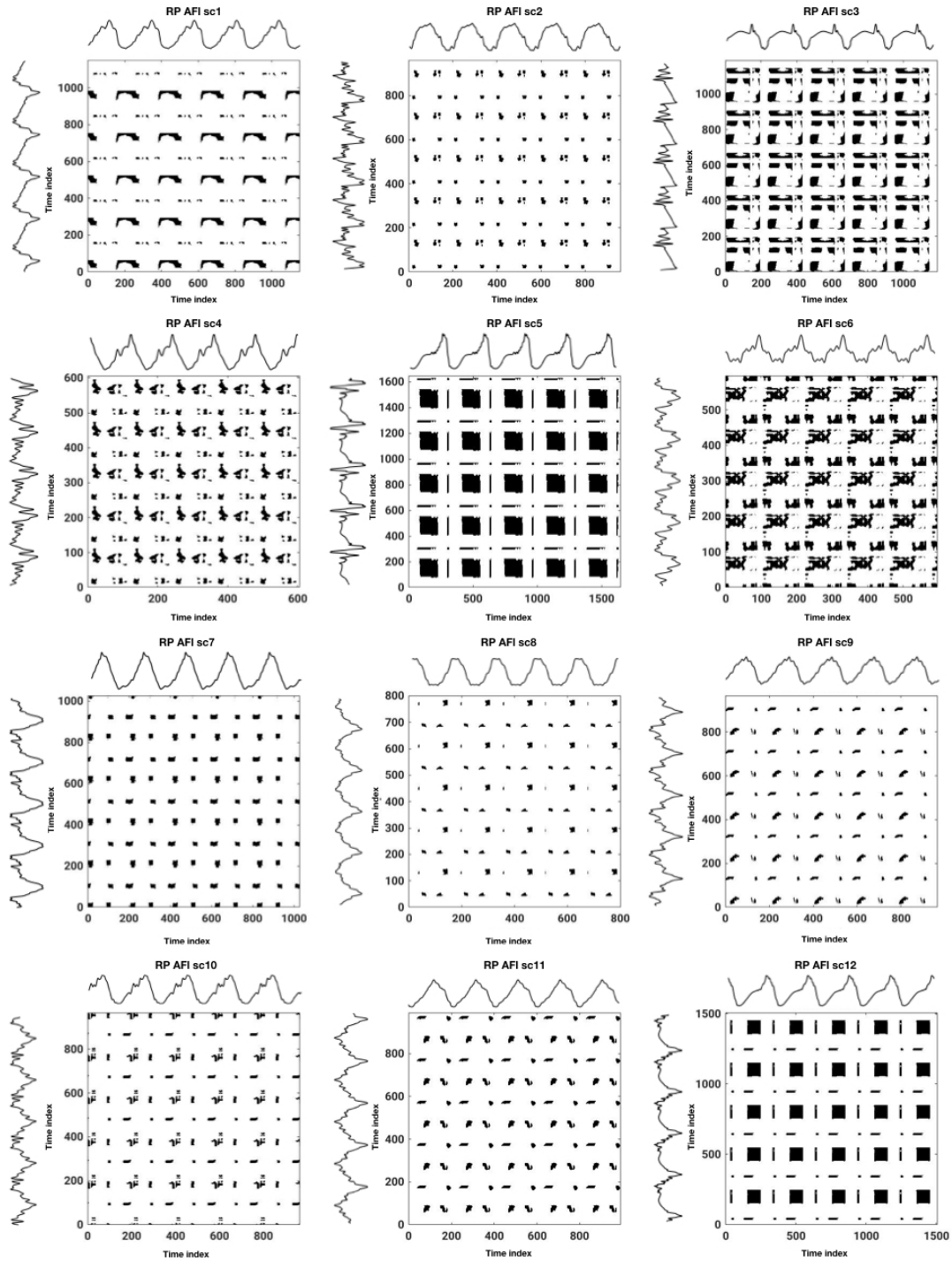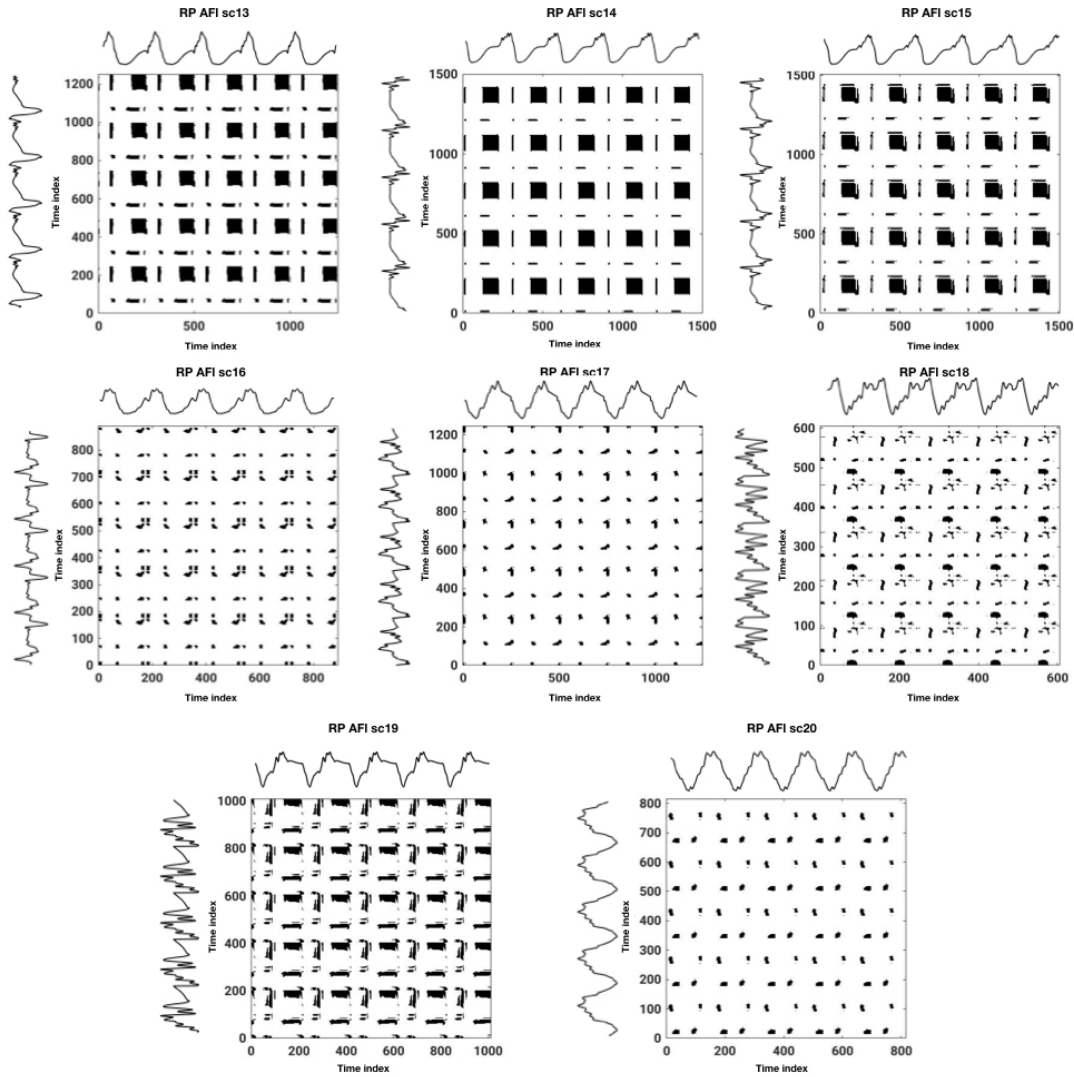
Fig. S23. The effect of different AFl scenarios in the srRQA. The RPs created using two different PCS (PCS 1 above, PCS 2 on the left) as dimensions for the all AFl mechanisms - from sc13 to sc20.

Hybrid Machine Learning to Localize Atrial Flutter Substrates Using Surface 12-lead ECG

-

Supplementary Material

Giorgio Luongo[1]*, Gaetano Vacanti[2]*, Vincent Nitzke[1], Deborah Nairn[1], Claudia Nagel[1],

Diba Kabiri[2], Tiago P Almeida[3], Diogo C Soriano[4], Massimo W Rivolta[5], G André Ng[3], Olaf

Dössel[1], Armin Luik[2], Roberto Sassi[5], Claus Schmitt[2], Axel Loewe[1]

[1]Institute of Biomedical Engineering (IBT), Karlsruhe Institute of Technology (KIT), Karlsruhe, Germany

[2]Medizinische Klinik IV, Städtisches Klinikum Karlsruhe, Karlsruhe, Germany

[3]Department of Cardiovascular Sciences, University of Leicester, NIHR Leicester Biomedical Research Centre, Leicester, UK

[4]Engineering, Modelling and Applied Social Sciences Centre, ABC Federal University, São Bernardo do Campo, Brazil

[5]Dipartimento di Informatica, Università degli Studi di Milano, Milan, Italy.

1   Feature extraction methods

Table 1: List of extracted features.

1.$\overline{AUPSDr}$	2. $AUPSDr_{V1}$	3. $\overline{FCI}$	4. FCI_{min}	5. FCI_{max}	6. $\overline{OMO}$
7.OMO_{min}	8-16.$\overline{WL_X^i}$	17-19. $R^R_{icRQA_{PCi}}$	20-22. $D_{icRQA_{PCi}}$	23-25. $L_{icRQA_{PCi}}$	26-28. $T_{icRQA_{PCi}}$
29-31. $E^{VL}_{icRQA_{PCi}}$	32-34. $E^{DL}_{icRQA_{PCi}}$	35. R^R_{srRQA}	36. D_{srRQA}	37. L_{srRQA}	38. T_{srRQA}
39. E^{VL}_{srRQA}	40. E^{DL}_{srRQA}	41. Pl	42-44. Rn_i	45-54. $SyDy_i$	55-59. $SyDy_X$
60-65. $SyDy_{XY}$	66. $SyDy_{SE}$	67-76. DCT_i	77. FwD		

1.1 Area under power spectrum density ratio

The area under the power spectrum density ratio describes the portion of power into frequency components composing the signal around the dominant frequency compared to the totality of the spectrum. The power spectrum density was calculated for each of the 12-lead ECGs by Fourier transform, and the respective dominant frequency was derived. The area under the power spectrum density ratio ($AUPSDr$) was calculated by making the ratio between the $AUPSD$ in the range 0Hz - 2 times the dominant frequency (DF) and the $AUPSDr$ of the total spectrum for each lead. The extracted $\overline{AUPSDr}$ and $AUPSDr_{V1}$ features are the mean $AUPSDr$ over the leads, and the $AUPSDr$ of lead V1, respectively (feat. 1-2 in Table 1).

1.2 Fragmented conduction index

The fragmented conduction index (FCI) is the sum of the number of relative maxima and minima of the signals. The FCI was calculated for each of the 12-lead ECGs. The extracted $\overline{FCI}$, FCI_{min}, and FCI_{max} features are the mean, the minimum, and the maximum FCI values over the leads, respectively (feat. 3-5 in Table 1) [1].

1.3 Optimal model order

The optimal model order (OMO) represents the number of Gaussian functions needed to fit the signals. The OMO was extracted for each of the 12-lead ECGs following the description in Censi *et al.* [1]. The extracted $\overline{OMO}$ and OMO_{min} features are the mean, and the minimum OMO values over the leads, respectively (feat. 6-7 in Table 1).

1.4 Wavelet analysis

Multilevel stationary wavelet decomposition was applied on each of the 12-lead ECGs [2]. The 5th, 6th, and 7th decomposition levels were used as signals to extract the following features: Mean over the leads of the sum of the number of relative maxima and minima of the wavelet signals ($\overline{WL_1^i}$); Standard deviation over the leads of the sum of the number of relative

maxima and minima of the wavelet signals ($\overline{WL_2^i}$); Mean over the leads of the prominence of the wavelet signals ($\overline{WL_3^i}$). The prominence was calculated using the output parameter *peak prominences* of the *findpeaks* MATLAB function. Features $\overline{WL_X^i}$, with *i* being the number of decomposition level and *X* being one of the three features previously described (feat. 8-16 in Table 1).

1.5 Individual component recurrence quantification analysis

From the 12-lead ECGs, the first three principal components (PCs) were extracted (representing more than 99% of the total variability of the ECGs). An individual component recurrence quantification analysis ($icRQA$) was applied on each of the first three PCs. Following a previous work from Luongo *et al.,* the extracted parameters were: determinism ($D_{icRQA_{PCi}}$), entropy of the diagonal lines ($E^{DL}{}_{icRQA_{PCi}}$), recurrence rate ($R^R{}_{icRQA_{PCi}}$), laminarity ($L_{icRQA_{PCi}}$), trapping time ($T_{icRQA_{PCi}}$), and entropy of the vertical lines ($E^{VL}{}_{icRQA_{PCi}}$), with *i* being the number of PC (feat. 17-34 in Table 1) [3].

1.6 Spatial reduced RQA

A spatial reduced RQA ($srRQA$) was applied on a state space reconstructed with the first three PCs that were used as dimensions. The extracted parameters were: determinism (D_{srRQA_d}), entropy of the diagonal lines (E^{DL}_{srRQA}), recurrence rate (R^R_{srRQA}), laminarity (L_{srRQA}), trapping time (T_{srRQA}), and entropy of the vertical lines (E^{VL}_{srRQA}) (feat. 35-40 in Table 1) [3].

1.7 Planarity & roundness

The vectocardiogram (VCG) was calculated from the 12-lead ECGs using the Dower's inverse transformation, and the 3-D VCG vector loops were used as state space plots for planarity and roundness features extraction. From the VCG loops, the optimal plane that best interpolates the VCG representation was derived. Next, the distance from the plane that interpolates each VCG loop with the optimal plane was calculated. These distances were

averaged across the loops to derive the feature Pl (feat. 41 in Table 1). Pl equal to 0 means that the VCG activity was perfectly planar. In addition, from the 3-D VCG, 1-D VCGs on the XY, YZ, and ZX planes were used to extract roundness features respectively. For each of the three Cartesian planes, the feature roundness was calculated by deriving the optimal circumference that interpolates the VCG representation on all loops. Then the correlation between each VCG loop and the optimal circumference was calculated. These correlations were averaged across loops to derive the feature Rn_i, with i being referring to the XY, YZ, and ZX Cartesian planes, respectively (feat. 42-44 in Table 1). Rn_i is a 0-1 values, where Rn_i equal to 1 means that the VCG activity was perfectly rounded.

1.8   Symbolic dynamic

The VCG was calculated from the 12-lead ECGs using the Dower's inverse transformation, and the three VCG signals were aligned in a single signal ($VCG_{XY}+VCG_{YZ}+VCG_{ZX}$) used for symbolic dynamic features extraction. The new VCG signal was cut into 10 segments over time of equal length. For each segment the mean value was extracted obtaining the $SyDy_i$ features, with i being the segment number (feat. 45-54 in Table 1).   Each of the 10 segments was then divided into 5 equal-sized amplitude sections. Based on the section in amplitude where the mean value of each segment was located over time, a symbol was assigned to the respective segment (T, H, Z, L, and B if the mean value was located in the first, second, third, fourth, or fifth section in descending order of amplitude). The number of T, H, Z, L, and B symbols present along the segments were counted, leading to the features $SyDy_X$, with X being the assigned symbol (feat. 55-59 in Table 1). The number of TT, LZ, LL, LB, BL, and BB symbol sequences present were also derived and extracted as $SyDy_{XY}$ features, with XY being the symbol sequence (feat. 60-65 in Table 1). In addition, the Shannon entropy of the symbol sequences was computed and used as a $SyDy_{SE}$ feature (feat. 66 in Table 1).

1.9   Discrete cosine transform

The VCG was calculated from the 12-lead ECGs using the Dower's inverse transformation, and the three VCG signals were aligned in a single signal (VCG$_{XY}$+VCG$_{YZ}$+VCG$_{ZX}$) used for discrete cosine transform (DCT) [4]. The first 10 DCT coefficients were used as DCT_i features, with i being the number of coefficients (feat. 67-76 in Table 1).

1.10   F-wave duration

The F-wave (flutter wave, P-wave during the atrial flutter - AFlut) duration (FwD) is the duration time of a complete cycle of atrial electrical activation of each specific AFlut mechanism, i.e., the length of the F-wave in the ECG signal (the feature was manually derived; feat. 77 in Table 1).

2   Feature set

The 18 features selected with the greedy forward selection technique were: FwD, $SyDy_H$, $SyDy_L$, $SyDy_B$, $SyDy_Z$, $SyDy_{TT}$, $SyDy_{LZ}$, $SyDy_{LL}$, $SyDy_{BL}$, OMO_{min}, $\overline{OMO}$, DCT_7, DCT_8, DCT_9, $\overline{WL_3^5}$, $\overline{WL_3^6}$, FCI_{min}, and $E^{VL}{}_{icRQA_{PC3}}$.

3   Feature importance analysis

Shapley calculation was implemented to analyze a posteriori the importance of the 18 features selected for the 3-class classification (CTI-dependent AFlut vs. peri-mitral AFlut vs. others LA AFlut) once the model has been trained [5]. The Shapley calculation has been run 1000 times with random samples to calculate the standard deviation (SD). In Figure 1 we can see the Shapley values (the contribution that each feature gives to the classification). We can observe that 10 features gave a positive contribution to the classification, 5 features gave an average null contribution, and 3 features gave a slightly negative contribution (it was expected, being all good features). However, the negative features have not been removed from the

feature set since the removal of such features a posteriori could have brought to overfitting on the model.

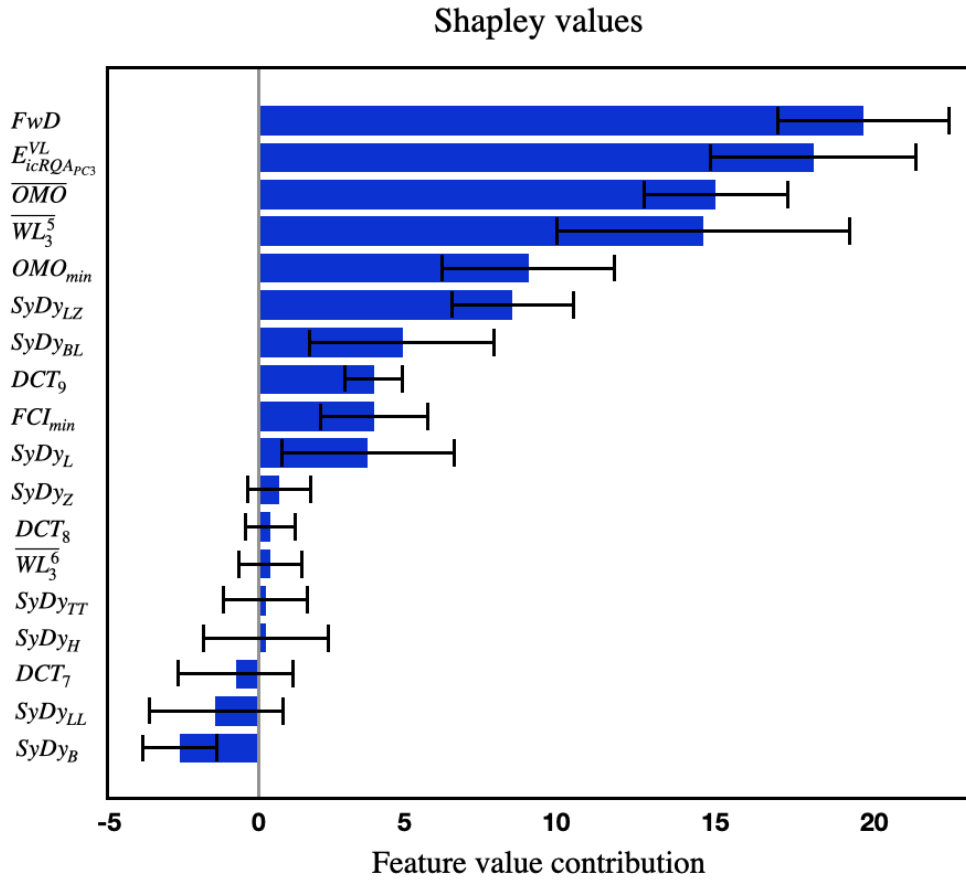In Figure 2 the distribution of the values of the 4 most important features is shown.

Figure 1: Shapley feature importance calculation on the 18 features selected for the 3-class classification CTI-dependent AFlut vs. peri-mitral AFlut vs. others LA AFlut. The Shapley calculation has been run 1000 times with random samples to calculate the SD (error bars in the plot).
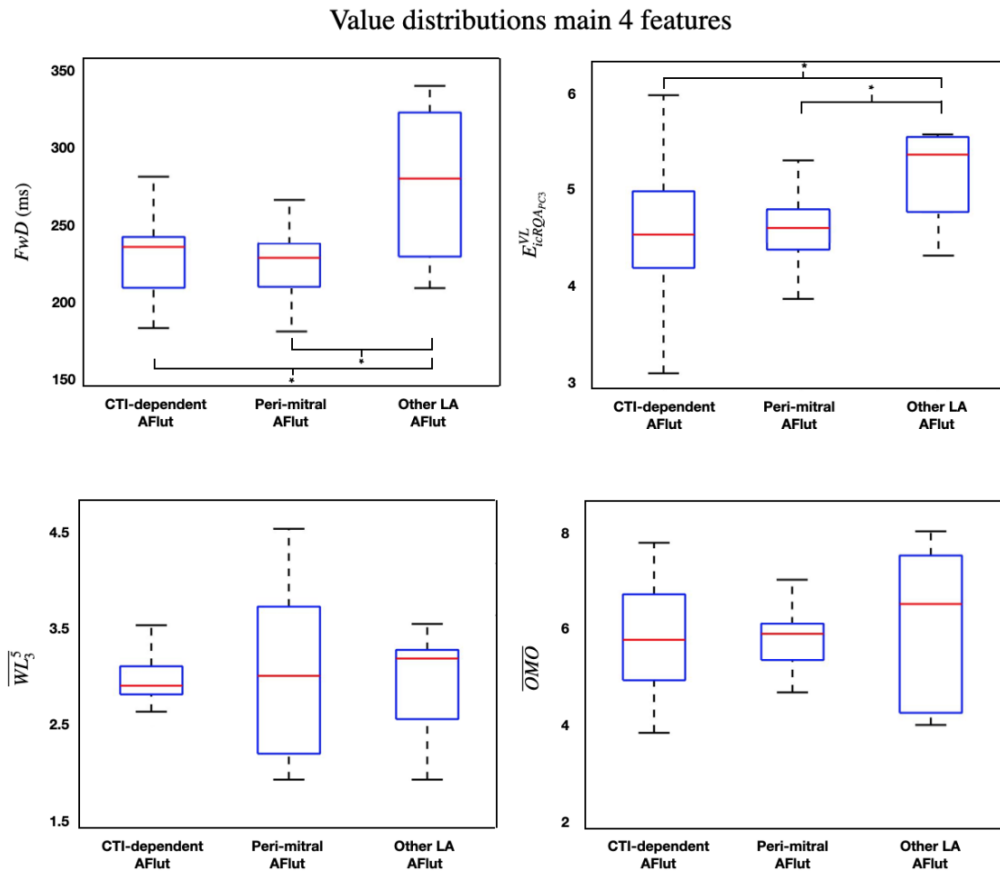
Figure 2: Boxplots of the 4 features identified as most important ones by the Shapley evaluation. The brackets with the asterisk indicate the significantly different features.

References

[1] F. Censi *et al.*, "P-Wave Morphology Assessment by a Gaussian Functions-Based Model in Atrial Fibrillation Patients," *IEEE Trans. Biomed. Eng.*, vol. 54, no. 4, pp. 663–672, 2007, doi: 10.1109/TBME.2006.890134.

[2] J.-C. Pesquet, H. Krim, and H. Carfantan, "Time-invariant orthonormal wavelet representations," *IEEE Trans. Signal Process.*, vol. 44, no. 8, pp. 1964–1970, 1996, doi: 10.1109/78.533717.

[3] G. Luongo *et al.*, "Non-Invasive Characterization of Atrial Flutter Mechanisms Using

Recurrence Quantification Analysis on the ECG: A Computational Study," *IEEE Trans. Biomed. Eng.*, vol. 68, no. 3, pp. 914–925, 2021, doi: 10.1109/TBME.2020.2990655.

[4]   A. V Oppenheim, R. W. Schafer, and J. R. Buck, *Discrete-Time Signal Processing (2nd Ed.)*. USA: Prentice-Hall, Inc., 1999.

[5]   L. S. Shapley, "A value for n-person games," in *The Shapley Value: Essays in Honor of Lloyd S. Shapley*, A. E. E. Roth, Ed. Cambridge University Press, 1988, pp. 31–40.

Machine learning-based non-invasive prediction of atrial fibrillation driver location and ablation outcome using the 12-lead ECG

-

Supplementary Material

Giorgio Luongo (MSc)[1], Luca Azzolin (MSc)[1], Steffen Schuler (MSc)[1], Massimo W Rivolta (PhD)[2], Tiago P Almeida (PhD)[3], Juan P Martínez (PhD)[4], Diogo C Soriano (PhD)[5], Armin Luik (MD)[6], Amir Jadidi (MD)[7], Olaf Dössel (PhD)[1], Roberto Sassi (PhD)[2], Pablo Laguna (PhD)[4], Axel Loewe (PhD)[1]

[1]*Institute of Biomedical Engineering, Karlsruhe Institute of Technology, Karlsruhe, Germany*
[2]*Dipartimento di Informatica, Università degli Studi di Milano, Milan, Italy*
[3]*Department of Cardiovascular Sciences, University of Leicester, Leicester, UK*
[4]*I3A, Universidad de Zaragoza, and CIBER-BNN, Zaragoza, Spain*
[5]*Engineering, Modelling and Applied Social Sciences Centre, ABC Federal University, São Bernardo do Campo, Brazil*
[6]*Medizinische Klinik IV, Städtisches Klinikum Karlsruhe, Karlsruhe, Germany*
[7]*Department of Electrophysiology, University-Heart-Center Freiburg-Bad Krozingen, Bad Krozingen Campus, Germany.*

Table 1: List of extracted features.

1. $\overline{\mathcal{H}}_0$	2. $\sigma^2_{\mathcal{H}_0}$	3. $\overline{\mathcal{H}}_1$	4. $\sigma^2_{\mathcal{H}_1}$	5. $\overline{\mathcal{H}}_2$	6. $\sigma^2_{\mathcal{H}_2}$	7. $\mathcal{D}_{VCG}$
8. $\mathcal{E}^{DL}_{VCG}$	9. $\mathcal{R}^R_{VCG}$	10. $\mathcal{L}_{VCG}$	11. $\mathcal{T}_{VCG}$	12. $\mathcal{E}^{VL}_{VCG}$	13-14. $\mathcal{D}_{srRQA_d}$	15-16. $\mathcal{E}^{DL}_{srRQA_d}$
17-18. $\mathcal{R}^R_{srRQA_d}$	19-20. $\mathcal{L}_{srRQA_d}$	21-22. $\mathcal{T}_{srRQA_d}$	23-24. $\mathcal{E}^{VL}_{srRQA_d}$	25-28. $\mathcal{R}^R_{idRQA_{PCi}}$	29-32. $\mathcal{D}_{idRQA_{PCi}}$	33-36. $\mathcal{L}_{idQA_{PCi}}$
37-40. $\mathcal{T}_{idRQA_{PCi}}$	41-44. $\mathcal{E}^{VL}_{idRQA_{PCi}}$	45-48. $\mathcal{E}^{DL}_{idRQA_{PCi}}$	49-60. $\overline{\lambda}_i$	61-72. σ_{λ_i}	73. $\overline{\lambda}_{PC}$	74. $\sigma_{\lambda_{PC}}$
75-86. $\overline{R}_i$	87-98. σ_{R_i}	99. $\overline{R}_{PC}$	100. $\sigma_{R_{PC}}$	101. $\overline{OI}$	102. σ_{OI}	103. $\overline{SE}$

1. Feature extraction methods

1.1. Hjort descriptors

The Hjort descriptors are closely related to the spectral moments. The first descriptor, $\mathcal{H}_0$, called activity, is defined by the total signal power. The second descriptor, $\mathcal{H}_1$, called mobility, reflects the dominant frequency of the signal under analysis. The third descriptor, $\mathcal{H}_2$, is used to define a measure related to half of the bandwidth of the signal and is termed complexity [1]. These descriptors were evaluated for each ECG lead. The mean values and the variances of these parameters over all 12 leads were calculated and used as features (feat. 1-6 in Table 1).

1.2. Recurrence quantification analysis on vectocardiogram

The vectocardiogram (VCG) was calculated from the 12-lead ECG using the Dower's inverse transformation, and the 3-D VCG vector loops were used as state space plots for a further recurrence quantification analysis (RQA) [2]. RQA allowed to analyse the topological structure of multidimensional dynamical systems, giving access to a signal's intermittency, regularity, and predictability [3]. A detailed explanation of the RQA and the respective extractable parameters can be found in the work of Marwan et al., [3]. The extracted parameters were: determinism ($\mathcal{D}_{VCG}$), entropy of the diagonal lines ($\mathcal{E}_{VCG}^{DL}$), recurrence rate ($\mathcal{R}_{VCG}^{R}$), laminarity ($\mathcal{L}_{VCG}$), trapping time ($\mathcal{T}_{VCG}$), and entropy of the vertical lines ($\mathcal{E}_{VCG}^{VL}$), (feat. 7-12 in Table 1).

1.3. spatial reduced RQA

From the 12-lead ECGs, the first four principal components (PCs) were extracted (representing more than 99% of the total variability). The first three PCs,

2

25 and the first four PCs, were used as dimensions (d) of a state space in which a

26 spatial reduced RQA ($srRQA_3$ and $srRQA_4$) was applied, respectively [4]. The

27 extracted parameters were: determinism ($\mathcal{D}_{srRQA_d}$), entropy of the diagonal lines

28 ($\mathcal{E}^{DL}_{srRQA_d}$), recurrence rate ($\mathcal{R}^{R}_{srRQA_d}$), laminarity ($\mathcal{L}_{srRQA_d}$), trapping time ($\mathcal{T}_{srRQA_d}$),

29 and entropy of the vertical lines ($\mathcal{E}^{VL}_{srRQA_d}$), (feat. 13-24 in Table 1).

30 *1.4. individual component RQA*

31 An individual component RQA (icRQA) was also applied on each of the first

32 four PCs calculated from the 12-lead ECGs [4]. The extracted parameters were:

33 determinism ($\mathcal{D}_{icRQA_{PCi}}$), entropy of the diagonal lines ($\mathcal{E}^{DL}_{icRQA_{PCi}}$), recurrence rate

34 ($\mathcal{R}^{R}_{icRQA_{PCi}}$), laminarity ($\mathcal{L}_{icRQA_{PCi}}$), trapping time ($\mathcal{T}_{icRQA_{PCi}}$), and entropy of the ver-

35 tical lines ($\mathcal{E}^{VL}_{icRQA_{PCi}}$), with *i* being the number of PC, (feat. 25-48 in Table 1).

36 *1.5. Ratio PCA eigenvalues*

37 The 12-lead ECGs were divided in 3 segments of the same length (i.e., 1 s con-

38 sidering the total length of each ECG of 3 s). For each segment j, the eigenvalues

39 ($\lambda_{i,j}$) corresponding to the spatial principal component analysis (PCA) compo-

40 nents over the 12 leads were extracted. From the $\lambda_{i,j}$, also the ratio was calculated:

$$R_{i,j} = \frac{\lambda_{i,j}}{\sum_{k \neq i} \lambda_{k,j}}, \tag{1}$$

41 with *k* being the number of PC.

42 The features extracted were: the mean λ values and the respective standard de-

43 viations for each PC over all segments ($\overline{\lambda_i}$ and σ_{λ_i}); from $\overline{\lambda_i}$, the mean over the

44 12 PCs and the respective standard deviation ($\overline{\lambda}_{PC}$ and $\sigma_{\lambda_{PC}}$); the mean R val-

45 ues and the respective standard deviations for each PC over all segments ($\overline{R_i}$ and

46 σ_{R_i}); from $\overline{R_i}$, the mean over the 12 PCs and the respective standard deviation

47   ($\overline{R}_{PC}$ and $\sigma_{R_{PC}}$), (feat. 49-100 in Table 1). The idea behind the R$_{i,j}$ parameter and

48   the extracted features was to increase the differences between the eigenvalues to

49   achieve a better discrimination due to the variability shown by the PCs over time

50   and between them.

51   *1.6. Organization index*

52   The organization index (OI) was used as a measure of atrial fibrillation spatio-

53   temporal organization, and it was computed as follows. The spectrum of each

54   12-lead ECGs was calculated. The areas under the five largest peaks of each

55   spectrum were computed using a 1 Hz frequency interval centred on each peak.

56   The OI was then defined as the ratio of the area under these five peaks to the total

57   spectrum area [5] for each lead. The feature extracted were: the mean OI and

58   the respective standard deviation over the leads ($\overline{OI}$ and σ_{OI}), (feat. 101-102 in

59   Table 1).

60   *1.7. Spectral entropy*

61   The spectral entropy (SE) of a signal is a measure of its spectral power dis-

62   tribution. The concept is based on the Shannon entropy, or information entropy,

63   in information theory. The SE treats the signal's normalized power distribution

64   in the frequency domain as a probability distribution, and calculates the Shannon

65   entropy of it. The Shannon entropy in this context is the spectral entropy of the

66   signal [6]. The SE was calculated for each of the 12-leads with the MATLAB *pen-*

67   *tropy* function and consecutively averaged along and between leads. The feature

68   extracted was the mean SE over the leads ($\overline{SE}$), (feat. 103 in Table 1).
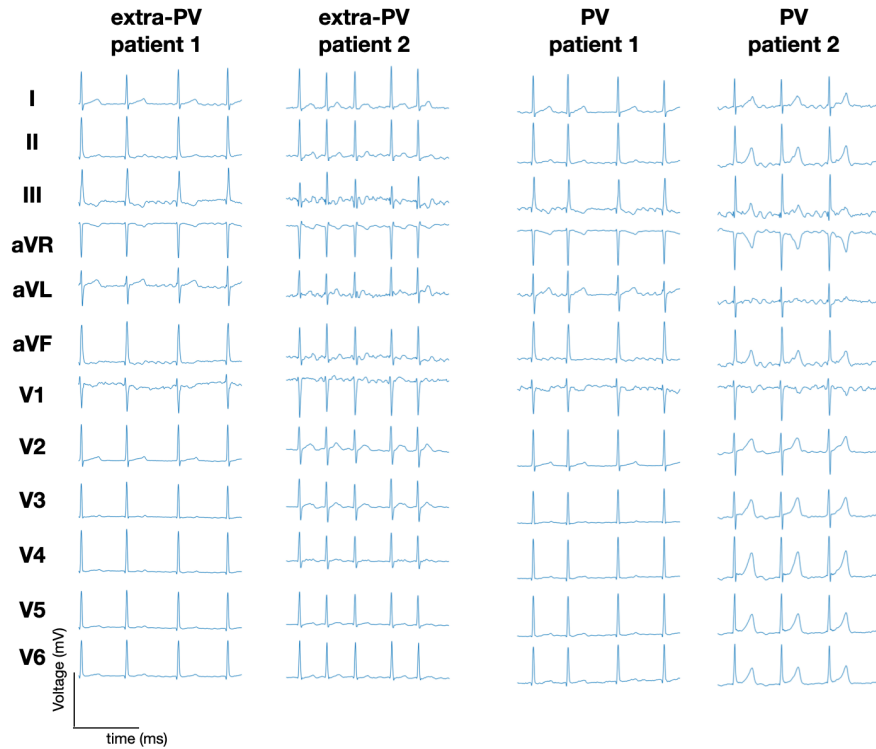
₆₉ **2. Clinical 12-lead ECG**

Figure 1: Examples of 12-lead ECGs from four representative clinical patients for the 2 classes (extra-PV class, left; PV class, right).

₇₀ **3. Alternative machine learning algorithm approaches**

₇₁   In this work, we focused on the implementation of a decision tree classifier for
₇₂ binary classification (AF drivers located at the PVs vs. extra-PV drivers) due to
₇₃ its simplicity and explainability. However, several machine learning approaches
₇₄ have been trained and tested (i.e., linear discriminant analysis - LDA, and radial

5

basis neural network - rbNN). The implementation and optimization of the classifiers followed the same procedure as described in the main text of this work for the decision tree (Section 2.5).

The binary LDA classifier achieved a G-Mean of 76.4±12.8% on the in silico test set with a sensitivity of 88.3±3.7%, a specificity of 66.1±17.1% on the simulated dataset (PV considered as the positive class). On the first unseen clinical dataset, the classifier achieved 71.7% G-Mean with a sensitivity of 69.6%, a specificity of 73.9%, and PPV of 72.7%. On the second clinical dataset the classifier achieved 68.4% G-Mean with a sensitivity of 69.6%, a specificity of 65.2%, and PPV of 66.6%.

The binary rbNN classifier achieved a G-Mean of 86.8±10.1% on the in silico test set with a sensitivity of 96.2±4.5%, a specificity of 78.4±16.3% on the simulated dataset (PV considered as the positive class). On the first unseen clinical dataset, the classifier achieved 78.1% G-Mean with a sensitivity of 69.6%, a specificity of 86.9%, and PPV of 84.2%. On the second clinical dataset the classifier achieved 69.6% G-Mean with a sensitivity of 69.6%, a specificity of 69.6%, and PPV of 69.6%.

4. Feature importance analysis

Shapley calculation was implemented to analyze a posteriori the importance of the 11 features selected for the binary PV vs. extra-PV classification once the model has been trained. In Fig. 2 we can see the Shapley values (the contribution that each feature gives to the classification). We can observe that the features gave all a positive contribution to the classification apart from two features that gave a slightly negative contribution (it was expected, being all good features). However,

99 the negative features have not been removed from the feature set since the removal

100 of such features a posteriori could have brought to overfitting on the model.
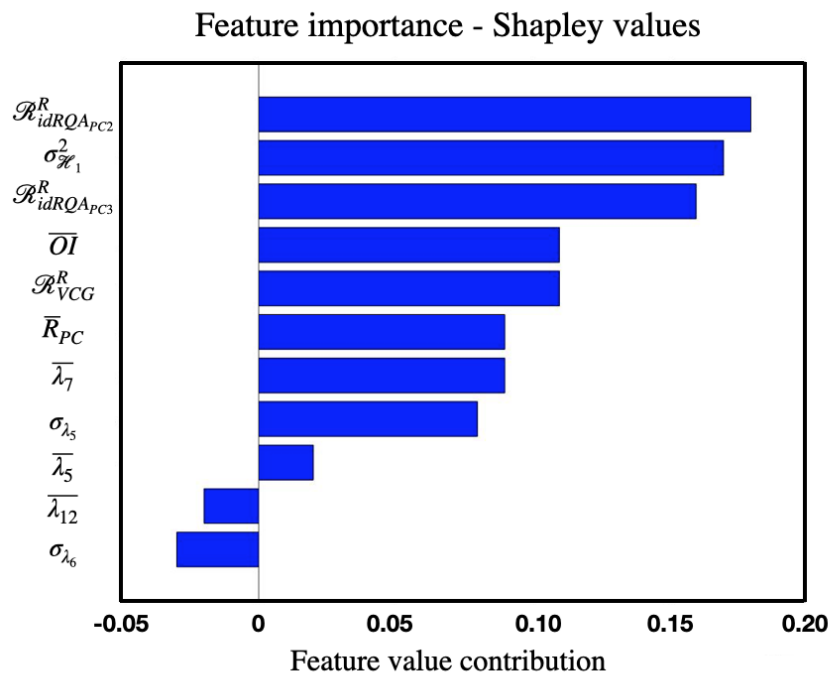

Figure 2: Shapley feature importance calculation on the 11 features selected for the binary classification PV vs. extra-PV AF drivers location.

101 **5. Multivariate regression analysis**

102 Multivariate regression analysis performed between the variables LVEF, LAD,

103 renal dysfunction, sex, age, and our classifier (Table 2).

7

Table 2: Multivariate regression analysis.

	Regression coefficient B	Standard error	Wald	df	Significance	Hazard ratio
Age	-0.069	0.055	1.575	1	0.210	0.934
Sex	0.557	1.114	0.251	1	0.617	1.746
LAD	-0.090	0.106	0.720	1	0.396	0.914
LVEF	-3.104	7.444	0.174	1	0.677	0.045
Renal dysfunction	1.982	1.216	2.655	1	0.103	7.256
Classifier	2.468	1.252	3.887	1	0.049	11.795
Constant	7.929	8.415	0.888	1	0.346	2777.043

6. Consistency analysis

A consistency analysis was implemented by running the classifier on a new ECG set composed of the same 46 patients but different ECG segments than those used in the clinical dataset showed in the main manuscript. In Table 3, the confusion matrix obtained on the "consistency" ECG set.

Table 3: Confusion matrix of the clinical set of different ECG segments extracted from the same 46 patients for a consistency analysis for PV vs. extra-PV AF driver location classification.

		True class	
		PV	extra-PV
Predicted class	PV	16	6
	extra-PV	7	17

References

[1] L. Sörnmo, P. Laguna, Chapter 3 - eeg signal processing, in: L. Sörnmo, P. Laguna (Eds.), Bioelectrical Signal Processing in Cardiac and Neurological Applications, Biomedical Engineering, Academic Press, Burlington, 2005, pp. 55 – 179. `doi:10.1016/B978-012437552-9/50003-9`.

[2] H. Yang, Multiscale recurrence quantification analysis of spatial cardiac vectocardiogram signals, IEEE Trans. Biomed. Eng. 58 (2) (2011) 339–347. `doi:10.1109/TBME.2010.2063704`.

[3] N. Marwan, M. Carmen Romano, M. Thiel, J. Kurths, Recurrence plots for the analysis of complex systems, Physics Reports 438 (5) (2007) 237 – 329. `doi:10.1016/j.physrep.2006.11.001`.

[4] G. Luongo, S. Schuler, A. Luik, et al., Non-invasive characterization of atrial flutter mechanisms using recurrence quantification analysis on the ECG: a computational study, IEEE Trans. Biomed. Eng.`doi:10.1109/TBME.2020.2990655`.

[5] L. Uldry, J. Van Zaen, Y. Prudat, L. Kappenberger, J.-M. Vesin, Measures of spatiotemporal organization differentiate persistent from long-standing atrial fibrillation, EP Europace 14 (8) (2012) 1125–1131. `doi:10.1093/europace/eur436`.

[6] A. Vakkuri, A. Yli-Hankala, P. Talja, et al., Time-frequency balanced spectral entropy as a measure of anesthetic drug effect in central nervous system during sevoflurane, propofol, and thiopental anesthesia, Acta Anaesthesiologica

9

131   Scandinavica 48 (2) (2004) 145–153. `doi:10.1111/j.0001-5172.2004.`

132   `00323.x.`

Machine Learning Using a Single-lead ECG to Identify Patients with Atrial Fibrillation-Induced Heart Failure

-

Supplementary Material

Giorgio Luongo[1]*, Felix Rees[2]*, Deborah Nairn[1], Massimo W Rivolta[3], Olaf Dössel[1], Roberto Sassi[3], Christoph Ahlgrim[2], Louisa Mayer[2], Franz-Josef Neumann[2], Thomas Arentz[2], Amir Jadidi[2], Axel Loewe[1], Björn Müller-Edenborn[2]

[1]Institute of Biomedical Engineering (IBT), Karlsruhe Institute of Technology (KIT), Karlsruhe, Germany

[2]Division of Cardiology and Angiology II, University Heart Center Freiburg-Bad Krozingen, Suedring 15, 79189 Bad Krozingen, Germany

[3]Dipartimento di Informatica, Università degli Studi di Milano, Milan, Italy

* these authors contributed equally

Postal addresses:

[1]Kaiserstr. 12, 76131, Karlsruhe, Germany; [2]Südring 15, 79189 Bad Krozingen, Germany; [3]Via Festa del Perdono 7, 20122, Milan, Italy.

Corresponding authors: Giorgio Luongo, MSc, Fritz-Haber-Weg 1, 76131 Karlsruhe, Germany, Tel.: +49721608-42650, Fax: +49721608-42789, publications@ibt.kit.edu.

1   Feature extraction

Table 1: List of extracted features.

1. $\overline{RR}$	2. $\overline{relRR}$	3. $SDRR$	4. $SDRR_{rel}$	5. $RMSSD_{RR}$
6. $RMSSD_{relRR}$	7. DC	8. DR	9. $ShanEn_{RR}$	10. $ShanEn_{relRR}$
11. $SampEn_{RR}$	12. $SampEn_{relRR}$	13. $SpecEn_{RR}$	14. $SpecEn_{relRR}$	

1.1   Beat-to-beat variability metrics

The mean value, the standard deviation, and the root mean square successive difference ($RMSSD$) of RR and relRR signals are very common clinical metrics that can easily represent the beat-to-beat variance in heart rhythm (1-2). The $RMSSD$ is a time domain measure of heart period variability in heart period series. All these features were calculated for both RR and relRR signals (feat. 1-6 in Table 1).

1.2   Deceleration capacity and reserve

Deceleration capacity (DC) is computed through the Phase-Rectified Signal Averaging technique (PRSA) introduced by Bauer et al. (3), it detects and quantifies quasi-periodic oscillations masked by non-periodic components, and artifacts. DC aims to provide a measure of cardiac vagal modulations. Following Bauer's approach, the hyperparameters of the methods T and s have been set to 1 and 2, respectively.

Deceleration reserve (DR) emphasizes asymmetric growing and decaying heart rate trends and non-stationarity. This parameter is calculated as the sum of the deceleration capacity and the acceleration capacity (parameter similar to the DC, and it is calculated with the PRSA as well). DC and DR were calculated on the RR signals according to Rivolta et al. (4) (feat. 7-8 in Table 1).

1.3   Entropy features

The Shannon entropy ($ShanEn$) is the measure of the uncertainty of occurrence of certain event, or information inherent in the signals' possible outcomes (5). The $ShanEn$ was calculated for the RR and the relRR signals, and the features extracted were the $ShanEn_{RR}$, and $ShanEn_{relRR}$ (feat. 9-10 in Table 1).

Sample entropy ($SampEn$) is a measure of complexity that can be easily applied to any type of time series data, including heart rate variability. $SampEn$ is conceptually similar to approximate entropy, but it does not count self-matching, and it depends less on the data size. The comparison is shown in the graph above. This property makes it amenable to applications with relatively short data size (6). The $SampEn$ was calculated for the RR and the relRR signals, and the features extracted were the $SampEn_{RR}$, and $SampEn_{relRR}$ (feat. 11-12 in Table 1). The embedding dimension parameter, m, was set to 1, and the tolerance parameter, r, was set to 0.2 (percentage applied to the SD).

The spectral entropy ($SpecEn$) of a signal is a measure of its spectral power distribution. The concept is based on the Shannon entropy, or information entropy, in information theory. The $SpecEn$ treats the signal's normalized power distribution in the frequency domain as a probability distribution, and calculates the Shannon entropy of it. The Shannon entropy in this context is the spectral entropy of the signal (7). The $SpecEn$ was calculated for the RR and the relRR signals with the MATLAB *pentropy*. The features extracted were the $SpecEn_{RR}$, and $SpecEn_{relRR}$ (feat. 13-14 in Table 1).

2 Patient's test set accuracy

Table 2: Number of segments and accuracy for each individual patient in the test set (%) for the full-day/night datasets, respectively. The last column shows which patients got correctly classified over the segments (+) and which were misclassified (-).

| Test set patient ID	No. segments (full-day/night)	Class	ACC_P_i (full-day/night)	Correct classification (full-day/night)
1	186/114	AF-HF	54.64/72.73	+/+
2	181/104	AF-HF	63.39/54.46	+/+
3	190/105	AF-HF	58.03/41.28	+/-
4	170/106	AF-HF	68.00/52.38	+/+
5	188/110	AF-HF	66.23/59.81	+/+
6	206/107	AF-HF	30.46/37.62	-/-
7	177/92	CTR	65.82/60.75	+/+
8	188/100	CTR	53.89/38.46	+/-
9	213/101	CTR	66.30/51.96	+/+
10	184/106	CTR	71.75/55.05	+/+
11	205/109	CTR	78.70/40.57	+/-
12	173/107	CTR	48.90/39.60	-/-

3 Circadian classifiers' accuracy
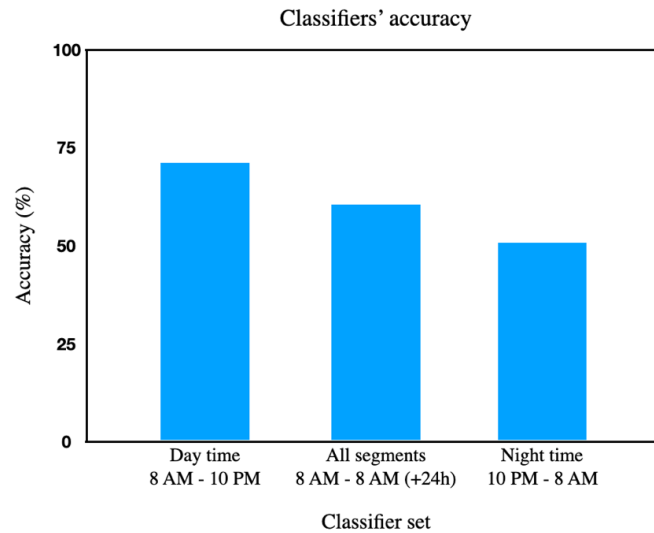
Figure 1: Accuracy of the proposed classifiers for the Full-day, Day, and Night sets, respectively.

References

1. F. Shaffer and J. P. Ginsberg, "An Overview of Heart Rate Variability Metrics and Norms," *Front. Public Heal.*, 2017;5:258. doi: 10.3389/fpubh.2017.00258.

2. M. Vollmer, "A robust, simple and reliable measure of heart rate variability using relative RR intervals," *2015 Computing in Cardiology Conference (CinC)*, 2015,609-612, doi: 10.1109/CIC.2015.7410984.

3. Bauer, J. W. Kantelhardt, A. Bunde, et al., "Phase-rectified signal averaging detects quasi-periodicities in non-stationary data," *Physica A*, 2006;364:423–434.

4. M. W. Rivolta, T. Stampalija, M. G. Frasch, and R. Sassi, "Theoretical Value of Deceleration Capacity Points to Deceleration Reserve of Fetal Heart Rate," *IEEE Trans. Biomed. Eng.*, 2020; 67(4):1176–1185. doi: 10.1109/TBME.2019.2932808.

5. C.E. Shannon, A mathematical theory of communication, The Bell System Technical Journal 1948;27(4):623-656. doi: 10.1002/j.1538-7305.1948.tb00917.x

6. Kijoon Lee (2021). Sample Entropy, MATLAB Central File Exchange. Retrieved October 13, 2021. https://www.mathworks.com/matlabcentral/fileexchange/35784-sample-entropy.

7. Vakkuri, A. Yli-Hankala, P. Talja, et al., Time-frequency balanced spectral entropy as a measure of anesthetic drug effect in central nervous system during sevoflurane, propofol, and thiopental anesthesia, *Acta Anaesthesiologica Scandinavica* 2004;48(2):145–153. doi:10.1111/j.0001-5172.2004.00323.x

References

[1] A. Timmis, N. Townsend, C. P. Gale, et al., "European Society of Cardiology: Cardiovascular Disease Statistics 2019," *European Heart Journal*, vol. 41, pp. 12–85, 2019. doi:10.1093/eurheartj/ehz859

[2] O. Union, "Cancer incidence and mortality," in *Health at a Glance: Europe 2020: State of Health in the EU Cycle*. OECD Publishing, 2020. doi:10.1787/b80245bd-en

[3] S. Bansilal, J. M. Castellano, and V. Fuster, "Global burden of cvd: focus on secondary prevention of cardiovascular disease," *International Journal of Cardiology*, vol. 201, pp. S1–S7, 2015, a polypill strategy for global secondary cardiovascular prevention: a worldwide reality. doi:10.1016/S0167-5273(15)31026-3

[4] Y. Tanaka, N. S. Shah, R. Passman, P. Greenland, D. M. Lloyd-Jones, and S. S. Khan, "Trends in cardiovascular mortality related to atrial fibrillation in the united states, 2011 to 2018," *Journal of the American Heart Association*, vol. 10, p. e020163, 2021. doi:10.1161/JAHA.120.020163

[5] E. Lee, E.-K. Choi, K.-D. Han, et al., "Mortality and causes of death in patients with atrial fibrillation: A nationwide population-based study," *PLOS ONE*, vol. 13, pp. 1–14, 2018. doi:10.1371/journal.pone.0209687

[6] F. Rahman, N. Wang, X. Yin, et al., "Atrial flutter: Clinical risk factors and adverse outcomes in the framingham heart study," *Heart Rhythm*, vol. 13, pp. 233–240, 2016. doi:10.1016/j.hrthm.2015.07.031

[7] A. Alonso, B. P. Krijthe, T. Aspelund, et al., "Simple risk model predicts incidence of atrial fibrillation in a racially and geographically diverse population: the charge‐af consortium," *Journal of the American Heart Association*, vol. 2, p. e000102, 2013. doi:10.1161/JAHA.112.000102

[8] E. J. Benjamin, D. Levy, S. M. Vaziri, R. B. D'Agostino, A. J. Belanger, and P. A. Wolf, "Independent Risk Factors for Atrial Fibrillation in a Population-Based Cohort: The Framingham Heart Study," *JAMA*, vol. 271, pp. 840–844, 1994. doi:10.1001/jama.1994.03510350050036

[9] A. D. Krahn, J. Manfreda, R. B. Tate, F. A. Mathewson, and T. E. Cuddy, "The natural history of atrial fibrillation: Incidence, risk factors, and prognosis in the manitoba follow-up study," *The American Journal of Medicine*, vol. 98, pp. 476–484, 1995. doi:10.1016/S0002-9343(99)80348-9

[10] S. Cunha, E. Antunes, S. Antoniou, et al., "Raising awareness and early detection of atrial fibrillation, an experience resorting to mobile technology centred on informed individuals," *Research in Social and Administrative Pharmacy*, vol. 16, pp. 787–792, 2020. doi:10.1016/j.sapharm.2019.08.036

[11] S. Joung, E. Dzubur, I. van den Broek, et al., "Early detection of atrial fibrillation-atrial flutter using remote patient monitoring," *Journal of Medical Cases*, vol. 10, 2019. doi:10.14740/jmc3151w

[12] S. M. Narayan and D. E. Krummen, "Targeting stable rotors to treat atrial fibrillation," *Arrhythmia & Electrophysiology Review*, vol. 1, pp. 34–38, 2012.

[13] S. Magnani, D. Muser, W. Chik, and P. Santangeli, "Adjunct ablation strategies for persistent atrial fibrillation-beyond pulmonary vein isolation," *Journal of Thoracic Disease*, vol. 7, pp. 178–184, 2015. doi:10.3978/j.issn.2072-1439.2015.01.25

[14] S. M. Narayan, K. Shivkumar, D. E. Krummen, J. M. Miller, and W.-J. Rappel, "Panoramic electrophysiological mapping but not electrogram morphology identifies stable sources for human atrial fibrillation: stable atrial fibrillation rotors and focal sources relate poorly to fractionated electrograms," *Circulation. Arrhythmia and Electrophysiology*, vol. 6, pp. 58–67, 2013. doi:10.1161/CIRCEP.111.977264

[15] M. Haissaguerre, M. Hocini, A. Denis, et al., "Driver domains in persistent atrial fibrillation," *Circulation*, vol. 130, pp. 530–538, 2014. doi:10.1161/CIRCULATIONAHA.113.005421

[16] J. Francis, "Ecg monitoring leads and special leads," *Indian Pacing and Electrophysiology Journal*, vol. 16, pp. 92–95, 2016. doi:10.1016/j.ipej.2016.07.003

[17] M. Rodrigo, A. Climent, A. Liberos, et al., "Minimal configuration of body surface potential mapping for discrimination of left versus right dominant frequencies during atrial fibrillation," *Pacing and Clinical Electrophysiology*, vol. 40, pp. 940–946, 2017. doi:10.1111/pace.13133

[18] B. Taccardi and B. B. Punske, "Chapter 87 - body surface potential mapping," in *Cardiac Electrophysiology (Fourth Edition)*, 4th ed., D. P. ZIPES and J. JALIFE, Eds. W.B. Saunders, 2004, pp. 803–811. doi:10.1016/B0-7216-0323-8/50090-7

[19] Z. F. Issa, J. M. Miller, and D. P. Zipes, "6 - advanced mapping and navigation modalities," in *Clinical Arrhythmology and Electrophysiology (Third Edition)*, 3rd ed., Z. F. Issa, J. M. Miller, and D. P. Zipes, Eds. Philadelphia: Elsevier, 2019, pp. 155–205. doi:10.1016/B978-0-323-52356-1.00006-2

[20] A. K. Yetisen, J. L. Martinez-Hurtado, B. Ünal, A. Khademhosseini, and H. Butt, "Wearables in medicine," *Advanced Materials*, vol. 30, p. 1706910, 2018. doi:10.1002/adma.201706910

[21] J. Tully, C. Dameff, and C. A. Longhurst, "Wave of wearables: Clinical management of patients and the future of connected medicine," *Clinics in Laboratory Medicine*, vol. 40, pp. 69–82, 2020, direct-to-Consumer Testing: The Role of Laboratory Medicine. doi:10.1016/j.cll.2019.11.004

[22] G. Luongo, S. Schuler, A. Luik, et al., "Non-invasive characterization of atrial flutter mechanisms using recurrence quantification analysis on the ecg: A computational study," *IEEE Transactions on Biomedical Engineering*, vol. 68, pp. 914–925, 2021. doi:10.1109/TBME.2020.2990655

[23] G. Luongo, S. Schuler, M. W. Rivolta, O. Dössel, R. Sassi, and A. Loewe, "Automatic ecg-based discrimination of 20 atrial flutter mechanisms: Influence of atrial and torso geometries," in *2020 Computing in Cardiology*, 2020, pp. 1–4. doi:10.22489/CinC.2020.066

[24] G. Luongo, G. Vacanti, V. Nitzke, et al., "Hybrid machine learning to localize atrial flutter substrates using the surface 12-lead ecg," *under review*, 2021.

[25] G. Luongo, L. Azzolin, S. Schuler, et al., "Machine learning enables noninvasive prediction of atrial fibrillation driver location and acute pulmonary vein ablation success using the 12-lead ecg," *Cardiovascular Digital Health Journal*, vol. 2, pp. 126–136, 2021. doi:10.1016/j.cvdhj.2021.03.002

[26] G. Luongo, F. Rees, D. Nairn, et al., "Machine learning using a single-lead ecg to identify patients with atrial fibrillation-induced heart failure," *under review*, 2021.

[27] P. A. Iaizzo, *Handbook of cardiac anatomy, physiology, and devices*, pp. 61–88. Cham : Springer, 1 2015.

[28] Wapcaplet. File:diagram of the human heart (cropped).svg. 2006-06-02, 07:02. https://commons.wikimedia.org/wiki/File:Diagram_of_the_human_heart_(cropped).svg

[29] S. Pollnow, "Characterizing cardiac electrophysiology during radiofrequency ablation: An integrative ex vivo, in silico, and in vivo approach," PhD thesis, Karlsruhe Institute of Technology (KIT), Karlsruhe, 2019. doi:10.5445/KSP/1000089807

[30] K. Wang, S. Y. Ho, D. G. Gibson, and R. H. Anderson, "Architecture of atrial musculature in humans," *British Heart Journal*, vol. 73, pp. 559–565, 1995.

[31] D. Sanchez-Quintana, J. A. Cabrera, V. Climent, J. Farre, M. C. d. Mendonca, and S. Y. Ho, "Anatomic relations between the esophagus and left atrium and relevance for ablation of atrial fibrillation," *Circulation*, vol. 112, pp. 1400–1405, 2005. doi:10.1161/CIRCULATIONAHA.105.551291

[32] C. Stöllberger, G. Ernst, E. Bonner, J. Finsterer, and J. Slany, *Left atrial appendage morphology: Comparison of transesophageal images and postmortem casts*, vol. 92, no. 4, pp. 303–308. Springer Berlin / Heidelberg Zeitschrift für Kardiologie, 1 2003.

[33] Image: The right atrium. https://cardiovascularsystemud.weebly.com/uploads/8/2/1/2/8212050/322140.jpg?824

[34] Image: The left atrium. https://cardiovascularsystemud.weebly.com/uploads/8/2/1/2/8212050/8622882.jpg?833

[35] T. U. o. N. School of Health Sciences. Image: The cardiac conduction system. https://www.nottingham.ac.uk/nursing/practice/resources/cardiology/function/conduction.php

[36] L. Schmidt, F. Lang, and M. Heckmann, *Physiologie des menschen*, vol. 31, pp. 518–20. überarb. und aktualisierte Aufl. Heidelberg: Springer, 2011.

[37] N. A. Pilia, "Electrocardiogram signal analysis and simulations for non-invasive diagnosis," PhD thesis, Institute of Biomedical Engineering, Karlsruhe Institute of Technology (KIT), 2021.

[38] A. A. Atkielski). File:sinusrhythmlabels.svg. 13 January 2007, 23:40. https://upload.wikimedia.org/wikipedia/commons/5/53/SinusRhythmLabels.png

[39] J. G. Betts, K. A. Young, J. A. Wise, et al., *Anatomy and physiology*. OpenStax, 2013. https://openstax.org/books/anatomy-and-physiology/pages/19-3-cardiac-cycle

[40] S. Meek and F. Morris, "Introduction. i—leads, rate, rhythm, and cardiac axis," *BMJ*, vol. 324, pp. 415–418, 2002. doi:10.1136/bmj.324.7334.415

[41] L. Sörnmo and P. Laguna, *Bioelectrical signal processing in cardiac and neurological applications*, pp. 55–179/419–423. Amsterdam: Elsevier, 1 2005.

[42] A. Grishman and E. Donoso, "Spatial vectorcardiography i," *Mod Concepts Cardiovasc Dis*, vol. 30, pp. 693–696, 1961. doi:10.1136/bmj.324.7334.415

[43] J. Carlson, R. Havmoller, A. Herreros, P. Platonov, R. Johansson, and B. Olsson, "Can orthogonal lead indicators of propensity to atrial fibrillation be accurately assessed from the 12-lead ECG?" *Europace*, vol. 7 Suppl 2, pp. 39–48, 2005. doi:10.1016/j.eupc.2005.04.012

[44] Jmarchn. File:precordial leads 2.svg. 08/02/2010, 08:01. https://commons.wikimedia.org/wiki/File:Precordial_Leads_2.svg

[45] L. S. Green and J. A. Abildskov, "Clinical applications of body surface potential mapping," *Clinical Cardiology*, vol. 18, pp. 245–249, 1995. doi:10.1002/clc.4960180505

[46] G. Lee, P. Sanders, and J. M. Kalman, "Catheter ablation of atrial arrhythmias: state of the art," *Lancet (London, England)*, vol. 380, pp. 1509–1519, 2012. doi:10.1016/S0140-6736(12)61463-9

[47] A. Chugh, H. Oral, K. Lemola, et al., "Prevalence, mechanisms, and clinical significance of macroreentrant atrial tachycardia during and following left atrial ablation for atrial fibrillation," *Heart Rhythm : the Official Journal of the Heart Rhythm Society*, vol. 2, pp. 464–471, 2005. doi:10.1016/j.hrthm.2005.01.027

[48] J. Villacastin, N. Perez-Castellano, J. Moreno, and R. Gonzalez, "Left atrial flutter after radiofrequency catheter ablation of focal atrial fibrillation," *Journal of Cardiovascular Electrophysiology*, vol. 14, pp. 417–421, 2003.

[49] A. B. Biviano, E. J. Ciaccio, J. Fleitman, et al., "Atrial tachycardias after atrial fibrillation ablation manifest different waveform characteristics: Implications for characterizing tachycardias," *Journal of Cardiovascular Electrophysiology*, 2015. doi:10.1111/jce.12770

[50] T. Yamada and G. N. Kay, "Atrial flutter following pulmonary vein isolation: what is the mechanism?" *Journal of Cardiovascular Electrophysiology*, vol. 24, pp. 1186–1188, 2013. doi:10.1111/jce.12167

[51] R. Kobza, G. Hindricks, H. Tanner, et al., "Late recurrent arrhythmias after ablation of atrial fibrillation: incidence, mechanisms, and treatment," *Heart Rhythm : the Official Journal of the Heart Rhythm Society*, vol. 1, pp. 676–683, 2004. doi:10.1016/j.hrthm.2004.08.009

[52] C. E. Mesas, C. Pappone, C. C. Lang, et al., "Left atrial tachycardia after circumferential pulmonary vein ablation for atrial fibrillation: electroanatomic characterization and treatment," *J Am Coll Cardiol*, vol. 44, pp. 1071–1079, 2004.

[53] K. S. HOFFMAYER, Y. YANG, S. JOSEPH, et al., "Predictors of unusual ecg characteristics in cavotricuspid isthmus-dependent atrial flutter ablation," *Pacing and Clinical Electrophysiology*, vol. 34, pp. 1251–1257, 2011. doi:10.1111/j.1540-8159.2011.03137.x

[54] A. J. Camm, P. Kirchhof, G. Y. H. Lip, et al., "Guidelines for the management of atrial fibrillation: the task force for the management of atrial fibrillation of the european society of cardiology (ESC)," *European Heart Journal*, vol. 31, pp. 2369–2429, 2010. doi:10.1093/eurheartj/ehq278

[55] A. Natale, K. H. Newby, E. Pisano, et al., "Prospective randomized comparison of antiarrhythmic therapy versus first-line radiofrequency ablation in patients with atrial flutter," *Journal of the American College of Cardiology*, vol. 35, pp. 1898–1904, 2000.

[56] A. Loewe, "Modeling human atrial patho-electrophysiology from ion channels to ECG: substrates, pharmacology, vulnerability, and p-waves," PhD thesis, Karlsruhe Institute of Technology (KIT), Karlsruhe, 2016. doi:10.5445/KSP/1000054615

[57] A. J. Camm, G. Y. H. Lip, R. De Caterina, et al., "2012 focused update of the ESC guidelines for the management of atrial fibrillation: an update of the 2010 ESC guidelines for the management of atrial fibrillation. developed with the special contribution of the european heart rhythm association." *European heart journal*, vol. 33, pp. 2719–47, 2012. doi:10.1093/eurheartj/ehs253

[58] M. Zoni-Berisso, F. Lercari, T. Carazza, and S. Domenicucci, "Epidemiology of atrial fibrillation: European perspective," *Clinical Epidemiology*, vol. 6, pp. 213–220, 2014. doi:10.2147/CLEP.S47385

[59] F. D. R. Hobbs, D. A. Fitzmaurice, J. Mant, et al., "A randomised controlled trial and cost-effectiveness study of systematic screening (targeted and total population screening) versus routine practice for the detection of atrial fibrillation in people aged 65 and over. the SAFE study," *Health Technol Assess.*, 2005.

[60] Y.-M. Cha, M. M. Redfield, W.-K. Shen, and B. J. Gersh, "Atrial fibrillation and ventricular dysfunction," *Circulation*, vol. 109, pp. 2839–2843, 2004. doi:10.1161/01.CIR.0000132470.78896.A8

[61] H. Calkins, K. H. Kuck, R. Cappato, et al., "2012 HRS/EHRA/ECAS expert consensus statement on catheter and surgical ablation of atrial fibrillation: recommendations for patient selection, procedural techniques, patient management and follow-up, definitions, endpoints, and research trial design," *J Interv Card Electrophysiol*, vol. 33, pp. 171–257, 2012. doi:10.1007/s10840-012-9672-7

[62] J. Andrade, P. Khairy, D. Dobrev, and S. Nattel, "The clinical profile and pathophysiology of atrial fibrillation: relationships among clinical features, epidemiology, and mechanisms," *Circulation Research*, vol. 114, pp. 1453–1468, 2014. doi:10.1161/CIRCRESAHA.114.303211

[63] U. Schotten, D. Dobrev, P. G. Platonov, H. Kottkamp, and G. Hindricks, "Current controversies in determining the main mechanisms of atrial fibrillation." *Journal of internal medicine*, vol. 279, pp. 428–38, 2016. doi:10.1111/joim.12492

[64] J. Waks and M. Josephson, "Mechanisms of atrial fibrillation - reentry, rotors and reality." *Arrhythmia & electrophysiology review*, vol. 3 2, pp. 90–100, 2014.

[65] P. Ganesan, K. E. Shillieto, and B. Ghoraani, "Simulation of spiral waves and point sources in atrial fibrillation with application to rotor localization." *Proceedings. IEEE International Symposium on Computer-Based Medical Systems*, vol. 2017, pp. 379–384, 2017. doi:10.1109/CBMS.2017.161

[66] A. Luik, A. Radzewitz, M. Kieser, et al., "Cryoballoon versus open irrigated radiofrequency ablation in patients with paroxysmal atrial fibrillation: The prospective, randomized, controlled, noninferiority freezeAF study," *Circulation*, vol. 132, pp. 1311–1319, 2015. doi:10.1161/CIRCULATIONAHA.115.016871

[67] M. Haissaguerre, P. Jaïs, D. C. Shah, et al., "Spontaneous initiation of atrial fibrillation by ectopic beats originating in the pulmonary veins," *New England Journal of Medicine*, vol. 339, pp. 659–666, 1998.

[68] G. Lin, H.-H. Lu, Y. Shen, J.-F. Huang, L.-S. Shi, and Y.-N. Guo, "Meta-analysis of the therapeutic effects of various methods for the treatment of chronic atrial fibrillation," *Experimental and Therapeutic Medicine*, vol. 6, pp. 489–496, 2013. doi:10.3892/etm.2013.1158

[69] M. Schmidt, U. Dorwarth, D. Andresen, et al., "German ablation registry: Cryoballoon vs radiofrequency ablation in paroxysmal atrial fibrillation-one-year outcome data," *Heart Rhythm*, vol. 13, pp. 836–844, 2016. doi:10.1016/j.hrthm.2015.12.007

[70] A. Verma, C.-y. Jiang, T. R. Betts, et al., "Approaches to catheter ablation for persistent atrial fibrillation." *The New England Journal of Medicine*, vol. 372, pp. 1812–22, 2015. doi:10.1056/NEJMoa1408288

[71] A. L. Hodgkin and A. F. Huxley, "A quantitative description of membrane current and its application to conduction and excitation in nerve," *Journal of Physiology*, vol. 117, pp. 500–544, 1952.

[72] M. Courtemanche, R. J. Ramirez, and S. Nattel, "Ionic mechanisms underlying human atrial action potential properties: insights from a mathematical model." *The American journal of physiology*, vol. 275, pp. H301–21, 1998.

[73] L. Tung, "A bidomain model for describing ischemic myocardial d-c potentials," PhD thesis, Massachusetts Institute of Technology. Dept. of Electrical Engineering and Computer Science, 1978.

[74] M. Wallman, N. P. Smith, and B. Rodriguez, "A comparative study of graph-based, eikonal, and monodomain simulations for the estimation of cardiac activation times," *IEEE Transactions on Biomedical Engineering*, vol. 59, pp. 1739–1748, 2012. doi:10.1109/TBME.2012.2193398

[75] J. A. Sethian and A. Vladimirsky, "Fast methods for the eikonal and related hamilton- jacobi equations on unstructured meshes," *Proceedings of the National Academy of Sciences of the United States of America*, vol. 97, pp. 5699–5703, 2000. doi:10.1073/pnas.090060097

[76] M. Sermesant, E. Konukoglu, H. Delingette, et al., "An anisotropic multi-front fast marching method for real-time simulation of cardiac electrophysiology," in *Functional Imaging and Modeling of the Heart*, F. Sachse and G. Seemann, Eds. Springer Berlin / Heidelberg, 1 2007, vol. 4466, pp. 160–169. doi:10.1007/978-3-540-72907-5_17

[77] M. Stenroos, "The transfer matrix for epicardial potential in a piece-wise homogeneous thorax model: the boundary element formulation." *Physics in medicine and biology*, vol. 54, pp. 5443–55, 2009. doi:10.1088/0031-9155/54/18/006

[78] G. Shou, L. Xia, M. Jiang, F. Liu, and S. Crozier, "Forward and inverse solutions of electrocardiography problem using an adaptive bem method," in *FIMH*, 2007.

[79] M. A. Escabí, "10 - biosignal processing," in *Introduction to Biomedical Engineering (Second Edition)*, 2nd ed., Biomedical Engineering, J. D. Enderle, S. M. Blanchard, and J. D. Bronzino, Eds. Boston: Academic Press, 2005, pp. 549–625. doi:10.1016/B978-0-12-238662-6.50012-4

[80] A. P. Yoganathan, R. Gupta, and W. H. Corcoran, "Fast fourier transform in the analysis of biomedical data," *Medical and biological engineering*, vol. 14, p. 239, 1976. doi:10.1007/BF02478755

[81] U. Kiencke, M. Schwarz, and T. Weickert, *Signalverarbeitung: Zeit-frequenz-analyse und schätzverfahren*, p. 117;294f. Oldenbourg Verlag, 2009.

[82] C. E. Shannon, "A mathematical theory of communication," *The Bell System Technical Journal*, vol. 27, pp. 623–656, 1948. doi:10.1002/j.1538-7305.1948.tb00917.x

[83] T. Schneider. (2013, 07) Information theory primer with an appendix on logarithms pdf version. doi:10.13140/2.1.2607.2000

[84] Y. N. Pan, J. Chen, and X. L. Li, "Spectral entropy: A complementary index for rolling element bearing performance degradation assessment," *Proceedings of the Institution of Mechanical Engineers, Part C: Journal of Mechanical Engineering Science*, vol. 223, pp. 1223–1231, 2009. doi:10.1243/09544062JMES1224

[85] A. Vakkuri, A. Yli-Hankala, P. Talja, et al., "Time-frequency balanced spectral entropy as a measure of anesthetic drug effect in central nervous system during sevoflurane, propofol, and thiopental anesthesia," *Acta Anaesthesiologica Scandinavica*, vol. 48, pp. 145–153, 2004. doi:10.1111/j.0001-5172.2004.00323.x

[86] N. Marwan. Recurrence plots and cross recurrence plots. 2021-03-25 16:11:10. http://www.recurrence-plot.tk

[87] N. Marwan, M. Carmen Romano, M. Thiel, and J. Kurths, "Recurrence plots for the analysis of complex systems," *Physics Reports*, vol. 438, pp. 237–329, 2007. doi:10.1016/j.physrep.2006.11.001

[88] L. Trulla, A. Giuliani, J. Zbilut, and C. Webber, "Recurrence quantification analysis of the logistic equation with transients," *Physics Letters A*, vol. 223, pp. 255–260, 1996. doi:10.1016/S0375-9601(96)00741-4

[89] N. Marwan, M. Thiel, and N. R. Nowaczyk, "Cross recurrence plot based synchronization of time series," *Nonlinear Processes in Geophysics*, vol. 9, pp. 325–331, 2002. doi:10.5194/npg-9-325-2002

[90] B. Hjorth, "EEG analysis based on time domain properties," *Electroencephalography and Clinical Neurophysiology*, vol. 29, pp. 306–310, 1970. doi:10.1016/0013-4694(70)90143-4

[91] P. Sprent, "Statistics in medical research," *Swiss Med Wkly*, vol. 133, pp. 522–9, 2003.

[92] A. P. King and R. J. Eckersley, "Chapter 5 - inferential statistics ii: Parametric hypothesis testing," in *Statistics for Biomedical Engineers and Scientists*, A. P. King and R. J. Eckersley, Eds. Academic Press, 2019, pp. 91–117. doi:10.1016/B978-0-08-102939-8.00014-1

[93] S. Geisser, *Testing hypotheses*. John Wiley & Sons, Ltd, 2005, ch. 4, pp. 25–43. doi:10.1002/0471743135.ch4

[94] A. P. King and R. J. Eckersley, "Chapter 8 - inferential statistics v: Multiple and multivariate hypothesis testing," in *Statistics for Biomedical Engineers and Scientists*, A. P. King and R. J. Eckersley, Eds. Academic Press, 2019, pp. 173–199. doi:10.1016/B978-0-08-102939-8.00017-7

[95] A. P. King and R. J. Eckersley, "Chapter 6 - inferential statistics iii: Nonparametric hypothesis testing," in *Statistics for Biomedical Engineers and Scientists*, A. P. King and R. J. Eckersley, Eds. Academic Press, 2019, pp. 119–145. doi:10.1016/B978-0-08-102939-8.00015-3

[96] J. Goecks, V. Jalili, L. M. Heiser, and J. W. Gray, "How machine learning will transform biomedicine," *Cell*, vol. 181, pp. 92–101, 2020. doi:https://doi.org/10.1016/j.cell.2020.03.022

[97] C. M. Bishop, *Pattern recognition and machine learning (information science and statistics)*. Berlin, Heidelberg: Springer-Verlag, 2006.

[98] Chabacano. File:overfitting.svg. 24/02/2008, 22:39. https://commons.wikimedia.org/wiki/File:Overfitting.svg#filehistory

[99] A. Navada, A. N. Ansari, S. Patil, and B. A. Sonkamble, "Overview of use of decision tree algorithms in machine learning," in *2011 IEEE Control and System Graduate Research Colloquium*, 2011, pp. 37–42. doi:10.1109/ICSGRC.2011.5991826

[100] H. A. Abu Alfeilat, A. B. Hassanat, O. Lasassmeh, et al., "Effects of distance measure choice on k-nearest neighbor classifier performance: A review," *Big Data*, vol. 7, pp. 221–248, 2019, pMID: 31411491. doi:10.1089/big.2018.0175

[101] A. Ajanki. File:knnclassification.svg. 28/05/2007, 18:27. https://commons.wikimedia.org/wiki/File:KnnClassification.svg

[102] O. Dössel, M. W. Krueger, F. M. Weber, M. Wilhelms, and G. Seemann, "Computational modeling of the human atrial anatomy and electrophysiology," *Medical & Biological Engineering & Computing*, vol. 50, pp. 47–50, 122–129, 2012. doi:10.1007/s11517-012-0924-6

[103] B. Dubuisson, "Neural networks, general principles," in *Encyclopedia of Vibration*, S. Braun, Ed. Oxford: Elsevier, 2001, pp. 869–877. doi:10.1006/rwvb.2001.0150

[104] Y. LeCun, Y. Bengio, and G. Hinton, "Deep learning," *Nature*, vol. 521, pp. 436–444, 2015. doi:10.1038/nature14539

[105] S.-S. Bun, D. G. Latcu, F. Marchlinski, and N. Saoudi, "Atrial flutter: more than just one of a kind." *European heart journal*, vol. 36, pp. 2356–63, 2015. doi:10.1093/eurheartj/ehv118

[106] F. G. COSIO, F. ARRIBAS, M. LÓPEZ-GIL, and J. PALACIOS, "Atrial flutter mapping and ablation i," *Pacing and Clinical Electrophysiology*, vol. 19, pp. 841–853, 1996. doi:10.1111/j.1540-8159.1996.tb03368.x

[107] F. G. Cosío, A. Pastor, A. Núñez, A. P. Magalhaes, and P. Awamleh, "Atrial flutter: an update," *Revista Española de Cardiología (English Edition)*, vol. 59, pp. 816–831, 2006. doi:https://doi.org/10.1016/S1885-5857(07)60047-4

[108] E. P. Gerstenfeld, S. Dixit, R. Bala, et al., "Surface electrocardiogram characteristics of atrial tachycardias occurring after pulmonary vein isolation," *Heart Rhythm*, vol. 4, pp. 1136–1143, 2007. doi:10.1016/j.hrthm.2007.05.008

[109] P. Pascale, L. Roten, A. J. Shah, et al., "Useful electrocardiographic features to help identify the mechanism of atrial tachycardia occurring after persistent atrial fibrillation ablation," *JACC: Clinical Electrophysiology*, vol. 4, pp. 33–45, 2018. doi:10.1016/j.jacep.2017.07.018

[110] U. R. Acharya, H. Fujita, M. Adam, et al., "Automated characterization of arrhythmias using nonlinear features from tachycardia ecg beats," in *2016 IEEE International Conference on Systems, Man, and Cybernetics (SMC)*, 2016, pp. 000 533–000 538. doi:10.1109/SMC.2016. 7844294

[111] B. Taha, S. Reddy, J. Xue, and S. Swiryn, "Automated discrimination between atrial fibrillation and atrial flutter in the resting 12-lead electrocardiogram," *Journal of electrocardiology*, vol. 33 Suppl, pp. 123–5, 2000. doi:10.1054/jelc.2000.20303

[112] J. P. Zbilut, N. Thomasson, and C. L. Webber, "Recurrence quantification analysis as a tool for nonlinear exploration of nonstationary cardiac signals," *Medical Engineering & Physics*, vol. 24, pp. 53–60, 2002, non-linear Processing of Biomechanical Signals. doi: 10.1016/S1350-4533(01)00112-6

[113] U. R. Acharya, H. Fujita, V. K. Sudarshan, D. N. Ghista, W. J. E. Lim, and J. E. Koh, "Automated prediction of sudden cardiac death risk using kolmogorov complexity and recurrence quantification analysis features extracted from hrv signals," in *2015 IEEE International Conference on Systems, Man, and Cybernetics*, 2015, pp. 1110–1115. doi:10.1109/SMC.2015.199

[114] C. Nagel, G. Luongo, L. Azzolin, S. Schuler, O. Dössel, and A. Loewe, "Non-invasive and quantitative estimation of left atrial fibrosis based on p waves of the 12-lead ECG—a large-scale computational study covering anatomical variability," *Journal of Clinical Medicine*, vol. 10, 2021. doi:10.3390/jcm10081797

[115] C. Nagel, S. Schuler, O. Dössel, and A. Loewe, "A bi-atrial statistical shape model and 100 volumetric anatomical models of the atria," *zenodo*, 2020. doi:10.5281/zenodo.4309958

[116] Y. Miyasaka, M. E. Barnes, B. J. Gersh, et al., "Secular trends in incidence of atrial fibrillation in olmsted county, minnesota, 1980 to 2000, and implications on the projections for future prevalence," *Circulation*, vol. 114, pp. 119–125, 2006. doi:10.1161/CIRCULATIONAHA.105. 595140

[117] S. A. Colilla, A. Crow, W. Petkun, D. E. Singer, T. A. Simon, and X. Liu, "Estimates of current and future incidence and prevalence of atrial fibrillation in the u.s. adult population." *The American journal of cardiology*, vol. 112 8, pp. 1142–7, 2013. doi:10.1016/j.amjcard.2013.05. 063

[118] S. S. Virani, A. Alonso, E. J. Benjamin, et al., "Heart disease and stroke statistics—2020 update: A report from the american heart association," *Circulation*, vol. 141, pp. e139–e596, 2020. doi:10.1161/CIR.0000000000000757

[119] B. Müller-Edenborn, J. Minners, J. Allgeier, et al., "Rapid improvement in left ventricular function after sinus rhythm restoration in patients with idiopathic cardiomyopathy and atrial fibrillation," *EP Europace*, vol. 21, pp. 871–878, 2019. doi:10.1093/europace/euz013

[120] M. Anselmino, M. Matta, F. D'Ascenzo, et al., "Catheter Ablation of Atrial Fibrillation in Patients With Left Ventricular Systolic Dysfunction," *Circulation: Arrhythmia and Electrophysiology*, vol. 7, pp. 1011–1018, 2014. doi:10.1161/CIRCEP.114.001938

[121] L.-F. Hsu, P. Jaïs, P. Sanders, et al., "Catheter Ablation for Atrial Fibrillation in Congestive Heart Failure," *New England Journal of Medicine*, vol. 351, pp. 2373–2383, 2004. doi:10.1056/NEJMoa041018

[122] G. Hindricks, T. Potpara, N. Dagres, et al., "2020 ESC Guidelines for the diagnosis and management of atrial fibrillation developed in collaboration with the European Association for Cardio-Thoracic Surgery (EACTS): The Task Force for the diagnosis and management of atrial fibrillation of the European Society of Cardiology (ESC) Developed with the special contribution of the European Heart Rhythm Association (EHRA) of the ESC," *European Heart Journal*, vol. 42, pp. 373–498, 2020. doi:10.1093/eurheartj/ehaa612

[123] S. M. Narayan, T. Baykaner, P. Clopton, et al., "Ablation of rotor and focal sources reduces late recurrence of atrial fibrillation compared with trigger ablation alone: Extended follow-up of the confirm trial (conventional ablation for atrial fibrillation with or without focal impulse and rotor modulation)," *Journal of the American College of Cardiology*, vol. 63, pp. 1761–1768, 2014. doi:10.1016/j.jacc.2014.02.543

[124] M. A. Allessie, N. M. de Groot, R. P. Houben, et al., "Electropathological substrate of long-standing persistent atrial fibrillation in patients with structural heart disease," *Circulation: Arrhythmia and Electrophysiology*, vol. 3, pp. 606–615, 2010. doi:10.1161/CIRCEP.109.910125

[125] K. Padmavathi and K. S. Ramakrishna, "Classification of ecg signal during atrial fibrillation using autoregressive modeling," *Procedia Computer Science*, vol. 46, pp. 53–59, 2015, proceedings of the International Conference on Information and Communication Technologies, ICICT 2014, 3-5 December 2014 at Bolgatty Palace & Island Resort, Kochi, India. doi:10.1016/j.procs.2015.01.053

[126] G. MOE, "On the multiple wavelet hypothesis of atrial fibrillation," *Arch Int Pharmacodyn Ther*, vol. 140, p. 183, 1962.

[127] M. A. Allessie, "Experimental evaluation of moe's multiple wavelet hypothesis of atrial fibrillation," *Card Electrophysiol Arrhythm.*, pp. 265–275, 1985.

[128] S. Zlochiver, M. Yamazaki, J. Kalifa, and O. Berenfeld, "Rotor meandering contributes to irregularity in electrograms during atrial fibrillation," *Heart Rhythm*, vol. 5, pp. 846–854, 2008. doi:10.1016/j.hrthm.2008.03.010

[129] B. J. Hansen, J. Zhao, T. A. Csepe, et al., "Atrial fibrillation driven by micro-anatomic intramural re-entry revealed by simultaneous sub-epicardial and sub-endocardial optical mapping in explanted human hearts," *European Heart Journal*, vol. 36, pp. 2390–2401, 2015. doi:10.1093/eurheartj/ehv233

[130] U. R. Acharya, H. Fujita, O. S. Lih, Y. Hagiwara, J. H. Tan, and M. Adam, "Automated detection of arrhythmias using different intervals of tachycardia ecg segments with convolutional neural network," *Information Sciences*, vol. 405, pp. 81–90, 2017. doi:https://doi.org/10.1016/j.ins.2017.04.012

List of Publications and Supervised Theses

Journal Articles

- **G. Luongo**, G. Vacanti, V. Nitzke, D. Nairn, C. Nagel, D. Kabiri, T.P. Almeida, D.C. Soriano, M.W. Rivolta, G.A. Ng, O. Dössel, L. Armin, R. Sassi, and A. Loewe *Hybrid Machine Learning to Localize Atrial Flutter Substrates Using the Surface 12-lead ECG*, EP Europace 2021
- **G. Luongo**, L. Azzolin, S. Schuler, M.W. Rivolta, T.P. Almeida, J.P. Martínez, D.C. Soriano, L. Armin, B. Müller-Edenborn, A. Jadidi, O. Dössel, , R. Sassi, P. Laguna, and A. Loewe *Machine learning enables noninvasive prediction of atrial fibrillation driver location and acute pulmonary vein ablation success using the 12-lead ECG*, Cardiovascular Digital Health Journal 2021;2(2):126-136
- **G. Luongo**, S. Steffen, L. Armin, T.P. Almeida, D.C. Soriano, O. Dössel, and A. Loewe *Non-Invasive Characterization of Atrial Flutter Mechanisms Using Recurrence Quantification Analysis on the ECG: A Computational Study*, IEEE Transactions on Biomedical Engineering 2020;68(3):914-925
- M. Vila, M.W. Rivolta, **G. Luongo**, L.A. Unger, A. Luik, L. Gigli, F. Lombardi, A. Loewe, and R. Sassi *Atrial flutter mechanisms detection using directed network mapping*, Frontiers in Physiology 2021,12:1835
- O. Dössel, **G. Luongo**, C. Nagel, A. Loewe *Computer Modeling of the Heart for ECG Interpretation—A Review*, Hearts 2021,2(3):350–368
- C. Nagel, **G. Luongo**, L. Azzolin, S. Schuler, O. Dössel, A. Loewe *Non-Invasive and Quantitative Estimation of Left Atrial Fibrosis Based on P Waves of the 12-Lead ECG—A Large-Scale Computational Study Covering Anatomical Variability*, Journal of Clinical Medicine 2021,10(8):1797
- J. Sánchez, **G. Luongo**, M. Nothstein, L.A. Unger, J. Saiz, B. Trenor, A. Luik, O. Dössel, A. Loewe *Using Machine Learning to Characterize Atrial Fibrotic Substrate From Intracardiac Signals With a Hybrid and Dataset*, Frontiers in Physiology 2021,12:699291

Journal Articles Under Review

- **G. Luongo**, F. Rees, D. Nairn, M.W. Rivolta, O. Dössel, R. Sassi, C. Ahlgrim, L. Mayer, F.J. Neumann, T. Arentz, A. Jadidi, A. Loewe, and B. Müller-Edenborn *Machine Learning Using a Single-lead ECG to Identify Patients with Atrial Fibrillation-Induced Heart Failure*, under review 2021;-(-):

Refereed Conference Articles

- **G. Luongo**, S. Schuler, M.W. Rivolta, O. Dössel, R. Sassi, and A. Loewe *Semi-supervised vs. Supervised Learning for Discriminating Atrial Flutter Mechanisms Using the 12-lead ECG*, 2021 Computing in Cardiology, Brno, Czech Republic, 2021
- **G. Luongo**, S. Steffen, M.W. Rivolta, O. Dössel, R. Sassi, and A. Loewe *Automatic ECG-based Discrimination of 20 Atrial Flutter Mechanisms: Influence of Atrial and Torso Geometries*, 2020 Computing in Cardiology, vol. 47, Rimini, Italy, 2020
- **G. Luongo**, L. Azzolin, M. W. Rivolta, T. P. Almeida, J. P. Martínez, D.C. Soriano, O. Dössel, R. Sassi, P. Laguna, and A. Loewe *Machine Learning to Find Areas of Rotors Sustaining Atrial Fibrillation from the ECG*, 2020 Computing in Cardiology, vol. 47, Rimini, Italy, 2020
- A.S. Bezerra, T. Yoneyama, D.C. Soriano, **G. Luongo**, X. Li, F. Ravelli, M. Masè, G.S. Chu, P.J. Stafford, F.S. Schlindwein, G.A. Ng, and T.P. Almeida *Optimizing Atrial Electrogram Classification Based on Local Ablation Outcome in Human Atrial Fibrillation*, 2020 Computing in Cardiology, vol. 47, Rimini, Italy, 2020
- L. Azzolin, **G. Luongo**, S.R. Ventura, J. Saiz, O. Dössel, and A. Loewe *Influence of Gradient and Smoothness of Atrial Wall Thickness on Initiation and Maintenance of Atrial Fibrillation*, 2020 Computing in Cardiology, vol. 47, Rimini, Italy, 2020
- **G. Luongo**, L. Azzolin, M.W. Rivolta, R. Sassi, J.P. Martìnez, P. Laguna, O. Dössel, and A. Loewe *Non-invasive identification of atrial fibrillation driver location using the 12-lead ECG: pulmonary vein rotors vs. other locations*, 42th Annual International Conference of the IEEE Engineering in Medicine and Biology Society (EMBC), Montréal, Canada, 2020

Refereed Conference Abstracts

- M. Vila, M.W. Rivolta, **G. Luongo**, A. Loewe, and R. Sassi *Directed network mapping hints the ablation strategy for atrial flutter: a proof of concept*, Atrial Signals 2021, Karlsruhe, Germany, 2021

- **G. Luongo**, G. Vacanti, D. Kabiri, S. Schuler, T.P. Almeida, D.C. Soriano, M.W. Rivolta, G.A. Ng, R. Sassi, O. Dössel, and A. Loewe *B-PO05-151 Automatic Classification of Macro-reentrant Atrial Tachycardia Mechanisms Using 12-lead ECG*, Heart Rhythm 21, vol. 18, no. 8, pp. S433-S434, Rimini, Italy, 2020
- **G. Luongo**, S. Schuler, M.W. Rivolta, O. Dössel, R. Sassi, and A. Loewe *Automatic classification of 20 different types of atrial tachycardia using 12-lead ECG signals*, European Heart Rhythm Association (EHRA) conference, Vienna, Austria, 2020
- **G. Luongo**, S. Schuler, M.W. Rivolta, O. Dössel, R. Sassi, and A. Loewe *Automatic Classification of 20 Different Types of Atrial Flutter Using 12-Lead ECG Signals: a Preliminary Computational Study*, Atrial Signals 2019, Bordeaux, France, 2019
- **G. Luongo**, S. Schuler, O. Dössel, and A. Loewe *12-Lead ECG Feature Identification to Discriminate Different Types of Atrial Flutter*, 41st Annual International Conference of the IEEE Engineering in Medicine and Biology Society (EMBC), Berlin, Germany, 2019
- **G. Luongo**, S. Schuler, T.P. Almeida, D.C. Soriano, O. Dössel, and A. Loewe *Discrimination of Atrial Flutter on Simulated 12-Lead-ECG Signals by Applying Biosignal Processing*, Gordon Research Conference - Cardiac Arrhythmia Mechanisms, Lucca, Italy, 2019

Invited Talks

- What can we learn about AFlut and AFib from the ECG using machine learning?, Atrial Signals 2021, Karlsruhe, Germany, 2021
- Machine Learning in Atrial Fibrillation, 2020 Computing in Cardiology, Rimini, Italy 2020

Supervised Student Theses

- Vincent Nitzke, *Implementation of AF and AFl simulations, and 12-lead ECG classification*, Student's Project, Institute of Biomedical Engineering, Karlsruhe Institute of Technology (KIT), 2021
- Anne Bernhart, *Automatic localization of atrial focal sources using the 12-lead ECG*, Bachelor's Thesis, Institute of Biomedical Engineering, Karlsruhe Institute of Technology (KIT), 2021
- Moritz Linder, *Machine learning approaches for a 20 AFl classification using BSPM and RQA images*, Master's Thesis, Institute of Biomedical Engineering, Karlsruhe Institute of Technology (KIT), 2020
- Vincent Nitzke, *Non-invasive atrial rotors and focal sources characterization using ECG*, Bachelor's Thesis, Institute of Biomedical Engineering, Karlsruhe Institute of Technology (KIT), 2020

- Kevin Hii, *Data Augmentation: Repositioning of atria in the torso to produce new 12-lead ECG signals*, Bachelor's Thesis, Institute of Biomedical Engineering, Karlsruhe Institute of Technology (KIT), 2020

Patent Applications

G. Luongo, A. Jadidi, A. Loewe, and B. Müller-Edenborn "Algorithm to identify patients with atrial fibrillation-induced heart failure," 2021

Awards

- Preis für Patientensicherheit in der Medizintechnik, 2nd prize, *Machine learning enables noninvasive prediction of atrial fibrillation driver location and acute pulmonary vein ablation success using the 12-lead ECG*, by the Deutsche Gesellschaft für Biomedizinische Technik (DGBMT), 2021